The Dissertation Committee for Jiabei Yuan Certifies that this is the approved version of the following dissertation:

Field Studies Comparing SASW, Beamforming and MASW Test Methods and Characterization of Geotechnical Materials Based on V_s

Committee:

Kenneth H. Stokoe II, Supervisor

Clark R. Wilson

Robert B. Gilbert

Loukas F. Kallivokas

Sung-Ho Joh

Brady R. Cox

Field Studies Comparing SASW, Beamforming and MASW Test Methods and Characterization of Geotechnical Materials Based on V_s

by

Jiabei Yuan, B.E.; M.E.

Dissertation

Presented to the Faculty of the Graduate School of

The University of Texas at Austin

in Partial Fulfillment

of the Requirements

for the Degree of

DOCTOR OF PHILOSOPHY

The University of Texas at Austin

August 2011

Dedicated

to

My Parents and My Wife

Acknowledgements

Field Studies Comparing SASW, Beamforming and MASW Test Methods and Characterization of Geotechnical Materials Based on V_s

Jiabei Yuan, PhD

The University of Texas at Austin, 2011

Supervisor: Kenneth H. Stokoe II

Estimating S-wave velocities (V_s) from Rayleigh-wave velocities (V_R) is widely used in field seismic testing for geotechnical engineering purposes.   In this research, two widely used surface-wave methods, the Spectral-Analysis-of-Surface-Waves (SASW) and Multichannel-Analysis-of-Surface-Waves (MASW) methods, are evaluated and compared in field experiments. F-K and Beamforming transforms are also evaluated to investigate the effectiveness of both techniques in determining experimental dispersion curves from synthetic and field data.

An experimental parametric study was undertaken for the MASW method. Conventional seismic sources in the SASW method are sledge hammers, bulldozers and vibroseises. For MASW testing, sledge hammers and small shakers are usually used as the seismic sources. In this research, MASW testing was performed with traditional and non-traditional sources at a site owned by the City of Austin, Texas. Experimental dispersion curves and V_s profiles from SASW tests are used as references for the field parametric study with the MASW method. The source type, source offset, receiver spacing and number of receivers were varied to evaluate the impact of each variable on

the field experimental dispersion curve. Two type of receivers, 1-Hz and 4.5-Hz natural-frequency geophones, were also compared in these tests.

The second part of this research involved studying the use of characterizing geotechnical materials based on V_s. This work included two projects. The first project involved basalt on the Big Island of Hawaii. To develop empirical ground motion prediction models for the purpose of earthquake hazard mitigation and seismic design on the Big Island, the subsurface site conditions beneath 22 strong-motion stations were investigated by SASW tests. V_s profiling was performed to depths of more than 100 ft. V_{s30}, the average V_s in the top 30 m, was also calculated to assign NEHRP site classes to different testing locations. Different materials, mainly thought to be stiff basalt, were characterized and grouped based on the V_s values. These groups were then compared with reference curves for sand and gravel (Menq, 2003) to differentiate the groups.

The second project dealing with characering geotechnical materials based on V_s involved of soil/rock profiles at a project site in British Columbia, Canada. The goals in terms of this research were to: (1) compare the V_s profiles from the different test locations to investigate the stiffnesses of different geologic materials, the variability in the material stiffnesses, and the estimated depth to bedrock, and (2) to compare the V_s profiles to existing geological and geotechnical information such as nearby boreholes, cone penetration tests and seismic cone penetration tests. Good agreement between SASW V_s profiles and boring records is expected when lateral variability at the site is low. However, when lateral variability is significant, then the difference between localized measurements, like borings and CPT results, and global measurements, like SASW V_s results, can further contribute to understanding the site conditions as shown at the site in British Columbia, Canada.

Table of Contents

List of Tables

List of Figures

xxii

xxvi

xxix

Chapter 1   Introduction

1.1 BACKGROUND

The recent 8.9-magnitude earthquake occurred near the east coast of Japan and its devastating effect on the Fukushima nuclear power plants emphasized the need for continued research in the area of soil-structure interaction during dynamic loading in geotechnical earthquake engineering. Under cyclic or dynamic loading conditions like foundation vibrations or earthquake shaking, soil exhibits behaviors that are strongly controlled by the strain level. The soil behavior is often represented by strain-level dependant modulus and damping. Correct estimates of modulus (stiffness) and damping (dissipative) characteristics of geotechnical materials (gravel, sand, silt, etc) play a critical role in structural design and site response analysis (Gazetas, 1982 and Kramer, 1996).

Dynamic properties of soil can be measured both in laboratory and field tests. The advantages of laboratory dynamic testing (for example, combined resonant column and torsional shear tests and cyclic simple shear tests) are that relationships between stiffness, damping, strain and pressure can be defined for samples under undisturbed or remolded conditions. However, in order to obtain representative knowledge of the dynamic soil characteristics at a specific site, soil samples from different depths at a number of locations need to be tested. To better characterize the site, small-strain seismic field tests are combined with dynamic laboratory tests in evaluating the stiffness of soil in the undisturbed state. Dynamic field tests, which evaluate stiffness properties by measuring seismic wave velocities are very important due to their advantages in making undisturbed measurement over large area of the site at relatively low costs. These advantages are especially true for field seismic methods that involve surface wave measurements.

Typical field seismic testing techniques can be divided into two groups: intrusive and nonintrusive. Intrusive seismic tests include crosshole, downhole, seismic cone penetration test (SCPT) and P-S suspension logging. Intrusive testing requires one or more boreholes to perform and generally compression (P) and shear wave (S) velocities are measured. The one exception is the SCPT which often does not work well for P-wave measurements. One of the features of intrusive testing is that the measured wave velocities are generally quite localized if only one or two boreholes are involved, thus the sampling is more like that of traditional geotechnical field measurement, for example, standard penetration tests (SPT), cone penetration tests (CPT) or other borehole tests. However, when strong lateral variability or irregular underground anomalies exist at sites, the credibility of any localized field testing can be questioned.

Nonintrusive field seismic testing techniques are generally evolved from the theory of seismic wave propagation in earth. The most common non-intrusive tests are refraction and reflection tests. These two techniques are widely used in geophysical exploration to detect layering, material boundaries, anomalies, water table and etc. The exploration depth of these techniques can go to thousands of feet deep. For geotechnical site investigation, the interested depth of material is generally within the top 30 to 60 m.

Spectral-Analysis-of-Surface-Waves (SASW) and Multichannel-Analysis-of-Surface-Waves (MASW) are the two non-intrusive dynamic testing in site characterization. Both methods are based on the fundamental theory of surface wave propagation in a multi-layered medium. Surface waves are stress waves that propagate along the vertically-oriented surfaces. They propagate slower than body waves, but they attenuate slower, possess larger fraction of energy as waves travel further away from source,. Since the characteristics of propagation and attenuation of surface waves are related to the physical properties of the near-surface medium, surface waves are well

suited to characterize geotechnical sites. An example of surface wave propagation is illustrated in Figure 1.1.
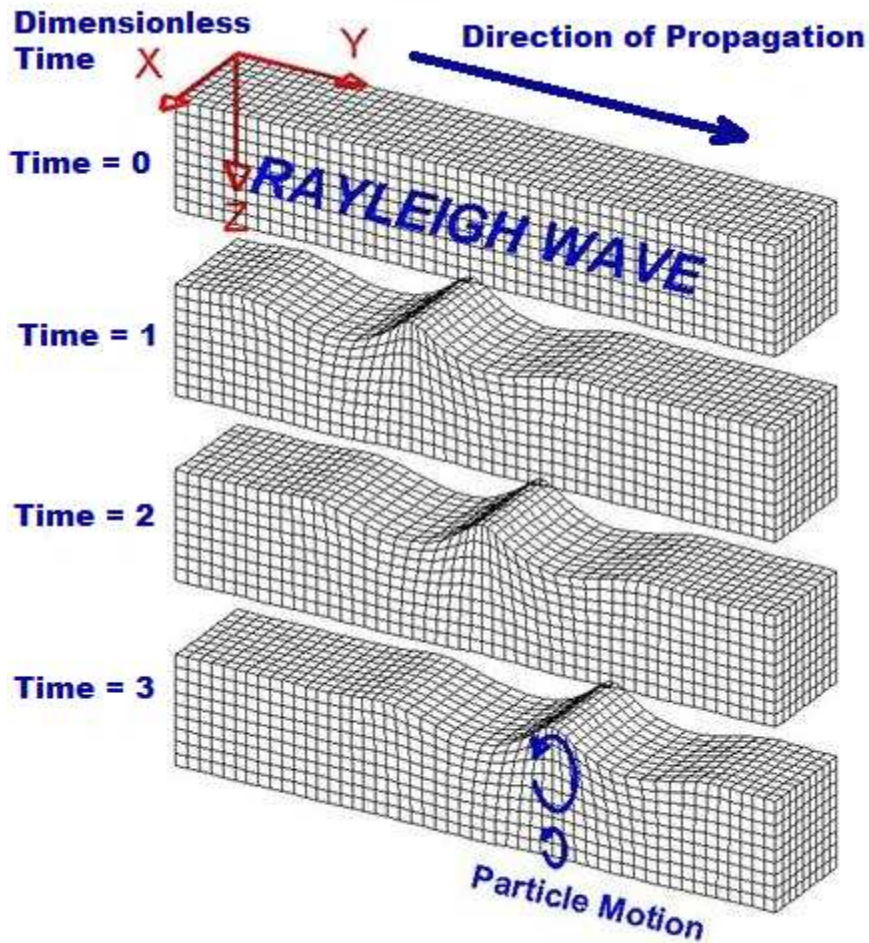
Figure 1.1   Example of Surface Wave Propagation and Particle Motion (after Lawrence Brail, http://www.geo.mtu.edu/UPSeis/waves.html)

Field surface wave tests generate shear wave velocity profiles, which can be used in building design, site characterization and seismic site response analysis: (1) combined with available or estimated information of material density, shear modulus, G, is calculated from $G = \rho \cdot V_s^2$; (2) measured shear wave velocity profiles can be compared with empirical equations of shear wave velocity for various materials and existing geological information to better characterize material distribution along depth; (3) V_{s30}, shear wave velocity averaged over the top 30m of soil, is an important parameter for evaluating dynamic behavior of soil.. Both the NEHRP Provisions and the Uniform Building Code use V_{s30} to classify sites according to type of soil for earthquake response analysis.

1.2 OBJECTIVES OF RESEARCH

The objective of this research are to:(1) to carry out field parametric studies on surface wave methods(SASW and MASW) with different test setups, and (2) to interpret test results(V_s profiles) from SASW and MASW without comparable geological information at testing sites, (3) to estimate material distribution whereas geological profiles exist at the sites.

Shear wave velocity profiles are the product of field surface wave tests. To better interpret material type and distribution at testing sites, V_s profiles can be divided and regrouped based on empirical equation of shear wave velocity for soft soil, sand and gravel. Idriss (1976) estimated behavior of soft clays under earthquake loading conditions. Hardin (1978) discovered and related small-strain shear moduli to void ratio and effective stress of soils. Menq (2003) built a comprehensive empirical equation for sand and gravel with different geotechnical parameters (C_u, D_{50}, etc.,) using data from laboratory dynamic tests at the University of Texas at Austin. Comparison studies for characterizing material distribution with V_s profiles based on above empirical equations

are used in this context. Shear wave velocity profiles from two projects, one at Hawaii Main Island and another in British Columbia, Canada, were characterized and regrouped based on material distribution. Identified material distribution from the second site were then compared with existing nearby geological information (CPT, SPT, boring and SCPT) to demonstrate the effectiveness of this method.

1.3 ORGANIZATION OF DISSERTATION

The dissertation has been organized in three different parts. The first part is to provide an insight into the characteristic of surface waves in soil system and its application in site characterization. The second part presents the parametric study of field surface wave testing at Hornsby Bend, Austin, Texas. The remaining part presents some applications of the methods in two projects and conclusions.

A briefly introduction of wave propagation in homogeneous isotropic media is shown in Chapter 2. This introduction is followed by a demonstration of how dispersion of surface waves forms in a layered system. Characteristics of Rayleigh wave dispersion is discussed accordingly. Several dominant methods, transfer matrix method (Knopoff, 1964, Youhua, 2001) and dynamic stiffness matrix methods (Kausel and Rosset, 1981) are briefly presented and discussed. Several theoretical soil models are built to present the impact of model parameters (layer thickness, density, V_s and V_p) on the shape of dispersion curves.

The history and development of surface wave tests in geotechnical engineering are introduced in Chapter 3. The chapter starts with the introduction of steady-state Rayleigh wave test developed in early 60s by Jones (1958, 1962) in United States. Invention of SASW testing in geotechnical area by Nazarian and Stokoe(1983) is then presented. Introduction of MASW in geotechnical site investigation by Park (Park, 1999)

is discussed and compared with SASW method. Development of both tests in forward modeling and inversion process are presented.

In Chapter 4, results are presented from the numerical simulation to validate the effectiveness of SASW, beamforming and F-K techniques in determining the dispersion curves from the synthetic seismograms. The synthetic wavefields were generated by FitSASW, a software based on the 3-D solution of dynamic stiffness matrix method. The studies are made by comparing the theoretical solutions from both transfer matrix method, which presented as modal phase velocities, and dynamic stiffness method, which presented as apparent phase velocities, with the calculated dispersion curves from SASW, beamforming and F-K techniques. Three models are used in generating the synthetic seismograms: a bedrock model, a normally dispersive model and a "sandwich" model where a low velocity zone is set as an interbed between the top layer and the halfspace.

A comprehensive parametric study on source type, receiver type and test set-up of surface wave testing at Hornsby Bend site is presented in Chapter 5 and 6. Chapter 5 summarizes test procedures for SASW and MASW methods as well as all test setups. Different source signals (chirp, step-sine and Ricker Wavelet) with different frequency components are used both in SASW and MASW tests. Sledge hammers, T-Rex and Liquidator, two powerful vibroseis own by the University of Texas at Austin, are seismic sources used in generating vibrations. Two types of geophones (vertical velocity transducers), one with a resonant frequency of 1Hz, another 4.5Hz, are used as receivers with different spacings in both tests. For MASW test, source-to-receiver spacing, number of geophones and geophone spacing are parametrically studied. Results from SASW and MASW are compared and discussed in terms of both dispersion curves and shear wave velocity profiles in Chapter 6. A few signal processing techniques is explored and applied

in both tests. CPT results, along with a boring log at Hornsby Bend site are then compared with V_s profiles from SASW and MASW tests.

A discussion of how shear wave velocity profiles is further interpreted into different material type and distribution is presented in Chapter 7 and 8. In Chapter 7, spectral-analysis-of-surface-waves (SASW) surveys were performed in Hawaii Main Island to obtain V_s information beneath the 22 USGS strong motion sites. Criteria for dividing and regrouping V_s profiles are proposed by using empirical sand and gravel V_s curves as references. Each site is assigned with a NEHRP site class based on V_{s30} measured at the site. Chapter 8 provides finding and characterization of site based on shear wave velocities from SASW and SCPT tests, and other geological information from CPT, SPT and boring logs. Comparison of material identification from SASW and other tests are shown. The study demonstrates that in many situations V_s profiling with SASW can contribute to improved subsurface information and better interpretation for geotechnical site investigations.

Summary, conclusions, and recommendations are presented in Chapter 9.

Chapter 2 Surface Wave Propagation and Dispersion

2.1 INTRODUCTION

Body and surface waves are generated by natural or human excitation on the ground surface or at depth. The velocities of these waves are directly related to the physical properties of the propagation medium. In this chapter, the fundamentals of surface wave propagation and dispersion are reviewed.

Body waves, compression waves (P) and shear waves (S), propagate through the interior of medium as well as on the surface. P waves are pressure waves that can travel through all types of materials. The direction of particle motions is parallel to the direction of propagation as shown in Figure 2.1a. S waves are slower than P-waves and displace the medium perpendicular to the direction of propagation (See Figure 2.1b). According to the polarization of particle motion, S waves with particle motion in a vertical plane are classified as SV-waves; whereas S waves with particle motion in horizontal plane are identified as SH-waves. Shear waves do not propagate in air or fluids, such as water.

Surface waves occur at the interface between two different medium. In a layered halfspace, two types of surface waves are generally encountered: Love waves (L) and Rayleigh waves (R) (Figure 2.1c and d, respectively). Love waves, mathematically predicted by Love (Love, 1911), travel in a similar pattern of transverse motion like SH-waves. Rayleigh waves, theoretically discovered and proven by Lord Rayleigh (Rayleigh, 1885), exhibit both longitudinal and transverse motion in the vertical plane, where retrograde elliptic motion is observed at the surface.

The phenomenon that body waves and surface waves gradually lose energy as they propagate through a medium is defined as attenuation. Uniform material attenuation
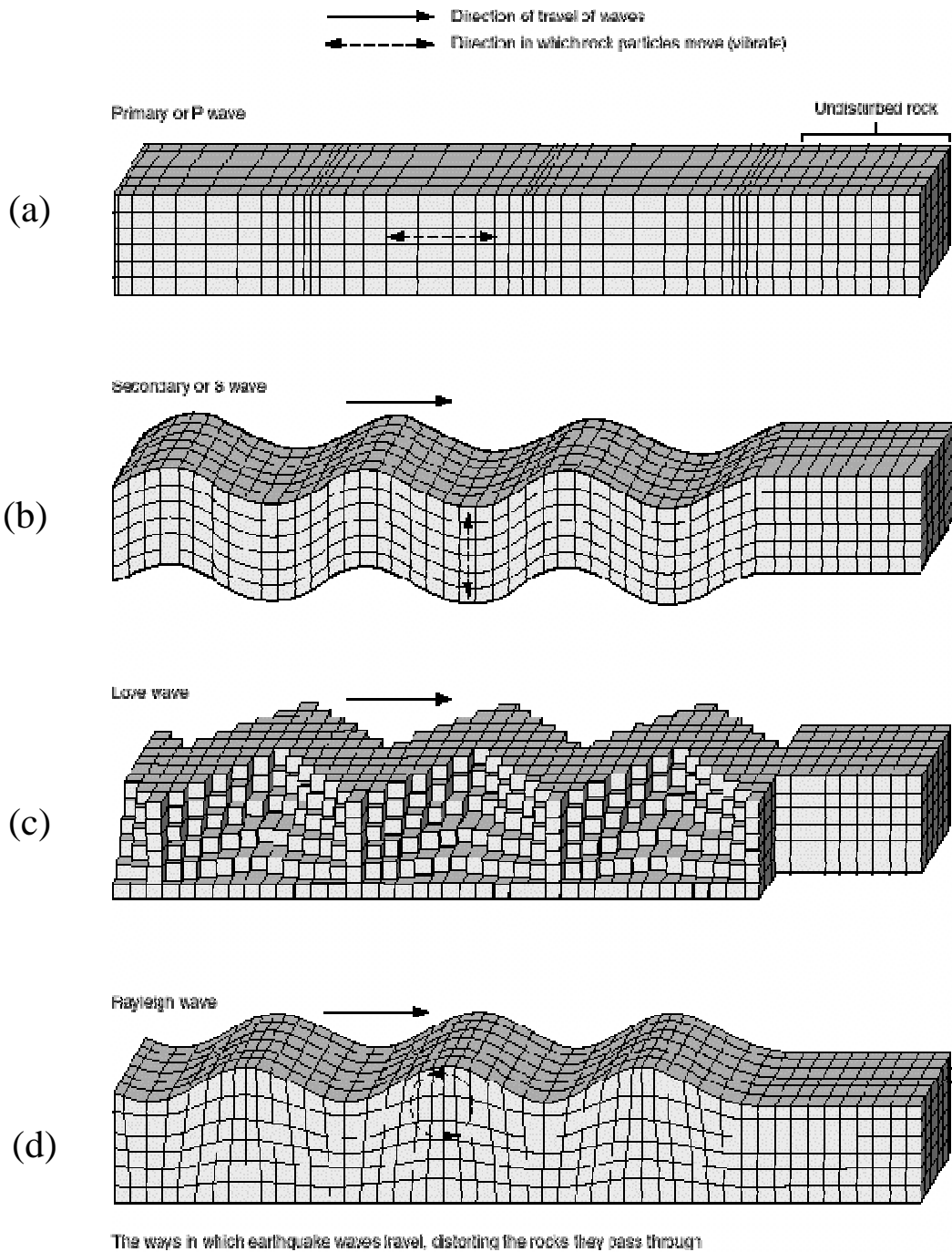
Figure 2.1   Illustration of Particle Motion and Propagation of Four Seismic Waves
(Bolt, 1976)

is due to two basic mechanisms: geometric attenuation and material attenuation (Aki and Richards, 1980). In a uniform material, geometric attenuation occurs because the amplitude of the wave decreases as the wavefront spreads over a larger volume when it travels away from the source point. When body waves propagate along the free surface of a uniform halfspace as shown in Figure 2.2, geometric attenuation of body waves is proportional to $1/r^2$, where r stands for the distance of wavefront from source point. The geometric attenuation of body waves in an infinite body is proportional to $1/r$. In contrast, Rayleigh waves, which propagate along material interfaces, have a geometric attenuation proportional to $1/r^{0.5}$ (Richart et al. 1970). An illustration of wave propagation and attenuation for body and Rayleigh waves is shown in Figure 2.2. In terms of vertical displacement, since R waves attenuate more slowly than body waves, the relative amplitude between Rayleigh waves and body waves increases as wavefront propagates further from the source.
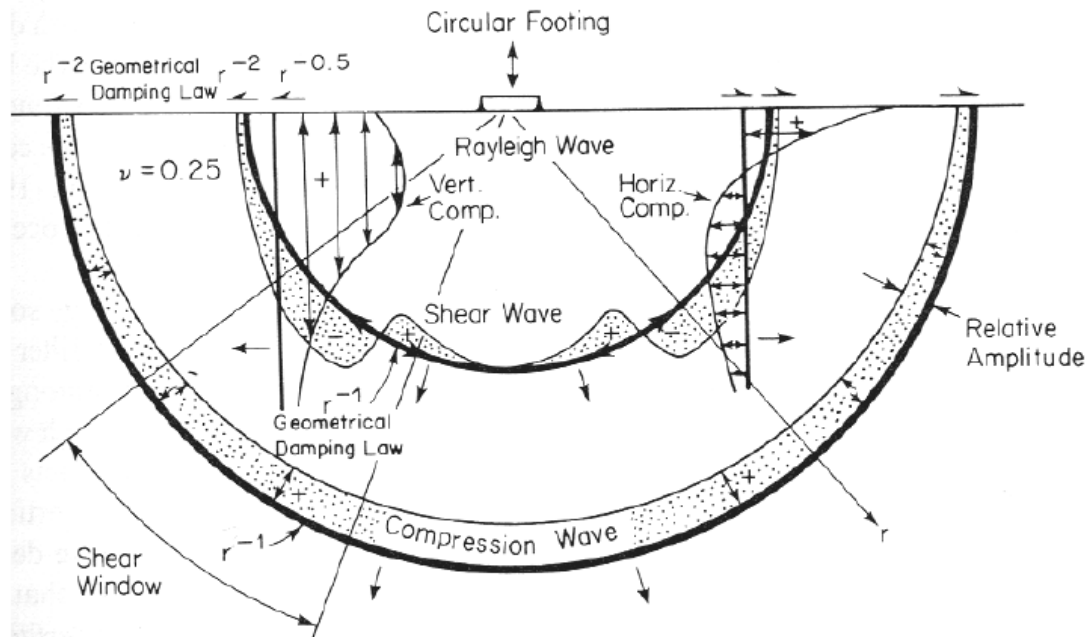
Figure 2.2   Example of Body Waves and Surface Waves Generated by a Circular
             Footing on a Homogeneous, Isotropic, Elastic Half-space (Richart, 1970)

2.2 PHYSICAL PROPERTIES

Waves are defined as disturbances that travel in medium with energy. Displacements at the ground surface or depth are captured by sensors to calculate wave velocity, and mechanical properties of the medium. Relationship between body wave velocities and elastic constants are:

$$V_P = \sqrt{\frac{E(1-v)}{\rho(1-2v)(1+v)}}$$ (2.1)

$$V_S = \sqrt{\frac{G}{\rho}} = \sqrt{\frac{E}{2\rho(1+v)}}$$ (2.2)

E = Young's Modulus,

G = Shear Modulus,

ν = Poisson's Ratio,

ρ = density.

Elastic properties that are widely used in engineering are summarized in Table 2.1. The relationships between the elastic constants are listed in Table 2.2.

Table 2.1   Definition of Elastic Constants

Name	Symbol	Definition
Young' Modulus	E	longitudinal stress / longitudinal strain for uniaxial loading
Shear Modulus	G	shear stess / shear strain
Bulk Modulus	K	hydrostatic pressure / volumetric strain
Poisson's Ratio	ν	longitudinal strain / transversal strain for uniaxial loading

Table 2.2   Relationships Among Mechanical Properties of Medium (http://www.efunda.com).

Input Constants	Output Relations				
	$E =$	$\nu =$	$G =$	$K =$	$\lambda =$
E, ν	-	-	$\dfrac{E}{2(1+\nu)}$	$\dfrac{E}{3(1-2\nu)}$	$\dfrac{E\upsilon}{(1+\nu)(1-2\nu)}$
E, G	-	$\dfrac{E-2G}{2G}$	-	$\dfrac{EG}{3(3G-E)}$	$\dfrac{G(E-2G)}{3G-E}$
E, K	-	$\dfrac{3K-E}{6K}$	$\dfrac{3KE}{9K-E}$	-	$\dfrac{3K(3K-E)}{9K-E}$
E, λ	-	$\dfrac{2\lambda}{E+\lambda+R}$	$\dfrac{E-3\lambda+R}{4}$	$\dfrac{E+3\lambda+R}{6}$	-
ν, G	$2G(1+\nu)$	-	-	$\dfrac{2G(1+\nu)}{3(1-2\nu)}$	$\dfrac{2G\nu}{1-2\nu}$
ν, K	$3K(1-2\nu)$	-	$\dfrac{3K(1-2\nu)}{2(1+\nu)}$	-	$\dfrac{3K\nu}{1+\nu}$
ν, λ	$\dfrac{\lambda(1+\nu)(1-2\nu)}{\nu}$	-	$\dfrac{\lambda(1-2\nu)}{2\nu}$	$\dfrac{\lambda(1+\nu)}{3\nu}$	-
G, K	$\dfrac{9KG}{3K+G}$	$\dfrac{3K-2G}{6K+2G}$	-	-	$\dfrac{3K-2G}{3}$
G, λ	$\dfrac{G(3\lambda+2G)}{\lambda+G}$	$\dfrac{\lambda}{2(\lambda+G)}$	-	$\dfrac{3\lambda+2G}{3}$	-
K, λ	$\dfrac{9K(K-\lambda)}{3K-\lambda}$	$\dfrac{\lambda}{3K-\lambda}$	$\dfrac{3}{2}(K-\lambda)$	-	-

2.3 FORMATION OF RAYLEIGH WAVES

Rayleigh waves can be described by a horizontal displacement-potential function, φ, representing P-waves and a vertical displacement-potential function, ψ, representing S-waves:

$$V_p^2 \nabla^2 \varphi = \frac{\partial^2 \varphi}{\partial t^2} \tag{2.3}$$

$$V_s^2 \nabla^2 \psi = \frac{\partial^2 \psi}{\partial t^2} \tag{2.4}$$

V_p = Compression wave velocity,

V_s = Shear wave velocity,

(a) A Uniform Halfspace   (b) A Layered System
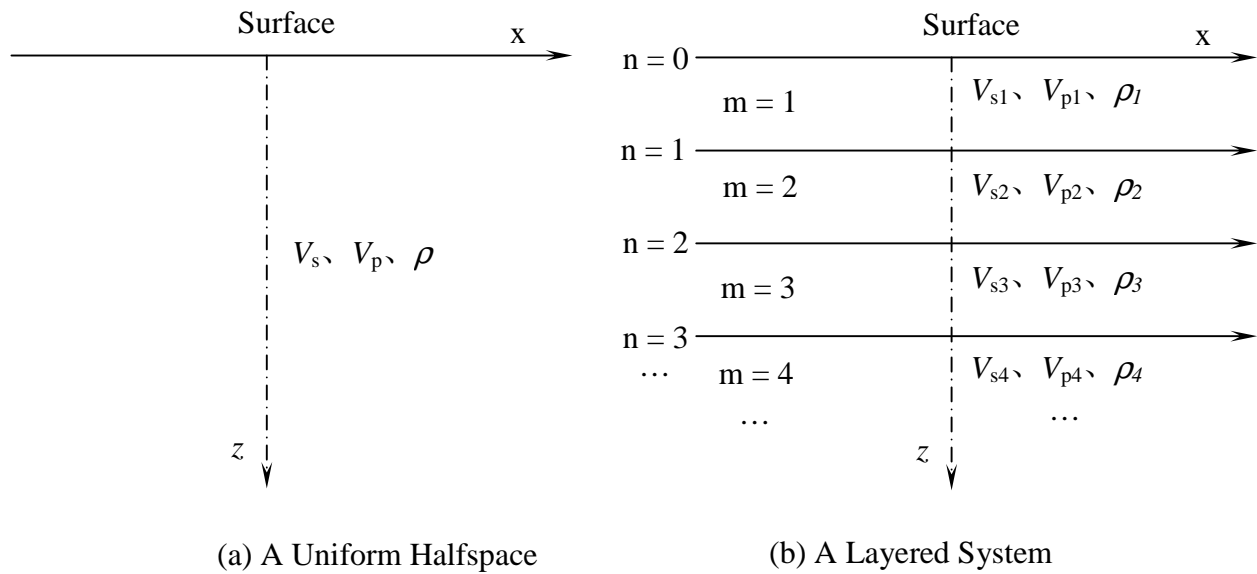
Figure 2.3   Illustration of Two Isotropic Halfspace Models

Two models shown in Figure 2.3 are used in discussing the formation of Rayleigh waves in solid: (1) an isotropic, homogeneous halfspace, and (2) an isotropic, homogeneous layered system.

2.3.1 Rayleigh Waves in a Uniform Halfspace

In Figure 2.3(a), the x-axis is both the direction of Rayleigh wave propagation and particle motion, and the z-axis is the direction of R-wave vertical motion. Two potential functions proposed to satisfy the conditions in Equations (2.3) and (2.4) are (Yang, 1993):

$$\varphi(x, z, t) = \Phi(z) \cdot \exp[ik(x - V_R \cdot t)] \tag{2.5}$$

$$\psi(x, z, t) = \Psi(z) \cdot \exp[ik(x - V_R \cdot t)] \tag{2.6}$$

where: $i = \sqrt{-1}$,

t = time,

k = wavenumber,

V_R = Rayleigh wave velocity.

The relationship between wavenumber, k, Rayleigh wavelength, λ_R and frequency, f, is:

$$k = \frac{2\pi f}{V_R} = \frac{2\pi}{\lambda_R} \tag{2.7}$$

Substituting Equations (2.5) and (2.6) into Equations (2.3) and (2.4) yields:

$$\Phi''(z) + k^2 \left(\frac{V_R^2}{V_P^2} - 1 \right) \Phi(z) = 0 \tag{2.8}$$

$$\Psi''(z) + k^2 \left(\frac{V_R^2}{V_S^2} - 1 \right) \Psi(z) = 0 \tag{2.9}$$

Several solutions can be derived from Equation (2.8) and (2.9) depending on the relationship among V_R, V_S and V_P. Since only the condition that $V_R < V_S$ is related to the interest of this paper, solutions of Equation based on $V_R < V_S$ are:

$$\Phi(z) = A_1 e^{k v_1 z} + A_2 e^{-k v_2 z} \tag{2.10}$$

$$\Psi(z) = B_1 e^{k v_2 z} + B_2 e^{-k v_2 z} \tag{2.11}$$

where $v_1 = \sqrt{1 - \left(\frac{V_R}{V_P} \right)^2}$, $v_2 = \sqrt{1 - \left(\frac{V_R}{V_S} \right)^2}$, and A_1, A_2, B_1, B_2 are constants.

Physically as depth approaches infinite, the amplitude of waves goes to zero. Therefore, $A_1 = B_1 = 0$. Substituting A_2 and B_2 by A and B, Equations (2.5) and (2.6) can be converted to:

$$\varphi\,(x,z,t) = Ae^{-kv_1 Z} \cdot \exp[ik(x - V_R t)] \qquad (2.12)$$

$$\psi\,(x,z,t) = Be^{-kv_2 Z} \cdot \exp[ik(x - V_R t)] \qquad (2.13)$$

Equations (2.12) and (2.13) stands for a Rayleigh wave traveling with a velocity of V_R in the halfspace. The amplitude decreases in an exponential pattern along depths, indicating energy of Rayleigh waves concentrates within a certain depth.

On the free surface, boundary conditions are applied as normal and shear stresses are zero:

$$\sigma_z\big|_{z=0} = 0 \qquad (2.14)$$

$$\tau_{zx}\big|_{z=0} = 0 \qquad (2.15)$$

A linear elastic material has the following stress-strain relations:

$$\sigma_z = \lambda\left(\frac{\partial u_x}{\partial x} + \frac{\partial u_z}{\partial z}\right) + 2G\frac{\partial u_z}{\partial z} \qquad (2.16)$$

$$\tau_{zx} = G\left(\frac{\partial u_z}{\partial x} + \frac{\partial u_x}{\partial z}\right) \qquad (2.17)$$

where: λ, G are lame constant and shear modulus, u_x, u_z are displacement in x and z directions：

$$u_x = \frac{\partial \varphi}{\partial x} - \frac{\partial \psi}{\partial z} \qquad (2.18)$$

$$u_z = \frac{\partial \varphi}{\partial z} + \frac{\partial \psi}{\partial x} \qquad (2.19)$$

By substituting Equations (2.12),(2.13),(2.16),(2.17), (2.18) and (2.19) into boundary conditions, Equation (2.14) and (2.15), one obtains:

$$\left(1 + v_2^2\right)A - i2v_2 B = 0 \qquad (2.20)$$

$$i2v_1 A + \left(1 + v_2^2\right)B = 0 \qquad (2.21)$$

To obtain non-zero solutions from Equations (2.20) and (2.21) for parameters A and B, it is derived that:

$$\begin{vmatrix} 1+v_2^2 & -i2v_2 \\ i2v_1 & \left(1+v_2^2\right) \end{vmatrix} = 0 \qquad (2.22)$$

By substituting v_1 and v_2 in to Equation (2.22), one obtains:

$$\left(\frac{V_R}{V_S}\right)^6 - 8\left(\frac{V_R}{V_S}\right)^4 + \left[24 - 16\left(\frac{V_S}{V_P}\right)^2\right]\left(\frac{V_R}{V_S}\right)^2 - 16\left[1 - \left(\frac{V_S}{V_P}\right)^2\right] = 0 \qquad (2.23)$$

As observed from the above equation, when $V_R=0$, the left term of the equation is equal to $-16 + \left(\frac{V_S}{V_P}\right)^2 < 0$. When $V_R=V_S$, the left term is equal to 1. Thus, V_R exists in the range of (0, V_S). Moreover, Equation (2.23) is independent of frequency, indicating that in a halfspace, Rayleigh wave velocity is not related to frequency; hence, no dispersion exists.

Substituting Equations (2.12) and (2.13) into Equations (2.18) and (2.19), horizontal and vertical displacements caused by Rayleigh waves are:

$$u_x = \left(iAke^{-kv_1z} + Bkv_2e^{-kv_2z}\right)\exp\left[ik\left(x-V_Rt\right)\right] \qquad (2.24)$$

$$u_z = \left(-Akv_1e^{-kv_1z} + iBke^{-kv_2z}\right)\exp\left[ik\left(x-V_Rt\right)\right] \qquad (2.25)$$

From Equations (2.20) and (2.21),

$$B = -\frac{i2v_1}{1+v_2^2}A \qquad (2.26)$$

By substituting Equation (2.26) into Equations (2.24) and (2.25) for the real part, one obtains:

$$u_x = Ak\left(e^{-kv_1z} - \frac{2v_1v_2}{1+v_2^2}e^{-kv_2z}\right)\sin\left[k\left(x-V_Rt\right)\right] \qquad (2.27)$$

$$u_z = Ak\left(-v_1e^{-kv_1z} + \frac{2v_1}{1+v_2^2}e^{-kv_2z}\right)\cos\left[k\left(x-V_Rt\right)\right] \qquad (2.28)$$

By re-ording Equations (2.27) and (2.28), one obtains:

$$u_x = D\left(e^{-\frac{k_1}{\lambda_R}z} - \frac{\varepsilon_1 C}{\pi}e^{-\frac{\varepsilon_1}{\lambda_R}z}\right)\sin[k(x-V_R t)] \qquad (2.29)$$

$$u_z = D\left(2Ce^{-\frac{\varepsilon_1}{\lambda_R}z} - \frac{k_1}{2\pi}e^{-\frac{k_1}{\lambda_R}z}\right)\cos[k(x-V_R t)] \qquad (2.30)$$

where:
$$k_1^2 = 4\pi^2\left[1 - \left(\frac{m}{n}\right)^2\right], \; (m = \frac{V_R}{V_S}, \; n = \frac{V_P}{V_S}) \qquad (2.31)$$

$$C = \sqrt{\frac{1}{m^2} - \frac{1}{n^2}} \Big/ \left(\frac{2}{m} - m\right) \qquad (2.32)$$

$$\varepsilon_1^2 = 4\pi^2\left(1 - m^2\right) \qquad (2.33)$$

$$D = Ak \qquad (2.34)$$

For a halfspace with known elastic properties, vertical and horizontal displacements of Rayleigh waves can be calculated for given wavelength. Figure 2.4 shows the relationship between amplitudes of both the vertical and horizontal components of Rayleigh waves and depth with a varying Poisson's ratio (Richard et al, 1970). As observed, energy in both the horizontal and vertical directions mainly concentrates above the depth of around one wavelength in a halfspace.

By designating the first components in Equation (2.29) and (2.30) with simpler expressions, one obtains:

$$D\left(e^{-k_1 z/\lambda_R} - \frac{\varepsilon_1 C}{\pi}e^{-\varepsilon_1 z/\lambda_R}\right) = D_x \qquad (2.35)$$

$$D\left(2Ce^{-\varepsilon_1 z/\lambda_R} - \frac{k_1}{2\pi}e^{-k_1 z/\lambda_R}\right) = D_z \qquad (2.36)$$

An ellipse-shape equation is formed as:

17
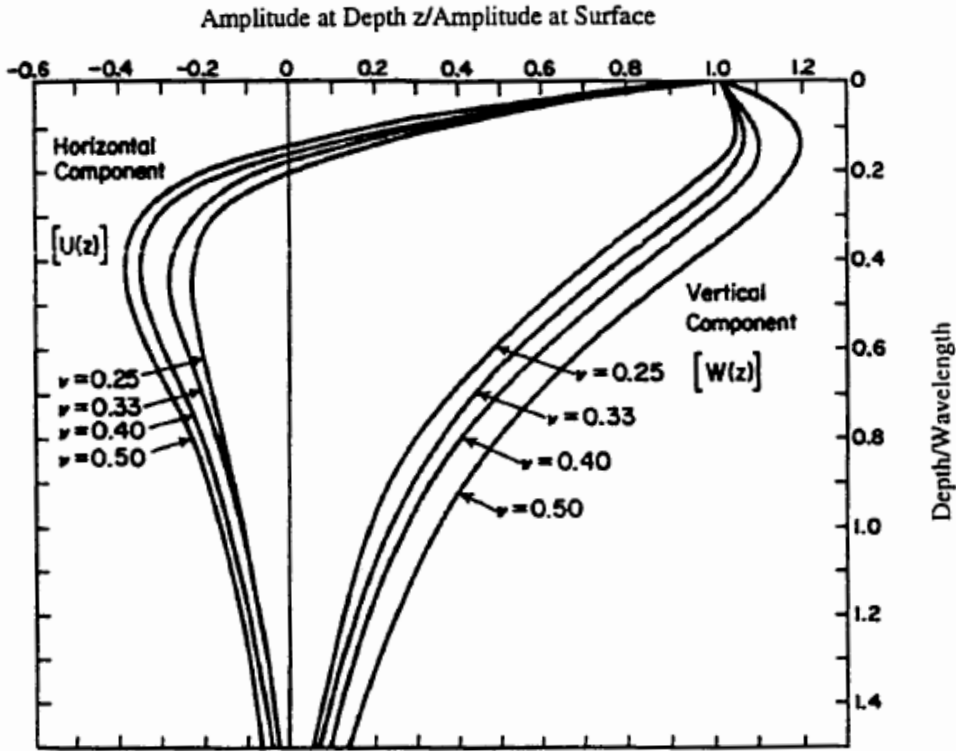
Figure 2.4   Illustrations of Rayleigh Wave Attenuation in a Halfspace (from Richard et al, 1970)

$$\left(\frac{u_x}{D_x}\right)^2 + \left(\frac{u_z}{D_z}\right)^2 = 1 \qquad (2.37)$$

Thus, particle motion for Rayleigh waves is proven to be in elliptical paths.

Using the relations between Poisson's ratio and body wave velocities as well as the designation of,

$$\left(\frac{V_S}{V_P}\right)^2 = \frac{1-2\nu}{2(1-\nu)} \qquad (2.38)$$

$$r = \left(\frac{V_R}{V_S}\right)^2 \qquad (2.39)$$

The propagation equation of Rayleigh waves in a homogeneous, isotropic halfspace simplifies as:

$$r^3 - 8r^2 + 8\frac{2-v}{1-v}r - \frac{8}{1-v} = 0 \qquad (2.40)$$

Equation 2.40 yields only one solution for r as Poisson's ratio ranges from 0 to 0.5, and for different Poisson's ratio, r can be calculated directly. Table 2.3 summarizes the relationship between r and Poisson's ration. As observed, Rayleigh wave velocity ranges from 0.874 to 0.955 times shear wave velocity as Poisson's ratio ranges from 0 to 0.5.

2.3.2 Rayleigh Waves in a Layered System

Haskell (1953) presented the transfer matrix method to obtain the phase velocity dispersion equations for Rayleigh and Love waves in a multilayered solid media. In this section, the derivation of matrix formulation for Rayleigh wave propagation in a horizontally layered system is presented (Haskell, 1993 and Yang, 1993).

A horizontally layered halfspace represented by homogeneous, isotropic materials is considered as a simplified approximation of a geotechnical soil system, as shown in Figure 2.3b. As seen in the figure, interfaces are denoted as n (n=0,1,2,…,N-1) and layers are denoted as m (m=0,1,2,…,N) for a system with N layers. Displacements and stresses in both the x and z axes should be continuous at layer interfaces. At the free surface, normal and shear stresses equal zero. For a system with N layers, there are 4*N-2 boundary conditions.

For the m layer, it is defined by the following parameters: ρ_m – density, d_m – layer thickness, λ_m - lame constant, G_m - shear modulus, V_{Pm} - compression wave velocity, V_{Sm} - shear wave velocity, U_{xm} - displacement in x-axis, U_{zm} - displacement in z-axis, σ_m - normal stress, τ_m - shear stress. Let V_R - Rayleigh wave velocity and k - wavenumber. Also, we denote:

Table 2.3   Relationships between Poisson's Ratio and r (V_R/V_S) (Yang, 1993)

ν	V_R/V_S	ν	V_R/V_S	ν	V_R/V_S
0.00	0.87402	0.24	0.917751	0.38	0.939372
0.02	0.877924	0.25	0.919402	0.39	0.940792
0.04	0.881780	0.26	0.921036	0.40	0.942195
0.06	0.885598	0.27	0.922654	0.41	0.943581
0.08	0.889374	0.28	0.924256	0.42	0.944951
0.10	0.893106	0.29	0.925842	0.43	0.946303
0.12	0.896789	0.30	0.927413	0.44	0.947640
0.14	0.900422	0.31	0.928965	0.45	0.948959
0.16	0.904003	0.32	0.930502	0.46	0.950262
0.18	0.907528	0.33	0.932022	0.47	0.951549
0.20	0.910995	0.34	0.933526	0.48	0.952820
0.21	0.912707	0.35	0.935018	0.49	0.954074
0.22	0.914404	0.36	0.936433	0.50	0.955313
0.23	0.916085	0.37	0.937936		

$$\gamma_{\alpha m} = \begin{cases} \left[\left[\left(V_{\mathrm{R}}\middle/V_{\mathrm{P}m}\right)-1\right]^{\frac{1}{2}} & \left(V_{\mathrm{R}} > V_{\mathrm{P}m}\right) \\ -i\left[1-\left(V_{\mathrm{R}}\middle/V_{\mathrm{P}m}\right)^2\right]^{\frac{1}{2}} & \left(V_{\mathrm{R}} < V_{\mathrm{P}m}\right) \end{cases} \tag{2.41}$$

$$\gamma_{\beta m} = \begin{cases} \left[\left(V_{\mathrm{R}}\middle/V_{\mathrm{S}m}\right)^2-1\right]^{\frac{1}{2}} & \left(V_{\mathrm{R}} > V_{\mathrm{S}m}\right) \\ -i\left[1-\left(V_{\mathrm{R}}\middle/V_{\mathrm{S}m}\right)^2\right]^{\frac{1}{2}} & \left(V_{\mathrm{R}} < V_{\mathrm{S}m}\right) \end{cases} \tag{2.42}$$

$$\gamma_m = 2\left(\frac{V_{\mathrm{S}m}}{V_{\mathrm{R}}}\right)^2 \tag{2.43}$$

Similar to Rayleigh waves in a uniform halfspace, displacement potential functions, φ_{m} and ψ_{m}, should satisfy:

$$\nabla^2\varphi_m = \frac{1}{V_{\mathrm{P}m}^2}\frac{\partial^2\varphi_m}{\partial t^2} \tag{2.44}$$

$$\nabla^2\psi_m = \frac{1}{V_{\mathrm{S}m}^2}\frac{\partial^2\psi_m}{\partial t^2} \tag{2.45}$$

The solutions to Equations (2.44) and (2.45) are:

$$\varphi_m(x,z,t) = \left(A_m e^{-ik\gamma_{\alpha m}z} + B_m e^{ik\gamma_{\alpha m}z}\right)\exp\left[ik\left(x-V_{\mathrm{R}}t\right)\right] \tag{2.46}$$

$$\psi_m(x,z,t) = \left(A_m' e^{-ik\gamma_{\beta m}z} + B_m' e^{ik\gamma_{\beta m}z}\right)\exp\left[ik\left(x-V_{\mathrm{R}}t\right)\right] \tag{2.47}$$

The displacement vector of particle in m layer is defined as:

$$\vec{S} = U_{xm}\vec{i} + U_{zm}\vec{j} \tag{2.48}$$

The divergence and curl of the vector are Δm and W_m, which stand for volumetric change coefficient of the P-wave and the angular displacement of the S-wave.

$$\Delta_m = div\vec{S} = \frac{\partial U_{xm}}{\partial x} + \frac{\partial U_{zm}}{\partial z} \tag{2.49}$$

$$W_m = rot\vec{S} = \frac{1}{2}\left(\frac{\partial U_{xm}}{\partial z} - \frac{\partial U_{zm}}{\partial x}\right) \tag{2.50}$$

We have:

$$U_{xm} = \frac{\partial \varphi_m}{\partial x} - \frac{\partial \psi_m}{\partial z} \tag{2.51}$$

$$U_{zm} = \frac{\partial \varphi_m}{\partial z} + \frac{\partial \psi_m}{\partial x} \tag{2.52}$$

By substituting Equations (2.46), (2.47), (2.51) and (2.52) into Equations (2.49) and (2.50), one obtains:

$$\Delta_m = -\left(\frac{\omega}{V_{Pm}}\right)^2 \varphi_m \tag{2.53}$$

$$W_m = \frac{1}{2}\left(\frac{\omega}{V_{Sm}}\right)^2 \psi \tag{2.54}$$

Turning Equations (2.53) and (2.54) into a similar form as Equations (2.46) and (2.47):

$$\Delta_m = \left(C_m e^{-ik\gamma_{\alpha m}z} + D_m e^{ik\gamma_{\alpha m}z}\right)\exp[i(\omega t - kx)] \tag{2.55}$$

$$W_m = \left(C'_m e^{-ik\gamma_{\beta m}z} + D'_m e^{ik\gamma_{\beta m}z}\right)\exp[i(\omega t - kx)] \tag{2.56}$$

where C_m, C'_m, D_m, D'_m are constants and $\omega = 2\pi f$.

Displacements and stresses in both the x and z directions are:

$$U_{xm} = \frac{\partial \varphi_m}{\partial x} - \frac{\partial \psi_m}{\partial z} \tag{2.57}$$

$$U_{zm} = \frac{\partial \varphi_m}{\partial z} + \frac{\partial \psi_m}{\partial x} \tag{2.58}$$

$$\sigma_m = \lambda_m\left(\frac{\partial U_{xm}}{\partial x} + \frac{\partial U_{zm}}{\partial z}\right) + 2G_m \frac{\partial U_{zm}}{\partial z} \tag{2.59}$$

$$\tau_m = G_m\left(\frac{\partial U_{xm}}{\partial z} + \frac{\partial U_{zm}}{\partial x}\right) \tag{2.60}$$

By substituting Equations (2.51), (2.52), (2.53) and (2.54) into Equations (2.57) through (2.60), one obtains:

$$U_{xm} = -\left(\frac{V_{Pm}}{\omega}\right)^2 \frac{\partial \Delta_m}{\partial x} - 2\left(\frac{V_{Sm}}{\omega}\right)^2 \frac{\partial W_m}{\partial z} \qquad (2.61)$$

$$U_{zm} = -\left(\frac{V_{Pm}}{\omega}\right)^2 \frac{\partial \Delta_m}{\partial z} + 2\left(\frac{V_{Sm}}{\omega}\right)^2 \frac{\partial W_m}{\partial x} \qquad (2.62)$$

$$\sigma_m = \rho_m\left\{V_{Pm}^2 \Delta_m + 2V_{Sm}^2\left[\left(\frac{V_{Pm}}{\omega}\right)^2 \frac{\partial^2 \Delta_m}{\partial x^2} + 2\left(\frac{V_{Sm}}{\omega}\right)^2 \frac{\partial^2 W_m}{\partial x \partial z}\right]\right\} \qquad (2.63)$$

$$\tau_m = 2\rho_m V_{Sm}^2\left\{-\left(\frac{V_{Pm}}{\omega}\right)^2 \frac{\partial^2 \Delta_m}{\partial x \partial z} + \left(\frac{V_{Sm}}{\omega}\right)^2\left(\frac{\partial^2 W_m}{\partial x^2} - \frac{\partial^2 W_m}{\partial z^2}\right)\right\} \qquad (2.64)$$

At any interface, continuity of displacement, stress and particle motion velocity must be satisfied. With $\dot{U}_x = \frac{\partial U_x}{\partial t}, \dot{U}_z = \frac{\partial U_z}{\partial t}, \frac{\dot{U}_x}{V_R}$ and $\frac{\dot{U}_z}{V_R}$ and substituting Equations (2.55) and (2.56) into Equations (2.61) through (2.64), one obtains:

$$\frac{\dot{U}_{xm}}{V_R} = -\left(\frac{V_{Pm}}{V_R}\right)^2\left[(C_m + D_m)\cos k\gamma_{\alpha m}z - i(C_m - D_m)\sin k\gamma_{\beta m}z\right]$$
$$+ \gamma_m \gamma_{\beta m}\left[(D'_m - C'_m)\cos k\gamma_{\beta m}z + i(D'_m + C'_m)\sin k\gamma_{\beta m}z\right] \qquad (2.65)$$

$$\frac{\dot{U}_{zm}}{V_R} = \left(\frac{V_{Pm}}{V_R}\right)^2 \gamma_{\alpha m}\left[i(D_m + C_m)\sin k\gamma_{\alpha m}z + (D_m - C_m)\cos k\gamma_{\alpha m}z\right]$$
$$+ \gamma_m\left[i(D'_m - C'_m)\sin k\gamma_{\beta m}z + (D'_m + C'_m)\cos k\gamma_{\beta m}z\right] \qquad (2.66)$$

$$\sigma_m = \rho_m V_{Pm}^2(1-\gamma_m)\left[(C_m + D_m)\cos k\gamma_{\alpha m}z - i(C_m - D_m)\sin k\gamma_{\alpha m}z\right]$$
$$+ \rho_m \gamma_m^2 V_R^2 \gamma_{\beta m}\left[(D'_m - C'_m)\cos k\gamma_{\beta m}z + i(D'_m + C'_m)\sin k\gamma_{\beta m}z\right] \qquad (2.67)$$

$$\tau_m = -\rho_m V_{Pm}^2 \gamma_m \gamma_{\alpha m}\left[i(D_m + C_m)\sin k\gamma_{\alpha m}z + (D_m - C_m)\cos k\gamma_{\alpha m}z\right]$$
$$+ \rho_m V_R^2 \gamma_m(1-\gamma_m)\left[i(D'_m - C'_m)\sin k\gamma_{\beta m}z + (D'_m + C'_m)\cos k\gamma_{\beta m}z\right] \qquad (2.68)$$

where dimensionless quantities $\frac{\dot{U}_{xm}}{V_R}$ and $\frac{\dot{U}_{zm}}{V_R}$ are also continuous.

23

Placing the origion of z (m-1)th interface, one obtains $\sin k\gamma z = 0$, $\cos k\gamma z = 1$ using z =0. We have displacements and stresses caused by Rayleigh wave in m layer at (m-1) interface.

$$\left(\frac{\dot{U}_{xm,1}}{V_R}, \frac{\dot{U}_{zm,1}}{V_R}, \sigma_{m,1}, \tau_{m,1}\right)^T = E_m\left(C_m + D_m, C_m - D_m, C'_m + D'_m, C'_m - D'_m\right)^T \quad (2.69)$$

where,

$$E_m = \begin{bmatrix} -\left(\dfrac{V_{Pm}}{V_R}\right)^2 & 0 & 0 & -\gamma_m\gamma_{\beta m} \\ 0 & -\left(\dfrac{V_{Pm}}{V_R}\right)^2\gamma_{\alpha m} & \gamma_m & 0 \\ \rho_m V_{Pm}^2(1-\gamma_m) & 0 & 0 & -\rho_m\gamma_m^2\gamma_{\beta m}V_R^2 \\ 0 & \rho_m V_{Pm}^2\gamma_m\gamma_{\alpha m} & \rho_m V_R^2\gamma_m(1-\gamma_m) & 0 \end{bmatrix} \quad (2.70)$$

Similarly, at (m) interface where z = d$_m$, Equations (2.65) through (2.68) give the displacements and stresses:

$$\left(\frac{\dot{U}_{xm,2}}{V_R}, \frac{\dot{U}_{zm,2}}{V_R}, \sigma_{m,2}, \tau_{m,2}\right)^T = F_m\left(C_m + D_m, C_m - D_m, C'_m + D'_m, C'_m - D'_m\right)^T \quad (2.71)$$

F$_m$ is similar to matrix E$_m$,

$$F_m = \begin{bmatrix} -\left(\dfrac{V_{Pm}}{V_R}\right)^2\cos P_m & i\left(\dfrac{V_{Pm}}{V_R}\right)^2\sin P_m \\ i\left(\dfrac{V_{Pm}}{V_R}\right)^2\gamma_{\alpha m}\sin P_m & -\left(\dfrac{V_{Pm}}{V_R}\right)^2\gamma_{\alpha m}\cos P_m \\ \rho_m V_{Pm}^2(1-\gamma_m)\cos P_m & i\rho_m V_{Pm}^2(\gamma_m-1)\sin P_m \\ -i\rho_m V_{Pm}^2\gamma_m\gamma_{\alpha m}\sin P_m & \rho_m V_{Pm}^2\gamma_m\gamma_{\alpha m}\cos P_m \end{bmatrix}$$

$$\begin{bmatrix} i\gamma_m\gamma_{\beta m}\sin Q_m & -\gamma_m\gamma_{\beta m}\cos Q_m \\ \gamma_m\cos Q_m & -i\gamma_m\sin Q_m \\ i\rho_m V_R^2\gamma_m^2\gamma_{\beta m}\sin Q_m & -\rho_m V_R^2\gamma_m^2\gamma_{\beta m}\cos Q_m \\ \rho_m V_R^2\gamma_m(1-\gamma_m)\cos Q_m & \rho_m V_R^2\gamma_m(\gamma_m-1)\sin Q_m \end{bmatrix}$$

$$(2.72)$$

where $P_m = k\gamma_{\alpha m}d_m$, $Q_m = k\gamma_{\beta m}d_m$.

From Equation (2.69) we have:

$$\left(C_m + D_m, C_m - D_m, C'_m + D'_m, C'_m - D'_m\right)^{\mathrm{T}} = E_m^{-1}\left(\frac{\dot{U}_{xm,1}}{V_{\mathrm{R}}}, \frac{\dot{U}_{zm,1}}{V_{\mathrm{R}}}, \sigma_{m,1}, \tau_{m,1}\right)^{\mathrm{T}} \quad (2.73)$$

By substituting (2.73) into (2.71), one obtains:

$$\left(\frac{\dot{U}_{xm,2}}{V_{\mathrm{R}}}, \frac{\dot{U}_{zm,2}}{V_{\mathrm{R}}}, \sigma_{m,2}, \tau_{m,2}\right)^{\mathrm{T}} = F_m E_m^{-1}\left(\frac{\dot{U}_{xm,1}}{V_{\mathrm{R}}}, \frac{\dot{U}_{zm,1}}{V_{\mathrm{R}}}, \sigma_{m,1}, \tau_{m,1}\right)^{\mathrm{T}} \quad (2.74)$$

where E_m^{-1} is the inverse of E_m and is given by:

$$E_m^{-1} = \begin{bmatrix} -2\left(\dfrac{V_{\mathrm{S}m}}{V_{\mathrm{P}m}}\right)^2 & 0 & \left(\rho_m V_{\mathrm{P}m}^2\right)^{-1} & 0 \\[2ex] 0 & \dfrac{V_{\mathrm{R}}^2(\gamma_m - 1)}{V_{\mathrm{P}m}^2 \gamma_{\alpha m}} & 0 & \left(\rho_m V_{\mathrm{P}m}^2 \gamma_{\alpha m}\right)^{-1} \\[2ex] 0 & 1 & 0 & \left(\rho_m V_{\mathrm{R}}^2 \gamma_m\right)^{-1} \\[2ex] \dfrac{(\gamma_m - 1)}{\gamma_m \gamma_{\beta m}} & 0 & -\left(\rho_m V_{\mathrm{R}}^2 \gamma_m \gamma_{\beta m}\right)^{-1} & 0 \end{bmatrix} \quad (2.75)$$

Using $\mathbf{A}_m = \mathbf{E}'_m \mathbf{E}_m^{-1}$, Equation (2.74) is converted into:

$$\left(\frac{\dot{U}_{xm,2}}{V_{\mathrm{R}}}, \frac{\dot{U}_{zm,2}}{V_{\mathrm{R}}}, \sigma_{m,2}, \tau_{m,2}\right)^{\mathrm{T}} = \mathrm{A}_m\left(\frac{\dot{U}_{xm,1}}{V_{\mathrm{R}}}, \frac{\dot{U}_{zm,1}}{V_{\mathrm{R}}}, \sigma_{m,1}, \tau_{m,1}\right)^{\mathrm{T}} \quad (2.76)$$

Similarly, if origin of z is placed to $(m-2)^{\mathrm{th}}$ interface and repeating the above steps, one obtains:

$$\left(\frac{\dot{U}_{xm-1,2}}{V_{\mathrm{R}}}, \frac{\dot{U}_{zm-1,2}}{V_{\mathrm{R}}}, \sigma_{m-1,2}, \tau_{m-1,2}\right)^{\mathrm{T}} = \mathbf{A}_{m-1}\left(\frac{\dot{U}_{xm-1,1}}{V_{\mathrm{R}}}, \frac{\dot{U}_{zm-1,1}}{V_{\mathrm{R}}}, \sigma_{m-1,1}, \tau_{m-1,1}\right)^{\mathrm{T}} \quad (2.77)$$

According to continuity of displacement and stress at interface (m-1), we have:

$$\left(\frac{\dot{U}_{xm,1}}{V_{\mathrm{R}}}, \frac{\dot{U}_{zm,1}}{V_{\mathrm{R}}}, \sigma_{m,1}, \tau_{m,1}\right)^{\mathrm{T}} = \left(\frac{\dot{U}_{xm-1,2}}{V_{\mathrm{R}}}, \frac{\dot{U}_{zm-1,2}}{V_{\mathrm{R}}}, \sigma_{m-1,2}, \tau_{m-1,2}\right)^{\mathrm{T}} \quad (2.78)$$

By substituting Equations (2.77) and (2.78) into Equation (2.76), one obtains:

$$\left(\frac{\dot{U}_{xm,2}}{V_{\mathrm{R}}}, \frac{\dot{U}_{zm,2}}{V_{\mathrm{R}}}, \sigma_{m,2}, \tau_{m,2}\right)^{\mathrm{T}} = \mathbf{A}_m \mathbf{A}_{m-1}\left(\frac{\dot{U}_{xm-1,1}}{V_{\mathrm{R}}}, \frac{\dot{U}_{zm-1,1}}{V_{\mathrm{R}}}, \sigma_{m-1,1}, \tau_{m-1,1}\right)^{\mathrm{T}} \quad (2.79)$$

Thus, repeat the above step for all layers, one obtains:

$$\left(\frac{\dot{U}_{xm,2}}{V_{\mathrm{R}}},\frac{\dot{U}_{zm,2}}{V_{\mathrm{R}}},\sigma_{m,2},\tau_{m,2}\right)^{\mathrm{T}}=\mathbf{A}_{m}\mathbf{A}_{m-1}\cdots\mathbf{A}_{1}\left(\frac{\dot{U}_{x1,1}}{V_{\mathrm{R}}},\frac{\dot{U}_{z1,1}}{V_{\mathrm{R}}},\sigma_{1,1},\tau_{1,1}\right)^{\mathrm{T}}\qquad(2.80)$$

Similarly on interface (m), we have:

$$\left(\frac{\dot{U}_{xm+1,1}}{V_{\mathrm{R}}},\frac{\dot{U}_{zm+1,1}}{V_{\mathrm{R}}},\sigma_{m+1,1},\tau_{m+1,1}\right)^{\mathrm{T}}=\left(\frac{\dot{U}_{xm,2}}{V_{\mathrm{R}}},\frac{\dot{U}_{zm,2}}{V_{\mathrm{R}}},\sigma_{m,2},\tau_{m,2}\right)^{\mathrm{T}}\qquad(2.81)$$

Comparing to Equation (2.78), one obtains:

$$\mathbf{A}_{m+1}^{-1}\left(\frac{\dot{U}_{xm+1,2}}{V_{\mathrm{R}}},\frac{\dot{U}_{zm+1,2}}{V_{\mathrm{R}}},\sigma_{m+1,2},\tau_{m+1,2}\right)^{\mathrm{T}}=\left(\frac{\dot{U}_{xm,2}}{V_{\mathrm{R}}},\frac{\dot{U}_{zm,2}}{V_{\mathrm{R}}},\sigma_{m,2},\tau_{m,2}\right)^{\mathrm{T}}\qquad(2.82)$$

$$\mathbf{A}_{m+1}^{-1}\mathbf{A}_{m+2}^{-1}\cdots\mathbf{A}_{n-1}^{-1}\left(\frac{\dot{U}_{xn-1,2}}{V_{\mathrm{R}}},\frac{\dot{U}_{zn-1,2}}{V_{\mathrm{R}}},\sigma_{n-1,2},\tau_{n-1,2}\right)^{\mathrm{T}}=\left(\frac{\dot{U}_{xm,2}}{V_{\mathrm{R}}},\frac{\dot{U}_{zm,2}}{V_{\mathrm{R}}},\sigma_{m,2},\tau_{m,2}\right)^{\mathrm{T}}\quad(2.83)$$

According to continuity on interface (n-1), one obtains:

$$\mathbf{A}_{m+1}^{-1}\mathbf{A}_{m+2}^{-1}\cdots\mathbf{A}_{n-1}^{-1}\left(\frac{\dot{U}_{xn,1}}{V_{\mathrm{R}}},\frac{\dot{U}_{zn,1}}{V_{\mathrm{R}}},\sigma_{n,1},\tau_{n,1}\right)^{\mathrm{T}}=\left(\frac{\dot{U}_{xm,2}}{V_{\mathrm{R}}},\frac{\dot{U}_{zm,2}}{V_{\mathrm{R}}},\sigma_{m,2},\tau_{m,2}\right)^{\mathrm{T}}\qquad(2.84)$$

Based on Equations (2.80) and (2.81), one obtains:

$$\left(\frac{\dot{U}_{xn,1}}{V_{\mathrm{R}}},\frac{\dot{U}_{zn,1}}{V_{\mathrm{R}}},\sigma_{n,1},\tau_{n,1}\right)^{\mathrm{T}}=\mathbf{A}_{n-1}\mathbf{A}_{n-2}\cdots\mathbf{A}_{1}\left(\frac{\dot{U}_{x1,1}}{V_{\mathrm{R}}},\frac{\dot{U}_{z1,1}}{V_{\mathrm{R}}},\sigma_{1,1},\tau_{1,1}\right)^{\mathrm{T}}\qquad(2.85)$$

Since we have:

$$\left(C_{n}+D_{n},C_{n}-D_{n},C_{n}'+D_{n}',C_{n}'-D_{n}'\right)^{\mathrm{T}}=\mathbf{E}_{n}^{-1}\left(\frac{\dot{U}_{xn,1}}{V_{\mathrm{R}}},\frac{\dot{U}_{zn,1}}{V_{\mathrm{R}}},\sigma_{n,1},\tau_{n,1}\right)^{\mathrm{T}}\qquad(2.86)$$

One obtains:

$$\left(C_{n}+D_{n},C_{n}-D_{n},C_{n}'+D_{n}',C_{n}'-D_{n}'\right)^{\mathrm{T}}=\mathbf{E}_{n}^{-1}\mathbf{A}_{n-1}\cdots\mathbf{A}_{1}\left(\frac{\dot{U}_{x1,1}}{V_{\mathrm{R}}},\frac{\dot{U}_{z1,1}}{V_{\mathrm{R}}},\sigma_{1,1},\tau_{1,1}\right)^{\mathrm{T}}(2.87)$$

At the ground surface (z=0), the stresses equal zero ($\sigma_{1,1}=\tau_{1,1}=0$). At an infinite depth ($z\to\infty$), $D_{\mathrm{n}}=D'_{\mathrm{n}}=0$. By substituting these boundary conditions into Equation (2.87), one obtains:

$$\left(C_{n},C_{n},C_{n}',C_{n}'\right)^{\mathrm{T}}=\mathbf{J}\left(\frac{\dot{U}_{x1,1}}{V_{\mathrm{R}}},\frac{\dot{U}_{z1,1}}{V_{\mathrm{R}}},0,0\right)^{\mathrm{T}}\qquad(2.88)$$

where $\mathbf{J} = \mathbf{E}_n^{-1}\mathbf{A}_{n-1}\cdots\mathbf{A}_1$ is a 4×4 matrix.

Up expanding Equation (2.88), one obtains:

$$
\left.\begin{aligned}
C_n &= J_{11}\frac{\dot{U}_{x1,1}}{V_R} + J_{12}\frac{\dot{U}_{z1,1}}{V_R} \\[6pt]
C_n &= J_{21}\frac{\dot{U}_{x1,1}}{V_R} + J_{22}\frac{\dot{U}_{z1,1}}{V_R} \\[6pt]
C'_n &= J_{31}\frac{\dot{U}_{x1,1}}{V_R} + J_{32}\frac{\dot{U}_{z1,1}}{V_R} \\[6pt]
C'_n &= J_{41}\frac{\dot{U}_{x1,1}}{V_R} + J_{42}\frac{\dot{U}_{z1,1}}{V_R}
\end{aligned}\right\}
\tag{2.89}
$$

By eliminating C_n and C'_n from Equation (2.89), one obtains:

$$
\frac{\dot{U}_{x1,1}}{\dot{U}_{z1,1}} = \frac{J_{22} - J_{12}}{J_{11} - J_{21}} = \frac{J_{42} - J_{32}}{J_{31} - J_{41}}
\tag{2.90}
$$

Matrix J_{ij} provides an implicit relationship between Rayleigh wave velocity, V_R, and wavenumber, k ($k = 2\pi f/V_R$). Thus dispersion curves can be extracted from this equation. An illustration of typical theoretical dispersion curves with multiple modes generated by transfer matrix method is shown in Figure 2.5.
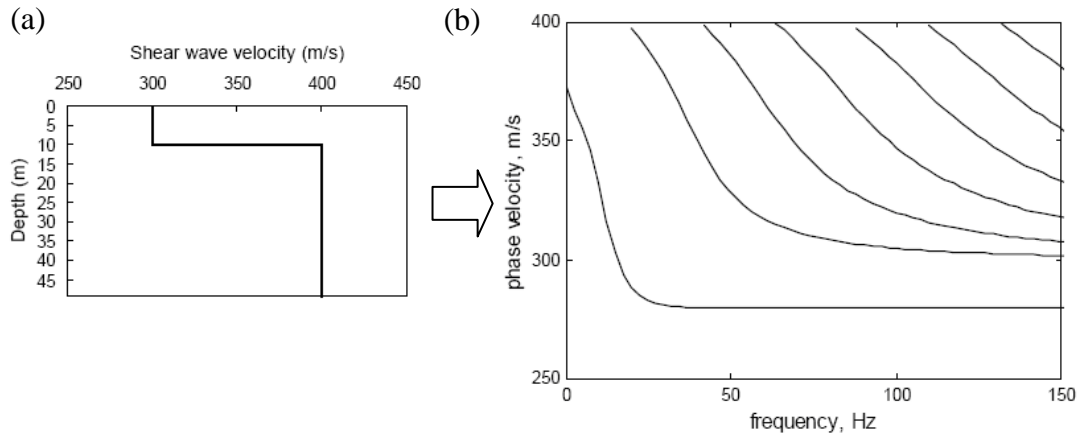
Figure 2.5   Illustrations of Typical Theoretical Dispersion Curves with Multiple Modes for Rayleigh Waves Propagating in a Layered Halfspace (from Foti, 2000)

2.3.3 Forward Modeling Algorithm

The original transfer matrix method of extracting theoretical dispersion curves as presented in section 2.3.2 suffers numerical instability at high frequencies. Many scientists have proposed algorithms to improve the calculation of theoretical dispersion curves and responses of layered system to dynamic loads. Several methods that have been used are: (1) the improved transfer matrix method (Knopoff 1964, Dunkin 1965, Watson 1970 and Youhua 2001), (2) the reflectivity method (Fuchs 1968, Fuchs and Muller 1971) and (3) the dynamic stiffness method (Kausel 1981, Kausel and Roesset 1981, Kausel and Peek 1982).

Thomson (1950) and Haskell (1953) first proposed a transfer matrix method to determine the dispersion relationship for the propagation of surface waves within the Earth modeled by a number of uniform layers. "In the Thomson-Haskell matrix formulation, the displacement–traction vector at the top surface of a layer is related to that at the bottom surface by a transfer matrix, and thus is carried across the interface

28

continuously through the entire stack by the product of transfer matrices. The unknown variables in the displacement-traction vector at each layer are then determined by reformulating the matrix product to satisfy the boundary conditions" (Lee, 1996). Gilbert and Backus (1966) described a general method, the propagator technique, which includes the Thomson-Haskell method and Knopoff's method as special cases.

Similar to the transfer matrix method, the reflectivity method was developed by Fuchs (1968) and Fuchs & Miller (1971). The reflection and transmission of plane waves in layered media were treated first, followed by the synthesis of wave fields created by point sources. The theoretical seismograms for each set of wave types were calculated by recursive methods. Based on the propagator technique and reflectivity method, Kennett & Kerry (1979) proposed a reflection matrix method, which can be used to construct the entire response in terms of reflection and transmission matrices, in analyzing the excitation induced by general sources in a stratified medium. The reflectivity method was extended later by Miller (1985).

The stiffness matrix method (Kausel 1981, Kausel and Roesset 1981, Kausel and Peek 1982, Wang and Rokhlin, 2001, Rokhlin and Wang, 2002) has been proposed to resolve the inherent computational instability for the large product of frequencies and thicknesses in the transfer matrix method. The stiffness matrix method formulation utilizes the stiffness matrix of each sub-layer in a recursive algorithm to obtain the stacked stiffness matrix for the multilayered solid (Tian 2000). In Kausel and Roesset's paper, both 2-D (assuming a plane Rayleigh wavefront) and 3-D (assuming a cylindrical wavefront and considering all waves with source and receiver locations) solutions are proposed. Ths 3-D solution is considered to be the most representative way to explain the dynamic response of a layered soil system under vertical excitation by a point source.

Many researchers have performed analyses with the 3-D solution of Kausel and Roesset(1981) with numerically simulated models (Gucunski and Woods, 1992, Foinquinos 1991, Al-Hunaidi 1994, Lee 1996). The contribution of different wave components to the 3-D solution (cylindrical wave front) were systematically studied and compared with the plane Rayleigh wave solution (2-D solution). The studies indicate that in a complicated soil system (hard-over-soft layered system), the 3-D solution is a true representation of the soil system.

Rayleigh wave propagation in inhomogeneous, anisotropic or more complex systems were theoretically explored by many researchers. Jones (1961) proved the existence of Rayleigh waves in a porous, elastic and saturated medium based on Biot's theory. Kirkwood (1978) discussed the error caused by applying the transfer matrix method in anisotropic medium, and studied the characteristics of Rayleigh wave propagation in anisotropic medium. Tajuddin (1984) performed research on Rayleigh wave in a porous halfspace. However, the application of these studies is limited by the complexity of deriving an analytical solution of dispersion curves in inhomogeneous, anisotropic medium.

2.4 SENSITIVITY STUDY

A homogeneous, isotropic, horizontally layered system can be physically defined by the layer thickness H, V_p, V_s and unit weight, γ. A system with n layers has (4n+3) parameters to define the shape of the theoretical dispersion curves. Sensitivity studies were performed in this study with a one-layer-over-halfspace model to illustrate the impact of those parameters on the shape of the theoretical dispersion curves. In this section, the results of these studies show the effect of each parameter (i.e. shear wave velocity, compression wave velocity, layer thickness and unit weight). Dynamic stiffness

matrix method is used to generate 2-D theoretical dispersion curves for Rayleigh waves. Comparison of 2-D and 3-D theoretical dispersion curves will be addressed in Chapter 5.

The parameters of the base model are summarized in Table 2.4. All four parameters of the first layer are varied with 10% to study their impacts.

Table 2.4   Parameters of the Base Model Used to Obtain the 2-D Theoretical Dispersion Curve for Rayleigh Waves

Layer No.	Thickness, ft	P-Wave Velocity, ft/s	S-Wave Velocity, ft/s	Poisson's Ratio	Total Unit Weight, pcf
1	30	1000	500	0.33 $^\circ$	100
2	Half-Space	2000	800	0.40 $^\circ$	120

$^\circ$ Poisson's ratio calculated from V_s and V_p.

2.4.1 Influence of Shear Wave Velocity

The variation of shear wave velocity of the first layer is shown in Figure 2.6. , shear wave velocity of the first layer varies from 450 ft/s to 550 ft/s. Theoretical dispersion curves for each parameter are plotted in Figure 2.7.

Theoretical dispersion curves generated from three different parameter sets (only V_{s1} changed) are plotted in Figure 2.7. As observed, the value of shear wave velocity of the first layer has a dominant effect on the shape of theoretical dispersion curve. As V_s of the first layer increases, 2-D theoretical dispersion curve at high frequencies starts to move up to higher velocity. At low frequencies, all dispersion curves approach to the same value, verifying the input model whose properties at halfspace remains unchanged for all three parameter sets. It is observed that 10% changes in shear wave velocity affect the 2-D theoretical dispersion curves since 3 Hz in wavelengths.
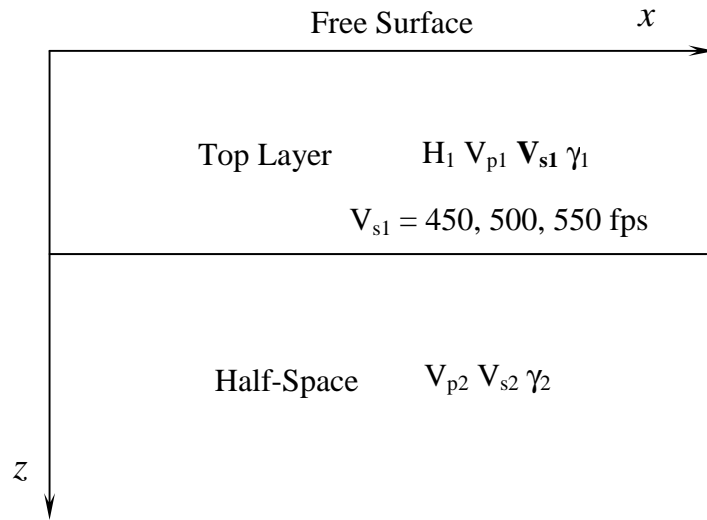
Figure 2.6   Theoretical Models of a Layered Half-Space with Varying Values of V_s in the Top Layer
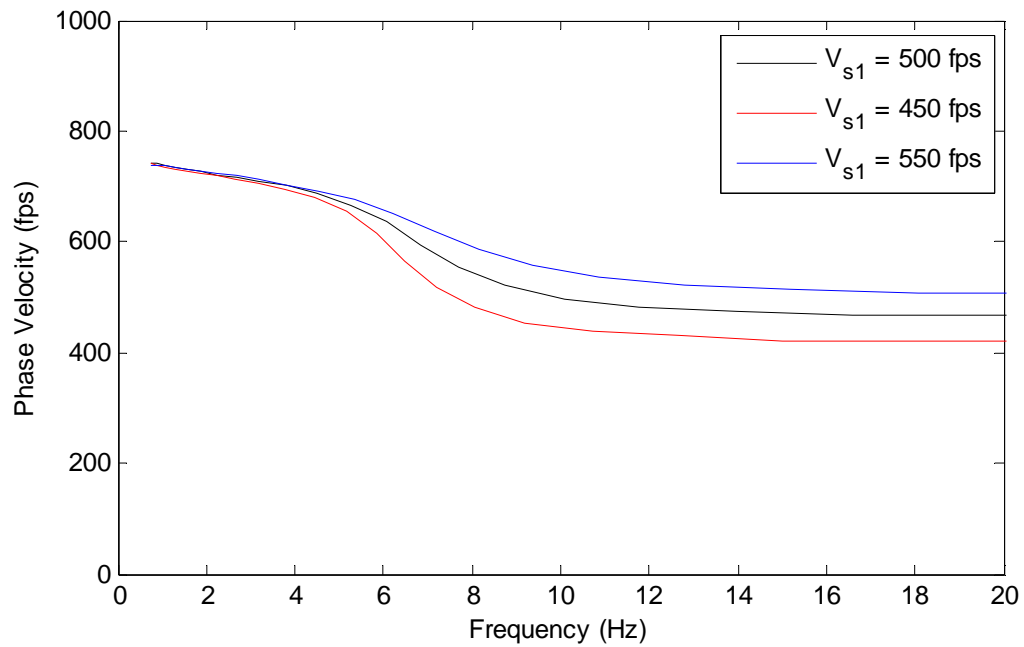
Figure 2.7   Impact of Shear Wave Velocity on 2-D Theoretical Dispersion Curves

2.4.2 Influence of Layer Thickness

Figure 2.8 shows the input model used to shown the impact of layer thickness of the top layer. The thickness of the top layer was varied by 10% from 27 ft to 33 ft. The theoretical dispersion curves for the fundamental mode of plane wave traveling along the surface of the model are plotted in Figure 2.9. As observed, the thickness of the top layer plays an important role in defining the shape of the theoretical dispersion curve. As the thickness of the top layer increases, dispersion curve starts to shift to the left on the frequency-velocity plot. The thicker the first layers is, the larger the gap between dispersion curves from different parameter sets. At both low and high frequency zone, theoretical dispersion curves arrive at same values, which verifies the input model whose shear wave velocities at both first layer and halfspace remain unchanged for all three parameter sets.

Free Surface x

Top Layer $\mathbf{H_1}$ V_{p1} V_{s1} γ_1

$H = 27, 30, 33$ ft

Half-Space V_{p2} V_{s2} γ_2

z
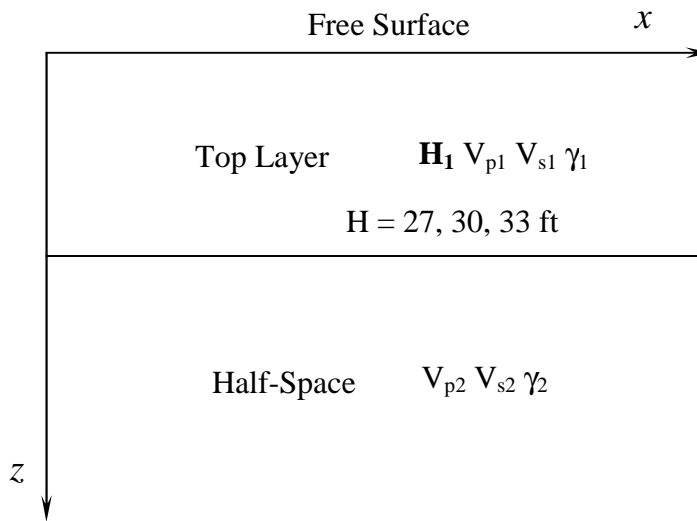
Figure 2.8   Theoretical Models of a Layered Half-Space with Varying Values of H in the Top Layer
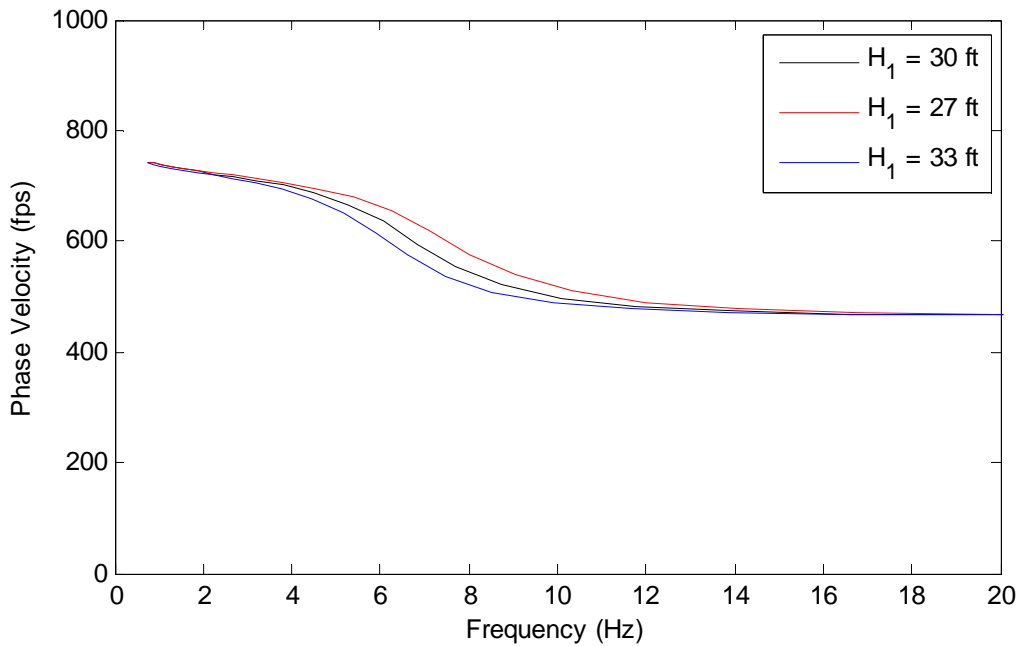
Figure 2.9   Impact of Layer Thickness on Theoretical Dispersion Curves

2.4.3 Influence of Compression Wave Velocity

The theoretical site profile of top layer used to show the impact of compression wave velocity of the first layer varying from 900 ft/s, 1000 ft/s to 1100 ft/s is shown in Figure 2.10. The theoretical dispersion curves generated from the casese where only V_{p1} changed are plotted in Figure 2.11. It can be seen that compression wave velocity of the first layer has a relatively small impact on the shape of theoretical dispersion curve. As V_p of the first layer increases, dispersion curve starts to shift up slightly on the frequency-velocity plot. It can be concluded that compression wave velocity affects propagation of Rayleigh wave in a layered system, but Rayleigh wave velocity is less sensitive to V_p than V_s of the materials.
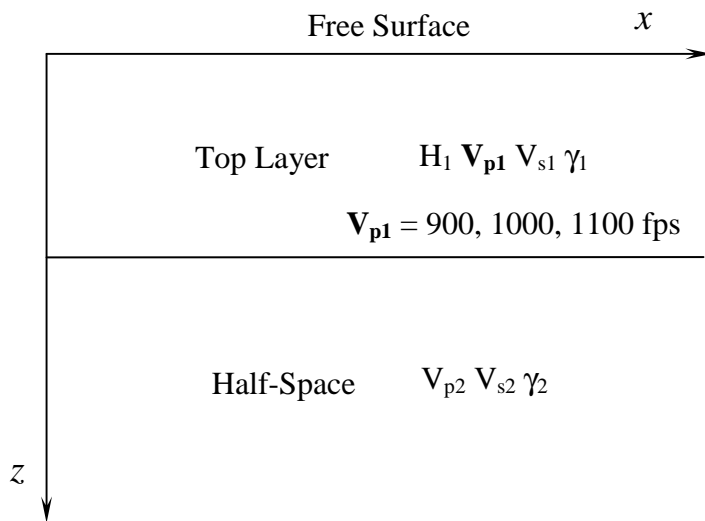
Figure 2.10 Theoretical Models of a Layered Half-Space with Varying Values of V_p in the Top Layer
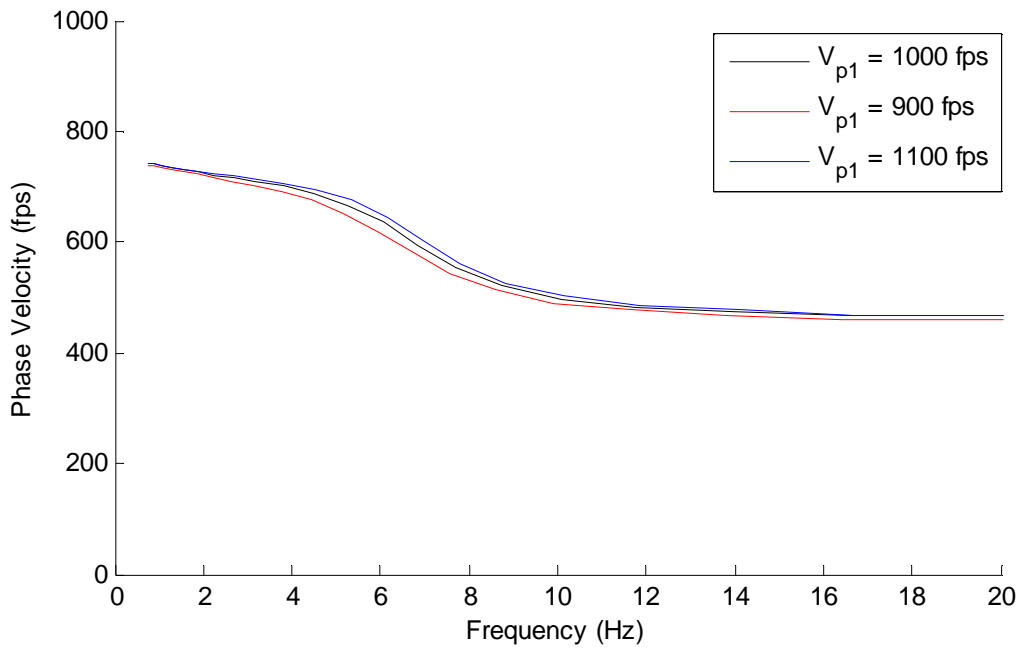
Figure 2.11   Impact of Compression Wave Velocity on Theoretical Dispersion Curves

2.4.4 Influence of Density

As shown in Figure 2.12, unit weight of the top layer is varied to study the impact of unit weight on theoretical dispersion curves from 90 pcf, 100 pcf to 110 pcf. Theoretical dispersion curves generated from three different parameter sets (only density of the top layer varied) are plotted in Figure 2.13.

Free Surface x

Layer 1 H_1 V_{p1} V_{s1} γ_1

$\gamma_1 = 90, 100, 110$ pcf

Half-Space V_{p2} V_{s2} γ_2

z
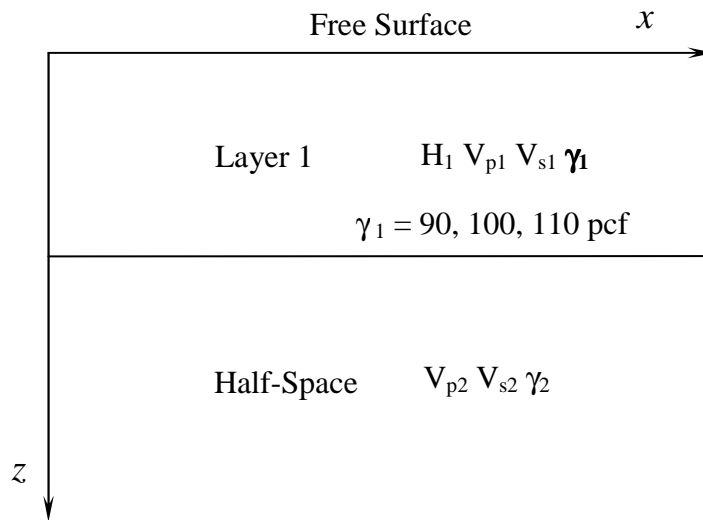
Figure 2.12   Theoretical Models of a Layered Half-Space with Varying Values of γ in the Top Layer

It can be seem that density of the top layer has a very small impact on the shape of theoretical dispersion curve. As density of the top layer increases, dispersion curve starts to shift down very slightly on the frequency-velocity plot. It can be concluded that density plays a minor role in defining theoretical dispersion curve and affecting propagation of Rayleigh wave in a layered system.
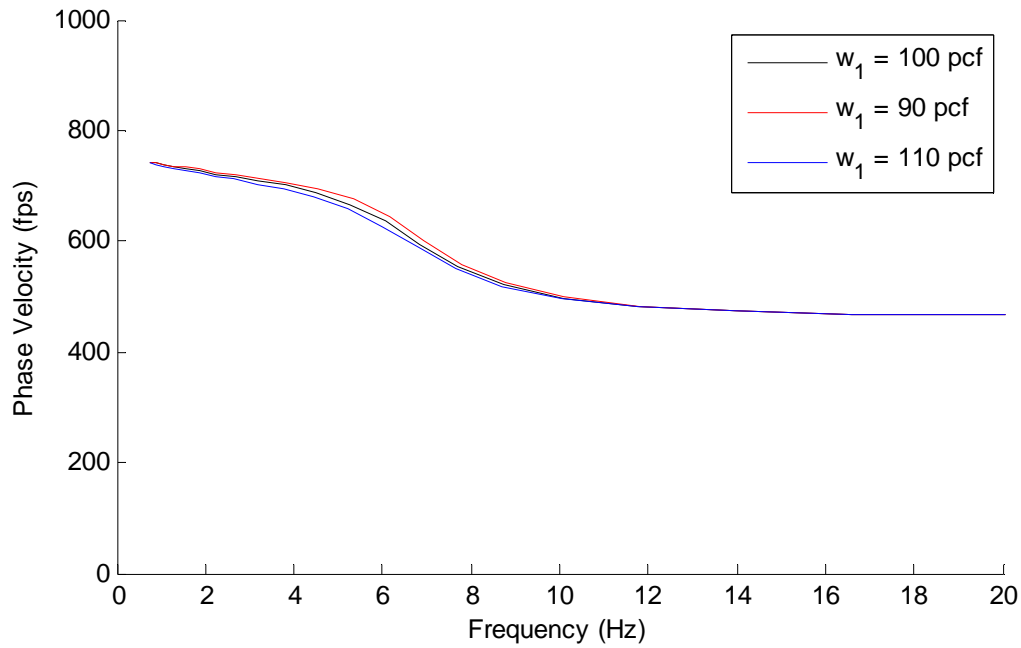
Figure 2.13   Impact of Unit Weight on Theoretical Dispersion Curves

2.5 SUMMARY

In this chapter, background knowledge regarding Rayleigh wave propagation in both uniform and layered half-space systems is presented. To facilitate the understanding of surface wave propagation in a geotechnical system, a uniform elastic half-space and a horizontally layered half-space were used to model the geotechnical sites. The impact of the dynamic properties on the shape of dispersion curves of Rayleigh waves is studied. In this context, only elastic constants are presented based on the assumption of wave propagation in elastic media.

Rayleigh wave propagation in an elastic half-space is first discussed and the partial differential equations that govern R-wave propagation are derived. Once the elastic parameters (E, G and Poisson's ratio) are specified, Rayleigh wave velocity can be determined ranging from 0.874 to 0.955 times shear wave velocity in a uniform halfspace for Poisson's ratio ranging from 0 to 0.5. It is easily seen that Rayleigh-wave dispersion

does not exist in a homogeneous, isotropic halfspace; that is, V_R is constant for all frequencies; In a layered elastic half-space, dispersion exists in Rayleigh-wave velocity and is shown by different frequencies propagating with different speeds. Low frequency R-waves sample deep material and travel faster than high-frequency Rayleigh waves. The phenomenon of velocity dispersion forms the basis for the development of surface wave testing methods.

The derivation of transfer matrix algorithm developed by Haskell (1953) is present in this chapter. Several algorithms (transfer matrix, reflection matrix and dynamic stiffness matrix algorithms) have been used for surface wave propagation in a half-space. Each algorithm is discussed in this chapter.

To illustrate the impact of four parameters (shear wave velocity, layer thickness, compression wave velocity and unit weight) on the shape of dispersion curves of R-waves, sensitivity studies are performed based on the 2-D theoretical solution from the dynamic stiffness method. A model composed of one layer over an elastic, uniform half-space is used in creating theoretical solution. The parameters, (shear wave velocity, compression wave velocity, layer thickness or density) were varied, one at a time. It is shown that the shear wave velocity and layer thickness are the two major factors that affect the Rayleigh wave velocity.

Chapter 3   Rayleigh Wave Testing

3.1 BACKGROUND

Rayleigh wave testing techniques are an advancement of seismological and geophysical exploration methods in the area of engineering site investigation. Geophysical methods, e.g. reflection and refraction tests, focus on: (1) the interpretation of travel paths of direct and indirect body waves, (2) the identification of first arrivals or group arrivals of body waves to detect material boundaries or anomalies and interpret material stiffness. Since Rayleigh waves, also called "ground roll" in geophysics, dominate seismic energy at the ground surface vibrations created by surface sources. It is typical for geophysicists to remove Rayleigh wave components in seismograms using various filter techniques before data reduction.

Rayleigh wave testing can be generally divided into three steps: (1) source generation and data collection in the field, (2) signal processing and dispersion curve construction and (3) inversion of experimental dispersion curves to estimate V_s profiles. There are two types of seismic sources, active and passive, used in R-wave testing. The first category use sledge hammers, explosives, bulldozers or vibroseises to create vertical surface vibrations which includes body and surface waves. Active sources are widely used in geotechnical site investigation due to their controlled frequency contents and flexibility in the field. The other category is passive sources. Low-frequency Rayleigh waves generated by large earthquakes, sometimes travel around the earth several times before dissipating. These R-waves are collected and used in studying the earth mantle system by seismologists. Turbulence caused by wind or highway traffic also yields Rayleigh waves, but uncontrolled source location brings complexity in reducing data when ambient noises are used as sources.

Field data are collected by sensors, usually either geophones or accelerometers, depending on exploration scale desired. Geophones convert ground response into voltage, which is proportional to the velocity of particles. Seismometers are also used as sensors which can measure motions with frequencies from less than 0.1 Hz to 100 Hz or more. Geophones generally function at low to moderate frequencies (1 to 1000Hz), thus are suitable to be used in moderate-depth material exploration. Accelerometers are electromechanical devices that measure ground accelerations and generally function in the range of 10 to 50,000 Hz or more. They are widely used in non-destructive testing in rock, concrete or metal systems due to their usability in high frequency ranges.

Signals (velocity or acceleration) are store on computers or digital analyzers before they pass certain filters to remove unwanted noises and aliasing. In geotechnical engineering, data collection systems include large 48- or 72-channel recorders which collect numerous signals simultaneously, or portable 4-channels analyzers. Digital analyzers with higher resolution capacity seem to be always desired to capture more information about the seismic motions.

Inversion is a process that is used to estimate shear wave velocity profiles based on experimental dispersion curves obtained from field surface wave testing. Wavelengths of Rayleigh waves are related to the penetration depth of the waves. A simple way to convert dispersion curves to V_s profiles is to relate shear wave velocity to Rayleigh wave velocity with Poisson's ratio, and approximate penetration depth with wavelengths times certain coefficients (Richart et al., 1970). The method provides a coarse estimation of material distribution. More accurate information about the soil system requires a precise matching between the field and theoretical dispersion curves.

3.2 DEVELOPMENT OF SURFACE WAVE METHODS

3.2.1 Steady-State Rayleigh Wave Method

The steady-state Rayleigh wave test, also called "continuous surface wave (CSW) test", was the first technique invented to measure stiffness of the soil system by measuring surface wave dispersion. The method was developed in the 1950s and 1960s (Jones, 1955; 1962). The initial try on pavement systems showed the possibility of acquiring dispersion of surface waves when the stiffness decreases as a function of depth. The method was further applied by using ultrasonics on concrete slabs to assess thickness and stiffness information. The success of this technique led to its application in geotechnical site investigation, where lower frequency sources and receivers are used.

In the steady-state method, an electro-magnetic shaker was used as an active source and two geophones were used as receivers. The second geophone was moved progressively away from the vibrator to measure wavelengths on the surface with a specified frequency. The length between two geophones which first showed the steady-state waveform in phase corresponds to one wavelength (λ), as illustrated in Figure 3.1. This procedure is repeated for different frequencies and gradually the phase velocity at different frequencies is obtained to construct the complete dispersion curve.

The wavelength (λ) and frequency (f) are used to calculate the phase velocity for a certain frequency based on Equation (3.1):

$$V_R = f \cdot \lambda \qquad\qquad (3.1)$$

To improve the precision, the following procedure can be applied: points corresponding to different locations at which the receiver is in phase with the source are represented in a diagram of source-receiver distance versus number of cycles (Figure 3.2). The slope of the straight line connecting the points represents the inverse of the wavelength for the current frequency.
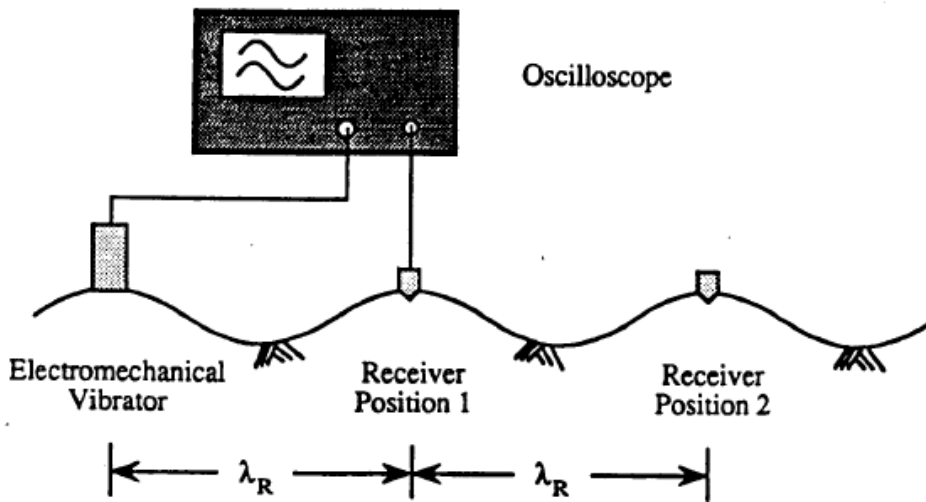
Figure 3.1   Illustration of Steady-State Rayleigh Wave Field Testing (from Rix, 1996)
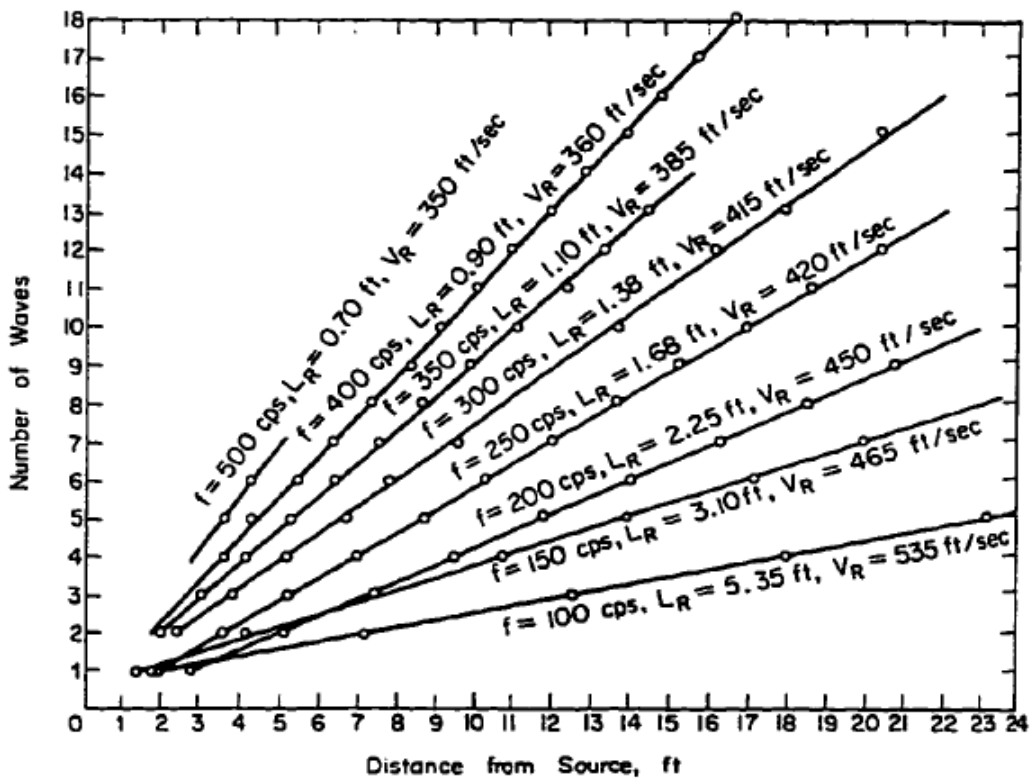
Figure 3.2   Determination of Average Wavelengths of Rayleigh Waves in Steady-State
R-Wave Testing (from Richart et al., 1970)

Compared to advanced inversion process in SASW and MASW methods, the steady-state method is empirical and obtains the shear wave velocity profile in a simplified way as:

$$V_S = 1.1 \cdot V_R \tag{3.2}$$

$$Z = 0.5 \cdot \lambda \tag{3.3}$$

where Z = sampling depth.

As mentioned in Chapter 2, Rayleigh waves propagate with energy concentrated within a certain depth near the ground surface. In the steady-state method, the depth of soil sampled by the Rayleigh wave is assumed to be one half of the wavelength (although one-third of the wavelength also used sometimes), as illustrated in Figure 3.3. With this assumption, the steady-state method may give a reasonable approximation of the V_s profile in a simple system with moderate velocity increases with depth, but it will fail to recover soil stratigraphy in terms of shear wave velocity when strong contrasts in material properties, or soft layers sandwiched between stiff layers.

3.2.2 Spectral-Analysis-of-Surface-Waves Method

The steady-state Rayleigh wave method was replaced by Spectral-Analysis-of-Surface-Waves (SASW) method in the early 1990s. The SASW has a faster field procedure and an accurate analysis method. The SASW method, originally developed by Nazarian and Stokoe during the 1980s (Nazarian and Stokoe 1984), is widely known for in-situ V_s measurements. The productivity and efficiency of the SASW method is attributed to the development of computing devices, which are capable of performing filtering and Discrete Fourier Transform (DFT) simultaneously on multiple channels in the field. Similar to the steady-state method, the SASW method can be divided in three steps: (1) field data recording; (2) dispersion curve extracting and (3) inversion to obtain
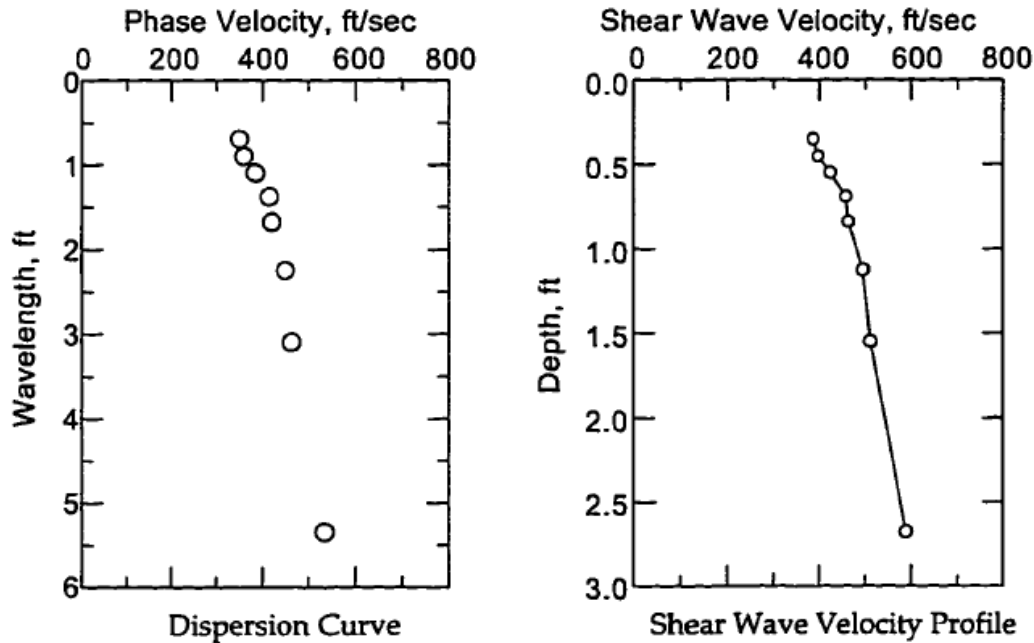
Figure 3.3   Illustration of Conversion from Dispersion Curve to V_s Profile by Steady-
                State Rayleigh Wave Method (from Joh, 1996)

the V_s profile.

As explained in articles (Stokoe et al,1994), "the SASW method utilizes the
dispersive nature of Rayleigh-type surface waves propagating through a layered material
to determine the shear wave velocity profile of the material. In this context, dispersion
arises when surface wave velocity varies with wavelength or frequency. Dispersion in
surface wave velocity arises from changing stiffness properties of the soil and rock layers
with depth.   The dispersion phenomenon is illustrated in Figure 3.4 for a multi-layered
solid. A high-frequency surface wave, which propagates with a short wavelength, only
stresses material near the exposed surface and thus only samples the properties of the
shallow, near-surface material (Figure 3.4b). A lower-frequency surface wave, which
has a longer wavelength, stresses material to a greater depth and thus samples the
properties of the shallower and deeper materials (Figure 3.4c). Spectral analysis is used

to separate the waves by frequency and wavelength to determine the experimental ("field") dispersion curve for the site. An analytical, forward - modeling procedure is then used to theoretically match the field dispersion curve with a one-dimensional layered system of varying layer stiffnesses and thicknesses (Joh, 1996). The one-dimensional shear wave velocity profile that generates a dispersion curve that most closely matches the field dispersion curve is presented as the shear wave velocity profile at the site."

Further, Stokoe explained that (Stokoe et al., 1994), "SASW testing involves generating surface waves at one point on the exposed material surface and measuring the motions perpendicular to the surface created by the passage of surface waves at two or more locations on the surface. All measurement points are arranged on the exposed surface along a single radial path from the source. Successively longer spacings between the receivers and between the source and first receiver are typically used to measure progressively longer and longer wavelengths. This general testing configuration for one source/receiver set-up is illustrated in Figure 3.5. In this example, a source and two receivers are used. The distance between the source and first receiver (d) is kept equal to the distance between the two receivers (d) as shown in Figure 3.5. Testing is performed with several (typically six or more) sets of source-receiver spacings for a total of 12 or more receive pairs, and the totality of the sets of source-receiver spacings is called an SASW array."

The variation in phase shift with frequency for surface waves propagating between adjacent receivers is recorded for each receiver spacing. From each receiver pair, the phase velocity of the surface wave can be calculated at each frequency from:
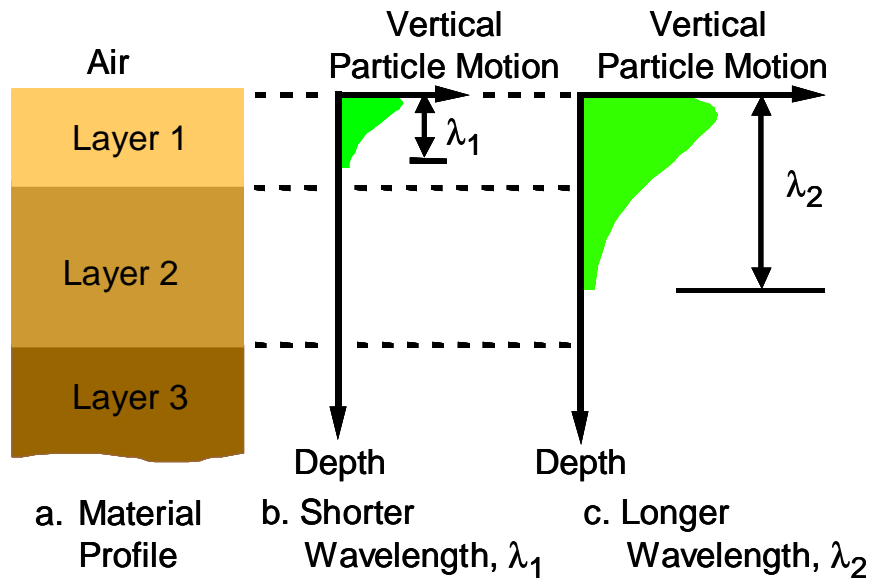
Figure 3.4   Illustration of Surface Waves with Different Wavelengths Sampling
Different Materials in a Layered System (after Stokoe et al., 1994)
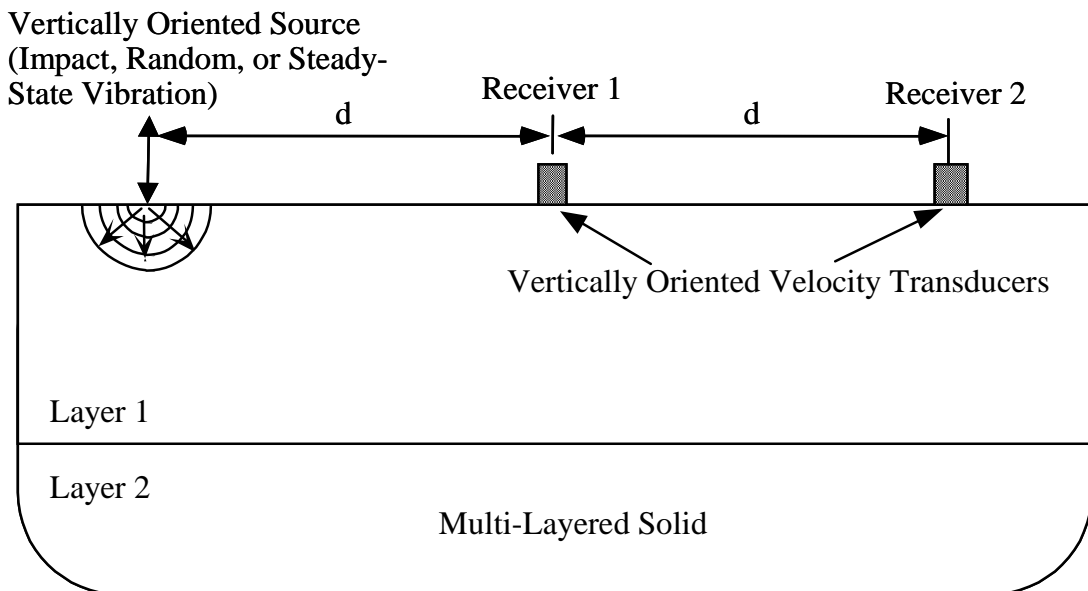
Figure 3.5   Schematic Diagram of the Generalized Equipment Arrangement Used in
Spectral-Analysis-of-Surface-Waves (SASW) Testing for One Receiver Pair
(after Stokoe et al., 1994)

$$V_R = f(\frac{360}{\phi})d \qquad (3.4)$$

where V_R is the phase velocity in ft / sec or m/s, f is the frequency in Hertz (cycles per sec), ϕ is the phase angle in degrees (at frequency f), and d is the distance between the receivers in the same length units as used to represent V_R.

The dynamic signal analyzer is used to measure time-domain records (x(t) and y(t)) from the two receivers in each receiver pair at each receiver spacing. These time records are then transformed into Laplace form X(s) and Y(s). Then the output is related to the input by the transfer function H(s) as:

$$X(s) = \mathcal{L}\{x(t)\} \overset{\text{def}}{=} \int_{-\infty}^{\infty} x(t)e^{-st}\, dt \qquad (3.5)$$

$$Y(s) = \mathcal{L}\{y(t)\} \overset{\text{def}}{=} \int_{-\infty}^{\infty} y(t)e^{-st}\, dt \qquad (3.6)$$

$$H(s) = \frac{Y(s)}{X(s)} \qquad (3.7)$$

$$G(\omega) = \frac{|Y|}{|X|} = |H(j\omega)| \qquad (3.8)$$

$$\phi(\omega) = \arg(Y) - \arg(X) = \arg(H(j\omega)) \qquad (3.9)$$

where $G(\omega)$ is the amplitude spectrum, $H(j\omega)$ is the frequency response, and $\phi(\omega)$ is the phase difference.

In a linear time-invariant system, the input circular frequency, ω, has not changed. Only the amplitude and phase angle of the sinusoid has been changed by the system. This change for every circular frequency, ω, is described by the frequency response, $H(j\omega)$. The phase shift between two receivers is given by $\phi(\omega)$.

"The phase shift calculated from the transfer function, $\phi(\omega)$, is the key spectral quantity in SASW testing. When a sledge hammer, bulldozer or vibroseis is used as the source, the spectral functions are determined by comparing the Fast Fourier Transform (FFT) of geophone signals in a certain frequency range. The record time and resolution control the length of the frequency span. The numbers of averages are adjusted in the

47

field to obtain an appropriate low-noise-level transfer function (determined by visual inspection in the field). Typically, ten averages are used in the determination of the spectral functions when an impact source (sledge hammer) is employed. Twenty or more averages are typically used when the bulldozer was employed. The number of averages at each frequency is typically no more than 25 or 30 when the vibroseis is used. The phase shift calculated from the transfer function, simply called the phase hereafter, represents the phase difference of surface motion at each frequency between two receivers. One set of spectral functions was measured for each receiver spacing and testing direction."

As an example, a wrapped phase spectrum evaluated from one receiver spacing (one receiver pair) is shown in Figure 3.6a. For these measurements, a Caterpillar D8k bulldozer was used as the source and the data were collected with a 25-ft receiver spacing at one site in Canada. A masking procedure is then performed to manually eliminate portions of the data with poor signal quality and/or portions of the data that were deemed to contain additional and unwanted near-field waveform components. Figure 3.6b shows the masking applied to the original wrapped phase plot in Figure 3.6a. The masking information is used to unwrap the phase plot, and then calculate the individual dispersion curve using the relationship presented in Equation 3.4. Individual dispersion curves from each receiver pair are determined and then combined to form the composite dispersion curve discussed below.

a. Wrapped Phase Calculated from Transfer Function for R1-R2 = 25 ft

Deleted ("masked") zone because of
near-field components
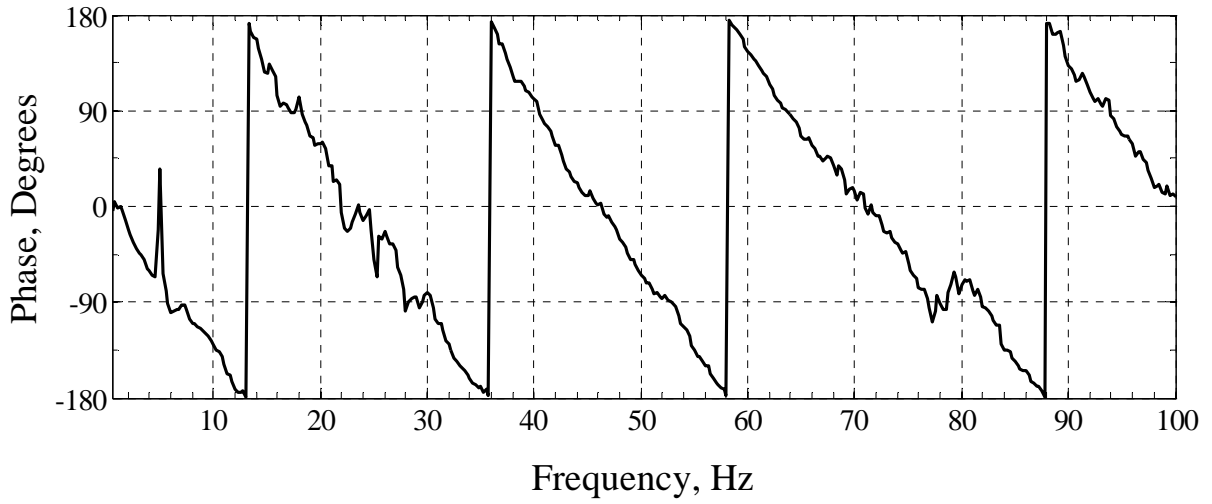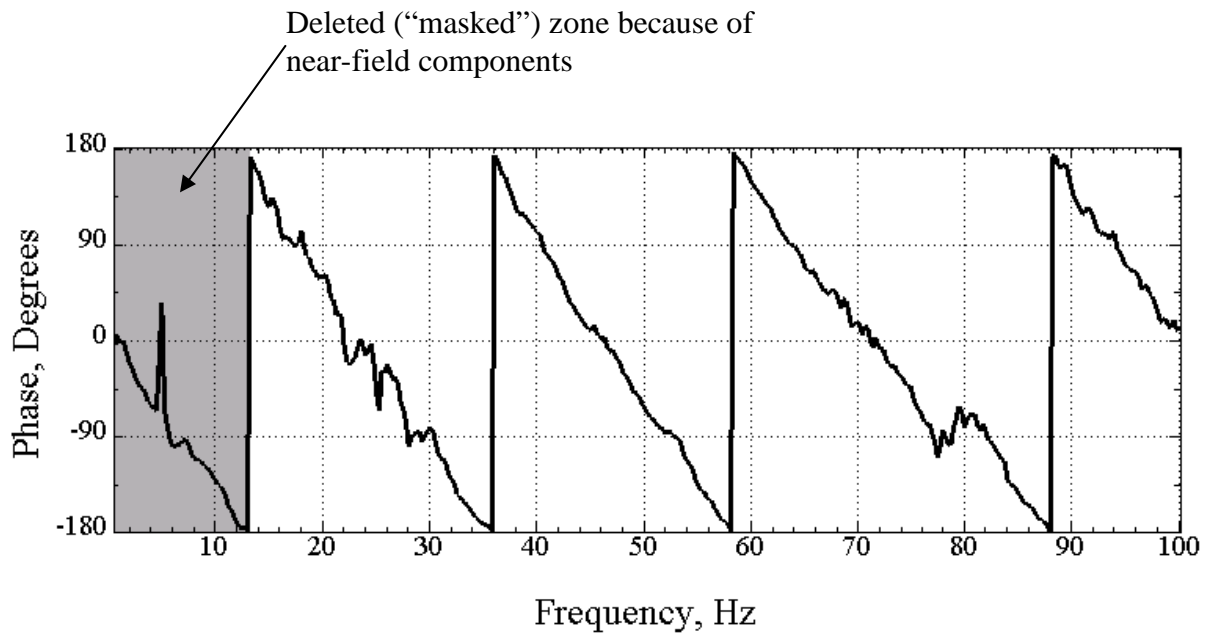
b. Masked Wrapped Phase to Minimize Near-Field Components

Figure 3.6   An Example of Wrapped Phase of the Transfer Function Measured with a
Bulldozer as the Seismic Source and a 25-ft, S-R$^{\#}$1 Receiver Spacing

From these calculations, a plot of phase velocity versus frequency, called an individual dispersion curve, is generated. The individual dispersion curve from the 25-ft spacing with the bulldozer as seismic source is shown in Figure 3.7. This procedure is repeated for all source-receiver spacings used at the site and typically involves significant overlapping in the dispersion data between adjacent receiver sets. The individual dispersion curves from all receiver spacings are combined into a single composite dispersion curve called the "experimental" or "field" dispersion curve as shown in Figure 3.8.

Once the composite field dispersion curve is generated for the site, an iterative forward modeling procedure is used to create a theoretical dispersion curve to match the experimental curve (Joh, 1996), which is usually termed "inversion". Different algorithms, for example, genetic algorithm and artificial neural network, were applied to study and improve the robustness of the searching progress (Orozco, 2005, Pezeshk and Zarrabi, 2005, Shirazi et al., 2006). WinSASW, a program written by Joh, is used in generating theoretical dispersion curves. In this program, values for Poisson's ratio and unit weight which are required input to obtain a V_s profile are usually estimated from local measurements or material types. An example of comparison between theoretical dispersion curve and experimental dispersion curve is shown in Figure 3.9. The stiffness profile that provides the best match to the experimental dispersion curve is presented as the shear wave velocity, V_s, profile at the site, as shown in Figure 3.10. Typical comparisons between V_s profiles measured by SASW testing and by independent crosshole and downhole seismic tests are presented in Figures 3.11 and 3.12 for work conducted in earlier studies (Joh, 1996; Fuhriman and Stokoe, 1993).
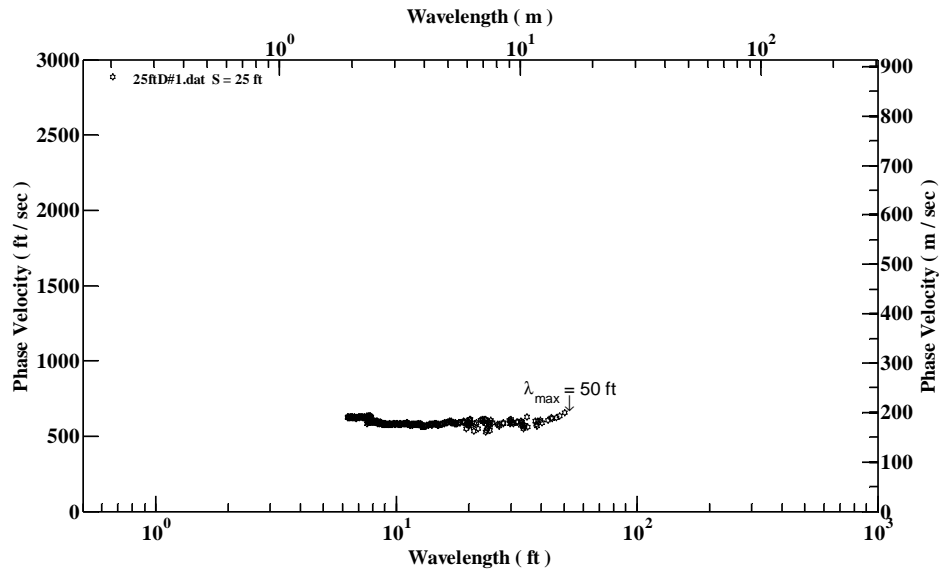
Figure 3.7   Individual Experimental Dispersion Curve Created from the Unwrapped
             Phase Record in Figure 3.6b Measured with a 25-ft Spacing between the
             Receiver Pair
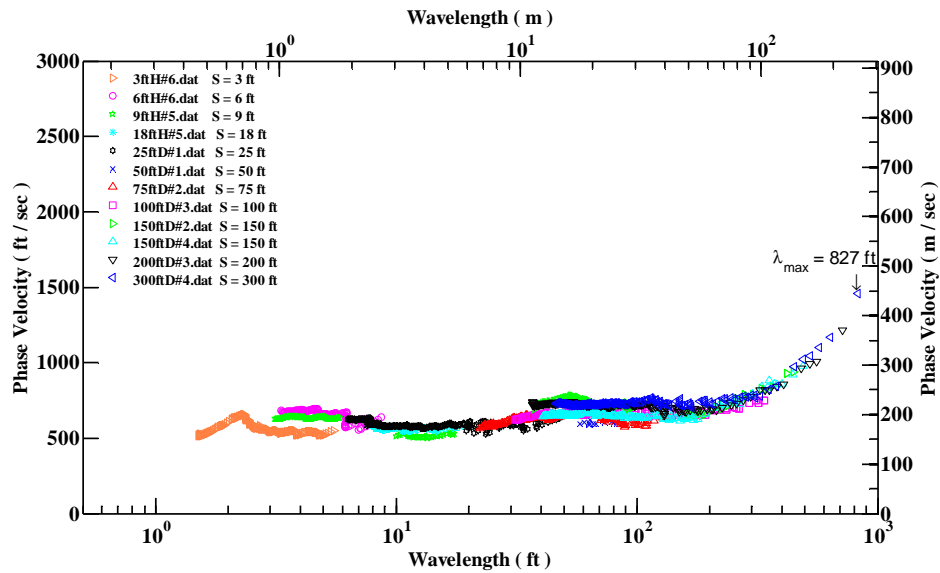
Figure 3.8   Composite Experimental Dispersion Curve Created from Phase
             Measurements Performed at One Site using a Sledge Hammer and Large
             Bulldozer as the Seismic Sources

51
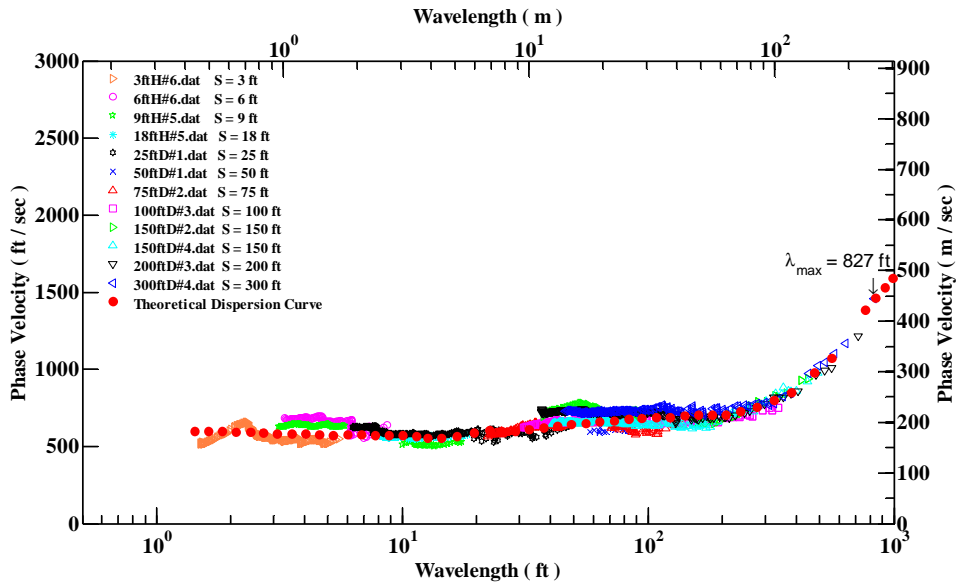
Figure 3.9   An Example of Comparison of the Fit of the Theoretical Dispersion Curve
             to the Composite Experimental Dispersion Curve
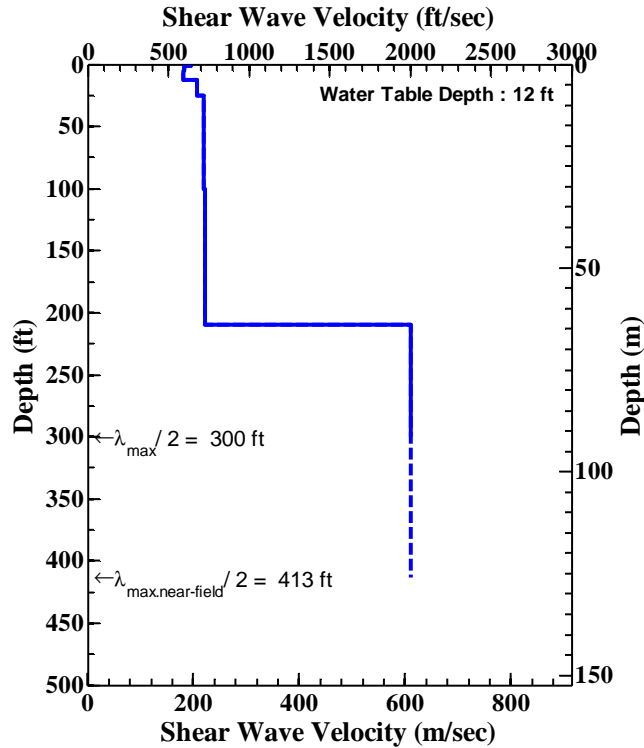
Figure 3.10 An Example of V_s Profile from Forward Modeling
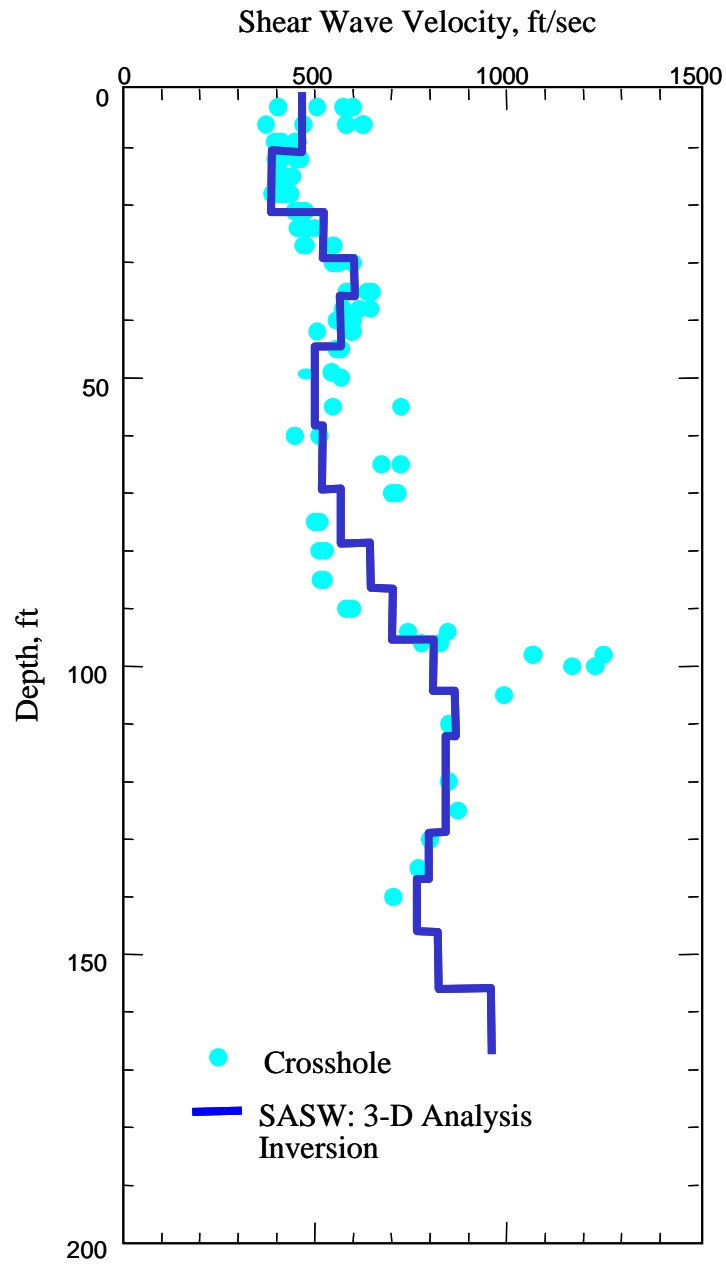
Figure 3.11 Comparison of Shear Wave Velocity Profiles from SASW and Crosshole
Measurements Performed at a Site on Treasure Island near San Francisco,
CA (Joh, 1996; Fuhriman and Stokoe, 1993)
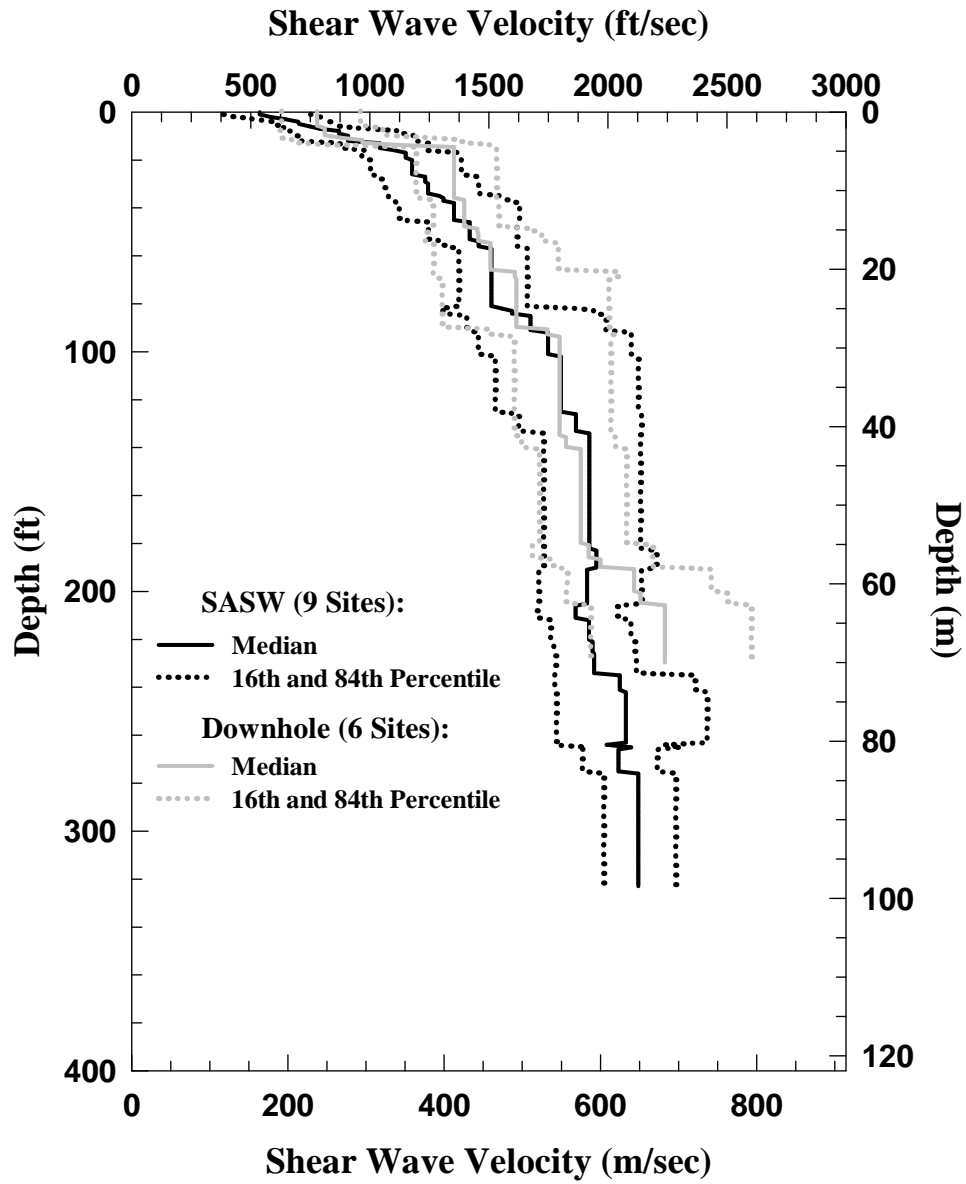
Figure 3.12 Comparison of SASW and Downhole Median Profiles of Both Sand and
Gravel Sequences in the Hanford Formation (Stokoe et al., 2005)

3.2.3 Multichannel-Analysis-of-Surface-Waves (MASW) Method

The MASW method, has evolved from the SASW method, becoming widely used in the measurement of shear wave velocity profiles in geotechnical investigation. The method involves placing multiple receivers in a linear, equally-spaced array on the ground surface to record seismic motions simultaneously. In this manner, one can analyze the data directly from field refraction and reflection tests. This method was first developed by researchers at Kansas Geological Survey in 1999 (Park et al, 1999). Similar to the SASW method, the MASW method use vertical geophones to capture propagation of Rayleigh waves for further interpretation. Data reduction of MASW method also includes extraction of field dispersion curves and inversion of V_s profiles.
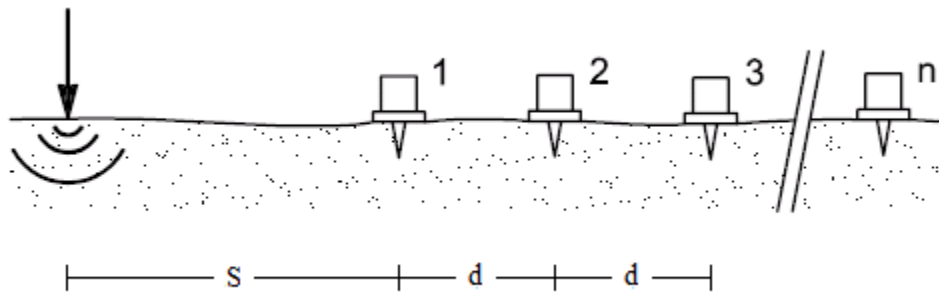
Figure 3.13   Typical MASW Field Setup (after Foti, 2000)

3.2.3.1 Field Testing

An illustration of an MASW field setup is shown in Figure 3.13. Similar to the SASW testing, surface waves are often generated by either hand-held sources like sledge hammers or small, swept-frequency sources. Vibrations induced by the sources are collected using a minimum of 12 to 60 sensors placed on the ground (Park et al., 1999).

The basic field configuration and acquisition procedure for MASW testing is generally the same as that used in conventional common midpoint (CMP) body-wave reflection surveys. Results from MASW tests can be affected by the field setup: source

type, source location, geophone spacing, geophone type, number of geophones and site conditions.

As in all seismic methods, source type plays a very important role in identifying material distribution at testing sites with the MASW method. Typical sources include sledge hammer and small shakers. Researchers (Park et al, 1999) suggested the use of a swept-frequency source for MASW testing since it can be optimized both in amplitude and frequency contents. However, he also concluded that both type of sources can produce similar results given that the desired depth of measurement is relatively shallow. MASW testing can also be performed in passive mode. Ambient noise and ground roll are used as sources in MASW testing. Park (2005) introduced a way to combine active and passive dispersion images to better identify the fundamental mode, designated as M0 in Figure 3.14.

The near offset, the distance between source and nearest geophone, is defined in the MASW method to avoid near-field effects in Rayleigh wave measurements. The common assumption is that after a certain distance from the source point, Rayleigh waves are fully developed (Richart et al., 1970). It is widely assumed that the Rayleigh wave is formed only after near-offset is larger than about half of the maximum required wavelength (Stokoe et al., 1994). This assumption is, of course, site-profile dependant. Based on Park's opinion, a near offset with 10 meters can be used to sample wavelengths as large as 60 meters without interference of near-field effects (Park et al., 2001). The far offset is also defined in the MASW method to describe the phenomenon of high-frequency component dissipation at larger distances from source. This effect limits the highest frequency at which phase velocity can be measured (Stokoe, 1994). Moreover, geophone spacing should be carefully chosen to avoid spatial aliasing, which occurs
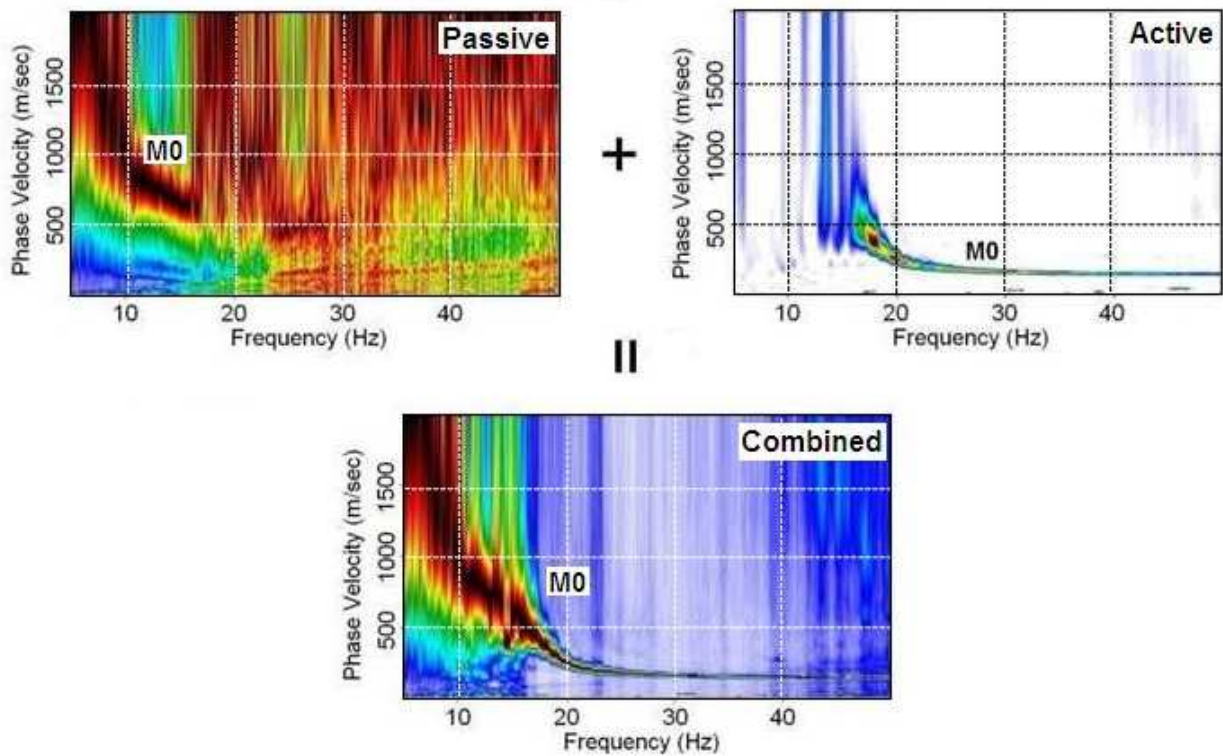
Figure 3.14   Utility of Combining Passive and Active Measurements in MASW Testing
to Enlarge the Frequency Range (Modified from Park, 2005)

when the measured wavelength is less than twice the geophone spacing.

In MASW testing, 4.5-Hz vertical geophones are typically used. This geophone type is sufficient for shallow (less than 50m) geotechnical site investigations, but a low-frequency geophone (1- or 2-Hz geophones) is preferred when deep material needs to be investigated. In terms of number of sensors, more sensors are preferred to improve the resolution in the frequency-wavenumber (F-K) domain. If the analyzer does not have enough channels to collect data simultaneously, a walkaway method is used to measure a test array several times with different source locations. The walkaway method simply means that multiple source points at increasing near-offsets are used. The records from all source points are then combined to form a comprehensive waveform. The walkaway

method can be performed with a portable analyzer, but takes longer time in data collection.

A summary compiled by Wood (2009) of the MASW tests with different test setups and analysis methods is presented in Table 3.1.

Table 3.1   Summary of MASW Test Set-up (from Wood, 2009)

Reference	Description	fn_{Sens} (Hz)[1]	$\#_{Sens}$[2]	Δx (m)[3]	offset (m)[4]	x (m)[5]	Δt (s)[6]	Analysis method	Source(s)
Hebeler (2001)	Mid-America[9]	low Accel[7]	15	Variable[8]	2.4	33.5	0.003	Beamformer	APS Dynamics Shaker
Long and Donohue (2007)	Fredrikstad, Norway N-S	10	24	1	0,2,4	23	NA	Surfseis	Sledgehammer
Tran and Hiltunen (2008)		NA	62	0.61	3,6,9,12,15	37	NA	Beamformer	Sledgehammer/vibrator
Edited by Asten and Boore (2004)	San Jose, California	NA	15	2.4	NA	33.5	NA	Beamformer	Harmonic oscillator
Xia, Miller, Park, Hunter, Harris (2000)	B.C. Canada FD92-11	4.5	60	0.6	18	35.4	0.001	Surfseis	Accelerated weight drop
"	B.C. Canada FD97-4	4.5	60	1.2	18	70.8	0.001	Surfseis	Accelerated weight drop
Foti and Fahey (2003)	Perth, Australia Ewing Street	2	NA	1-3	NA	NA	NA	f-k	Sledgehammer/Drop weight
"	Perth, Australia Vincent street	2	NA	1-3	NA	NA	NA	f-k	Sledgehammer/Drop weight
Park,Miller,Xia (1997)	KGS test site, Kansas	10	40	1	27	39	0.001	CCSAS	IVI Minivib (Vibroseis)

1.   The natural frequency of the geophones used during testing
2.   The number of sensors used for testing
3.   The sensor spacing used during testing
4.   The source offset used for testing
5.   The total array length used during testing
6.   The sampling rate used during testing
7.   Low frequency accelerometers
8.   The spacing varied between 0.61 m to 4.6 m over the length of the array
9.   11 different sites were tested across Mid-America using the same parameters

3.2.3.2 Extraction of Experimental Dispersion Curves

MASW field dispersion curves are generated as separated modes of surface waves. There are currently several methods to convert the time-domain into the frequency-velocity domain. The most widely used method in geophysics for creating dispersion curves is the intercept-slowness (τ-p) transform (McMechan and Yedlin, 1981). The signals in the offset-time format are transformed to intercept time-slowness wavefield by slant stacking. Then, a 1-D Fourier transform is applied to achieve the slowness-frequency (p-ω) domain. Thus, the data wave field is linearly transformed from the time-distance domain into the slowness-frequency domain, where dispersion curves

are imaged. All data are present throughout the transformations. Dispersion curves of fundamental and higher modes are directly observed in the frequency domain. McMechan and Yedlin applied the method to both synthetic and field data and achieved good results. An illustration of an intercept-slowness (τ-p) transform is shown in Figure 3.15.
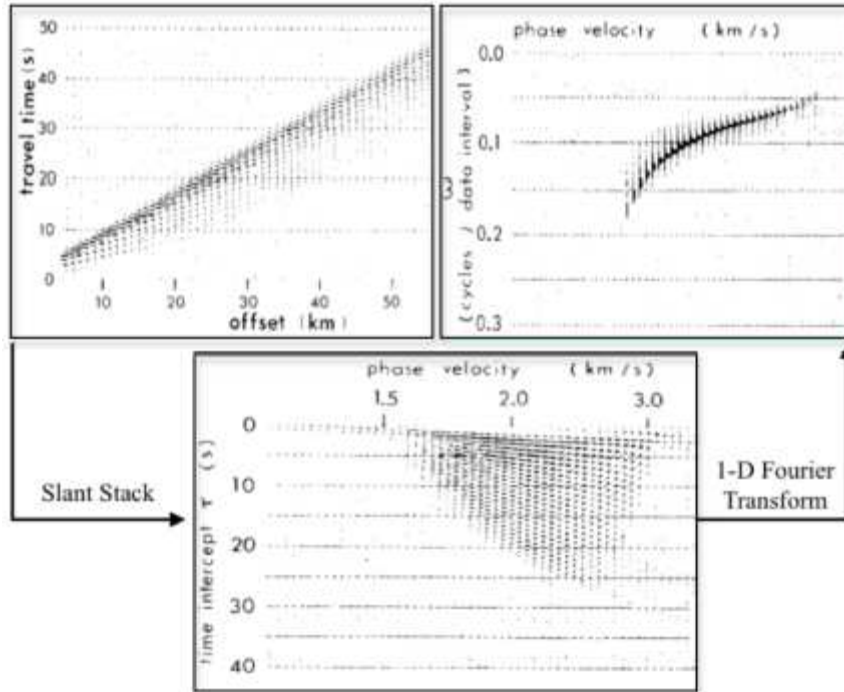
Figure 3.15   Intercept-Slowness Transform on a Synthetic Wavefield (McMechan and
              Yedlin, 1981, Modified by Dulaijian, 2008)

Similarly, Park (1998) developed a method to transform time-domain signals into a space-angular frequency domain (u(x,t) to U(x, ω)) using a Fourier Transform as:

$$U(x,\omega) = \int u(x,t)e^{i\omega t}\,dt \tag{3.10}$$

U(x, ω) can be considered as the multiplication of the phase spectrum and the amplitude spectrum. The phase spectrum contains wave-velocity information, and the amplitude spectrum contains attenuation information(Dulaijian, 2008) as:

$$U(x,\omega) = A(x,\omega)e^{-i\phi x} \tag{3.11}$$

where $\phi = \dfrac{\omega}{c_\omega}$, and c_ω is the phase velocity.

After the following integral transformation, one obtains:

$$S(\omega,\theta) = \int e^{i\theta x}\left[\frac{U(x,\omega)}{|U(x,\omega)|}\right]dx = \int e^{i(\theta-\phi)x}\left[\frac{A(x,\omega)}{|A(x,\omega)|}\right]dx \qquad (3.12)$$

The transformation is considered to be summing over the offset of the wavefields of a frequency after applying the offset-dependent phase shift, θ, determined for an assumed phase velocity. For a given circular frequency, S(ω, θ) have a maximum at $\phi = \theta = \dfrac{\omega}{c_\omega}$.

Phase velocity is estimated where the peak of S occurs. The peak at the lowest velocity corresponds to the fundamental mode of the circular frequency. Peaks with higher velocity are treated as higher modes. After changing frequency and velocity, all peaks over desired frequency ranges are determined and thus dispersion curves are formed. It is noted that this method yields dispersion curves with better resolution than the τ-p transform when a small number of traces are used over a limited range of offsets (Park at al., 1998).

The frequency-wavenumber (f-k) method is widely used in geophysics and has recently been used in MASW testing for shallow geotechnical investigations. In the f-k method, time-domain signals are converted to the frequency-wavenumber domain by performing 1-D Fourier transform twice, one on the time interval, and another on the spatial intervals. The transform is generally called the 2-D Fourier transform. It can be used to enhance data quality through the discrimination of noise (Foti, 2000). However, one concern about the frequency-wavenumber domain transformation is spatial aliasing, which is similar to temporal aliasing in time domain revealed by the Nyquist criterion. In the time domain, signals are collected by analyzers with built-in anti-aliasing filters. In the spatial domain, it is necessary to post-process the collected data to avoid spatial

aliasing. Similar to other methods, frequency-wavenumber method can also resolve higher modes of surface waves.

The most influential transform technique is the cylindrical beamforming method proposed by Zywicki (1999). The method treats multi-channel records as a cylindrical wavefield, thus yields the most accurate representation of the wavefield when an active source is used. The method provides the highest resolution of dispersion curves compared to other methods (Tran and Hiltunen, 2008). Also, it allows phase velocities to be estimated for relatively long wavelengths compared to the length of the receiver arrays (Zywicki, 1999).

In the beamforming method, a spatiospectral correlation matrix is formed. The matrix consists of the cross power spectrum between all collected signals of all frequencies. The beamforming term is derived from the ability of an array or signal processing algorithm to focus on a particular direction or wavenumber (Johnson and Dudgeon, 1993). The main lobe of the array smoothing function is defined as a beam. The beamforming method determines the power of each f-k pair by multiplying the spatiospectral correlation matrix by the steering vector (e) and summing the total power over all sensors. The steering vector provides an exponential phase shift which is controlled by a set of trail wavenumbers. The beamforming method can use weighting vectors to account for geometric spreading, but the conventional beamforming analysis uses uniform weighting for all sensors (Zywicki 1999). Each power can be calculated using Equation 3.13:

$$P_{FDBF}(f,k) = e^{H}(k)R(f)e(k) \qquad (3.13)$$

where H represents the Hermitian transpose, e(k) represents phase shift vector associated with a trial k, R represents correlation matrix.

Calculations made using Equation 3.13 give estimates of the power of f-k pairs. The calculations lead to a ridge of maximums formed in frequency-wavenumber space (Wood, 2009). The ridge is used to calculate the Rayleigh phase velocity for each test frequency using the fundamental relationship between wavelength, frequency, and phase velocity shown in Equation 3.1.

A comparison of the frequency-velocity spectrum achieved by different transform methods is shown in Figure 3.16.
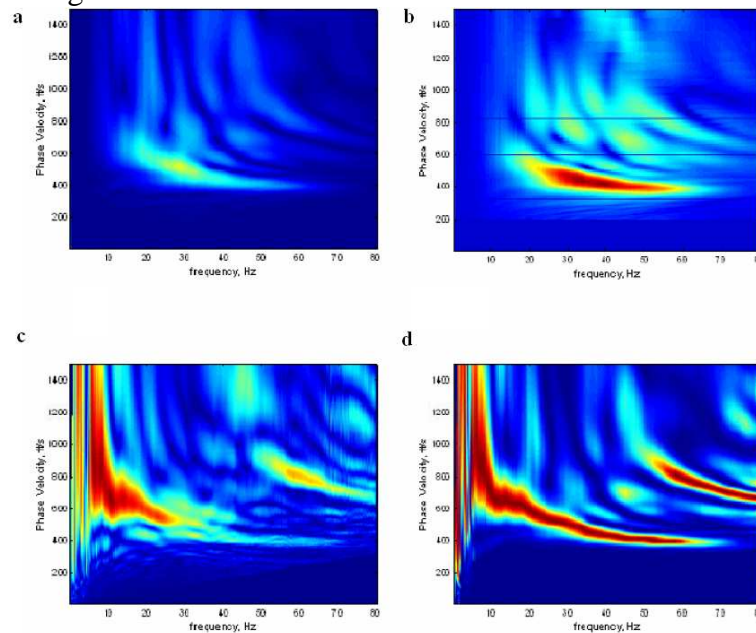
Figure 3.16 Frequency-Velocity Spectrum Generated by: a) f-k method, b) f-p method, c) Park's method and d) cylindrical beamforming method (from Tran and Hiltunen, 2008)

3.2.3.3 Inversion

Inversion of the experimental dispersion curve has been the focus of many studies over decades, beginning with the basis of Haskell's contribution in multilayer dispersion computation (Haskell, 1953). Since it can be very difficult to match several theoretical modes of the Rayleigh wave to the field dispersion curves, the MASW method generally

uses only the fundamental mode in the inversion process. At normally dispersive sites (increasing stiffness with increasing depth without any inverse velocity contrasts), the fundamental mode of dispersion curves is applicable to an inversion analysis. An example comparison of MASW and SASW test results is shown in Figure 3.17 (Tran and Hiltunen, 2008).

Park (2003) developed SurfSeis, a software based on a leaset-square method of automatically solving the inversion problem. The performance of automated inversion algorithms still needs further improvement for sites with complicated geometries or material distributions, particularly with velocity inversions.

3.3 SUMMARY

In this chapter, a brief introduction to various surface wave testing techniques is presented. The first method that introduced surface wave testing is the steady-state, Rayleigh-wave test. This method was quite practical and empirical but was helpful in geotechnical site investigation. Due to its inefficiency in the test procedure and its empirical nature, it was replaced by the SASW and MASW methods. The SASW method provides good convenience in data acquisition by viewing wrapped phase plots during data collection. This ability for real-time monitoring in the field provides more flexibility in field operation once poor data is encountered. The algorithm it uses provides an accurate estimate of wave propagation and energy distribution. The only disadvantage of the SASW method is that the phase unwrapping process takes time, and can require knowledgeable and experienced personnel to reduce the data in difficult situations. The MASW method operates on an automated inversion program, thus this process is rapid. However, geophone type, spacing and source should be carefully chosen to acquire representative results. Also, the assumption of considering only the fundamental mode in
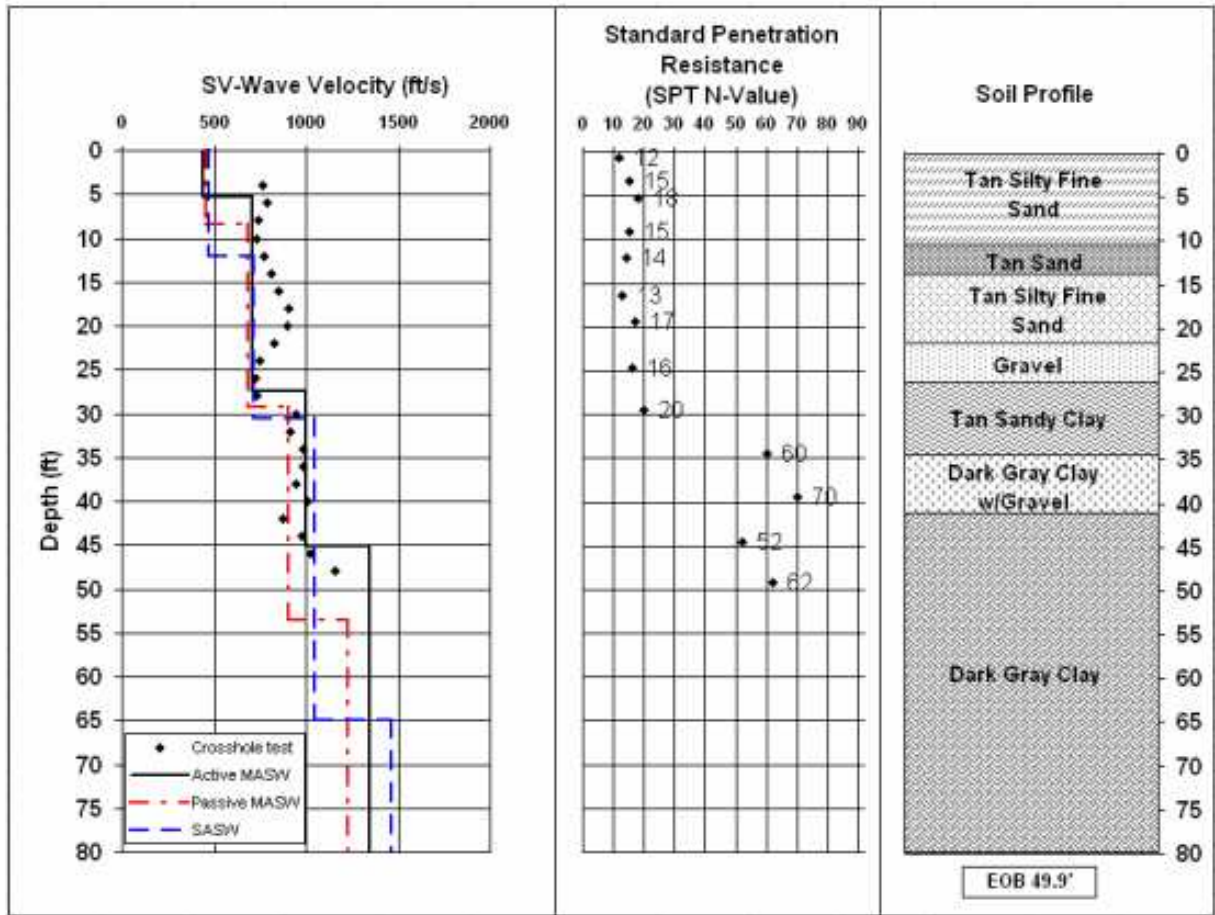
Figure 3.17   Shear Wave Velocity Profiles from Various Surface Wave Methods and
Geological Information at one site. (from Tran and Hiltunen, 2008)

the inversion process may lead to erroneous profiles once higher-mode energy dominates in certain wavefields.

Chapter 4   Numerical Simulation

4.1 BACKGROUND

Numerical simulation was performed to validate the effectiveness of SASW, beamforming and F-K techniques in determining the dispersion curves from the synthetic seismograms. The synthetic wavefields were generated by FitSASW, a software based on the 3-D solution of dynamic stiffness matrix method. The studies are made by comparing the theoretical solutions from both transfer matrix method, which presented as modal phase velocities, and dynamic stiffness method, which presented as apparent phase velocities, with the calculated dispersion curves from SASW, beamforming and F-K techniques.

Three models are used in generating the synthetic seismograms: a bedrock model, a normally dispersive model and a "sandwich" model where a low velocity zone is set as an interbed between the top layer and the halfspace. The parameters of three models are shown in Tables 4.1 through 4.3. The corresponding synthetic seismograms are shown in Figure 4.1 through Figure 4.3. The V_s profiles for three models are shown in Figure 4.4.

4.2 DATA PROCESSING

Synthetic waveforms are processed into dispersion curves by (1) calculating phase plots of different signal pairs to construct a composite dispersion curve, (2) calculating spatial correlation matrix to form a frequency – wavenumber (f-k) curve with the maximum energy at each frequency and (3) performing a 2D Fourier transform on time and spatial domains to form the dispersion relationship in the f-k domain.

The parameters used to generated the synthetic waveforms are the same for all three models. 60 channels are equally spaced with 3.28-ft (1-m) spacings and a source

offset of 3.28ft (1 m). The time interval is 0.0025 sec and the number of data point on each signal is 2048.

Table 4.1   Parameters of the Bedrock Model to Generate Synthetic Seismograms

Layer No.	Thickness, ft	Depth to Top of Layer, ft	P-Wave Velocity, ft/s	S-Wave Velocity, ft/s	Poisson's Ratio	Total Unit Weight, pcf
1	16.41	0	984	492	0.33	119
2	99999*	16.41	2411	1476	0.20	150

* Layer as Halfspace

Table 4.2   Parameters of the Normally Dispersive Model to Generate Synthetic Seismograms

Layer No.	Thickness, ft	Depth to Top of Layer, ft	P-Wave Velocity, ft/s	S-Wave Velocity, ft/s	Poisson's Ratio	Total Unit Weight, pcf
1	32.81	0	984	492	0.33	119
2	65.62	32.81	1968	984	0.33	119
3	99999*	98.43	2411	1476	0.20	150

* Layer as Halfspace

Table 4.3   Parameters of the Inversion (Sandwich) Model to Generate Synthetic Seismograms

Layer No.	Thickness, ft	Depth to Top of Layer, ft	P-Wave Velocity, ft/s	S-Wave Velocity, ft/s	Poisson's Ratio	Total Unit Weight, pcf
1	16.41	0	1968	984	0.33	119
2	32.82	16.41	984	492	0.33	119
3	99999*	49.23	1968	984	0.33	119

* Layer as Halfspace
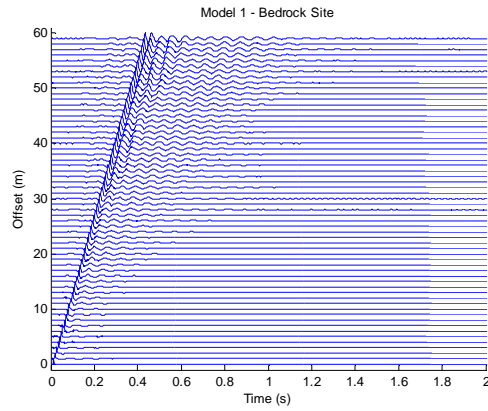
Figure 4.1   Synthetic Seismogram for Model 1 – A Bedrock Site
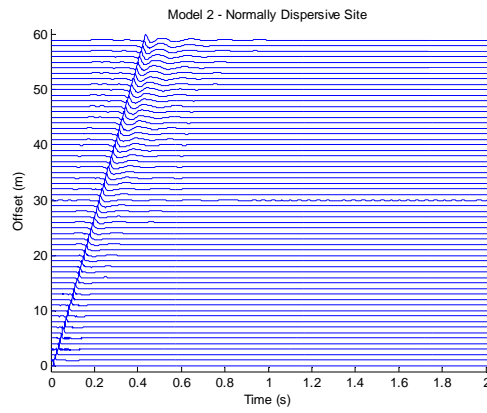
Figure 4.2   Synthetic Seismogram for Model 2 – A Normally Dispersive Site
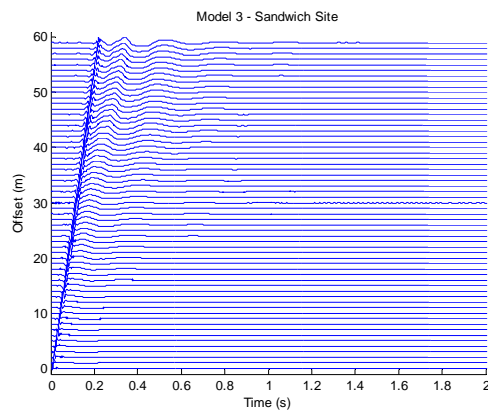
Figure 4.3   Synthetic Seismogram for Model 3 – A Inversion (Sandwich) Site
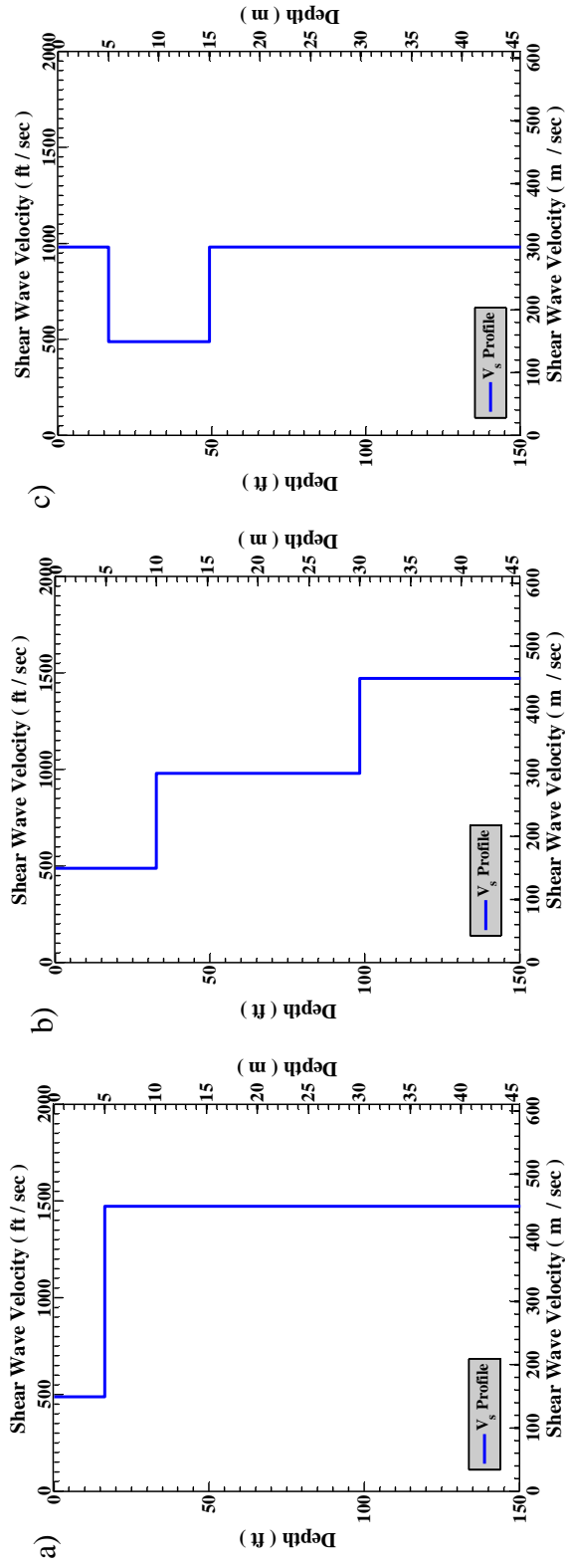
Figure 4.4 V_s Profiles for a) Model 1 – A Bedrock Site, b) Model 2 – A Normally Dispersive Site and c) Model 3 – A Inversion (Sandwich) Site

69

4.2.1 SASW Method

For each model, the phase difference of a signal pair is calculated while the source offset is maintained as the same as the distance between the signal pair. An example of a phase plot with a 6.56-ft (2-m) spacing from the first model is shown in Figure 4.5. A composite dispersion curve is constructed by combining the dispersion curves from various spacings.
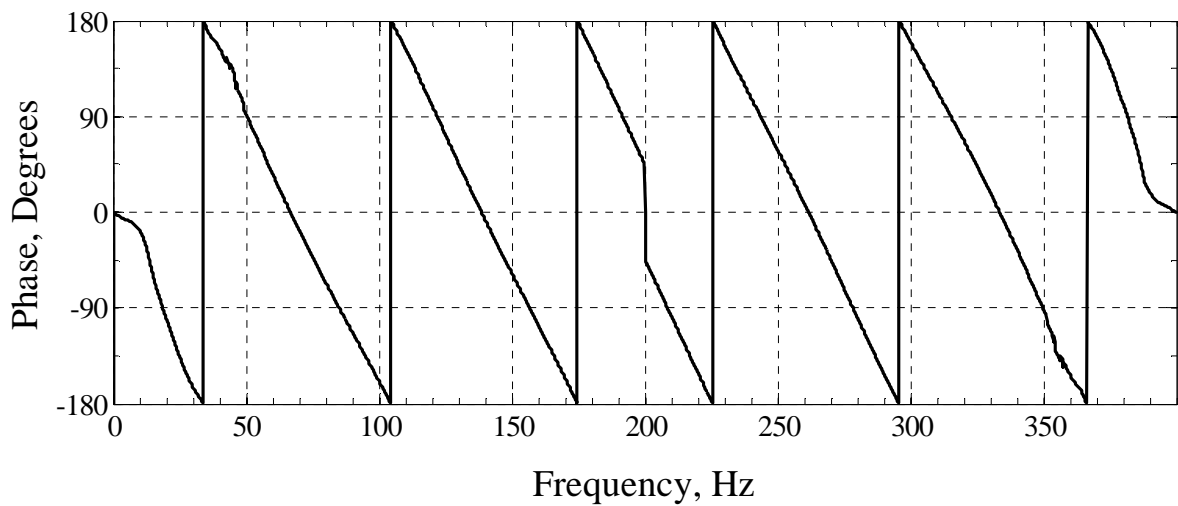
Figure 4.5   A Phase Plot Calculated with a 6.56-ft Receiver Spacing from the Synthetic Seismograms for the Bedrock Model

4.2.2 Beamforming Method

The result of beamforming transform of the 60-channel synthetic seismograms is shown in Figure 4.6. The ridge with the maximum energy is plotted as to calculate the experimental dispersion curve.

4.2.3 F-K Method

A two-dimensional Fourier transform over both time and space is termed an F-K transform where F is the frequency (Fourier transform over time) and K refers to

70
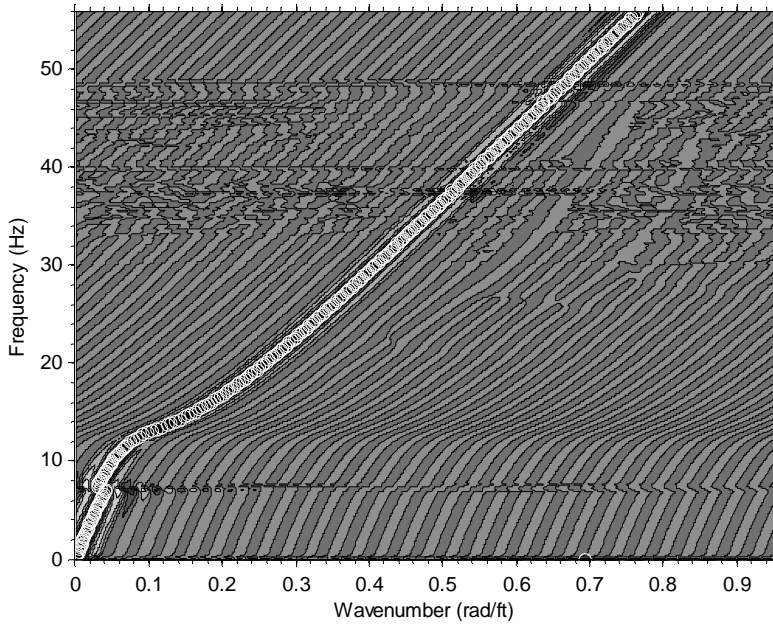
Figure 4.6   A Wavenumber – Frequency Plot from the Beamforming Transform with
the Synthetic Seismograms of Model 1- A Bedrock Site
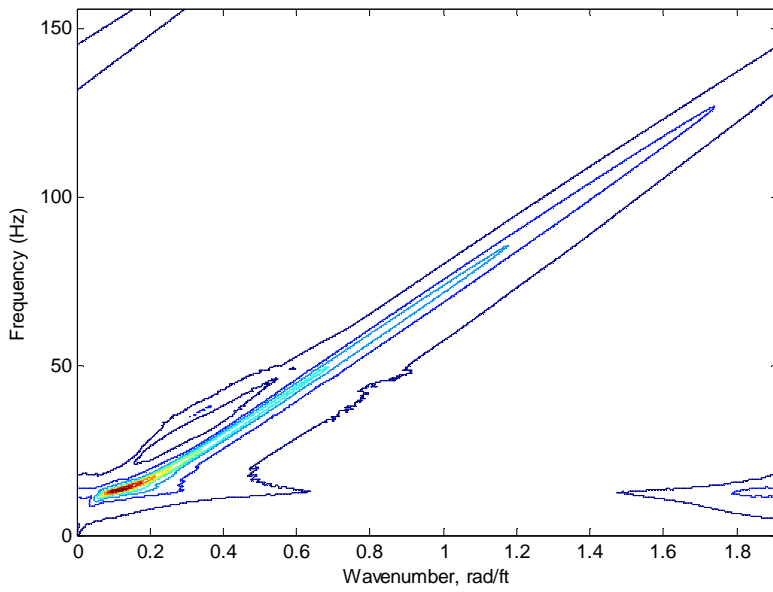
Figure 4.7   A Wavenumber – Frequency Plot from the 2D Fourier Transform with the
Synthetic Seismograms of Model 1- A Bedrock Site

wavenumber. A Example of the F-K plot generated by a 2D Fourier transform on the synthetic seismograms for the first model is shown in Figure 4.7.

4.3 SIMULATION RESULTS

4.3.1 Model 1 – A Bedrock Site

Both modal velocity and apparent phase velocity for the model of a bedrock site are calculated from transfer matrix method and dynamic stiffness method for the bedrock model as shown in Figure 4.8a. It is observed that the 2-D solution of apparent phase velocity agrees well with the fundamental mode of modal phase velocity. The 3-D solution is slightly higher than the 2-D solution except at the frequency range between 10 to 15 Hz, where the 3-D solution overlaps with the 1st mode of modal phase velocity. Thus, at the site with no velocity inversion, higher mode may still play a dominant role in defining the apparent phase velocity at certain frequency ranges.

The dispersion curves processed from the synthetic seismograms with Beamforming and F-K transform are shown in Figure 4.8b. It is observed that both techniques produced similar results. By comparing them with the theoretical modal dispersion curves, it is found that results from both techniques agree with the fundamental mode after 12 Hz. Before 12 Hz, both techniques show two trends which are slightly lower than fundamental mode and 1st mode (second lowest modal velocity) correspondingly.

The dispersion curve from SASW analysis is compared with dispersion curve from F-K transform and modal dispersion curves in Figure 4.8c. It is observed that SASW and F-K methods generated similar results which stand for apparent phase
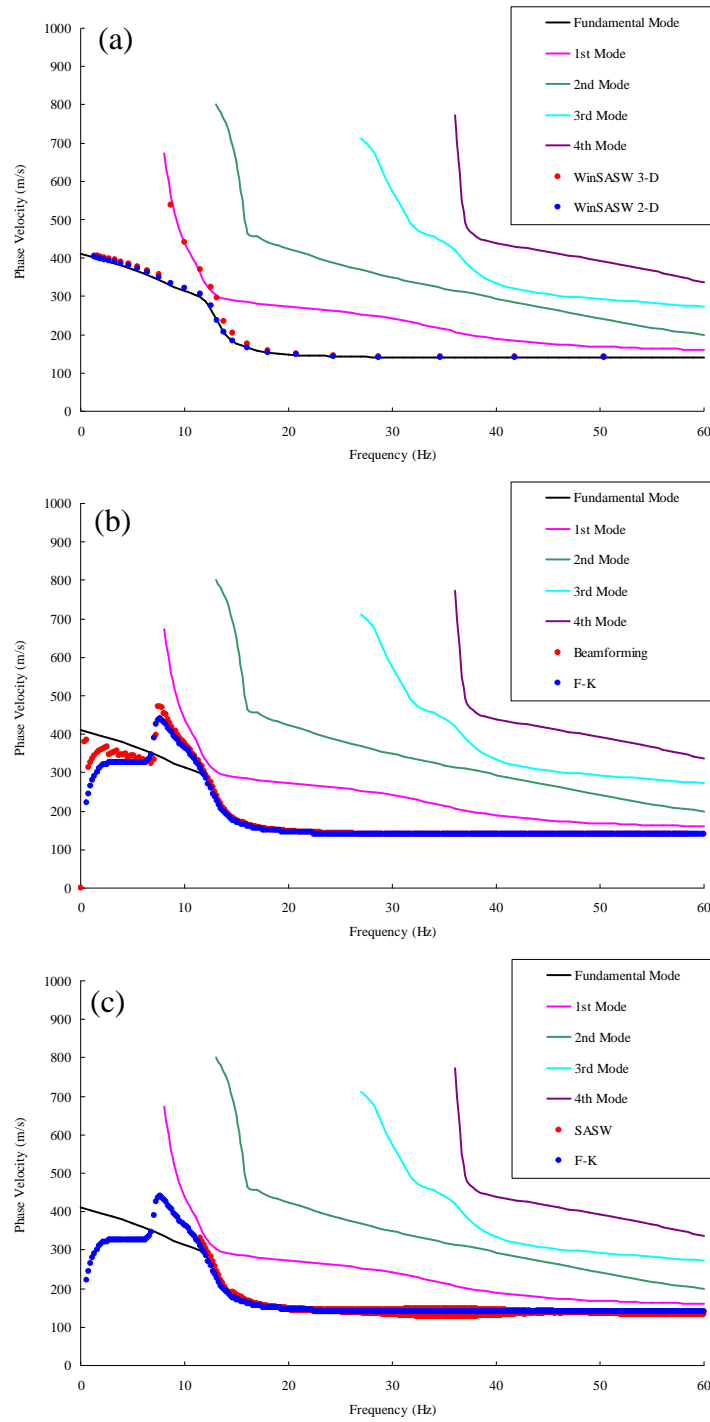
Figure 4.8   Frequency – Velocity Plots from (a) Theoretical Modal and Apparent Phase
Velocity Methods, (2) Beamforming and F-K Transform and (3) SASW
Analysis with the Synthetic Seismograms of Model 1 – A Bedrock Site

velocities.

4.3.2 Model 2 – A Normally Dispersive Site

For the second model - a normally dispersive site as shown in Figure 4.4b, theoretical solutions from transfer matrix method and dynamic stiffness method are calculated. Both modal velocity and apparent phase velocity for the model are shown in Figure 4.9a. It is again observed that the 2-D solution of apparent phase velocity agrees well with the fundamental mode of modal phase velocity. The 3-D solution is slightly higher than the 2-D solution except at the frequency range between 1 to 4 Hz, where the 3-D solution overlaps with the 1st mode of modal phase velocity.

The results from the transform by both Beamforming and F-K methods on the synthetic waveforms are Figure 4.9b. It is observed that both techniques produced similar results above 3 Hz, where dispersion curves agree with the fundamental mode of modal dispersion curves. F-K method produced two trends at frequency less than 3 Hz, while Beamforming method yielded phase velocity even lower than the theoretical fundamental mode.

The dispersion curve from SASW analysis is compared with dispersion curve from F-K transform and modal dispersion curves in Figure 4.9c. It is observed that SASW and F-K methods generated similar results for the normally dispersive model, and both of them agree well on the fundamental mode.

4.3.3 Model 3 – An Inversion (Sandwich) Site

The results from the analyses of the synthetic seismograms of an inversion site, as shown in Figure 4.4c, are presented in Figure 4.10. The comparison between apparent phase velocity and modal phase velocity is shown in Figure 4.10a. It is observed that WinSASW 2-D, 3-D and fundamental mode agree well at the frequency range from 0 to
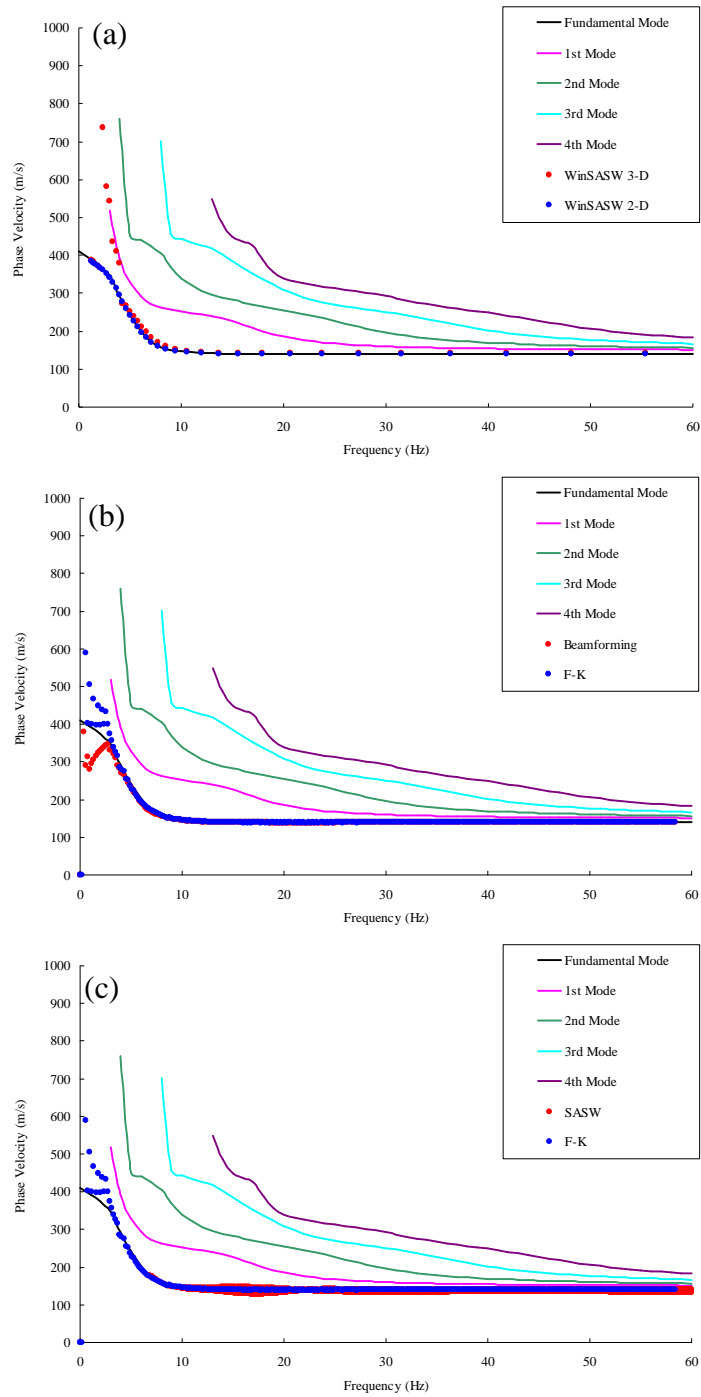
Figure 4.9   Frequency – Velocity Plots from (a) Theoretical Modal and Apparent Phase
Velocity Methods, (2) Beamforming and F-K Transform and (3) SASW
Analysis with the Synthetic Seismograms of Model 2 – A Normally
Dispersive Site
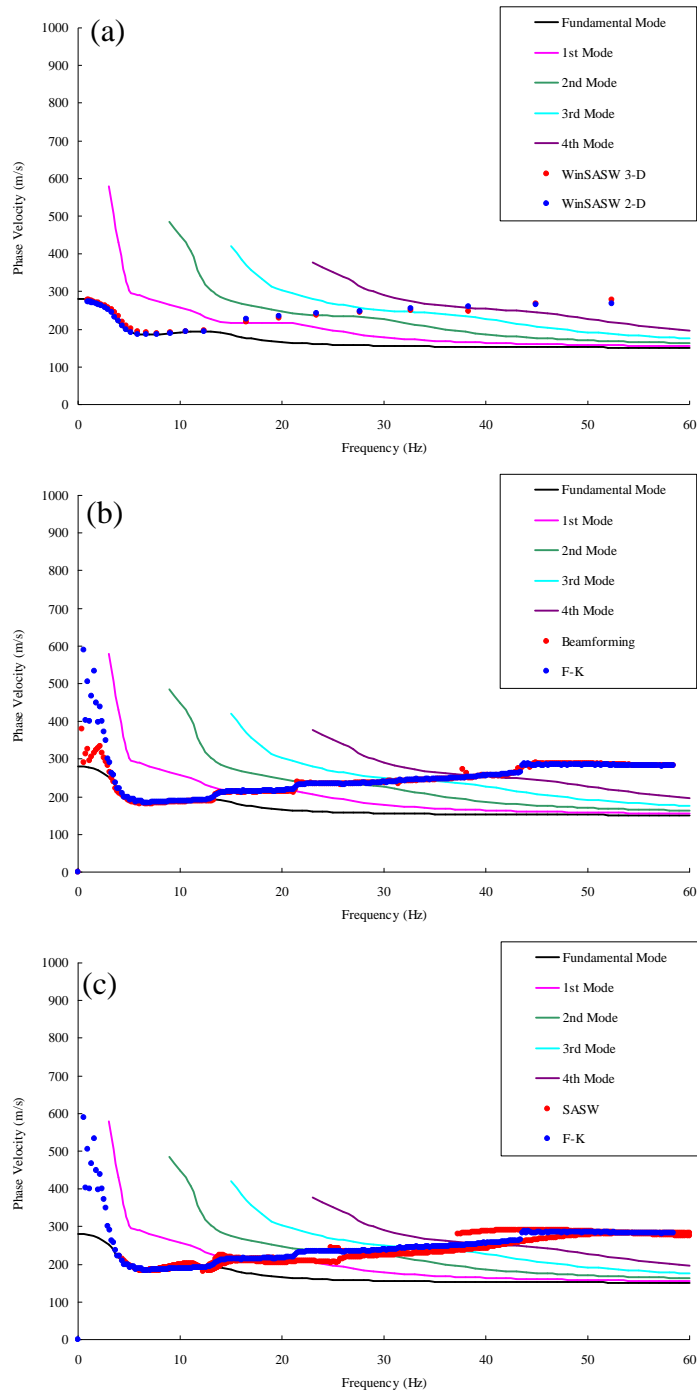
Figure 4.10 Frequency – Velocity Plots from (a) Theoretical Modal and Apparent Phase Velocity Methods, (2) Beamforming and F-K Transform and (3) SASW Analysis with the Synthetic Seismograms of Model 3 – A Inversion (Sandwich) Site

12 Hz. After that frequency, the theoretical apparent phase velocity gradually moves to higher modes as frequency increases.

The results from the transform by both Beamforming and F-K methods on the synthetic waveforms are Figure 4.10b. It is observed that both techniques produced similar results above 2 Hz, where dispersion curves agree with the fundamental mode of modal dispersion curves up to 13 Hz. Both dispersion curves start to move to higher modes after 13 Hz.

The dispersion curve from SASW analysis is compared with dispersion curve from F-K transform and modal dispersion curves in Figure 4.10c. It is observed again that SASW and F-K methods generated similar results for the inversion model, and both of them are considered to be the apparent phase velocity.

4.4 CONCLUSIONS

In this chapter, analyses were performed on numerically simulated waveforms for three different models. The theoretical solutions from both transfer matrix method and stiffness matrix method are compared to investigate the influence of higher modes on apparent phase velocity. Dispersion curves from the SASW, Beamforming and F-K transform are also compared. It is found that three techniques produced similar apparent phase velocity, when the data corresponding to maximum energy among all modes along the frequency axis are used

Chapter 5   Field Surface Wave Testing

5.1 BACKGROUND

A series of SASW and MASW tests was performed as a parametric study on the characteristics of surface wave testing at a site in Austin, Texas. The site tha was selected is called Hornsby Bend. The site was selected because of: (1) the extensive series of in situ tests that have been performed at the site in the past, (2) a large open level area and (3) the proximity (about 5 miles away) of the site to the UT campus. The Hornsby Bend site, own the by City of Austin, is used as a waster-water treatment site which located in the southeast side of the city.

Since 1980s, various tests have been performed at the Hornsby Bend site. In September of 1985, Southwestern Laboratories performed a routine geotechnical investigation of the site for a proposed waste-to-energy plant. A series of crosshole tests were performed at the site since then by personnel from the University of Texas. During 1986 and 1987, Dr. Mok (Mok, 1987) also conducted extensive studies using the crosshole and downhole seismic methods at the site. CPT tests were also conducted in 2011 by Mr. Kim to assist the site investigation.

In this chapter, the field test equipment and procedures used to perform the SASW and MASW tests at the Hornsby Bend site are summarized. Results from various tests used to support this study are presented and discussed in the following sections.

5.2 SITE LOCATION

The Hornsby Bend site is located at the north-west corner of Highways 130 and 71 as shown in Figure 5.1. The site is own by the City of Austin, and has been extensively characterized by SASW, CPT tests and geotechnical boreholes. The site was chosen for the current research due to its proximity to many previous tests, the low

ambient noise level, the open field and the relatively flat ground surface. The exact location of the center of the test site is given by coordinates: 30.230454467N and 97.64187911W. The altitude at the center of test array is 133.782 meters above mean sea level. The variance of elevation at the site is less than 0.3 meter.
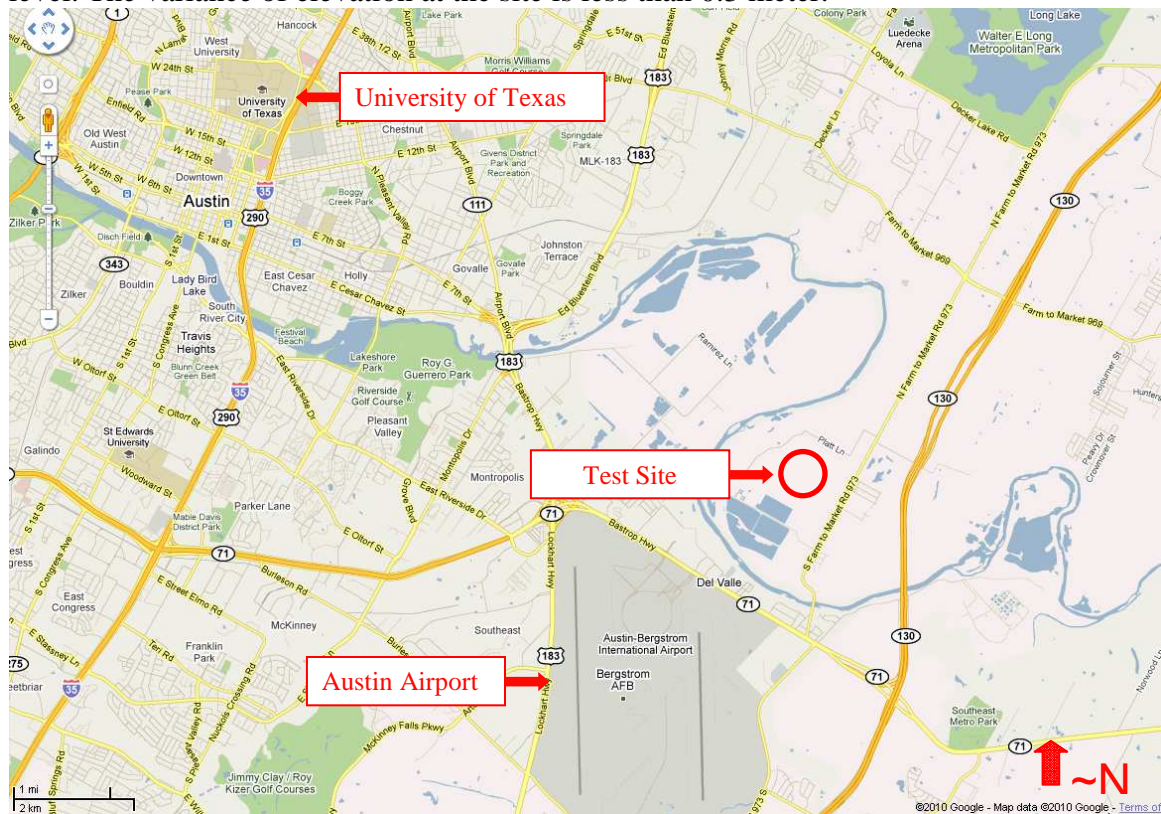
Figure 5.1   Map of Hornsby Bend Site (Courtesy of Google Map)

Two sets of field tests were performed to evaluate shear wave velocity profiles at the site. The first set of tests was performed from October 30 through 31, 2010. SASW and MASW tests were performed using T-Rex, a vibroseis own by the University of Texas at Austin, and sledge hammers as seismic sources and 1-Hz geophones as seismic receivers. The second set of tests was performed from January 24 through 25, 2011. MASW and SASW tests were conducted along the same test array used in the first set of

tests. In this case, Liquidator and sledge hammers were used as seismic sources, and 1-Hz and 4.5Hz geophones were used as receivers. CPT and SCPT tests were also conducted at the center, and at both ends of the array as well as at other locations. Mr. Kim was in charge of this work. A satellite image of the test location is shown in Figure 5.2

Figure 5.2   Satellite Image of the Test Array at the Hornsby Bend Site (Courtesy of Google Map)

5.3 TEST SETUP

In this section, test equipment, procedures and other related issues associated with the SASW and MASW tests are presented. All Source signals used are list in Table 5.1.

5.3.1 Seismic Sources

Drop-weights, bulldozers and vibroseis are the three most common seismic sources in surface wave testing to depths equal to or greater than 30m. Sledge hammers

are good for shallow measurements (5 to 15m), whereas large vibroseises provide enough energy to seismically sample deep material (>200m). Continental Oil Company (Now ConocoPhillips) developed a series of Vibroseises in the 1950s. They are still widely used to create various source signals (sinusoid, chirp or Ricker wavelet) for different purposes. The University of Texas at Austin owns four vibroseises, named Thumper, Raptor, T-Rex and Liquidator, with which powerful land seismic investigations are performed. In this context, T-Rex and Liquidator were used in this study. Features of T-Rex and Liquidator are summarized in Table 5.2. Pictures of Liquidator and T-Rex are shown in Figures 5.3 and 5.4, respectively.

An Agilent 33220A function generator was used to create different drive source signals that were used to control T-Rex and Liquidator. In this research, a step-sine, chirp and Ricker wavelet were used as the source signals besides hammer impacts for the short receiver spacings. An example of the source signals used in both sets of tests is listed in Table 5.1. Illustrations of the different source signals are shown in Figure 5.5.

Table 5.1   Source Signals used in SASW and MASW Testing

Signal #	Signal Type
1	Chirp 3-8Hz
2	Chirp 8-20 Hz
3	Chirp 20-25Hz
4	Chirp 25-35Hz
5	Ricker Wavelet 20Hz
6	Step Sine 25-3Hz
7	Step Sine 110-20Hz
8	Hammer Impulsive

Table 5.2   T-Rex Features (from Stokoe et al, 2004)

Vibrator	T-Rex	Liquidator`	Thumper
Vehicle Type	Buggy-mounted vibrator, articulated body	Buggy-mounted vibrator, articulated body	Built on Ford F650 Truck
Driving Speed	Hydraulic drive system (<15 mph)	Hydraulic drive system (<15 mph)	Highway Speeds
Total Weight	29,030 kg (64,000 lb)	29,030 kg (64,000 lb)	9980 kg (22,600 lb)
Length	9.8 m (32 ft)	9.8 m (32 ft)	7.1 m (23 ft)
Width	2.4 m (8 ft)	2.4 m (8 ft)	2.4 m (8 ft)
Height	3.2m (10.5 ft)	3.2m (10.5 ft)	2.4 m (8 ft)
Hydraulic System Pressure	207 bar (3,000 psi)	207 bar (3,000 psi)	476 bar (4000 psi)
Vibrator Pump Flow	757 l/m (200 gpm)	530 l/m (140 gpm)	151 l/m (40 gpm)
Vibration Orientations	(1) Vertical, (2) Horizontal in-line, and (3) Horizontal cross-line	(1) Vertical, and (2) Horizontal cross-line	(1) Vertical, (2) Horizontal in-line, and (3) Horizontal cross-line
Shaking Orientation Transformation	Push-button transformation of shaking orientation	Shop transformable in one day	Field transformable in about hour hours
Maximum Output Force: (1) Vertical, and (2) Shear	(1) 267 kN (60,000 lb) (2) 134 kN (30,000 lb)	(1) 89 kN (20,000 lb) (2) 89 kN (20,000 lb)	(1) 26.7 kN (6000 lb) (2) 26.7 kN (6000 lb)
Base Plate Area	4.11 m^2 (44.2 ft^2)	4.34 m^2 (46.7 ft^2)	0.698 m^2 (7.50 ft^2)
Moving Mass: (1) Vertical, and (2) Shear	(1) 3,670 kg (8,100 lb) (2) 2,200 kg (4,850 lb)	(1) 13,475 lb (6,110 kg) (2) 13,475 lb (6,110 kg)	(1) 311 lb (140 kg) (2) 311 lb (140 kg)
Stroke (Peak to Peak): (1) Vertical, and (2) Shear	(1) 8.9 cm (3.5 in.) (2) 17.8 cm (7.0 in.)	(1) 40.6 cm (16.0 in.) (2) 40.6 cm (16.0 in.)	(1) 7.6 cm (3.0 in.) (2) 7.6 cm (3.0 in.)
Hydraulic Oil	Vegetable-based hydraulic oil	Vegetable-based hydraulic oil	Vegetable-based hydraulic oil
Special Features	(1) Cone pushing capacity (2) Hydraulic pressure take-off (3) Variable vertical hold-down force (4) Must be transported by tractor-trailer rig	(1) Optimized for low freq. (down to 0.5 Hz) (2) Cone pushing capacity (3) Hydraulic pressure take-off (4) Must be transported by tractor-trailer rig	(1) Built for high-frequency output (above 200 Hz) (2) Built for use in urban environments (3) Can be driven on highways

Figure 5.3   Liquidator Used as a Seismic Source at the Hornsby Bend Site (Courtesy of NEES@UTexas)

Figure 5.4   T-Rex Used as a Seismic Source at the Hornsby Bend Site (Courtesy of NEES@UTexas)
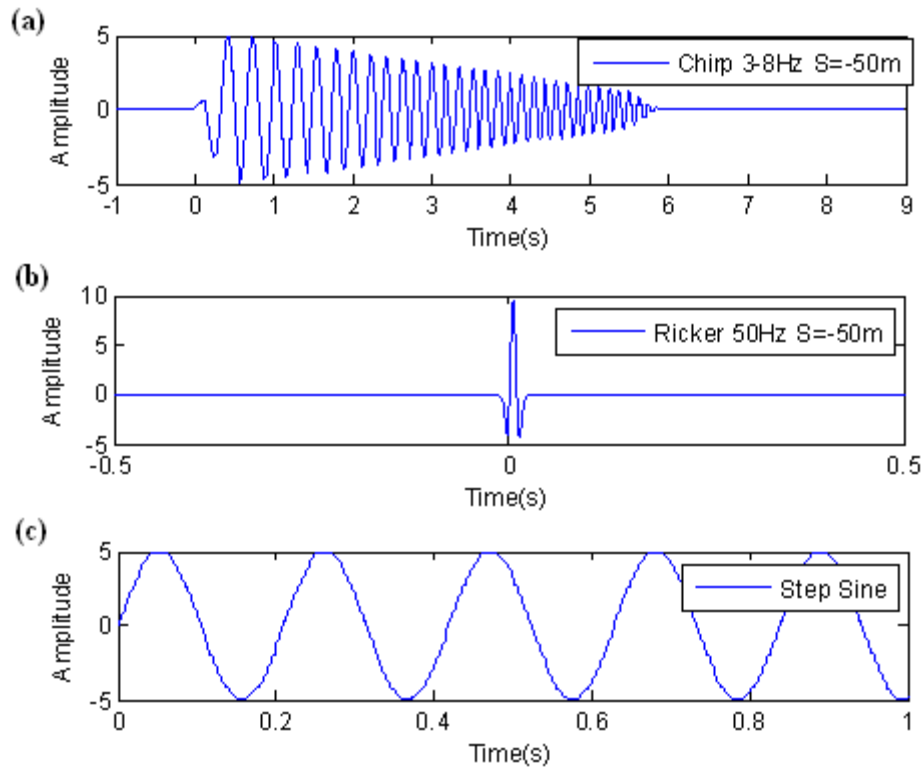
Figure 5.5   Source Signals Used at the Hornsby Bend Site (a. - Chirp, b. – Ricker, c. –
             Step Sine at 4.75 Hz)

Transient signals are associated with impact-type sources like explosives, drop-weights and sledge hammers. They are characterized by a pulse of relatively short duration which contains energy over a range of frequencies. The ideal transient impact is a delta function with equal amounts of energy at all frequencies. In reality, this frequency range is not possible to create in soil and the truncated from depends on the source energy.   The advantages of a transient source are low cost and rapid deployment. However, transient sources generate less energy than a vibroseis and are not flexible in controlling the frequency content.

Step-sine signals were implemented using the vibroseises with controlled frequency and amplitude contents. For transient input with the vibroseises, a wide range

in frequencies was excited simultaneously. In comparison, the step-sine introduces one frequency at a time and steps through the frequency range selected. This method is also referred as swept-sine because the seismic source sweeps through from one frequency to another frequency with a preselected number of cycles at each frequency. As such, the method provides a robust way to concentrate energy at individual frequencies, generally resulting in a high signal-to-noise ratio. Compared to transient signals, the only disadvantage of step-sine signals is that this testing procedure is more time-consuming.

The functional form of a step-sine signal can be written as a sinusoidal wave:

$$x(t) = A\sin[2\pi f t] \tag{5.1}$$

A chirp signal is a shorter durational signal in which the frequency increases ('up-chirp') or decreases ('down-chirp') with time. Two types of chirps are generally used in geophysical exploration: linear chirp and exponential chirp. In a linear chirp, the instantaneous frequency, f(t), varies linearly with time. In an exponential chirp, the frequency of the signal varies exponentially as a function of time. In this research, linear chirps were used as input signals. The corresponding time-domain function of a sinusoidal linear chirp is:

$$x(t) = A(t)\sin[2\pi(f_0 + \frac{k}{2}t)t] \tag{5.2}$$

where amplitude A is a function of time, k is the rate of frequency change, and f_o is the start frequency.

A Ricker wavelet signal is a wave-like oscillation with an amplitude starting out at zero, increasing, and then decreasing again back to zero. The Ricker wavelet is usually used as source signal in forward modeling of seismic and electromagnetic wavefields.   It is often written as:

$$x(t) = \left\{1 - 2[\pi f_p(t - d_r)]^2\right\}\exp\left\{-[\pi f_p(t - d_r)]^2\right\} \tag{5.3}$$

85

where f_p is the peak frequency, and d_r is the temporal delay.

Random input motions are sometimes used with a continuous-type source such as an electromechanical vibrator or a bulldozer (see Figure 5.6). When random input motions are used, a weighting function such as the Hanning window is necessary to reduce leakage because the random signal is not periodic in the time domain. Rix (1988) compared the performance among transient, step-sine and random input motions and concluded the step-sine yields the best results.
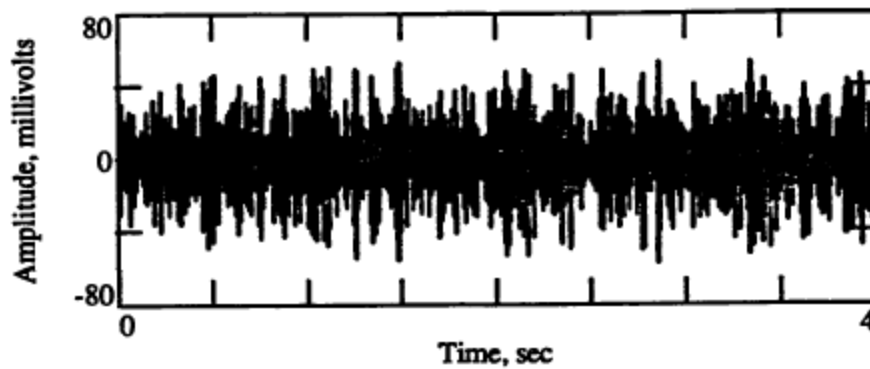
Figure 5.6   Typical Random Input Motion Time Record (from Rix, 1988)

In this research, transient, step-sine, Ricker and chirp signals were used as drive signals for T-Rex and Liquidator, the high-energy seismic sources.

5.3.2 Recording Systems

Two recording devices were used in the SASW and MASW tests: a 4-channel Quattro analyzer and a 72-channel VXI analyzer. The Data Physics Quattro is a ultra portable, USB 2.0 powered, 24-bit, 40-kHz bandwidth, 4-channel analyzer. It has the ability to record signals and convert them to various forms including auto-power spectrum, transfer functions, synchronous average, auto- and cross-correlation, histogram

analysis. The VXI analyzer is a 72-channel analyzer (formally manufactured by Agilent) that is primarily used for surface wave studies and liquefaction tests at the University of Texas at Austin. The VXI analyzer has a sampling rate up to 100k samples/s and allows data to be streamed to a computer through a cable or over a network. In this study, both analyzers were connected to a laptop for data storage.

Two types of geophones were used in the field: L-4, 1-Hz low-frequency geophones and GS-11D, 4.5-Hz geophones. These two types of geophones are shown in Figure 5.7. All geophones were calibrated before testing to find the best combination with controlled phase difference for SASW testing. An example of a phase difference ("relative" to some references) vesus frequency plot for 15, 1-Hz geophones is shown in Figure 5.8. As seen in Figure 5.8, these geophones are well matched as shown by a maximum phase difference (relative to Geophone B) of 4º in the frequency range of 1 to 200 Hz.

Figure 5.7   1-Hz and 4.5 Hz Geophones used at the Hornsby Bend Testing Site
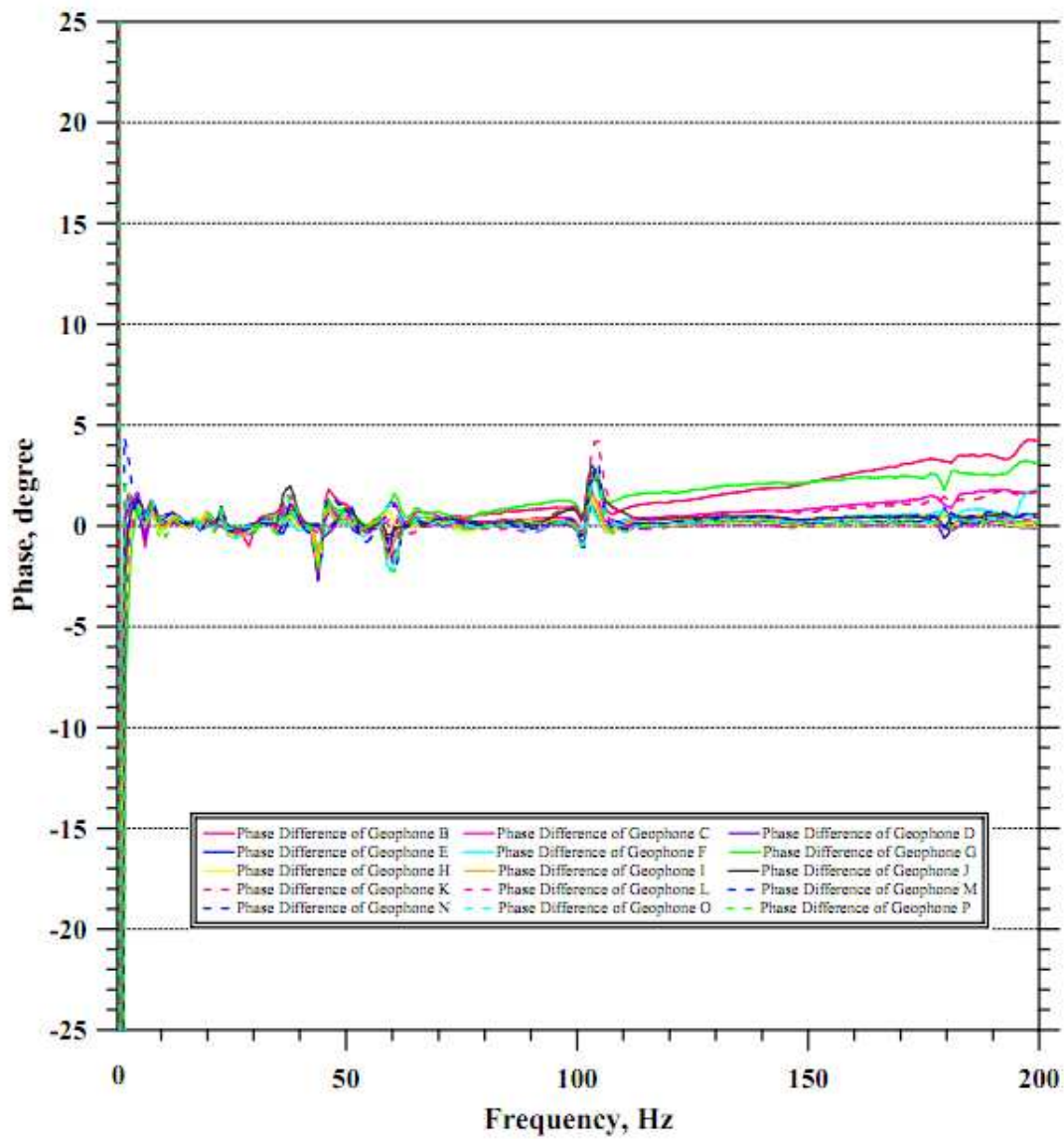
Figure 5.8   Phase Difference for 15, 1-Hz Geophones in the Frequency Range of 1 to 200Hz; Geophone B used as Reference

88

5.3.3 Test Procedure

One set of SASW tests were performed at locations around the Hornsby Bend Site during the first trip with T-Rex as the large seismic source and the 1-Hz Geophones. The center of the test array had an elevation of 134 meter with coordinates of 30.230380479N, 93.641901611W. During the second trip, three sets of SASW tests were performed, one at center and one at each end of the test array with 1-Hz geophones and Liquidator as the large seismic source.

The basic configuration of the source and receivers used in field SASW testing at the array location is illustrated in Figure 5.9. Three receivers were used at each source/receiver set-up. This arrangement enabled two SASW set-ups (two individual dispersion curves as discussed below) to be obtained at the same time, thereby cutting testing time in half as compared to using only two receivers. The middle receiver (Receiver #2) was located at the center line of the test array at all times. When different spacings were used and/or reverse directions were tested, only Receivers #1 and #3 and the source were moved. For the shorter spacings, usually source-to-receiver spacings of 2, 4, 5 and 10 ft, tests were performed in both the forward and reverse directions using a sledge hammer for an impact source in the first trip. In some cases, the sledge-hammer source was also used at spacings of 20 and 40 ft. For the larger spacings, often beginning at source-to-receiver spacings of 50 ft, testing was performed only in the forward direction using T-Rex as the source. During the second trip, short spacings of 2, 4, 8, 16, 32 ft were used. For longer spacings, 64, 200 and 400 ft were used. Reverse direction testing was typically not performed with Liquidator or T-Rex due to the testing time and space. Table 5.3 shows the geophone spacing, impact direction, source type, record information of the SASW tests from the second trip.

Ȼ

(Source: Hammer or "T-Rex")   Receivers

Forward

#1   #2   #3

|← X →|← X →|←—— 2X ——→|

Receivers   Source

Reverse

#3   #2   #1

|←—— 2X ——→|← X →|← X →|
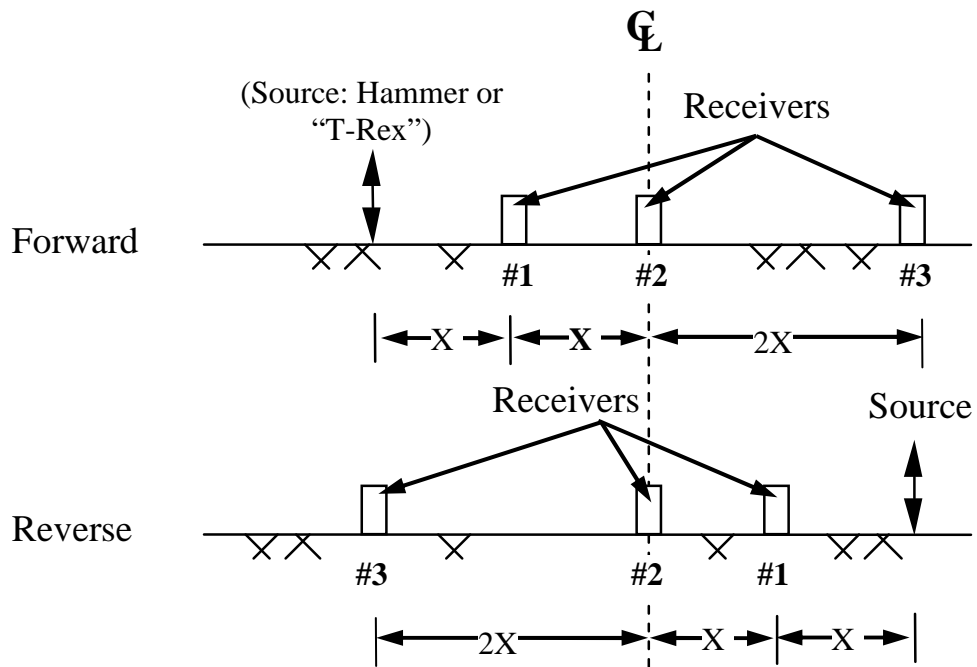
Figure 5.9   Common-Middle-Receiver Geometry Used in SASW Testing at Each Test Set-up at the Hornsby Bend Test Site

Table 5.3   Typical Source-Receiver Spacings Used in SASW at the Hornsby Bend Site During the Second Trip

Distance			Impact Direction		Source	Frequency (Hz) Range	No. of Pts.
S-R1*	R1-R2[#]	R2-R3[Δ]	Forward	Reverse			
2	2	4	√		Hammer	0 - 800	1600
2	2	4		√	Hammer	0 – 800	1600
8	8	16	√		Hammer	0 - 200	400
8	8	16		√	Hammer	0 - 200	400
32	32	64	√		Hammer	0 – 50	100
32	32	64		√	Hammer	0 – 50	100
50	50	100	√		Liquidator	3 – 40	80
200	200	400	√		Liquidator	1 – 4	10

[*] S-R1: Distance from source to first receiver
[#] R1-R2: Distance from first receiver to second receiver
[Δ] R2-R3: Distance from second receiver to third receiver

90

Distances between receivers ranging from 2 to 300 ft were generally used (see Table 5.3). Eight receiver spacings were used in each series of tests. The largest receiver spacing was typically based on space considerations and the energy level delivered by the seismic source.   This number and progression of receiver spacings resulted in significant overlapping of the individual dispersion curves used to develop a composite field curve, thereby enhancing the test reliability and allowing the assumption of lateral uniformity over the test array to be studied.   Regardless of the spacing between receivers, at no point in the data analysis were wavelengths considered that were longer than twice the distance between the source and first receiver in the receiver pair.   This array geometry results in minimizing near-field effects while simultaneously recording long wavelengths.

Vertical velocity transducers were used as receivers in the SASW (and MASW) tests.   All tests on the first and second trips were conducted with Mark Products Model L-4C transducers, which have a natural frequency of 1 Hz. The key points with regard to these receivers are that: (1) they have significant output over the primary measurement frequency range at the Hornsby Bend site(1 Hz to 200 Hz), (2) they are matched so that any differences in phase are negligible over the measurement frequency range, (3) they are coupled well to the soil, (4) the coupling is similar for each receiver, and (5) ambient temperatures were low enough (below 90°F) so as temperature did not impact the geophone performance.   These 1-Hz geophones have outputs in excess of 10 volts/(in./sec) and phase shifts between receivers of less than 5 degrees for frequencies from 1 Hz to 200 Hz, the range used in testing with these receivers.

MASW tests were performed with a 5-m geophone spacing using the 1-Hz geophones, sledge hammer and T-Rex source during the first trip. The layout of field test equipment is shown in Figure 5.10. A summary of source type and location is in Table 5.4. An example of wavefield from a 20-Hz Ricker signal is shown in Figure 5.11.
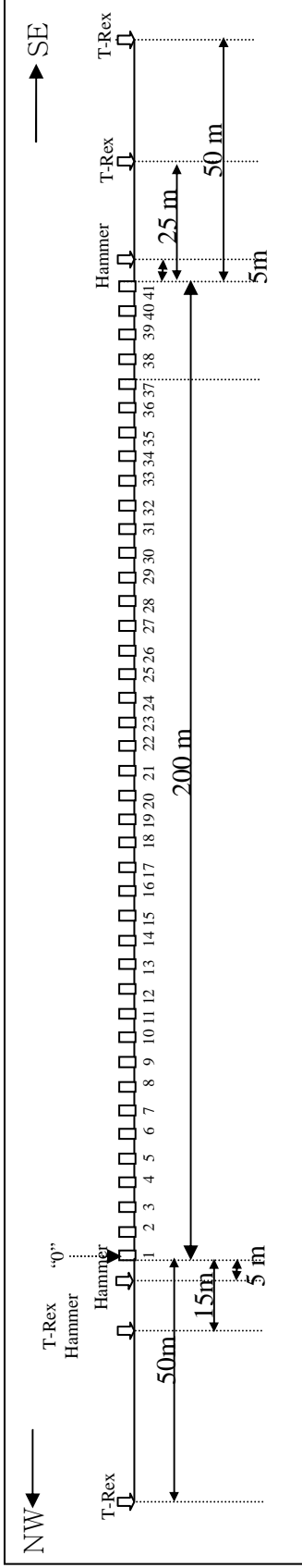
Figure 5.10   General Layout of MASW Testing at the Hornsby Bend Test Site During the First Trip

Table 5.4   Typical Source Type and Location Used in MASW Test at the Hornsby Bend Site During the First Trip

Source Location(m)	Source Type	Signal Type	Start_Freq(Hz)	End_Freq(Hz)
-15	T-Rex	Stepped Sine	100	10
-15	T-Rex	Stepped Sine	20	3
-15	T-Rex	Chirp	3	8
-15	T-Rex	Chirp	8	20
-15	T-Rex	Chirp	20	25
-15	T-Rex	Chirp	25	35
-15	T-Rex	Ricker	20	20
-15	Hammer	Impulsive		
-50	T-Rex	Step Sine	100	10
…	…	…		
250	T-Rex	Stepped Sine	100	10
…	…	…		
225	T-Rex	Stepped Sine	100	10
…	…	…		

Note: The first geophone is at location "0".
      …: Same source and signal types applied

92
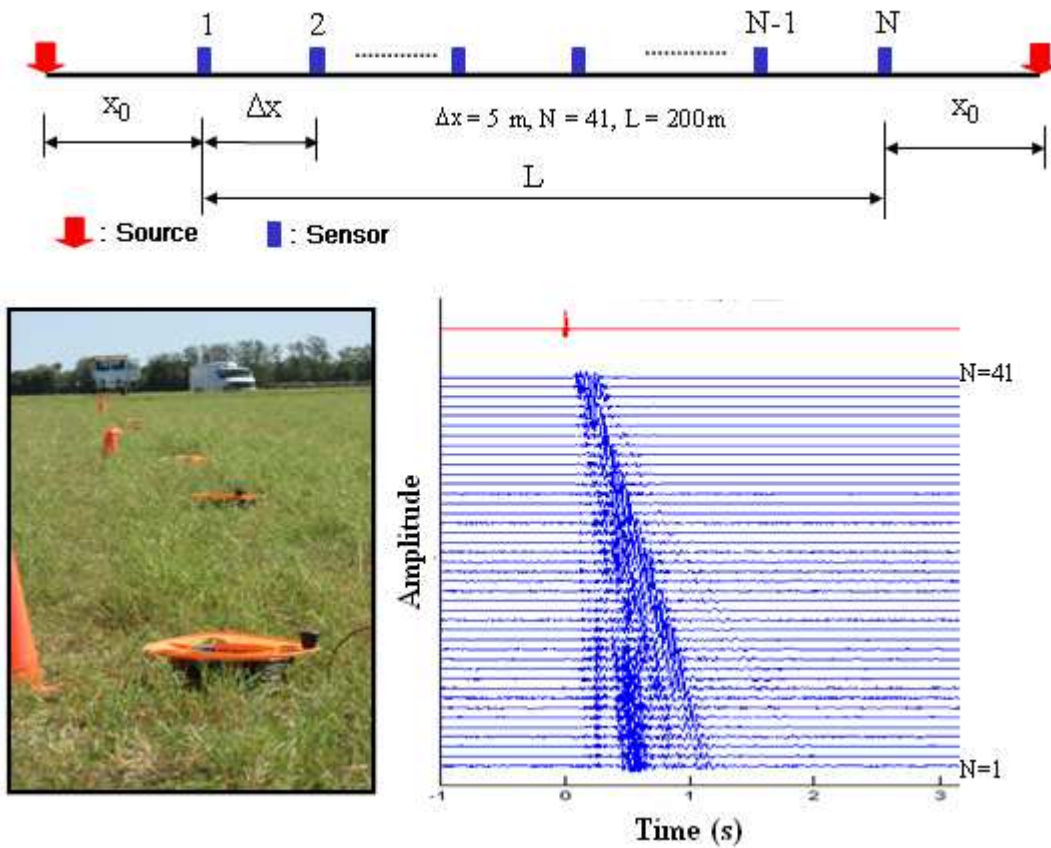
Figure 5.11 Example of 41-Channel Wavefields with a 20-Hz Ricker Source Signal at 225 meter

The weedy surface that covered most of the site complicated data acquisition. Thus, the geophones were buried to a depth of 1.5 inch below the ground to avoid poor coupling and interference from the weed roots and irregular-sized gravel. Particularly, when sledge hammers were used as the seismic sources, weeds were removed to create a flat surface for consistent impacts. A 12-lb sledge hammer was used in the shallow material measurement. In the MASW tests, 1-Hz Geospace geophones spaced 5-m apart along the test array were used. Miller and Xia (1999) advised that the source-to-nearest receiver offset should be two times the geophone spacing. In this study, one, five and ten the times of geophone spacings were used as the source-to-nearest-receiver offset.

93

During the second trip of in which MASW tests were performed, sledge hammers and Liquidator were used with both 1-Hz and 4.5-Hz geophones. Receiver spacings of 3ft and 10ft were used in these MASW tests. One, three, five and ten times the geophone spacing were used as source-to-nearest receiver offset. It is noted that in both trips, time domain signals were recorded for further calculations of the power spectrum, transfer function and other useful information. Cross-power spectrum were also recorded during the step-sine excitation for the beamforming transformations (Wood, 2009).

The cone penetration test (CPT) is an in-situ testing method used to determined soil properties and soil stratigraphy. It was initially developed in the 1950s at the Dutch Laboratory for Soil Mechanics in Delft to investigate soft soils. It is now recognized as one of the most widely used in-situ geotechnical tests. In the United States, cone penetration testing has gained rapid popularity in the past twenty years. The cone penetration test consists of advancing a cylindrical rod with a conical tip into the soil and measuring the forces required to push this rod. The friction cone penetrometer measures two forces during penetration. These forces are: (1) the total tip resistance (q_c) which is the soil resistance to advance the cone tip, and (2) the sleeve friction (f_s) which is the sleeve friction developed between the soil and the sleeve of the cone penetrometer. The friction ratio (R_f) is defined as the ratio between the sleeve friction and tip resistance and is expressed in percent. A schematic of the electric cone penetrometer is depicted in Figure 5.12. The resistance parameters are used to classify soil strata and to estimate strength and deformation characteristics of soils.

Eleven CPT tests were performed at the Hornsby Bend sites to assist in charactering the site. CPT tests were conducted at the site with a depth interval of 0.5 ft. Figure 5.13 shows the coordinates of the eleven CPT test points. CPT 11 is at the center of test array.
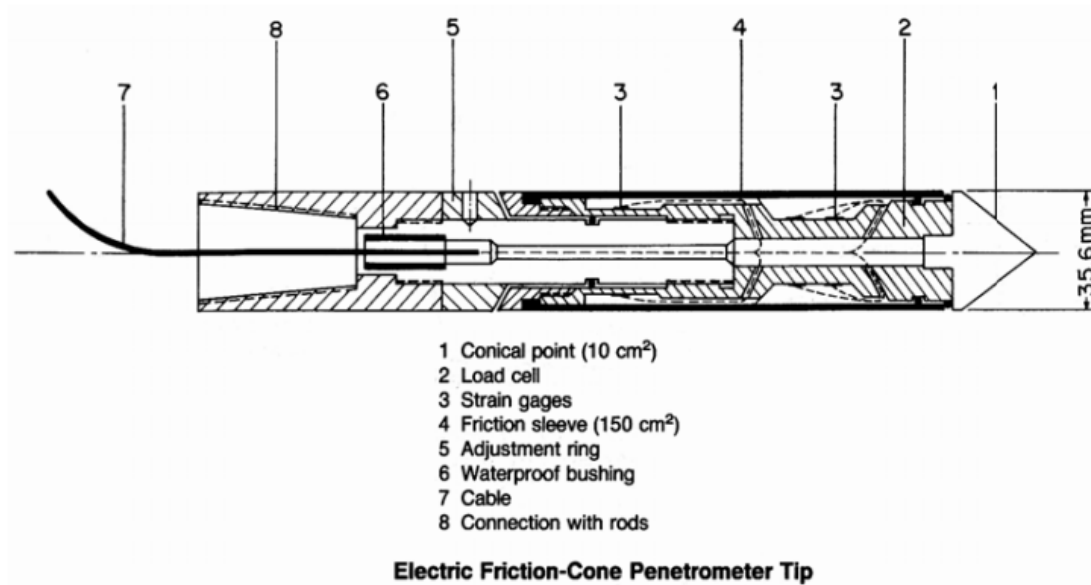
Figure 5.12   An example of the Cone Penetrometer from ASTM D5778
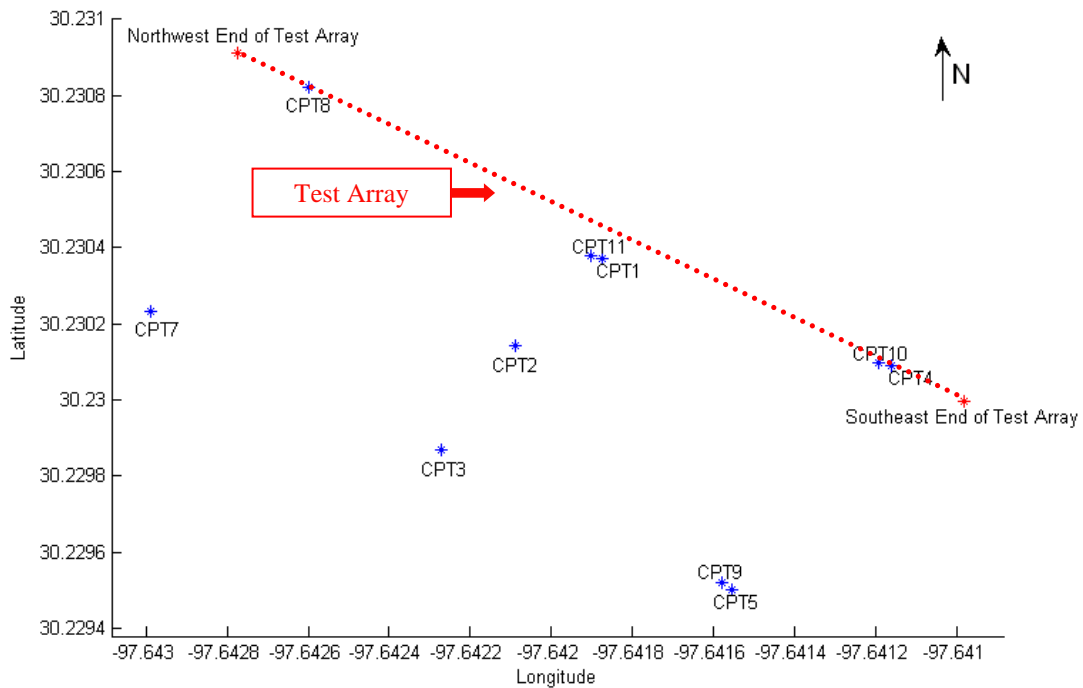
Figure 5.13   Location of Eleven CPT Tests at the Hornsby Bend Site

Seismic Cone Penetration Testing (SCPT) was also performed at the site. A schematic layout of SCPT equipments is shown in Figure 5.14. SCPT is a rapid and cost-effective method which measures in situ shear wave velocity of soils. Coupled with CPT data, SCPT method gives details on soil types, engineering parameters with additional information about shear wave velocity, thus modulus in the same test location. Mr. Kim performed the SCPT tests at the center of SASW test array. The results will be compared to V_s profiles from both SASW and MASW methods in Chapter 6.
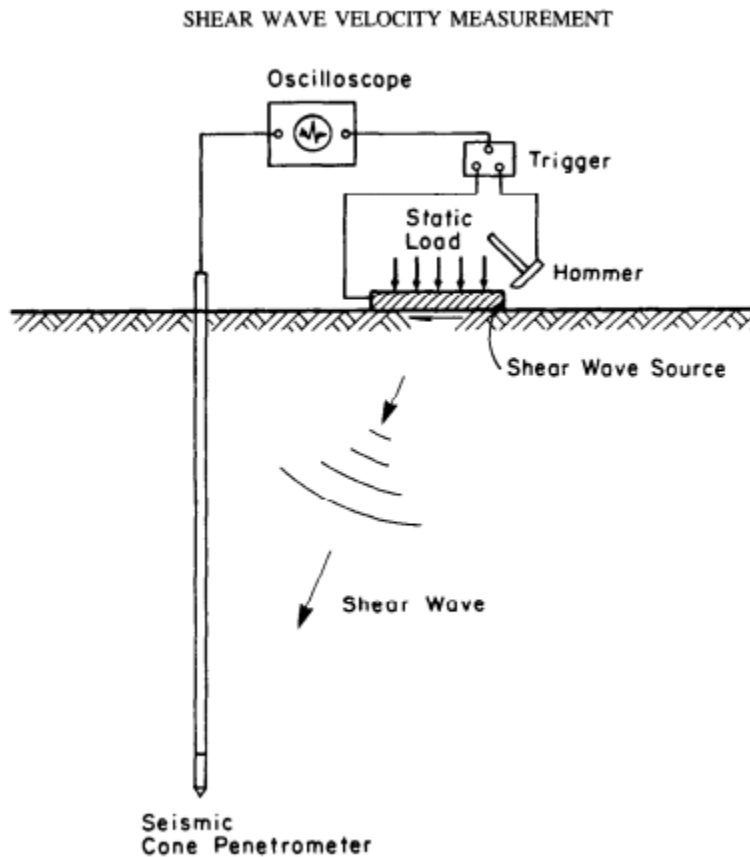
Figure 5.14   Schematic Layout of Seismic Cone Penetration Test (from Robertson et al., 1986)

5.4 SUMMARY

Spectral-Analysis-of-Surface-Waves (SASW) and Multichannel-Analysis-of-Surface-Waves (MASW) tests were performed at the Hornsby Bend site for a comprehensive site investigation and for parametric studies. Two trips were made with different large seismic sources (T-Rex for the first trip and Liquidator for the second one). The receivers employed in this study were 1-Hz and 4.5-Hz geophones. The source signals were varied (impulsive, Ricker wavelet, step-sine and chirp) and geophone spacing was varied, specifically 3 ft, 10 ft and 16.4 ft (5 meter). Also, cone penetration tests and SCPT were conducted at multiple locations to assist the material characterization. Test results, comparison and further discussion will be presented in the next chapter.

Chapter 6   Surface Wave Test Results

6.1 INTRODUCTION

The SASW and MASW results from the data collected and analyzed at the Hornsby Bend site are presented in this chapter. The results are first presented in the form of experimental dispersion curves and V_s profiles from standard SASW analyses with hammers, T-Rex and Liquidator as the seismic sources. The MASW results are then presented. Comparisons are made with the surface wave dispersion curves obtained from various source offset distances, receiver spacings, or source types. Last, V_s Profile from the SASW test is compared with other geological information at the site.

For MASW tests, the extraction of the fundamental field dispersion curve is based on the observation of the experimental dispersion data. Wood (2009) extracted MASW field dispersion curves by removing data points that were obvious outliers or inconsistent with the primary dispersive trend. In this study, points in f-k plots with the following characteristics were removed: (1) any point with a surface wave velocity over 10,000 ft/sec, (2) any point with a wavelength greater than 1000 ft for the 3-ft receiver spacings, (3) any point with a wavelength greater than 3000 ft for the 10-ft receiver spacings, or (4) any data points that showed higher mode behavior where a lower mode was clearly present. Also, the frequency ranges of data are kept according to the frequency spans of the source, if the frequency contents of the source signals are available. It is noted that all recorded waveforms with source signals rather than stepsine were processed with both Beamforming and F-K transform, while the data from a source signal of stepsine were processed with Beamforming methods.

The 2-D and 3-D theoretical dispersion curves determined from the SASW V_s profiles are used as references for the MASW experimental dispersion curves. The

theoretical dispersion curves were created using the layer thicknesses, S-wave velocities, Poisson's ratio above the water table or P-wave velocities below the water table. The water table at Hornsby Bend site was set at 46 ft based on existing information. Plotting the theoretical dispersion curves on top of the MASW experimental data provided reference dispersion curves that represent the averaged shear wave velocity profile along the test array at the site. The results from each trip (first for a total array length of 200 meters with 16.4-ft (5-m) geophone spacing, and second trip with 3-ft and 10-ft geophones spacing) are compared separately.

During the first trip, different source-to-first-receiver locations were used. The distances ranged from three, five and ten times geophones spacing for T-Rex, and ranged from one and three times geophone spacing for sledge hammers. The impact of the source location is studied by comparing the experimental dispersion curves from MASW and SASW methods with 2-D and 3-D theoretical curves. The experimental dispersion curves generated by various source signals (hammer, chirp, Ricker wavelet and stepsine) are presented with the receiver spacing and source type held constant. The frequency contents of the source signals are known, thus their effects on the MASW field dispersion curves can be traced. Then, the receiver spacing is compared by reducing the number of collected signals in analysis while maintaining the total measurement array. After this, the effect of number of receivers on the test results is studied by reducing the number of analyzed signals while keeping the same geophone spacing as 16.4 ft (5 meter). It is expected that larger spacing causes severer spatial aliasing.

During the second trip, Liquidator was used as the input seismic source along with sledge hammers. Liquidator was used in place of T-Rex so that lower frequencies in the range of 1 to 3 Hz could be studied. Different source signals at different offsets are compared. Also, both 1-Hz and 4.5-Hz geophones are used. Different modes of the

experimental dispersion curves from the MASW test are again compared with the 2-D and 3-D solutions from WinSASW. V_s profiles from the SASW measurements are also compared with CPT and SCPT results.

Finally several signal processing techniques are presented. The resolution in the phase plots can possibly be improved by the extension of the time domain signal which is equal to interpolation in the frequency domain. Moreover, a spatial interpolation technique is applied to the MASW data to explore the possibility of retrieving lost or heavily contaminated signals based on geophone records with high signal-to-noise ratios. The experimental dispersion curves are derived from interpolated wavefields (thus a smaller sampling space with the same total array length) to study the previously aliased spectrum uncovered by an artificial increase in number of traces. It is shown that the technique may recover some portion of experimental dispersion curves, but mainly for high modes.

6.2 SASW TEST RESULTS

6.2.1 Test Results from the Second Trip

The test results from the second trip are presented first in this section because standard SASW and MASW test setups were used. For SASW tests, Liquidator and a sledge hammer were used as seismic sources. 1-Hz geophones were used. Data reduction of SASW tests consisted of the following steps. For each receiver spacing, the phase plot was plotted in a wrapped fashion. Four phase plot with receiver spacing of 2, 8, 32 and 200 are shown in Figures 6.1 through 6.4. A masking procedure was then performed to manually eliminate portions of the data with poor signal quality or portions of the data contaminated by near-field waveform components. In this section, data in phase plots falls within one half to two cycles were kept. Figures 6.5 through 6.8 show the masking
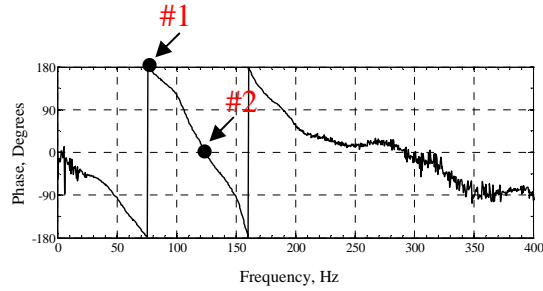
Figure 6.1   Wrapped Phase Calculated from Transfer Function for R1-R2 = 2 ft with a Sledge Hammer as the Seismic Source
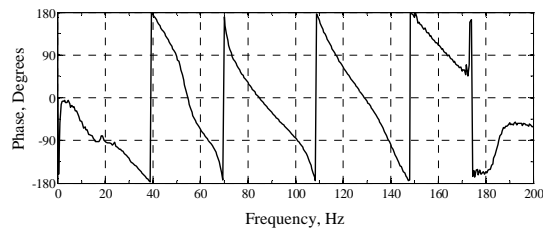
Figure 6.2   Wrapped Phase Calculated from Transfer Function for R1-R2 = 8 ft with a Sledge Hammer as the Seismic Source
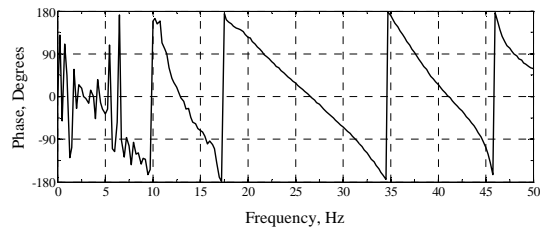
Figure 6.3   Wrapped Phase Calculated from Transfer Function for R1-R2 = 32 ft with a Sledge Hammer as the Seismic Source
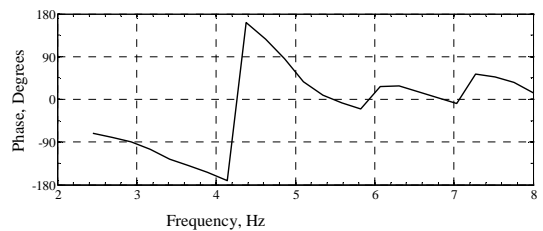
Figure 6.4   Wrapped Phase Calculated from Transfer Function for R1-R2 = 200 ft with Liquidator as the Seismic Source

101

applied to the phase plots with the 2-, 8-, 32-ft and 200-ft spacings at the test array. The masking information was used to unwrap the phase plot, and then calculate the individual dispersion curve for each geophone pair. For instance, Points #1 and #2 in Figure 6.1 represent one half and one wavelengths, respectively, between the receiver pair. Hence, the unwrapped phase angles are 180° and 360°. The frequencies associated with Points #1 and #2 are about 74 and 123 Hz, respectively, which results in phase velocities of 296 and 246 fps, respectively. The complete individual dispersion curve calculated from the unmasked portion of the wrapped phase record in Figure 6.5 is shown in Figure 6.9. Again, similar process was applied on the phase plot of 8-, 32- and 200-ft spacing as shown in Figures 6.6 through 6.8. The resulting dispersion curve is also shown in Figure 6.9. This process was repeated for all receiver spacings resulting in a composite experimental dispersion curve that covers a wide range of wavelengths. Figure 6.10 shows the composite experimental dispersion curve created at the Hornsby Bend site during the second trip when a minimum of 2-ft spacing was used. The maximum wavelength, λ_{max}, measured was about 747 ft. The maximum depth to which the V_s profile was determined is λ_{max} /2 or about 374 ft.

The fit to the composite experimental dispersion curve for the Hornsby Bend site during the second trip is shown in Figure 6.11. The comparison between the 2-D and 3-D theoretical dispersion curves is shown in Figure 6.12. It is observed that the 3-D solution is generally higher than the 2-D solution from a wavelength of 100 ft. The final shear wave velocity profile for the site is shown in Figure 6.13. It is clearly observed that several distinct velocity contrasts exist at the site. The first contrast occurs at a depth of 50 ft. The shear wave velocity increase from 900 to 1150 fps, indicating a different material is encountered. The second contrast occurs at 105 ft where V_s profile increases from 1150 to 1530 fps. The V_s profile increase from 1500 fps to 2900 fps at a depth of
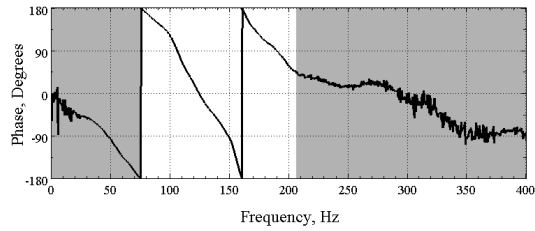
Figure 6.5   Masked Wrapped Phase Calculated from Transfer Function for R1-R2=2 ft
               with a Sledge Hammer as the Seismic Source
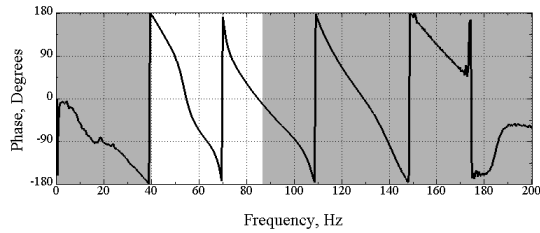
Figure 6.6   Masked Wrapped Phase Calculated from Transfer Function for R1-R2=8 ft
               with a Sledge Hammer as the Seismic Source
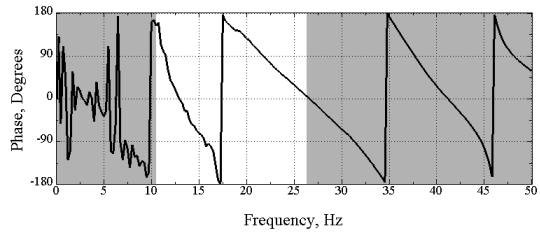
Figure 6.7   Masked Wrapped Phase Calculated from Transfer Function for R1-R2=32 ft
               with a Sledge Hammer as the Seismic Source
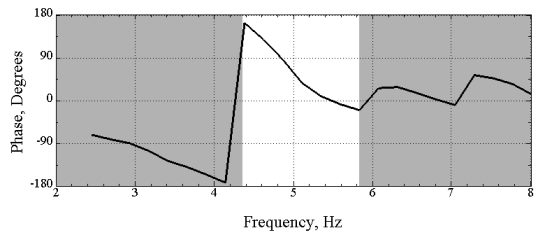
Figure 6.8   Masked Wrapped Phase Calculated from Transfer Function for R1-R2=200
               ft with Liquidator as the Seismic Source

103
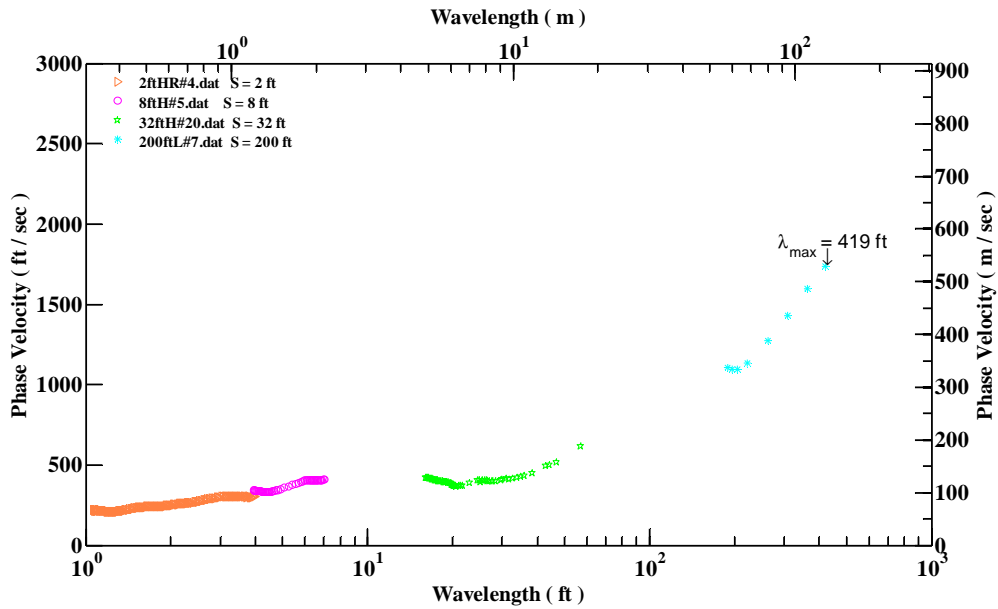
Figure 6.9   Individual Experimental Dispersion Curve Created from the Unwrapped
              Phase Record with 2-, 8-, 32-ft and 200-ft Spacing between the Receiver
              Pair during the Second Trip
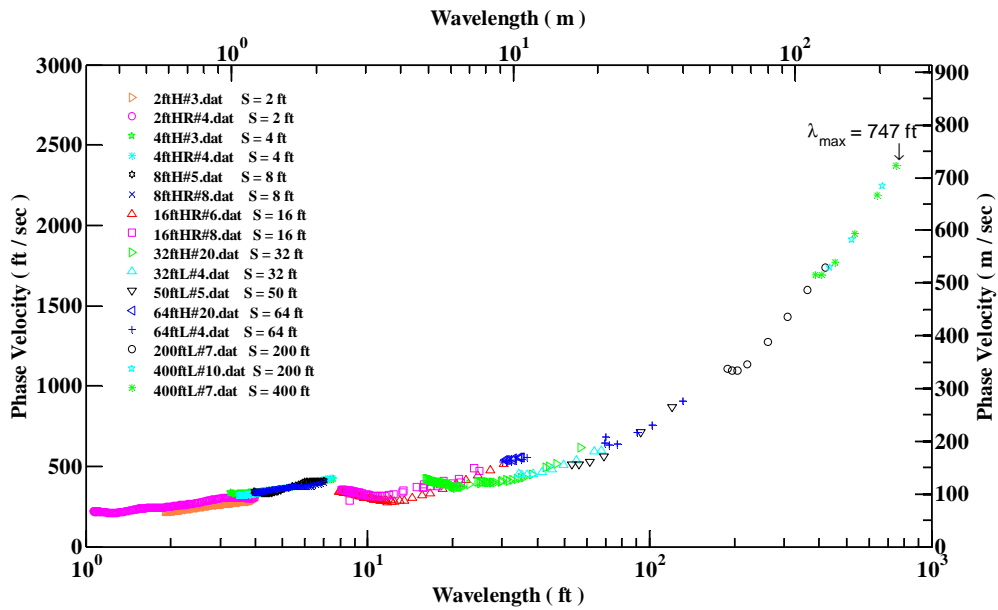
Figure 6.10 Composite Experimental Dispersion Curve Created from Phase
              Measurements Performed at Center of the Test Array using a Sledge
              Hammer and Liquidator as the Seismic Sources during the Second Trip
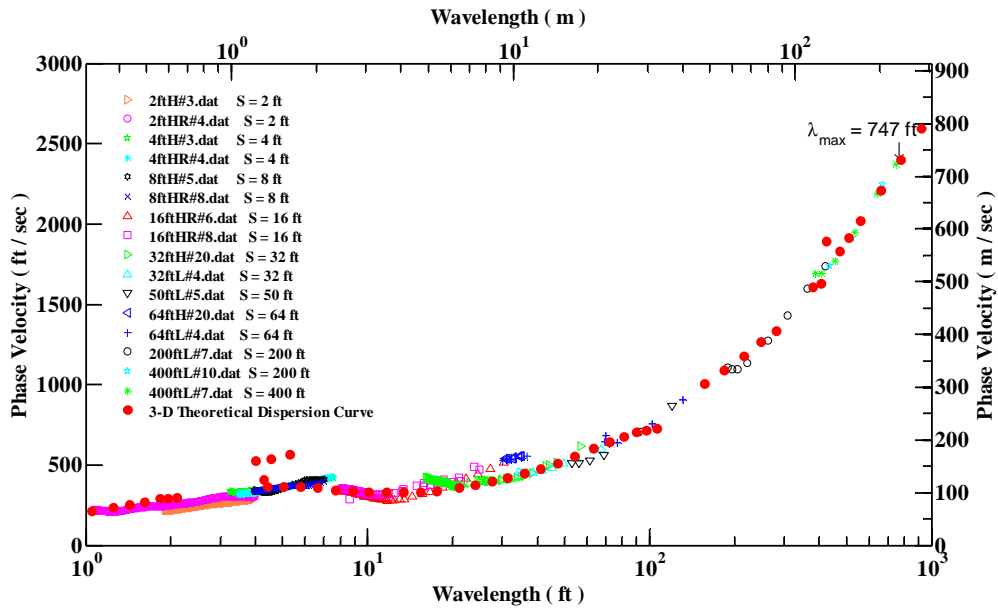
Figure 6.11   Comparison of the Fit of the 3-D Theoretical Dispersion Curve to the
SASW Composite Experimental Dispersion Curve during the Second Trip
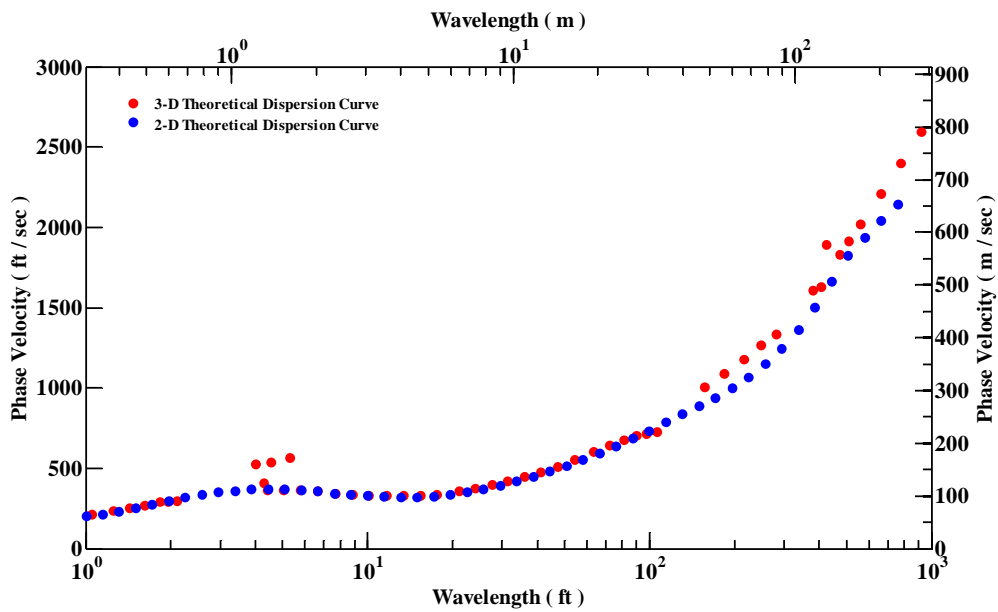
Figure 6.12   Comparison between the 3-D and 2-D Theoretical Dispersion Curves of the
SASW Test during the Second Trip
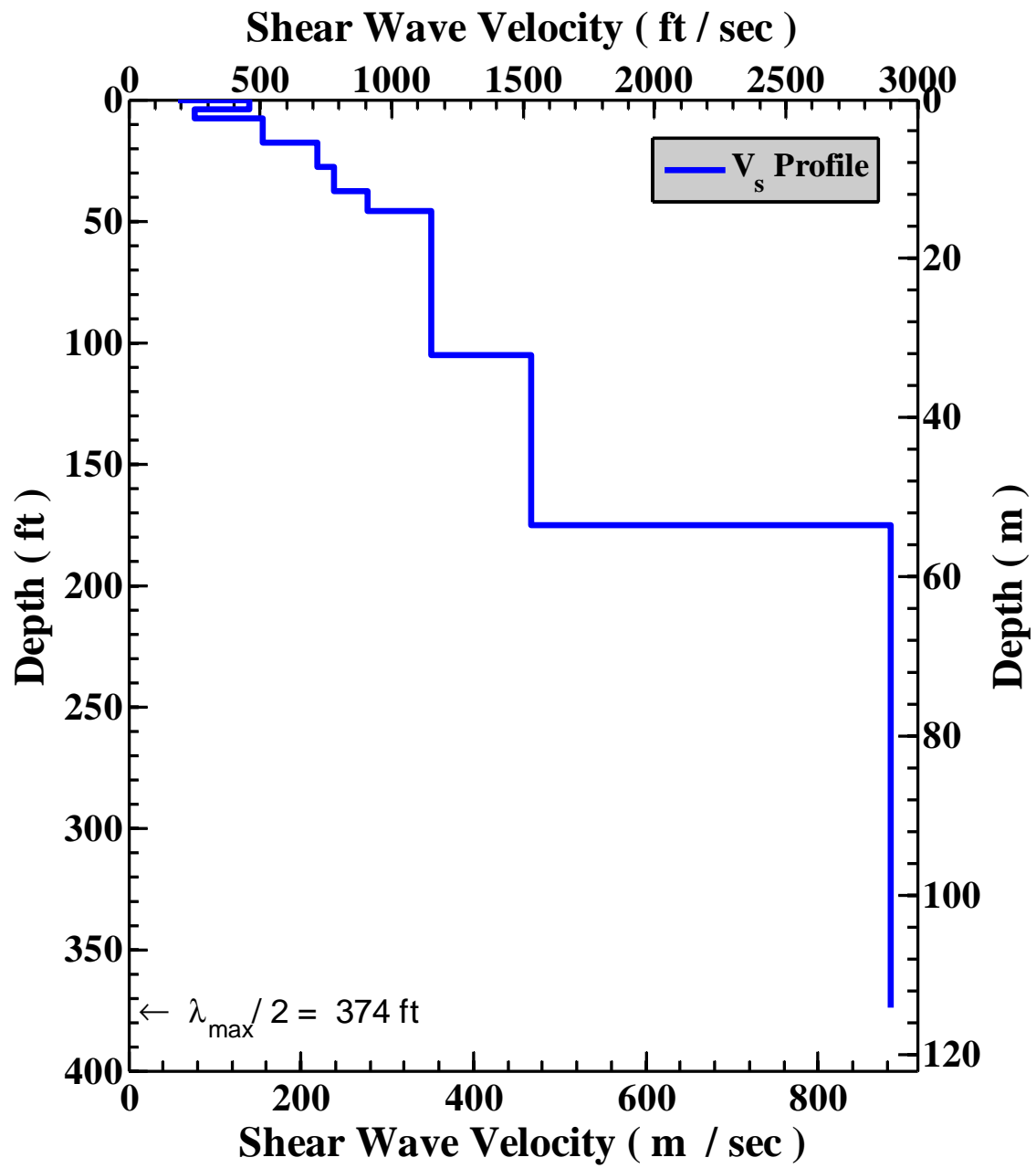
Figure 6.13   Shear Wave Velocity Profile Measured by SASW Testing during the
Second Trip at the Hornsby Bend Site

Table 6.1   Profile Parameters Used to Develop Theoretical Dispersion Curve at the Hornsby Bend Site during the Second Trip

Layer No.	Thickness, ft	Depth to Top of Layer, ft	P-Wave Velocity, ft/s	S-Wave Velocity, ft/s	Assumed Poisson's Ratio	Assumed Total Unit Weight, pcf
1	0.5	0	377 ^{o}	190	0.33	100
2	3.5	0.5	794 ^{o}	460	0.33	100
3	3.5	4	615 ^{o}	250	0.33	100
4	10.5	7.5	1013 ^{o}	510	0.33	100
5	10	18	1429 ^{o}	720	0.33	100
6	10	28	1628 ^{o}	780	0.33	100
7	8	38	1807 ^{o}	910	0.33	120
8	59	46 $^{\diamond}$	5000	1150	0.47 $^{+}$	120
9	70	105	5000	1530	0.47 $^{+}$	120
10	Half Space	175	5000	2900	0.25 $^{+}$	120

^{o} P-wave velocity calculated from V_s and assumed value of Poisson's ratio.
$^{\diamond}$ Water table assumed at a depth of 46 ft
$^{+}$ Not assumed but back-calculated from V_p = 5000 fps and V_s

175 ft, indicating a possible "bedrock" material is encountered. Table 5.1 lists the parameters used to generate the theoretical dispersion curve in Figure 6.13. Unit weight for each layer is assumed. Water table is set to 46 ft. All layers beneath this depth are assumed to be fully saturated thus compression wave velocity travel at a speed of 5000 fps. It is important to note that small changes in the assumed values of unit weight (say 10% or less) have an insignificant change on the final V_s profile as verified in Chapter 2.

6.2.2 Test Results from the First Trip

Test results of SASW test with T-Rex and a sledge hammer as seismic sources from the first trip is shown in this section. Again, a few field data are listed: Two phase plot, one for 16.4 ft (5 m) and another for 164 ft (50 m) receiver spacings are shown in Figures 6.14 and 6.15. Figures 6.16 and 6.17 show the masking applied to the phase plots with the 16.4-ft and 164-ft spacing at the test array. Points #1 and #2 in Figure 6.14 represent one and two wavelengths, respectively, between the receiver pair.   Hence, the
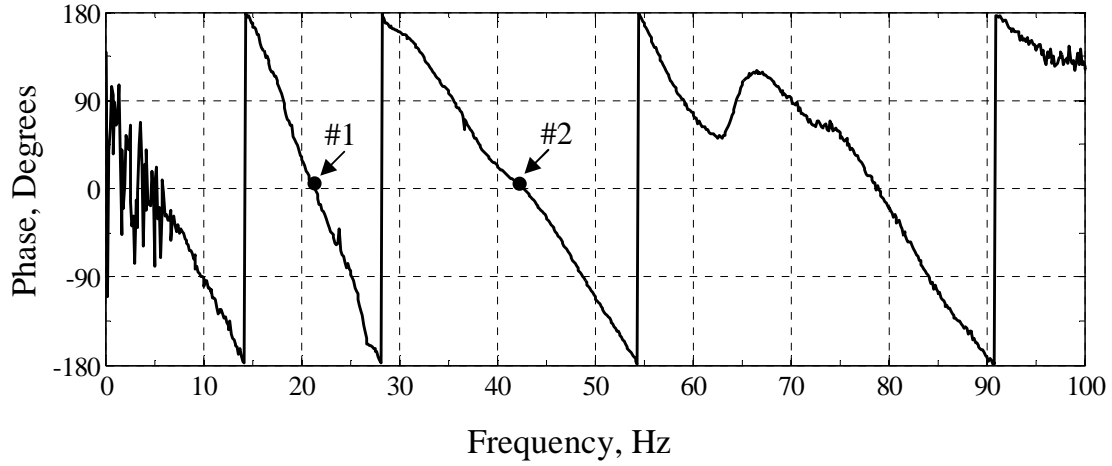
Figure 6.14   Wrapped Phase Calculated from Transfer Function for R1-R2 = 16.4 ft (5m)
with a Sledge Hammer as the Seismic Source
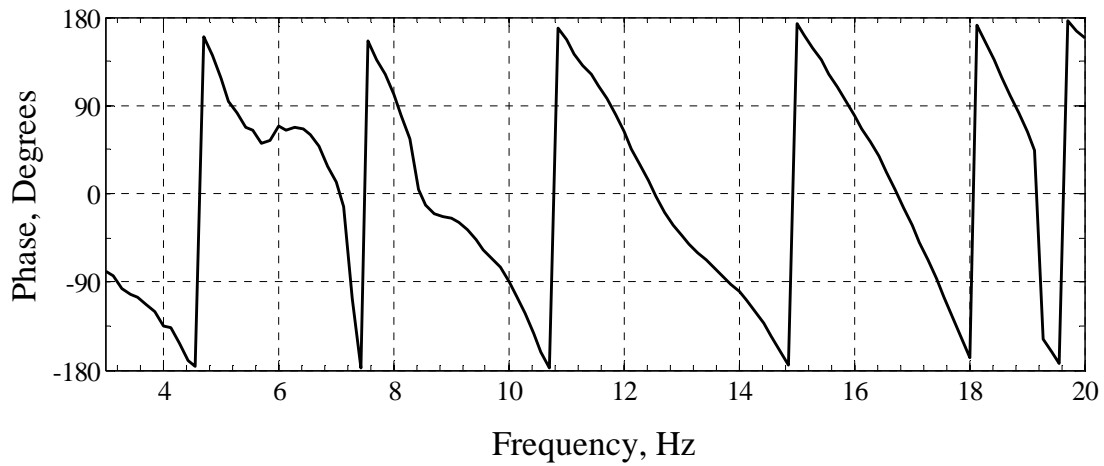
Figure 6.15   Wrapped Phase Calculated from Transfer Function for R1-R2 = 164 ft
(50m) with Liquidator as the Seismic Source
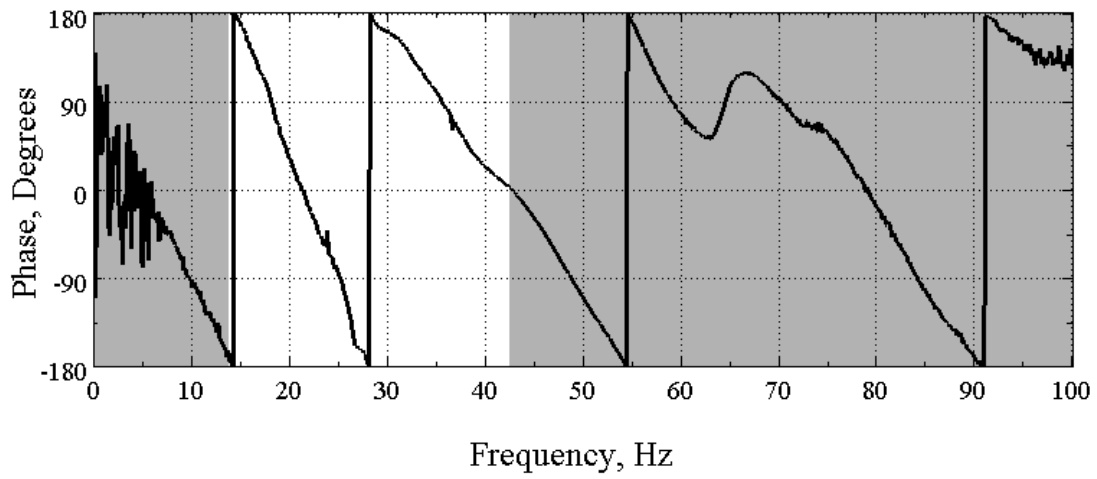
Figure 6.16 Masked Wrapped Phase Calculated from Transfer Function for R1-R2 = 16.4 ft with a Sledge Hammer as the Seismic Source
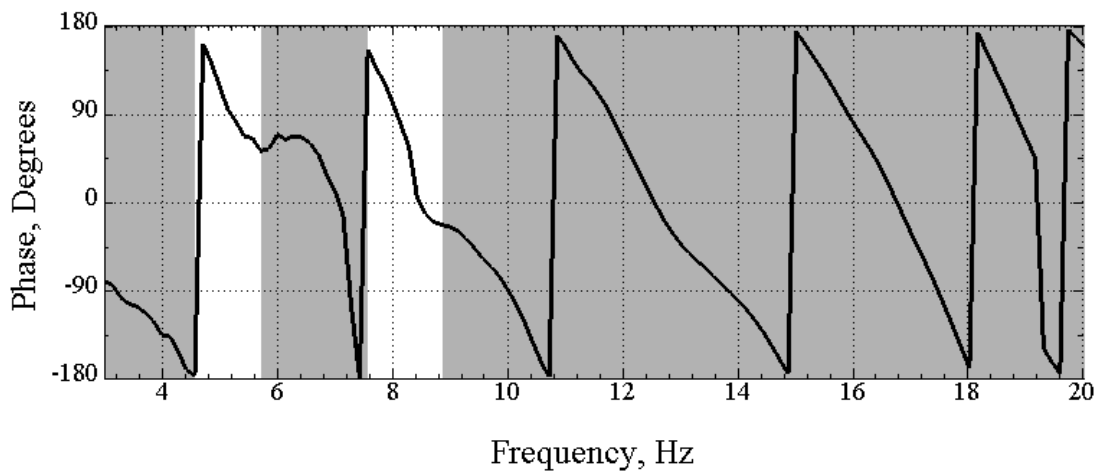
Figure 6.17 Masked Wrapped Phase Calculated from Transfer Function for R1-R2 = 164 ft with Liquidator as the Seismic Source

unwrapped phase angles are 360° and 720°. The frequencies associated with Points #1 and #2 are about 22 and 43 Hz, respectively, which results in phase velocities of 361 and 353 fps, respectively. The complete individual dispersion curve calculated from the unmasked portion of the wrapped phase record in Figure 6.14 is shown in Figure 6.18. Figure 6.19 shows the composite experimental dispersion curve created at the Hornsby Bend site during the first trip when a minimum of 16.4-ft (5-m) spacing was used. The maximum wavelength, λ_{max}, measured was about 337 ft. The maximum depth to which the V_s profile was determined is $\lambda_{max}/2$ or about 169 ft.

The fit to the composite experimental dispersion curve for the Hornsby Bend site during the first trip is shown in Figure 6.20. The comparison between the 2-D and 3-D theoretical dispersion curves is shown in Figure 6.21. The final shear wave velocity profile for the site is shown in Figure 6.22. It is clearly observed from both experimental dispersion curves and final V_s profiles that, both trips produced a similar result, which prove the stability of the SASW testing technique with different, but still qualified equipments and setups (T-Rex vs Liquidator). It is also observed that measured experimental dispersion from the second trip covered a broader range of the wavelength span from 1 to 747 ft, verifying that proper receiver spacings are required for SASW test to sample both shallow and deep materials.

From Figure 6.22 it is noted that V_s profile from the first trip has a maximum exploration depth of 169 ft, which is not deep enough to capture the "bedrock" boundary discovered by the V_s profile from the second trip. To investigate the possibility of using near-field data in extending the SASW experimental dispersion curves further, thus sampling material at deeper depths, phase plots with 164-ft spacings are used from 90 degree (corresponding to a wavelength of four times spacing). The resulting dispersion
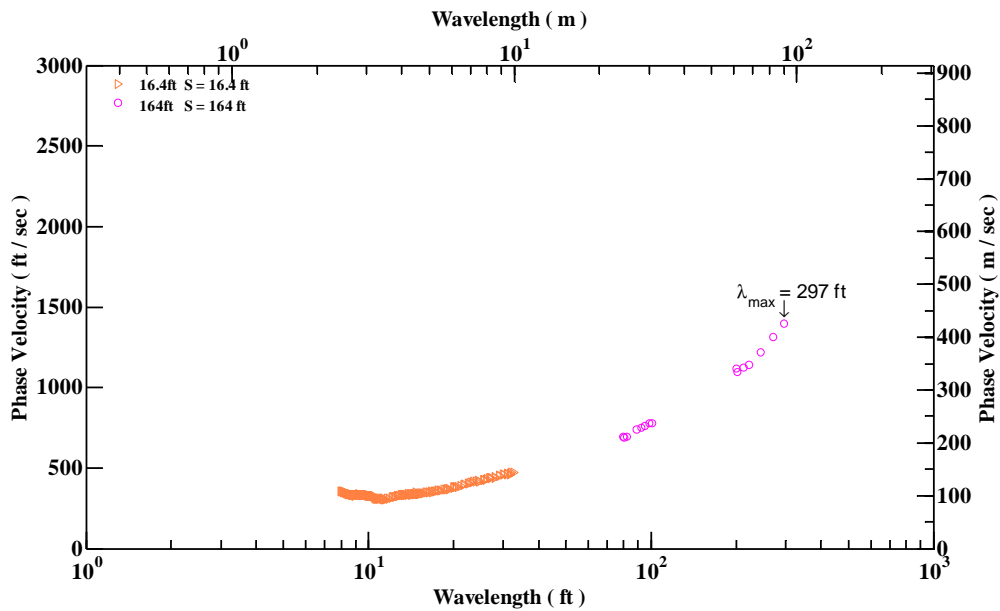
Figure 6.18   Individual Experimental Dispersion Curve Created from the Unwrapped
Phase Record with 16.4-ft and 164-ft Spacing between the Receiver Pair
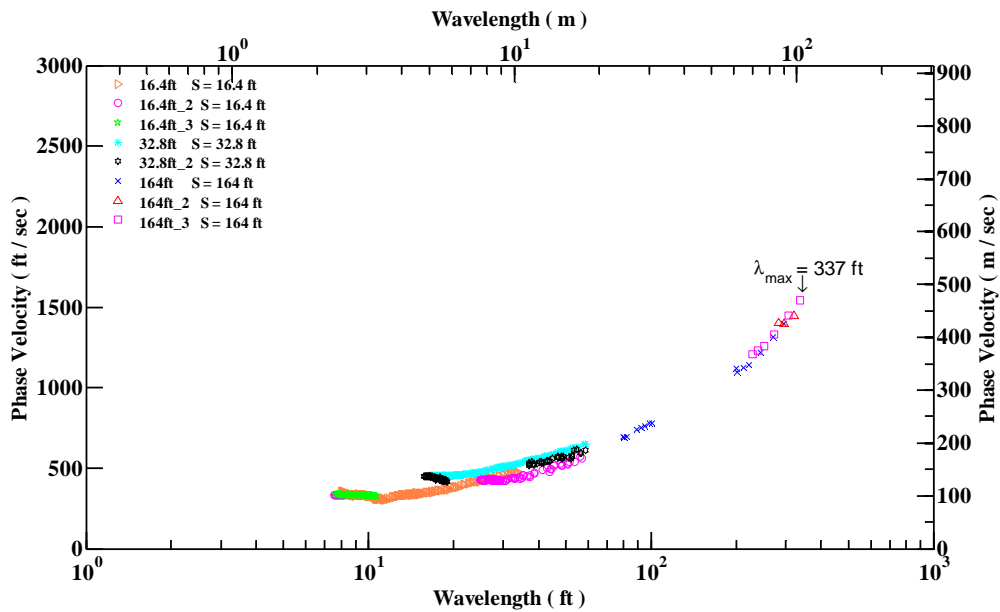
Figure 6.19 Composite Experimental Dispersion Curve Created from Phase
Measurements Performed at Center of the Test Array using a Sledge
Hammer and T-Rex as the Seismic Sources
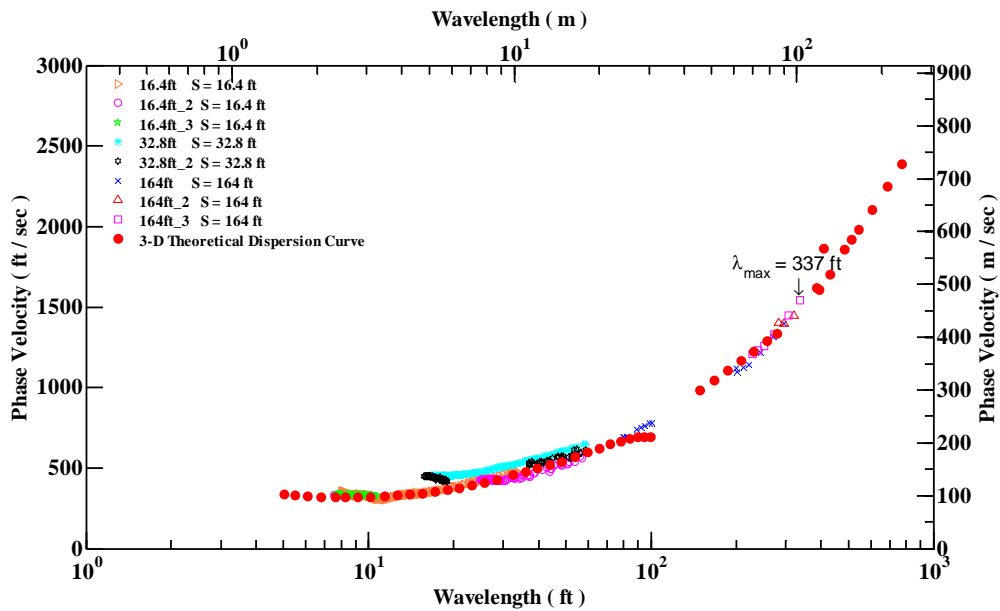
Figure 6.20   Comparison of the Fit of the 3-D Theoretical Dispersion Curve to the
SASW Composite Experimental Dispersion Curve during the First Trip
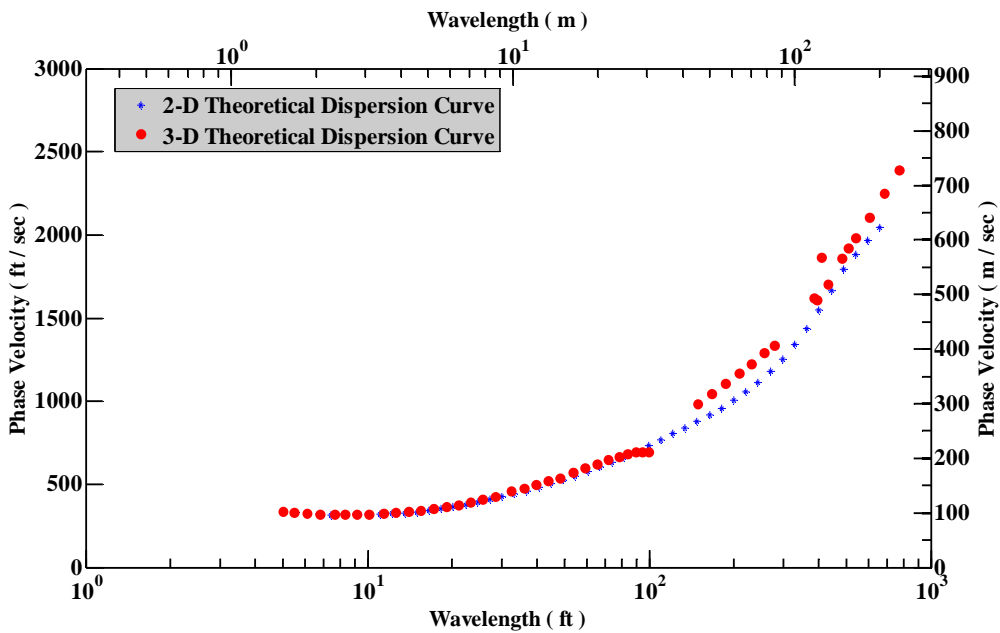
Figure 6.21   Comparison between the 3-D and 2-D Theoretical Dispersion Curves of the
SASW Test during the First Trip

112
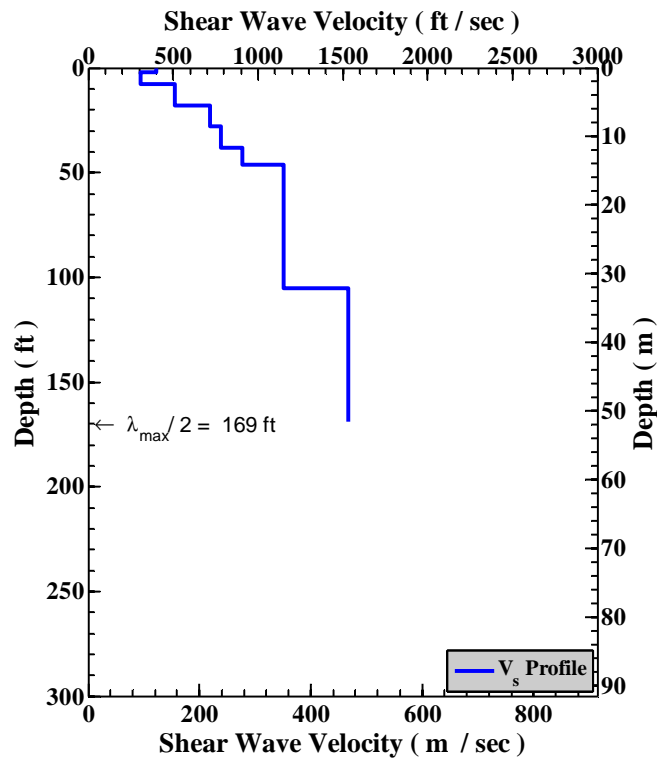
Figure 6.22   Shear Wave Velocity Profile Measured by SASW Testing during the First
Trip at the Hornsby Bend Site

Table 6.2   Profile Parameters Used to Develop Theoretical Dispersion Curve at the
Hornsby Bend Site during the First Trip

Layer No.	Thickness, ft	Depth to Top of Layer, ft	P-Wave Velocity, ft/s	S-Wave Velocity, ft/s	Assumed Poisson's Ratio	Assumed Total Unit Weight, pcf
1	2	0	794 [o]	400	0.33	100
2	5.5	2	615 [o]	310	0.33	100
3	10.5	7.5	1013 [o]	510	0.33	100
4	10	18	1429 [o]	720	0.33	100
5	10	28	1628 [o]	780	0.33	100
6	8	38	1807 [o]	910	0.33	120
7	59	46 [◊]	5000	1150	0.47 [+]	120
8	70	105	5000	1530	0.47 [+]	120
9	Half Space	175	5000	2900	0.25 [+]	120

[o] P-wave velocity calculated from V_s and assumed value of Poisson's ratio.

[◊] Water table assumed at a depth of 46 ft

[+] Not assumed but back-calculated from V_p = 5000 fps and V_s

113

curves are shown and compared with the 2-D and 3-D theoretical dispersion curve generated by standard data in Figure 6.23. As observed, the 3-D theoretical dispersion curve matches well with the near-field experimental data, extending the maximum wavelength from 337 ft to 632 ft.
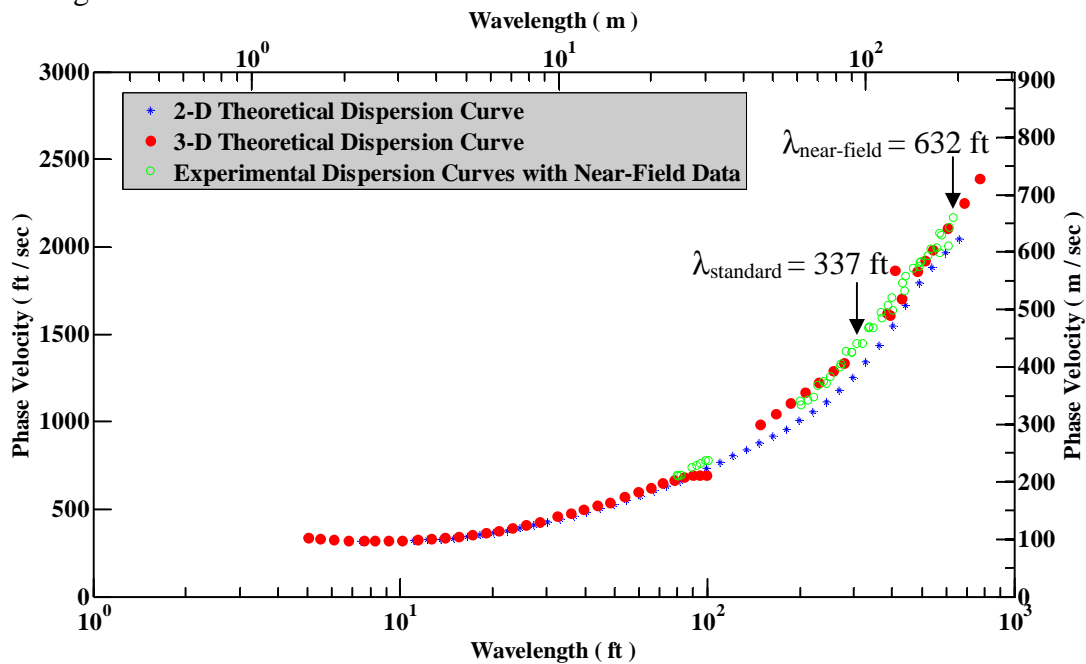
Figure 6.23   Comparison between the 3-D and 2-D Theoretical Dispersion Curves with Experimental Dispersion Curves from Near-Field Data during the First Trip

The experimental dispersion curves composed with "moving centers" is illustrated in Figure 6.24. In this case, the distance between source and first receiver is always maintained as the same of the distance between first receiver and second receiver (S-R1 = R1-R2), and distance between source and second receiver equals the distance between second receiver and third receiver (S-R2 = R2-R3). An illustration of test arrays with moving centers is shown in Figure 6.25. By comparing the experimental dispersion curves of the array with"moving centers" to the 2-D and 3-D theoretical dispersion curves from standard SASW analysis, it is seen that lateral variability occurs at a
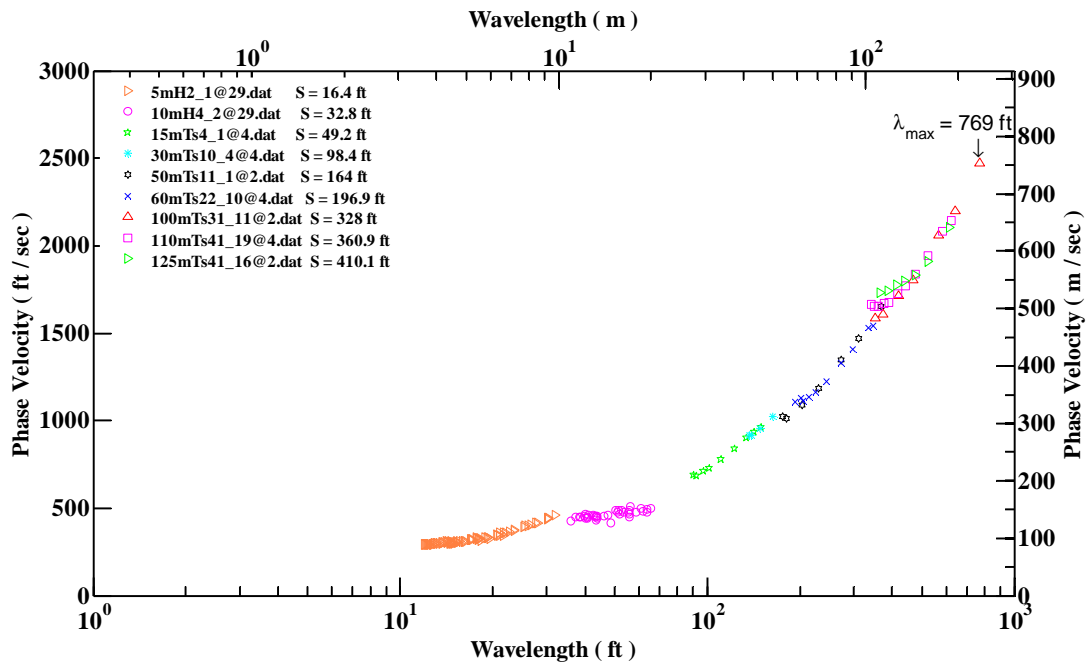
Figure 6.24 Experimental Dispersion Curves from Test Arrays with Moving Centers
during the First Trip
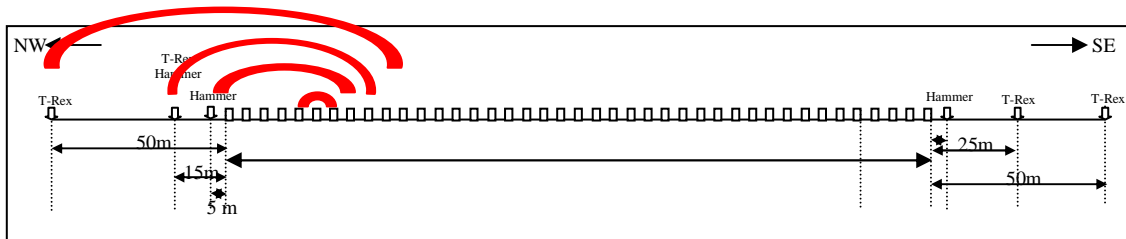
Figure 6.25 Illustration of Test Arrays with Moving Centers during the First Trip

wavelength range from about 30 to 70 ft. At wavelengths larger than 100 ft, the experimental dispersion curves agree well with the 3-D solution. The result indicates the uniformity of the material distribution at deep depths.
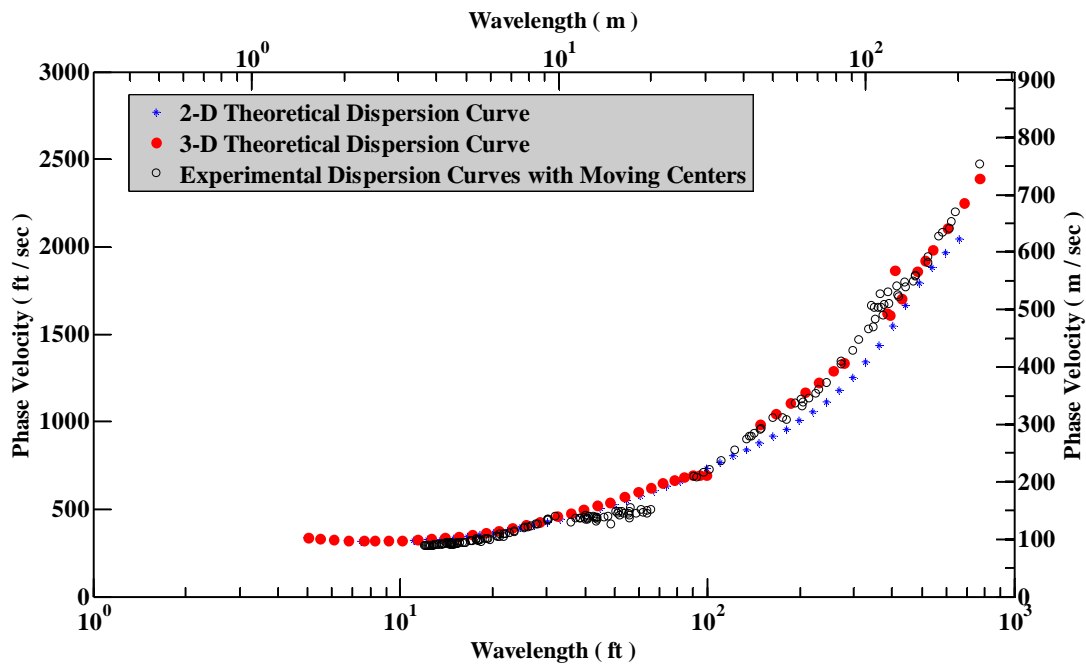
Figure 6.26   Comparison of the 2-D and 3-D Theoretical Dispersion Curves to the
Composite Experimental Dispersion Curve from Moving Centers

6.3 MASW TEST RESULTS

In this section, the results from a traditional MASW test setup are first presented. Based on Park's suggestion (Park et al., 2002), a system composing of a 24-channel signal analyzer, 24 geophone with resonant frequency equal or smaller than 4.5 Hz, a sledge hammer heavier than 10 lb, a source offset from 12 to 60 ft, a geophone spacing from 2 to12 ft is capable of measuring material down to a 100-ft deep. In this section, a test result from the traditional MASW setup is presented to show the effectiveness of the setup in material characterization. 24 1-Hz geophones with a 3-ft spacing and a 12-lb

sledge hammer were used when the sledge hammer was 12-ft away from the first geophone (S-R1=12ft). Field parametric studies are then presented based on the MASW data from both first and second trips. The SASW experimental and theoretical 2-D and 3-D dispersion curves, obtained from a V_s profile with an acceptable fit to the experimental data from the second trip, are used as references for the MASW parametric studies.

6.3.1 Results from a Traditional MASW Setup

The experimental dispersion curves of MASW tests with a 12-lb sledge hammer as the seismic source are shown in Figure 6.27. The fundamental mode of the experimental dispersion curves clearly exists from about 33 ft to 100 ft in wavelength. The trend of the fundamental mode at larger wavelength (>100 ft) is not clear as observed by a large amount of scattered data points. Higher modes are shown from 6 to 90 ft in wavelength.
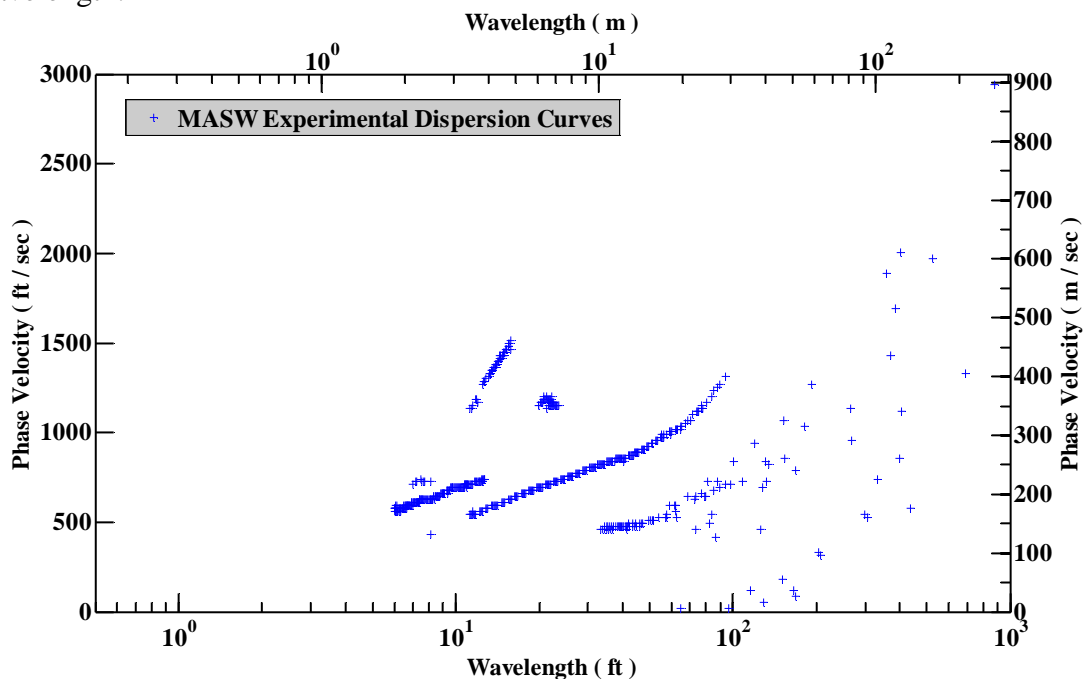
Figure 6.27   Experimental Dispersion Curves of a Typical MASW Test Setup from the Second Trip

117
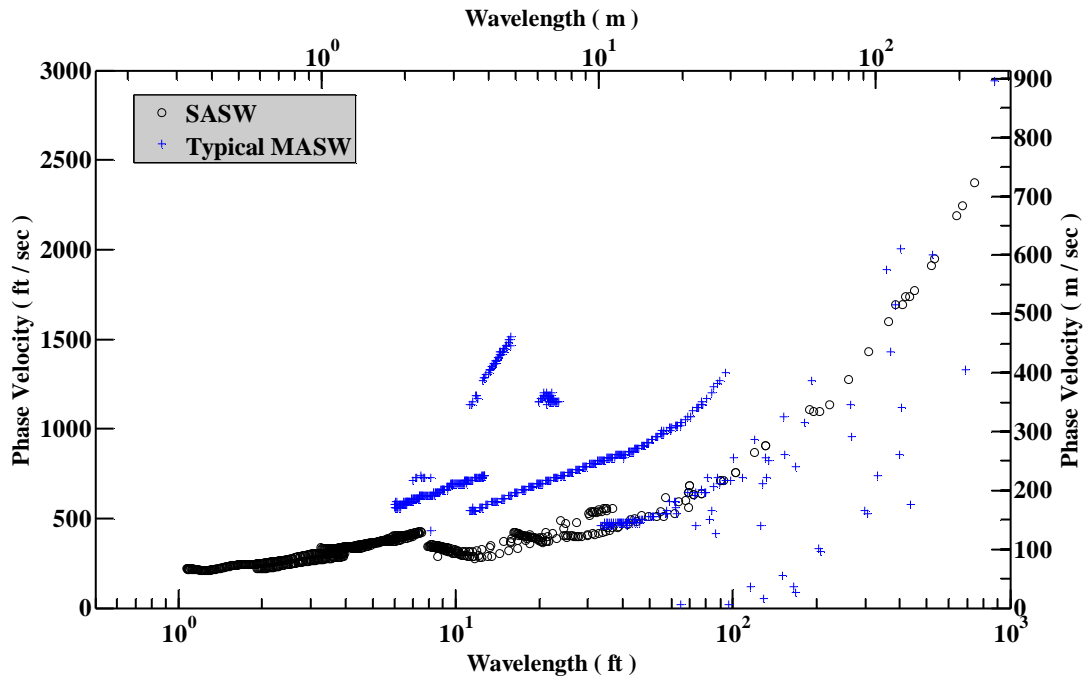
Figure 6.28 Comparison of Experimental Dispersion Curves from a Typical MASW
Setup to the SASW Experimental Dispersion Curves from the Second Trip

The experimental dispersion curves from MASW test are compared to the SASW experimental dispersion curves from the second trip, as shown in Figure 6.28. It is seen that the MASW fundamental dispersion curve overlaps with the SASW curves from 30 to 100 ft in wavelength. After 100 ft, the sledge hammer was unable to provide energy strong enough to reveal a clear, robust trend in dispersion curves. Second modes, which are higher than the fundamental mode in the wavelength – velocity plot, are observed from 10 to 90 ft in terms of wavelength.

The comparison of fundamental dispersion curve from the typical MASW setup and SASW 2-D and 3-D theoretical solutions is shown in Figure 6.29. Good agreement is observed from 30 to 100 ft between the 3-D and fundamental MASW curve. As limited by the source energy, the experimental curve does not have data showing its trend after 100 ft.

118

Figure 6.29 Comparison of SASW 2-D and 3-D Theoretical Dispersion Curves with
MASW Fundamental Dispersion Curves with a 12-lb Sledge Hammer with
S-R1 = 12 ft, 24 1-Hz geophones, and a 3-ft receiver spacing

   To conclude, the data from the traditional MASW test setup generated a reliable
estimate of experimental dispersion curve from about 30 ft to 100 ft in terms of
wavelength. Bigger sources are necessary to provide stronger energy, thus sampling into
deeper material for investigation. The MASW tests performed with Liquidator are
discussed in the following section.

119

6.3.2 Parametric Studies from the Second Trip

Both experimental and theoretical dispersion curves from SASW tests during the second trip are used as references for MASW results. For the MASW tests, 47 1-Hz geophones were placed with two different intervals: 3 ft and 10 ft. Also, 17 4.5H-z geophones were placed with a 10-ft spacing. Two different sources were used: a sledge hammer and Liquidator. A function generator was used to create different source signals as summarized in Table 5.2 with an addition of a 80-1Hz Stepsine signal. Geophones were equally placed. Seismic sources were place at the distances of one, three and five times of geophone spacings when a sledge hammer was used. The near offsets were usually set to ten and thirty times of geophone spacings when Liquidator was used. The receiver spacing, source type, source offset and number of geophones in use were varied to study their impacts on test results. 3-ft spacing is first used for the field parametric studies, followed by the studies with a 10-ft geophone spacing. Experimental and theoretical dispersion curves from SASW tests are used as references.

6.3.2.1 Comparison: Source Location

In this section, field experimental dispersion curves from MASW test are presented with 3-ft receiver spacing first and 10-ft receiver spacing.

3-ft Receiver Spacing

Parametric studies are made with the hammer impact as the source. The sledge hammer was placed at 1, 3, 5 and 10 times receiver spacing away from the first geophone. MASW experimental dispersion curves are first compared with their equivalents from SASW. Then, 2-D and 3-D theoretical dispersion curves are used as reference for MASW curves.

120

Figure 6.30 shows MASW experimental dispersion curves measured with a 3-ft receiver spacing, a sledge hammer and various source offsets. It is observed that fundamental MASW dispersion curves from four different source locations agree well with each other from 50 to 90 ft. The further the source was, the less data points on the fundamental mode. Higher modes are generally observed for all source offsets. By comparing to SASW results, all curves show good agreement on the portion of wavelength from 50 to 120 ft. None of the four test setups with sledge hammer provides material information after 120 ft, as illustrated by the scattered data points on the wavelength – velocity plot.

Figure 6.30 Comparison of Experimental Dispersion Curves between SASW Tests and MASW Tests Measured with a Sledge Hammer at Various Source Locations, a 3-ft Receiver Spacing and 47 Geophones

In Figure 6.31, fundamental modes of MASW experimental dispersion curves from four different source locations (with a sledge hammer) are compared with 2-D and 3-D theoretical dispersion curves from SASW test. Experimental dispersion curves from all source locations show a good agreement with 3-D theoretical solution from 40 to 120 ft. It is clear that as the sledge hammer moves away from the test array, the less the energy that possessed by the fundamental mode. In this case, a source offset of one times geophone spacing provides most amount of reliable data compared to results from other source offsets.
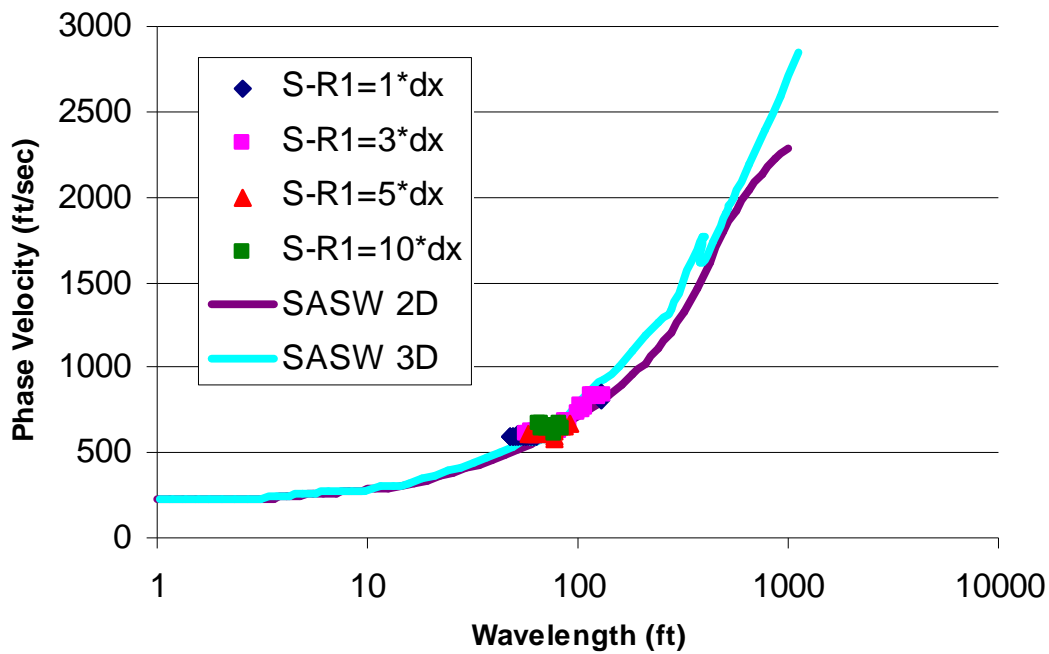
Figure 6.31   Comparison of SASW 2-D and 3-D Theoretical Dispersion Curves with MASW Fundamental Dispersion Curves with a Sledge Hammer at Various Source Locations, a 3-ft Receiver Spacing and 47 Geophones

10-ft Receiver Spacing

The sledge hammer was placed at 1, 3 and 5 times receiver spacing away from the first geophone when receivers were placed 10 ft apart. The MASW experimental dispersion curves from three different setups are compared to the SASW curves in Figure 6.32. It is again observed that fundamental dispersion curves overlap with the SASW curves from 70 to about 200 ft. Data at longer wavelengths are so scattered that no clear trend is found for deeper material. All setups show clear second modes. As noted, the shortest source offset (S-R1=1*dx) yields the most amount of data that follow SASW dispersion curves.

Figure 6.32   Comparison of Experimental Dispersion Curves between SASW Tests and MASW Tests Measured with a Sledge Hammer at Various Source Locations, a 10-ft Receiver Spacing and 47 Geophones

The comparison of fundamental modes from three source offsets and theoretical solutions from SASW tests is shown in Figure 6.33. It is seen that all fundamental mode curves overlap with the SASW 3-D theoretical dispersion curve from 90 to 180 ft. Comparing to results from 3-ft spacing, the MASW setup with 10-ft spacings provided slightly larger measurement wavelength. However, the exploration depth is still restricted by the relatively small energy of hammer impacts.
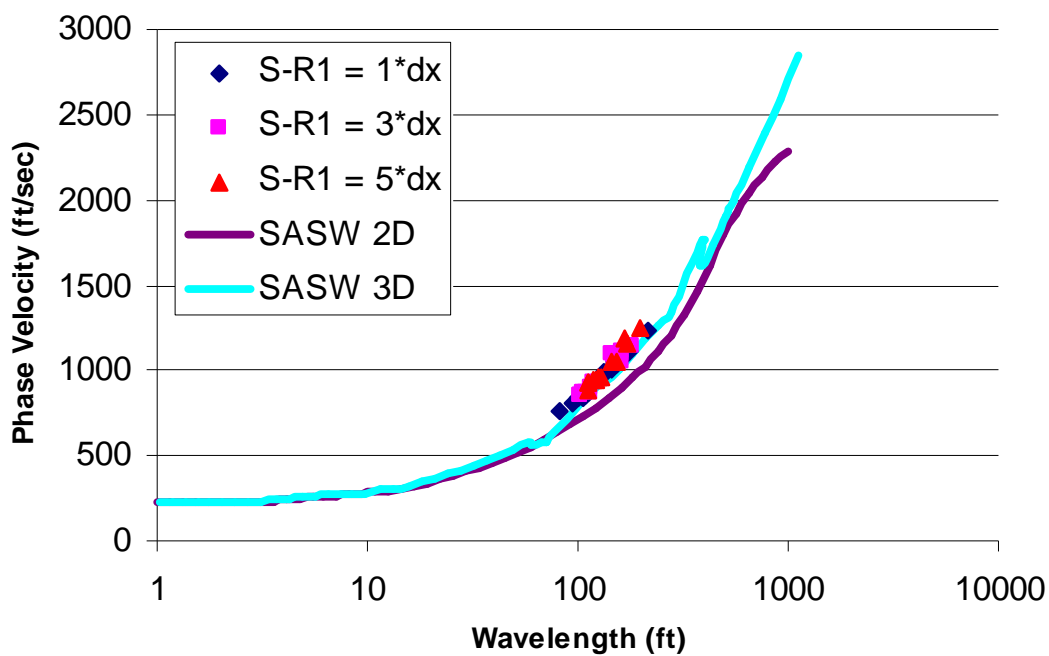
Figure 6.33 Comparison of SASW 2-D and 3-D Theoretical Dispersion Curves with MASW Fundamental Dispersion Curves with a Sledge Hammer at Various Source Locations, a 10-ft Receiver Spacing and 47 Geophones

6.3.2.2 Comparison: Source Type

In this section, field experimental dispersion curves from MASW tests with different source signals (hammer impact, chirp, stepsine, ricker wavelet) are presented with the 3-ft receiver spacing first and 10-ft receiver spacing.

3-ft Receiver Spacing

The sources were placed at ten times the receiver spacing, which is 30 ft away from the first geophone. The experimental dispersion curves for four chirp signals are shown in Figure 6.34 with the SASW curves as references. As observed, the 3-8Hz chirp signal provided the longest estimation of dispersion curves up 1000 ft in wavelength. As the frequency span of the source signal shifts to higher frequency, the available data on the fundamental mode decrease. All four signals show the significant second mode energy. By comparing to SASW experimental dispersion curves, the MASW curves generally overlap with SASW curves from about 60 to 200 ft. From 300 ft to 800 ft, the MASW experimental dispersion curve is slightly lower than the SASW reference curve.

The comparison of dispersion curves from two stepsine, one ricker wavelet and one hammer impact is shown in Figure 6.35. The hammer impact with the 3-ft spacing only reveal a fundamental dispersion curve from 60 to 100 ft comparing to SASW reference curve. The Ricker wavelet and the 25-3.5Hz Stepsine yield similar results of a reliable dispersion curve up to 200 ft. The 110-20Hz stepsine does not provide any information on the fundamental mode curve. To better understand the source effect, fundamental modes of the 3-8Hz chirp, 25-3.5Hz stepsine, 20Hz ricker wavelet and the hammer impact are plotted against the 2-D and 3-D theoretical solutions in Figure 6.36.
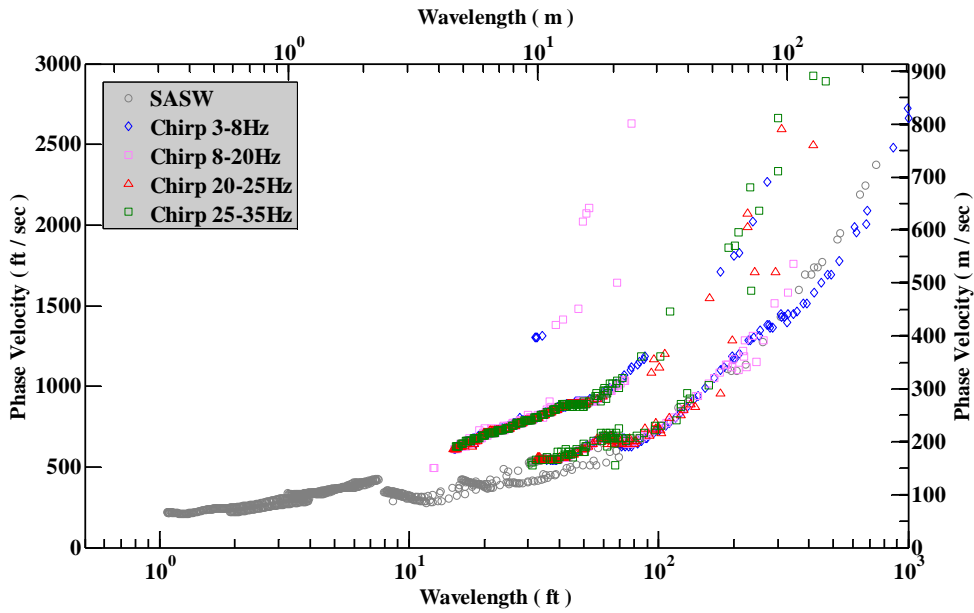
Figure 6.34   Comparison of Experimental Dispersion Curves between SASW Tests and
MASW Tests Measured with Four Chirp Signals at 30 ft away from the First
Geophone, a 3-ft Receiver Spacing and 47 Geophones

Figure 6.35   Comparison of Experimental Dispersion Curves between SASW Tests and
MASW Tests Measured with Various Source Signals at 30 ft away from the
First Geophone, a 3-ft Receiver Spacing and 47 Geophones

Figure 6.36   Comparison of SASW 2-D and 3-D Theoretical Dispersion Curves with MASW Fundamental Dispersion Curves with Various Source Signals at 30 ft away from the First Geophone, a 3-ft Receiver Spacing and 47 Geophones

As shown in Figure 6.36, the frequency contents of the source signals control the usable range of experiment dispersion curves in MASW testing. The 12-lb sledge hammer has the least energy comparing to signals created by Liquidator thus yields the least usable range of dispersion curves (below 100 ft). The 20Hz Ricker wavelet and 25-3.5Hz stepsine produce similar result of curves ranging from 80 to 300 ft. The 3-8Hz chirp signal which overlap with the 3-D theoretical solution. It is noted that 25-3.5Hz stepsine and 3-8Hz chirp both capture the trend of 2-D solution up to 650 ft but only the 3-8Hz chirp, which produces the longest wavelength up to 1000 ft, overlap with the 3-D solution at long wavelength (870 to 1000 ft). This phenomenon is a good indication that larger seismic source with lower frequency excitation is needed to correctly capture the

deep material properties.

10-ft Receiver Spacing

The sources were placed at five times the receiver spacing, which is 50 ft away from the first geophone. In this case, a 80-1Hz stepsine was used to explore the material at deeper depths. The fundamental experimental dispersion curves for all source signals are shown in Figure 6.37 with the SASW theoretical curves as references. In general, dispersion curves from all four source signals overlap with the SASW 3-D solution. Again, the hammer produces the shortest usable wavelength from about 100 to 200 ft. The 20Hz ricker wavelet covers a wavelength range from 100 to 270 ft. The 3-8Hz chirp signal produces a fundamental dispersion curve from 110 to 900 ft, which overlap with the 3-D solution along the whole range. The 80-1Hz stepsine provides the furthest wavelength to 1335 ft, which still overlaps with the 3-D solution. It is seen that a stable, low-frequency source signal is always desired for measurement at deep depths.

6.3.2.3 Comparison: Number of Receiver

In this section, field experimental dispersion curves from MASW tests with a 3-8Hz chirp source signal with varied numbers of receivers (N = 47, 36, 24, 12) used in the analysis.

3-ft Receiver Spacing

The sources were placed at ten times the receiver spacing (3 ft), which is 30 ft away from the first geophone. The fundamental experimental dispersion curves for four sets of receiver number are shown in Figure 6.38 with the SASW theoretical dispersion curves as references. It is seen that as number of receiver decreases, the fundamental dispersion curve shifts to lower velocity. All MASW curves are lower than the 3-D SASW theoretical solution from about 300 to 700 ft in terms of wavelength, which can
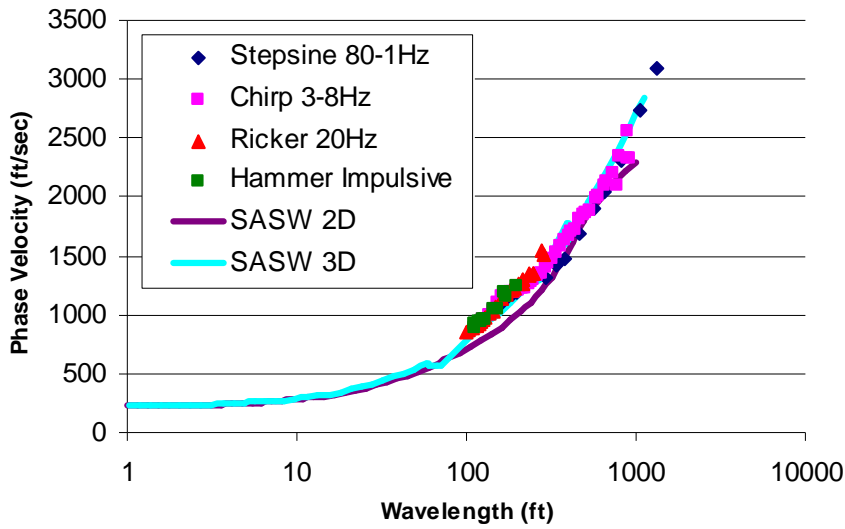
Figure 6.37   Comparison of SASW 2-D and 3-D Theoretical Dispersion Curves with MASW Fundamental Dispersion Curves with Various Source Signals at 50 ft away from the First Geophone, a 10-ft Receiver Spacing and 47 Geophones
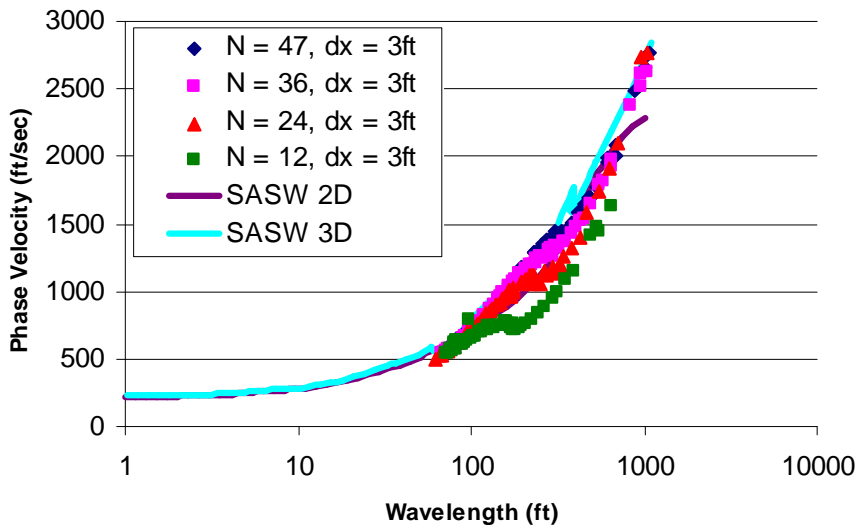
Figure 6.38   Comparison of SASW 2-D and 3-D Theoretical Dispersion Curves with MASW Fundamental Dispersion Curves with a 3-8Hz Chirp at 30 ft away from the First Geophone, a 3-ft Receiver Spacing and Different Numbers of Receivers

possibly be attributed to the near-field effect that caused by the usage of a short test array in measuring deep materials (Yoon and Rix, 2009). By evaluating the maximum measured wavelength with Yoon's criteria ($\bar{x}/\lambda_R > 0.5$, where $\bar{x}$ is the mean distance of all receiver relative to the source), the maximum useable wavelength is about 100 ft for the test setup with a total of 12 receivers, a 30-ft source offset and a 3-ft spacing.

10-ft Receiver Spacing

The sources were placed at five times the receiver spacing, which is 50 ft away from the first geophone. In this case, the 3-8Hz chirp signal was again used. The fundamental experimental dispersion curves for all source signals are shown in Figure 6.39 with the SASW theoretical curves as references. In general, dispersion curves from all setups agree well with the 3-D theoretical dispersion curve from the SASW analysis. No near-field effect is found even the maximum wavelength from the setup of N = 12 is close to 1000 ft, which is about five times the mean distance, $\bar{x}$. Also, it is observed that none of these setups provides information smaller than 90 ft in wavelength.
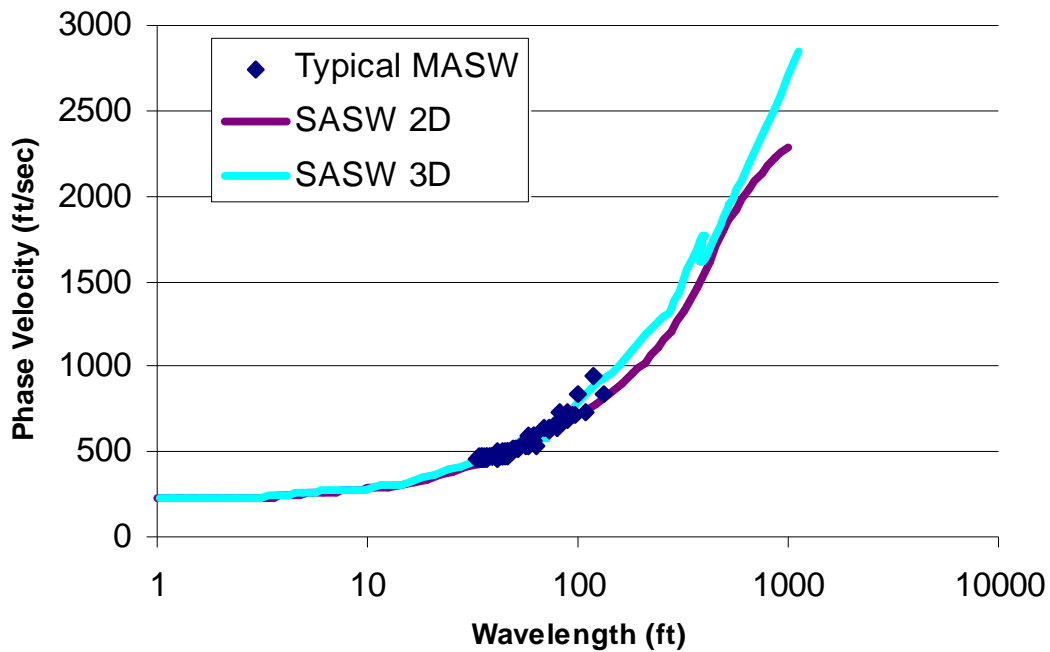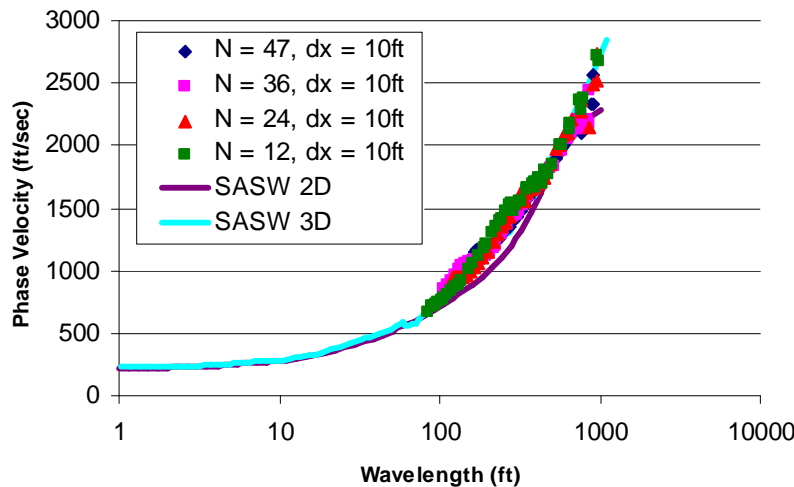

Figure 6.39   Comparison of SASW 2-D and 3-D Theoretical Dispersion Curves with MASW Fundamental Dispersion Curves with a 3-8Hz Chirp at 50 ft away from the First Geophone, a 10-ft Receiver Spacing and Different Numbers of Receivers

6.3.2.4 Comparison: Receiver Spacing

In this section, field experimental dispersion curves from MASW tests with a 3-8Hz chirp source signal with varied receiver spacings used in the analysis.

3-ft Receiver Spacing

The sources were placed at ten times the receiver spacing (3 ft), which is 30 ft away from the first geophone. The receiver spacing is varied with the same total test array (3, 6, 12 ft, when number of receiver, N, equal to 45, 23 and 12, respectively. The total length was maintained as 132 ft). The fundamental dispersion curves are compared to the 2-D and 3-D theoretical dispersion curves in Figure 6.40. The results from three different test sets are similar to each other. All dispersion curves overlap with the SASW 3-D solution from 70 to 300 ft and from 850 to 1000 ft in wavelength. The 3-D solution from SASW analysis is slight higher than all MASW fundamental dispersion curves from 300 to 850 ft, which indicates a small lateral variability of the site.

10-ft Receiver Spacing

The sources were placed at five times the receiver spacing (10 ft), which is 50 ft away from the first geophone. 10-, 20-, and 40-ft spacings were used. The numbers of receivers used in the MASW analysis are 45, 23 and 12, corresponding to a total length of 440 ft. The fundamental dispersion curves from three setups are compared to the SASW 2-D and 3-D theoretical dispersion curves in Figure 6.41. It is seen that all MASW fundamental curves agree with the 3-D solution along the whole measured wavelength range. The minimum wavelength for all setups is about 120 ft.

It is observed that three setups with 10-ft spacing generally agree better with the 3-D solution than the 3-ft spacing setups do. This is because 10-ft spacing setups cover a wider test array like SASW test while 3-ft setups only cover a total of 132 ft.

Figure 6.40 Comparison of SASW 2-D and 3-D Theoretical Dispersion Curves with MASW Fundamental Dispersion Curves with a 3-8Hz Chirp at 30 ft away from the First Geophone, a 3-ft Receiver Spacing and Different Receiver Spacings

Figure 6.41 Comparison of SASW 2-D and 3-D Theoretical Dispersion Curves with MASW Fundamental Dispersion Curves with a 3-8Hz Chirp at 50 ft away from the First Geophone, a 10-ft Receiver Spacing and Different Receiver Spacings

132

6.3.2.5 Comparison: Receiver Type

In this section, field experimental dispersion curves from MASW tests with a sledge hammer and a 3-8Hz chirp source signal with 17 geophones of two different resonant frequencies (1-Hz and 4.5-Hz) and a 10-ft receiver spacing are studied. The SASW experimental dispersion curves are used as the reference.

The comparison of MASW experimental dispersion curves from 1-Hz and 4.5-Hz geophones with a hammer impact is shown in Figure 6.42. It is observed that two curves overlap with each other from 40 to 100 ft on the fundamental mode, and from 25 to 80 ft on the second mode. None of them provides information above 200 ft in wavelength.
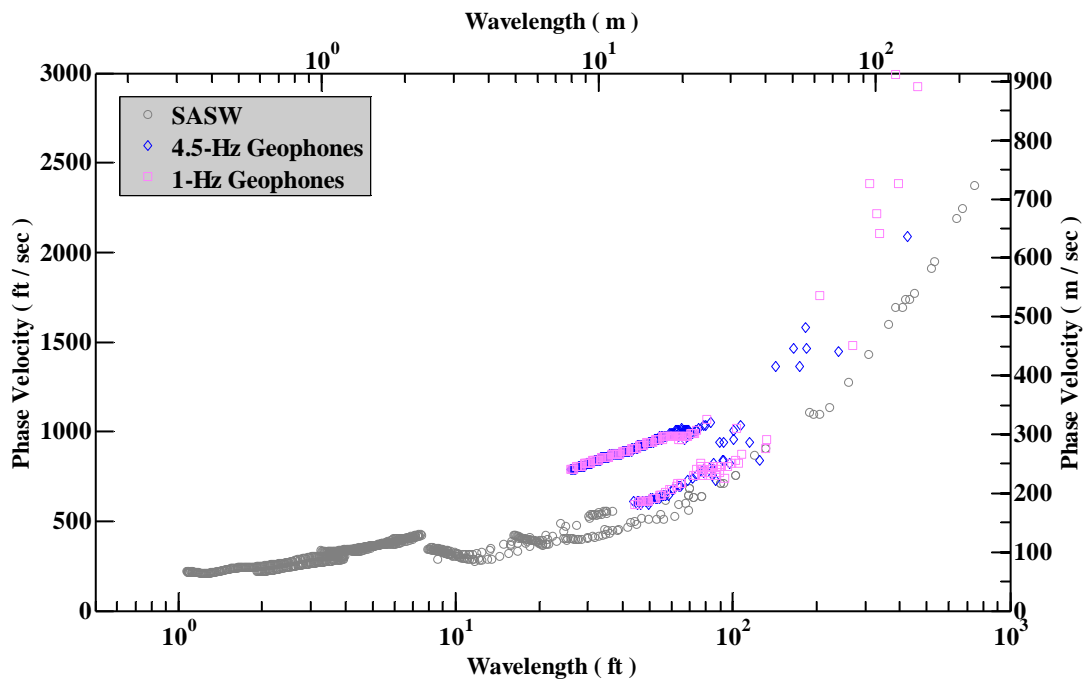
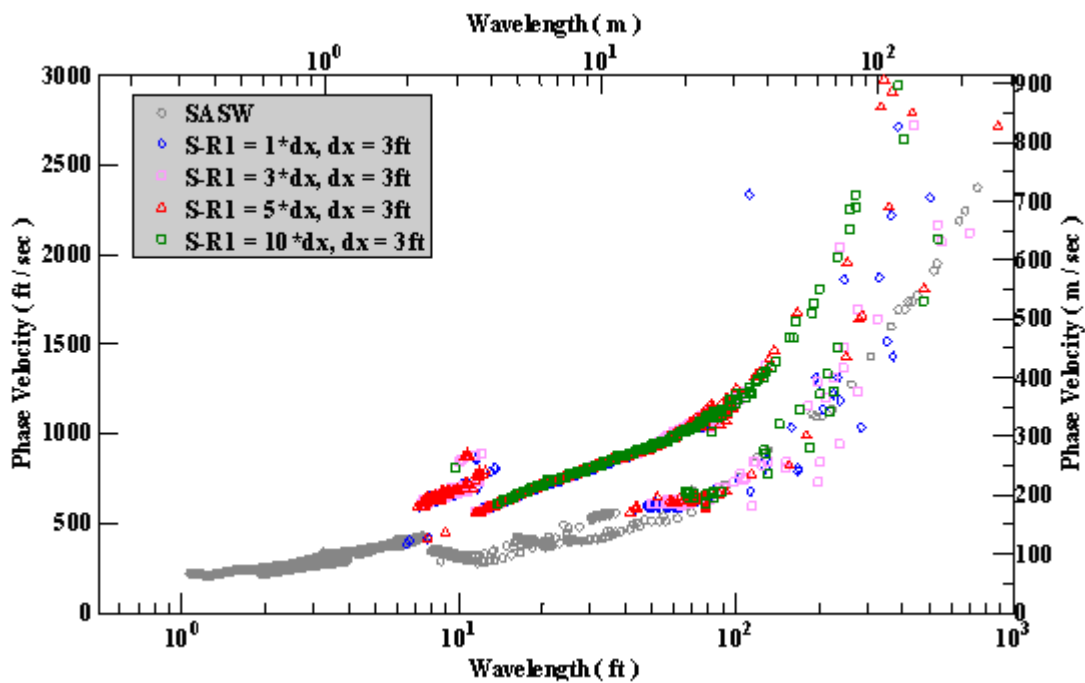Figure 6.42   Comparison of Experimental Dispersion Curves between SASW Tests and MASW Tests Measured with a Sledge Hammer at 20 ft away from the First Geophone, a 10-ft Receiver Spacing and 17 Geophones (1-Hz and 4.5-Hz)

133

The comparison of MASW experimental dispersion curves from 1-Hz and 4.5-Hz geophones with a 3-8Hz chirp signal is shown in Figure 6.43. Generally, two setups produce similar dispersion curves on both fundamental and second modes. It is seen that at the wavelength between 100 and 200 ft, the result from 1-Hz geophone has a better distinction between fundamental and second modes. At larger wavelength about 800 to 1000 ft, it is observed that 1-Hz geophone performed better in defining a clear trend like SASW curves, whereas the fundamental dispersion curve of 4.5-Hz geophones started to become scattered. The performance of the 4.5-Hz geophone is restricted by its mechanical design at low frequency (<3 Hz).

Figure 6.42 Comparison of Experimental Dispersion Curves between SASW Tests and MASW Tests Measured with a 3-8Hz chirp at 20 ft away from the First Geophone, a 10-ft Receiver Spacing and 17 Geophones (1-Hz and 4.5-Hz)

6.3.3 Parametric Studies from the First Trip

In this section, a comprehensive field parametric study of MASW field setup is presented for the first trip. The MASW data collection employed a 16.4 ft (5m) receiver spacing with 41, 1-Hz geophones. Two different sources were used: a sledge hammer and T-Rex. A digital function generator was used to drive T-Rex and create different source signals as summarized in Table 5.2. Geophones were placed from 0 to 656 ft (200m) while T-Rex were placed at -164, -49.2, 738.2 and 820.2 ft (-50, -15, 225 and 250 meters). The receiver spacing, source type and source offset were varied in an effort to establish which combination provides the best dispersion curve for the MASW analysis, and what wavelength can be reasonably measured for various combinations of source and receiver setups. The MASW test results are discussed below.

6.3.3.1 Source Location Comparison

In this section, field experimental dispersion curves from MASW test are presented while sources were placed at -164, -49.2, 738.2 and 820.2 ft (10* and 3* receiver spacing from one end, and 5* and 10*spacing from the other end). Two source signals, a 3-8Hz Chirp and a 20-3Hz Stepsine, are used as illustration. The MASW experimental dispersion curves are first compared with their equivalents from SASW. Then, 2-D and 3-D theoretical dispersion curves are used as a reference for the MASW fundamental dispersion curves.

Figure 6.43 shows MASW experimental dispersion curves measured with a 16-4 ft (5 m) receiver spacing, a 3-8Hz Chirp source signal and various source locations. It is observed that experimental dispersion curves from four different source locations agree well with each other. Comparing to SASW results, all curves show good agreement with SASW curves when wavelength is equal or larger than 300ft. Between 200 and 300 ft,
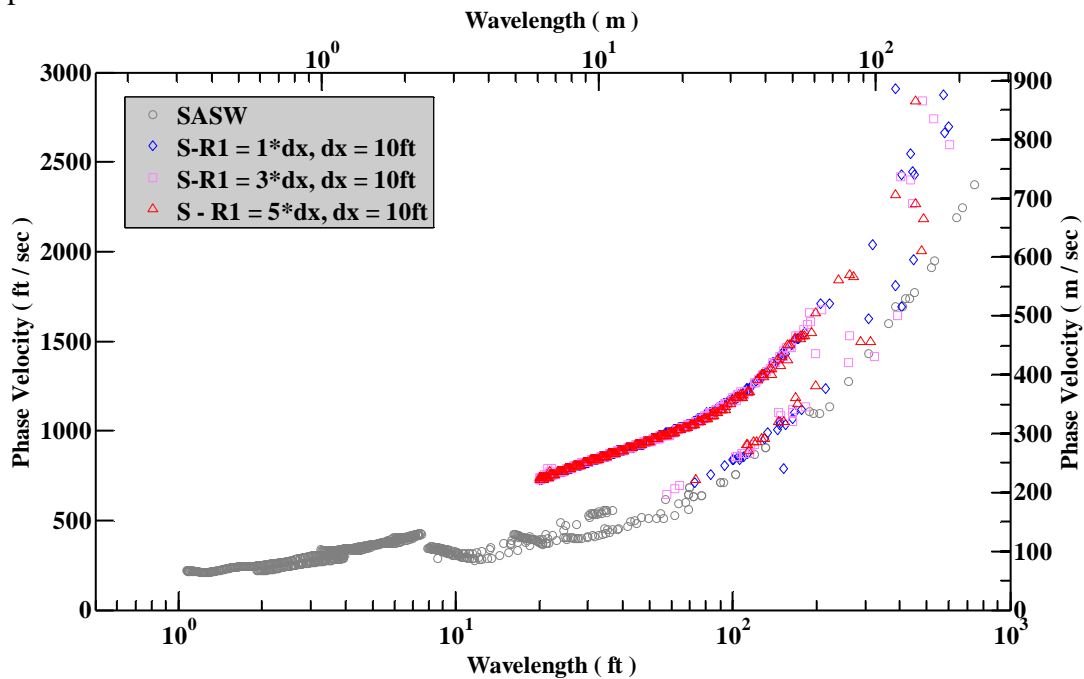
Figure 6.43   Comparison of Experimental Dispersion Curves between SASW Tests and
MASW Tests Measured with a 3-8Hz Chirp Signal at Various Source
Locations, a 16.4-ft (5 m) Receiver Spacing and 41 Geophones

they stand on the upper portion of SASW experimental curves. However, none of these

MASW curves reveals the dispersion curve below a wavelength of 100 ft, indicating a

smaller receiver spacing is required for shallow depth measurement. One thing needs to

be mentioned is that all MASW curves show a significant higher mode from about 40 to

200 ft in wavelength.

In Figure 6.44, fundamental modes of MASW experimental dispersion curves

from four different source locations (Chirp 3-8Hz) are compared with 2-D and 3-D

theoretical dispersion curves from SASW test. Experimental dispersion curves from all

source locations show a good agreement with 3-D theoretical solution at large

wavelength from SASW method. At a wavelength of approximately 600 ft, the 2-D

Figure 6.44   Comparison of SASW 2-D and 3-D Theoretical Dispersion Curves with MASW Fundamental Dispersion Curves with a 3-8Hz Chirp Signal at Various Source Locations, a 16.4-ft (5-m) Receiver Spacing and 41 Geophones

SASW theoretical solution starts to roll off, while both MASW experimental curves and 3-D theoretical dispersion curves continue to climb. The agreement between 3-D SASW theoretical curve and MASW field curves is observed at large wavelength (>500 ft). At wavelength between 200 and 300 ft, MASW curves are generally higher than the SASW 3-D theoretical curve. No MASW experimental curve is acquired below a wavelength of 100 ft.

Figure 6.45 shows MASW experimental dispersion curves measured with a 16.4-ft (5 meter) receiver spacing, a 20-3Hz Stepsine source signal and four different source locations. It is again observed that MASW curves overlap with SASW curves when wavelength is larger than 400 ft. Similarly, none of the MASW curves from various
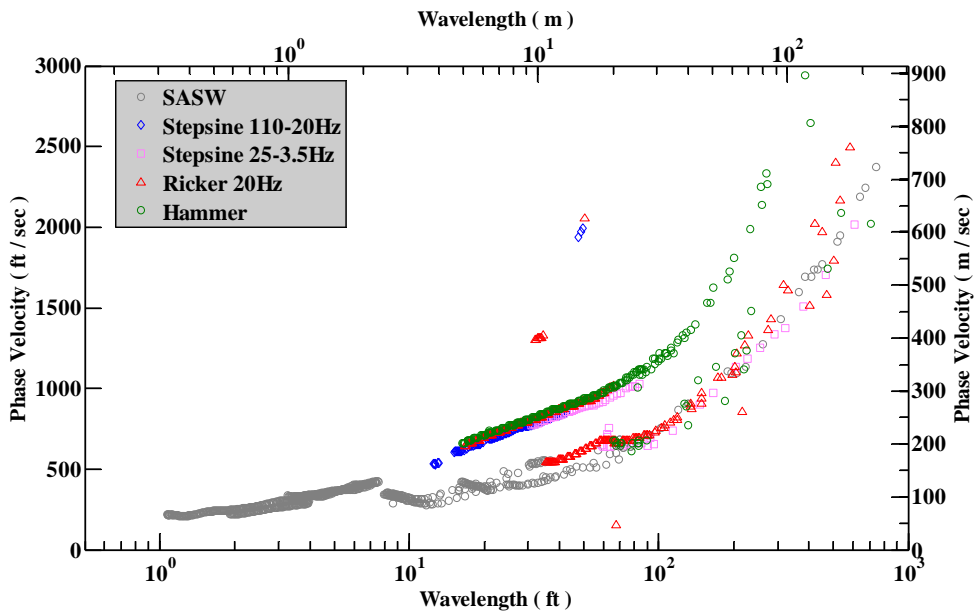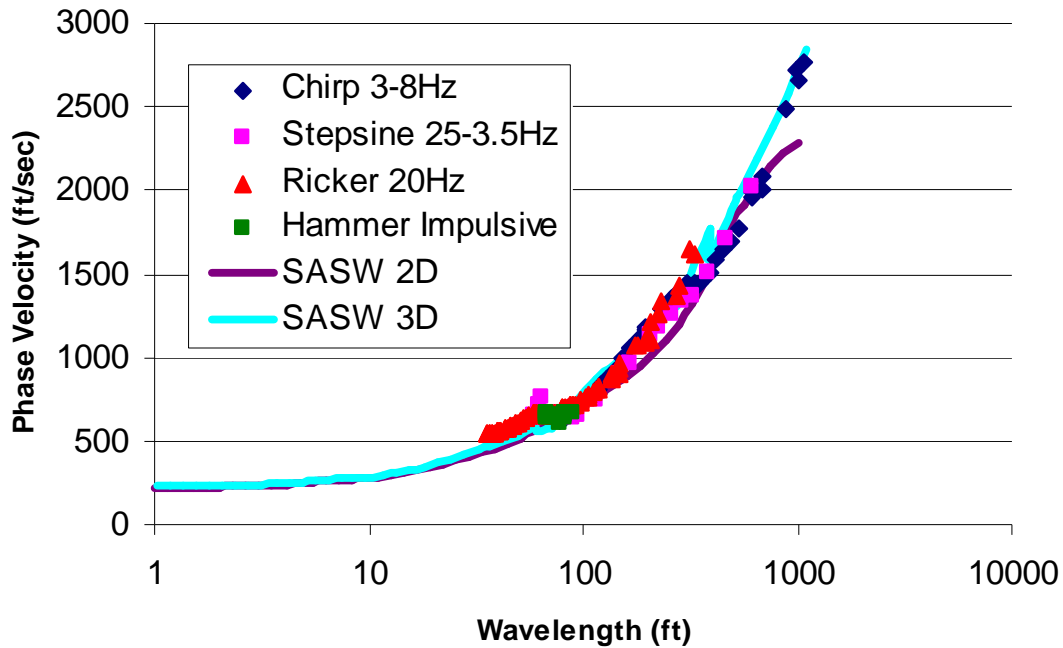
Figure 6.45   Comparison of Experimental Dispersion Curves between SASW Tests and MASW Tests Measured with a 20-3Hz StepSin Signal at Various Source Locations, a 16.4-ft (5-m) Receiver Spacing and 41 Geophones

source locations provide information at wavelength smaller than 100 ft. Second mode of experimental dispersion exists in all four MASW curves.

The comparison between SASW 2-D and 3-D theoretical dispersion curves and MASW fundamental mode dispersion curves is shown in Figure 6.46 when a 20-3Hz Stepsine is used as the source signal. As observed, all four MASW curves agree with SASW 3-D solution at wavelengths > 300 ft. Between 200 and 300 ft, the MASW dispersion curves are slightly higher than 3-D solution. Only the experimental dispersion curve with source at -49.2 ft (-15 m) has data points below 200 ft in wavelength. Generally, the 3-8 Hz chirp and 20-3Hz stepsine yield similar results.

Overall, MASW experimental dispersion curves from four different locations with a receiver spacing of 16.4-ft (5 m) are very similar. It is concluded at Hornsby Bend site,

138
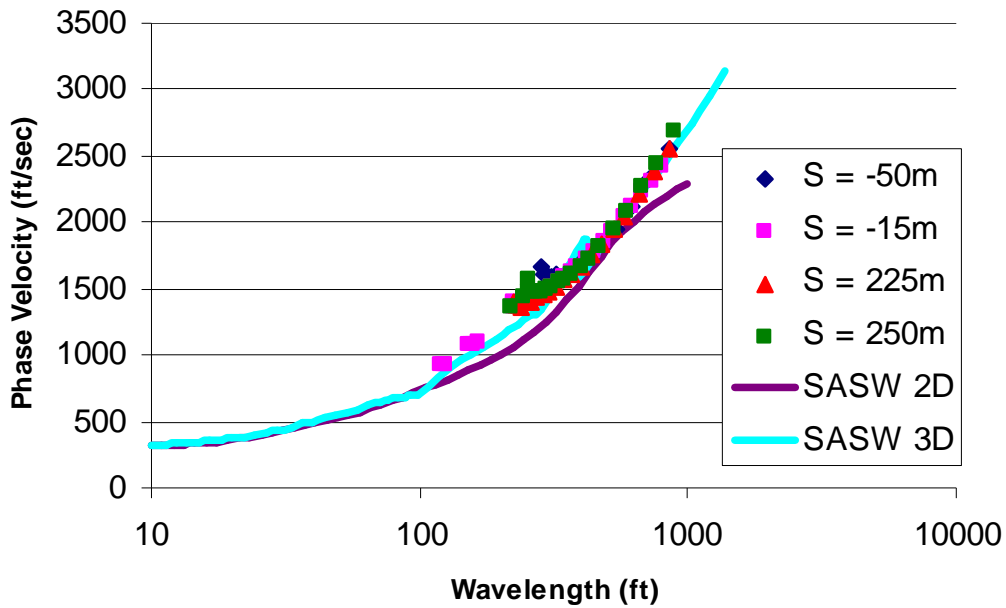
Figure 6.46   Comparison of SASW 2-D and 3-D Theoretical Dispersion Curves with
MASW Fundamental Dispersion Curves with a 20-3Hz StepSine Signal at
Various Source Locations, a 16.4ft (5 m) Receiver Spacing and 41
Geophones

source location (up to ten times of receiver spacing) plays a negligible role in defining
shape of dispersion curves for MASW tests. This is attributed to the fact that T-Rex can
provide sufficient energy for waves with desired frequency contents to propagate along
the whole test array. Also, stepsine and chirp source signals yields similar test results. It
is possible that chirp signals can be used as a supplement to stepsine signals in field
surface wave testing.

Mode jumps from fundamental to second modes in MASW experimental
dispersion curves are observed. With such geophone spacing and source signals, it is not
sufficient enough for MASW method to explore shallow material up to 100 ft in
wavelength. This phenomenon emphasizes the importance of recognizing different modes

in MASW experimental dispersion curves. Given a second mode is mistakenly treated as the fundamental mode, the calculated material property will be much stiffer than its true property, caused by overestimation of shear wave velocity profiles.

6.3.3.2 Source Type Comparison

To study the contribution of different sources to the shape of MASW experimental dispersion curves, four different Chirp signals (3-8Hz, 8-20Hz, 20-25Hz, 25-35Hz), one 20Hz Ricker wavelet, sledge hammer and two StepSine signals (20-3Hz) were applied at a location of -49.2 ft (-15 m). In Figure 6.47 experimental dispersion curves from four Chirp signals are compared with SASW field curves. The comparison between 3-8Hz Chirp, 8-20Hz Chirp, sledge hammer, 20-3Hz Stepsine and SASW field curves is shown in Figure 6.48.

It is clear illustrated that frequency content of input source signal has a major effect on the formation of MASW experimental dispersion curves as illustrated in Figure 6.47. Only the 3-8Hz Chirp achieved a similar, comparable result to SASW field curves at larger wavelength from 200 to 700 ft. The usable range of experimental dispersion curves from a 8-20Hz Chirp source signal is about from 120 to 400 ft in wavelength. The 20-25 Hz and 25-35 Hz Chirp signals failed to reveal any dispersion curve on fundamental mode. All four source signals show the existence of a significant second mode from about 45 to 220 ft in wavelength. Still, shallow depth information is not discovered by all Chirp signals in the MASW test setup.

From Figure 6.48, performance of different type of sources is compared to SASW experimental dispersion curves. Again, 20-3Hz Stepsine and 3-8Hz Chirp yield similar results, both successfully overlapping with the reference SASW dispersion curves after

140
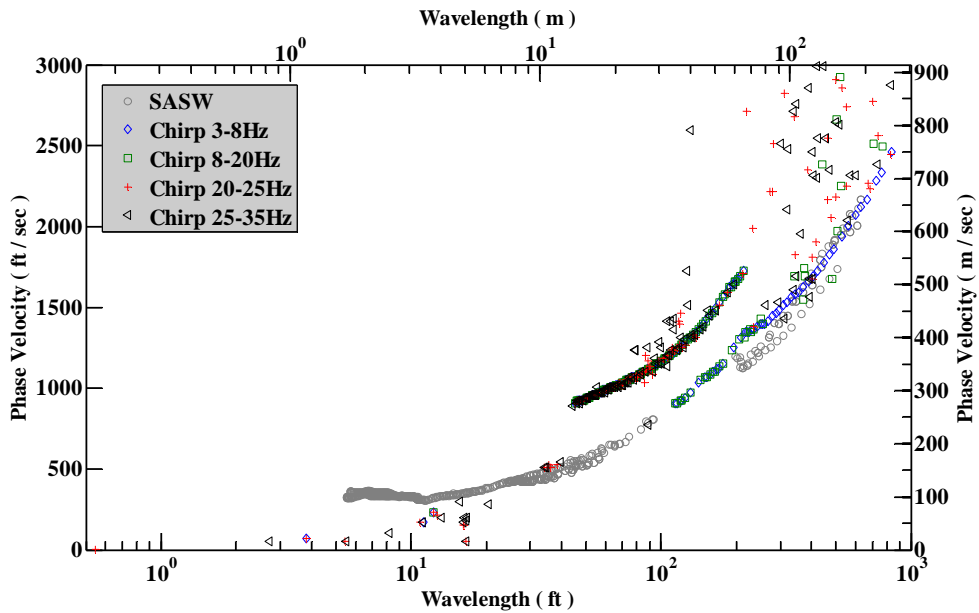
Figure 6.47   Comparison of Experimental Dispersion Curves between SASW Tests and MASW Tests Measured with Four Different Chirp Signals at -49.2 ft (-15 m), a 16.4-ft (5 m) Receiver Spacing and 41 Geophones
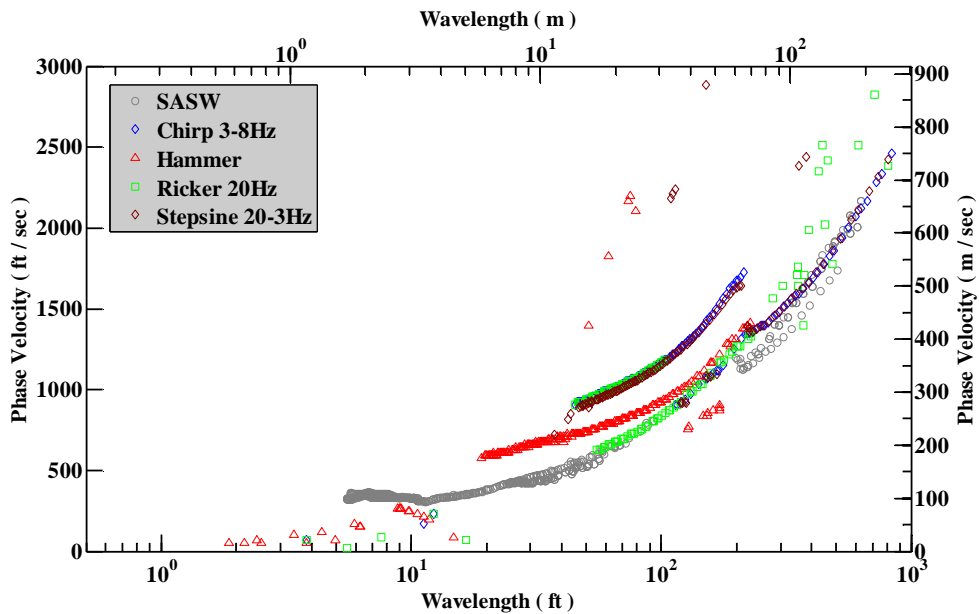
Figure 6.48   Comparison of Experimental Dispersion Curves between SASW Tests and MASW Tests Measured with Various Signals at -49.2 ft (-15 m), a 16.4-ft (5 m) Receiver Spacing and 41 Geophones

200 ft in wavelength. The 20Hz Ricker provided a correct representation of fundamental mode from 50 to 230 ft but failed to reveal information any further. The dispersion curves created by sledge hammer do not overlap with any mode. One reason to explain is that energy generated by sledge hammer is not strong enough to propagate through the whole 200 meter array length, thus MASW method is unable to differentiate collected signals into fundamental and higher modes. The credibility of sledge hammer applied as seismic source in a long array (656.2 ft, 200 m) with relatively large spacing (16.4 ft, 5 m) is somewhat questionable as shown in Figure 6.48.

The comparison between 2-D and 3-D SASW theoretical dispersion curves and MASW curves from various sources is shown in Figure 6.49. The 20-25 Hz and 25-35Hz Chirp, hammer impulsive and 100-10Hz Stepsine signals are excluded due to their failure in providing fundamental dispersion curves for MASW analysis. It is observed that all four source signals (3-8Hz Chirp, 8-20Hz Chirp, 20Hz Ricker and 20-3Hz Stepsine) generate convenient fundamental dispersion curves that match with SASW 3-D solution. 3-8Hz Chirp and 20-3Hz Stepsine gave the furthest dispersion curves up to 800 ft in wavelength while 20Hz Ricker performed better at short wavelength range from 50 to 250 ft in wavelength due to its wide-spread energy spectrum. The 8-20Hz Chirp can provide a reliable field dispersion curve ranging from about 120 to 350 ft in wavelength. Experimental dispersion curves generated by all four source signals show the existence of second mode.

Overall, it is shown that frequency span of input source plays a dominant role in affecting the shape of experimental dispersion curve as results of MASW method. Sledge hammer alone can not provide enough energy to test a long array with large spacing and consequently yield misleading result. A 20Hz Ricker wavelet as the input source generate dispersion curve at an intermediate wavelength range. Chirp and Stepsine with low

142
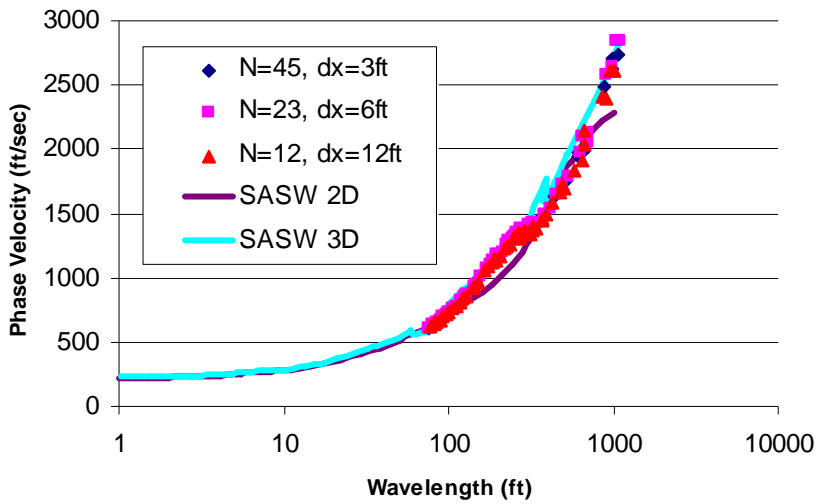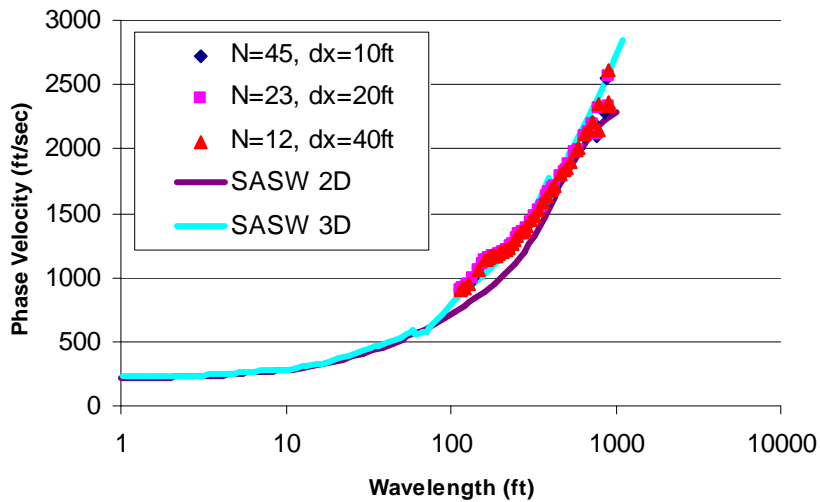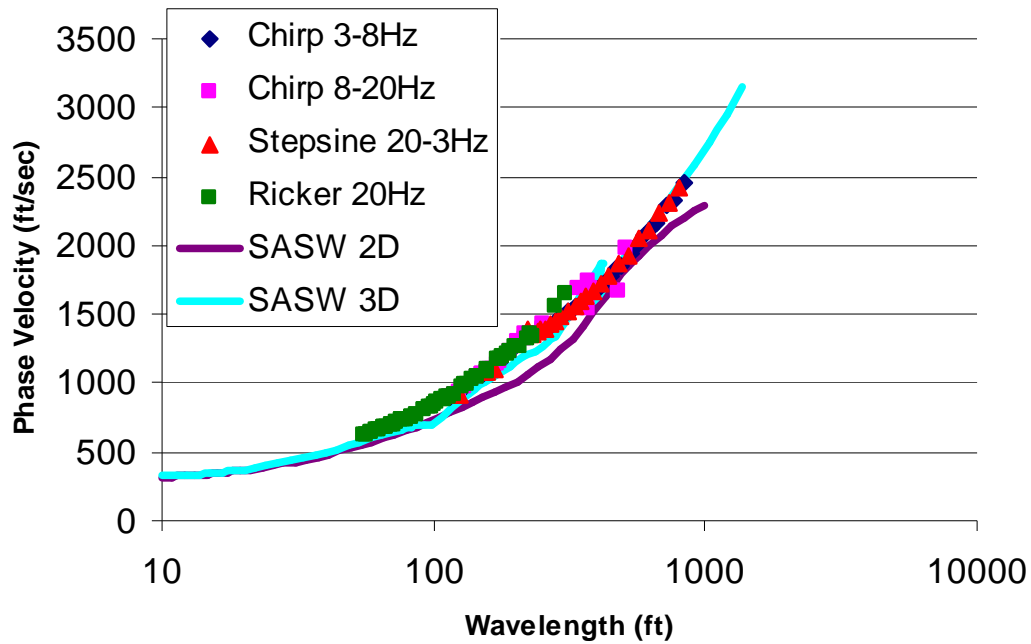
Figure 6.49   Comparison of SASW 2-D and 3-D Theoretical Dispersion Curves with
MASW Fundamental Dispersion Curves with Various Source Signals at -
49.2 ft (-15 m), a 16.4-ft (5-m) Receiver Spacing and 41 Geophones

frequency span can measure deep material, depending on lowest frequency component it
generates. To conclude, T-Rex is a power source that can generate energy in various
frequency contents. However, input signal should be chosen wisely to achieve a pleasant
result at proposed measurement range.

6.3.3.3 Receiver Number Comparison

In this section, field experimental dispersion curves from MASW test during the
first trip are presented while sources are placed at -49.2 ft (-15 m) with a receiver spacing
of 16.4 ft (5 m). Three sets of geophone number are used: 41, 21 and 11, which
correspond to a total length of 656.2, 328.1 and 164 ft (200, 100 and 50 meters). Two
source signals, a 3-8Hz Chirp and a 20Hz Ricker, are used as illustration. Again, MASW

experimental dispersion curves are first compared with their equivalents from SASW. Then, 2-D and 3-D theoretical dispersion curves are used as references for MASW curves to compare.

Figure 6.50 shows MASW experimental dispersion curves measured with a 5 meter receiver spacing, a 3-8Hz Chirp source signal and three different geophone numbers: 41, 21 and 11.
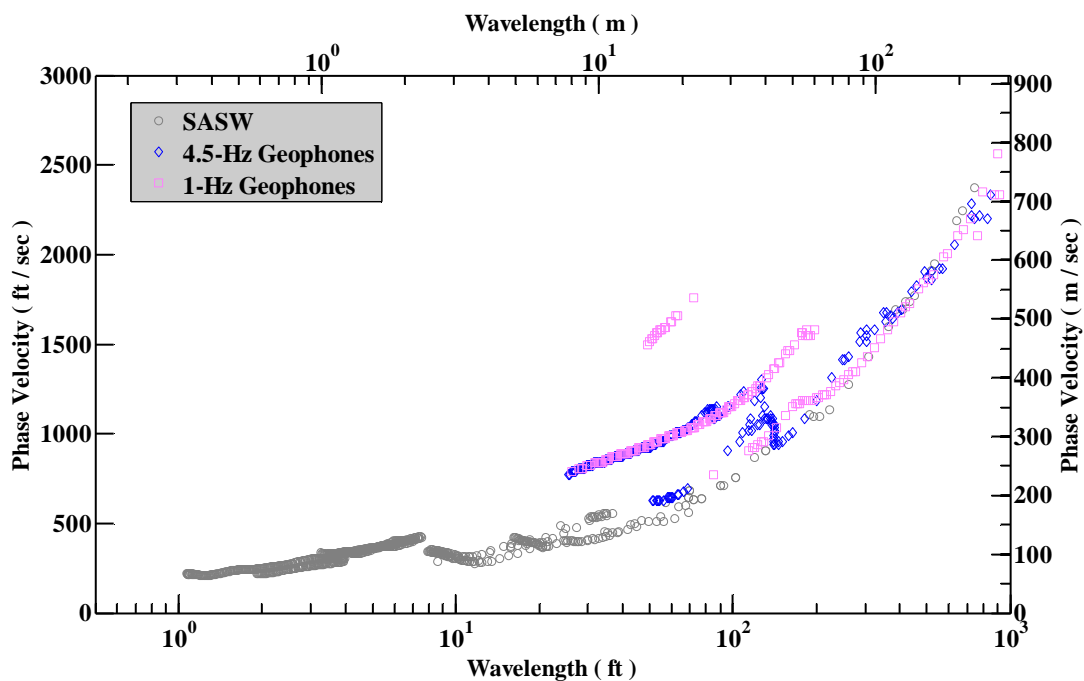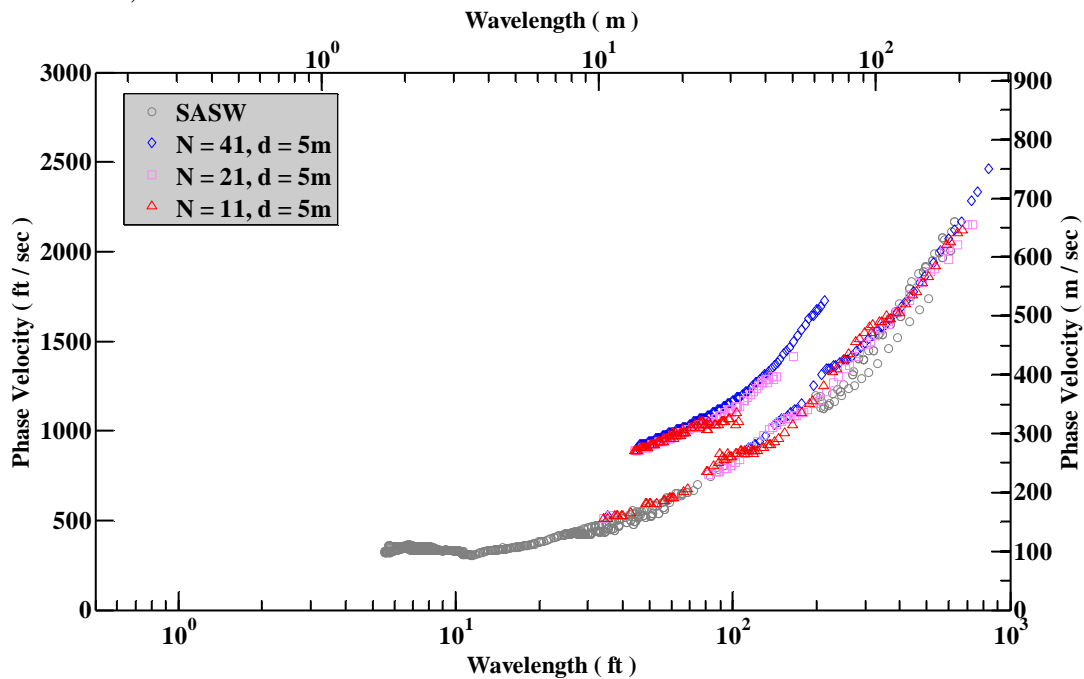

Figure 6.50   Comparison of Experimental Dispersion Curves between SASW Tests and MASW Tests Measured with a 3-8Hz Chirp as source signal at -49.2 ft (-15 m), a 16.4-ft (5-m) Receiver Spacing and 41, 21 and 11 Geophones

The difference of experimental dispersion curves generated by three set of receivers is clearly shown in Figure 6.50. A total of 41 geophones with a 16.4-ft (5-m) spacing cover a total length of 656.2 ft (200 m). The maximum exploring wavelength for this setup at fundamental mode is about 800 ft. The 41-geophone setup also provides the longest measurement at second mode in terms of wavelength. The setup with 21

144

geophones yields the second longest measurement on fundamental mode, ranging from 80 to 700 ft in wavelength. The setup with a total of 11 geophones used in MASW analysis provides similar results as 21 geophones. The shortest wavelength that all of the three setups can reveal is about 40 ft. It is noted that difference among three setups attributes to lateral variability. The comparison between MASW experimental dispersion curves and SASW 2-D and 3-D curves are shown in Figure 6.51.
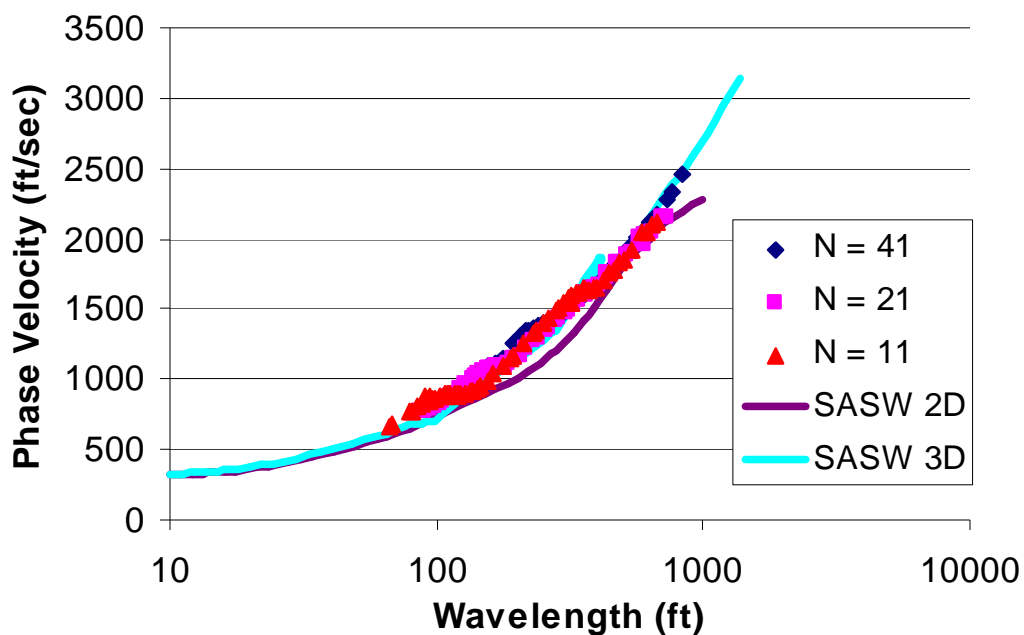
Figure 6.51 Comparison of SASW 2-D and 3-D Theoretical Dispersion Curves with MASW Fundamental Dispersion Curves with a 3-8Hz Chirp as source signal at -49.2 ft (-15 m), a 16.4-ft (5 m) Receiver Spacing and 41, 21 and 11 Geophones

Generally, the fundamental dispersion curves from three setups agree well with SASW 3-D solution on most part of its wavelength range. The first setup, N = 41, successfully capture the trend of 3-D theoretical dispersion curve at large wavelength (>

750 ft). The second and third setup (N = 21 and 11) produce dispersion curves which are slight slower than the 3-D solution.

Figure 6.52 shows the comparison between SASW and MASW experimental dispersion curves measured with a 16.4-ft (5-m) receiver spacing, a 20Hz Ricker source
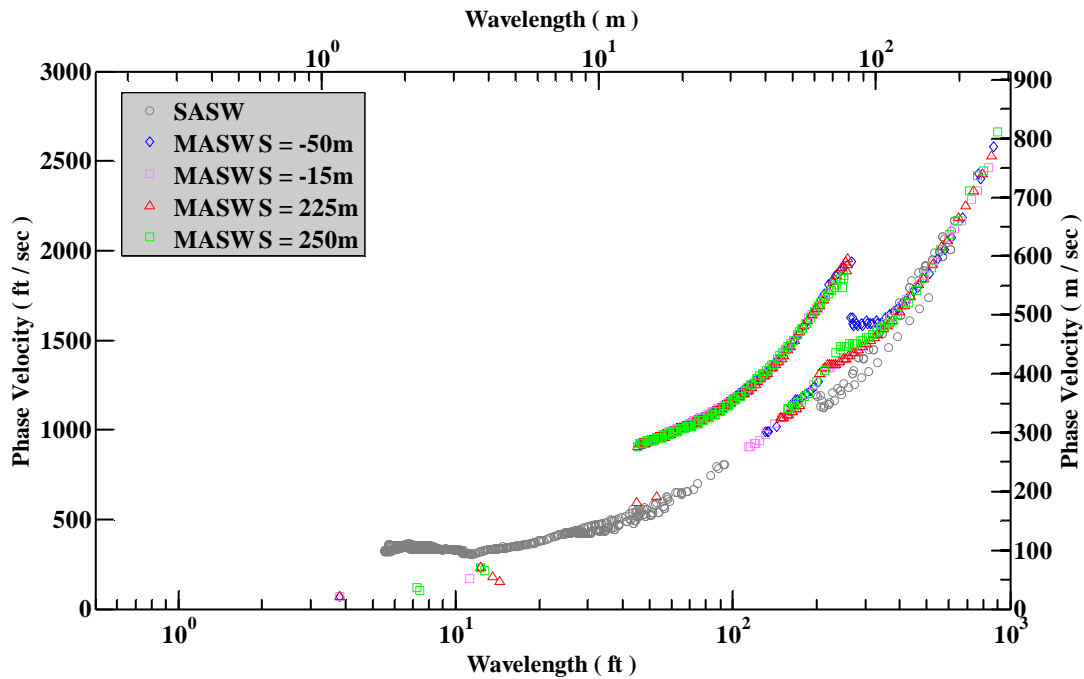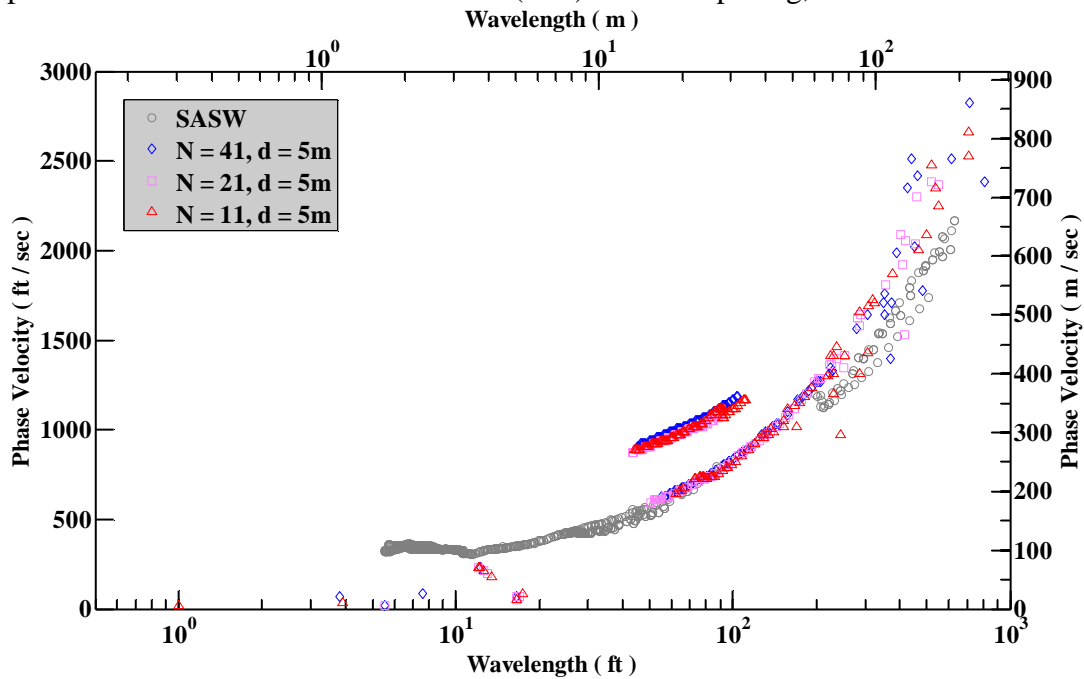

Figure 6.52   Comparison of Experimental Dispersion Curves between SASW Tests and MASW Tests Measured with a 20Hz Ricker as source signal at -49.2 ft (-15 m), a 16.4-ft (5-m) Receiver Spacing and 41, 21 and 11 Geophones

signal and three different geophone numbers: 41, 21 and 11.

It is observed that all three setups yield similar results. The usable wavelength range for them is from 50 to 200 ft at fundamental mode. When wavelength exceeds 200 ft, the experimental dispersion curves acquired from all three setups become scattered and hard to recognize a clear trend like SASW results. Comparison between SASW theoretical solutions and MASW fundamental modes for three setups is shown in Figure 6.53. All fundamental dispersion curves from MASW method overlap with SASW 3-D

146

solution. However, none of them reveal both shallow and deep material information due to the limited frequency band of the input source signal (20 Hz Ricker). It is again demonstrated that source energy and frequency content have a dominant contribution in formation of experimental dispersion curve for surface wave test.
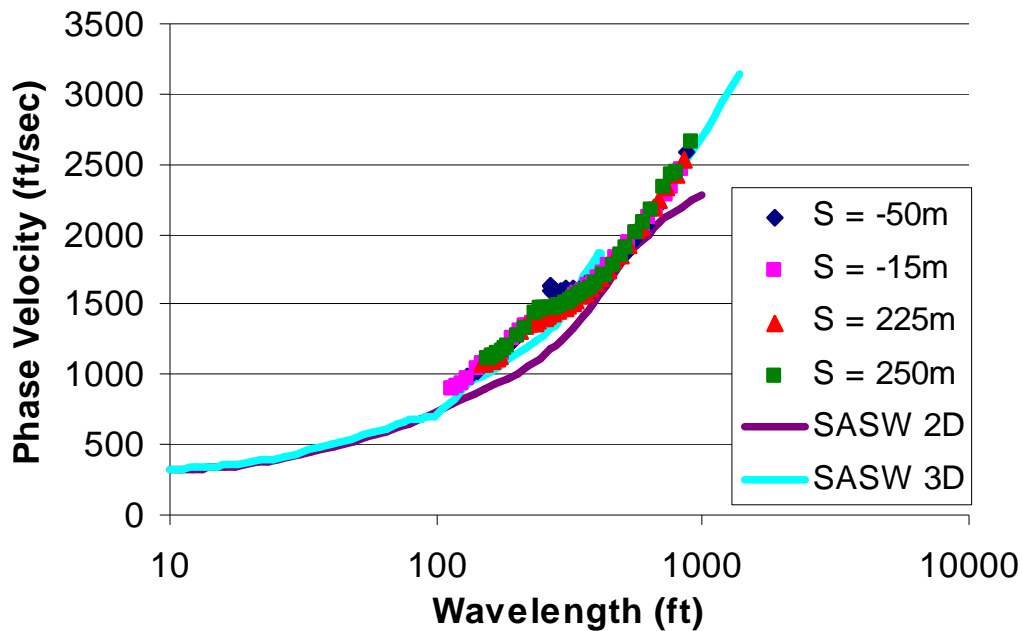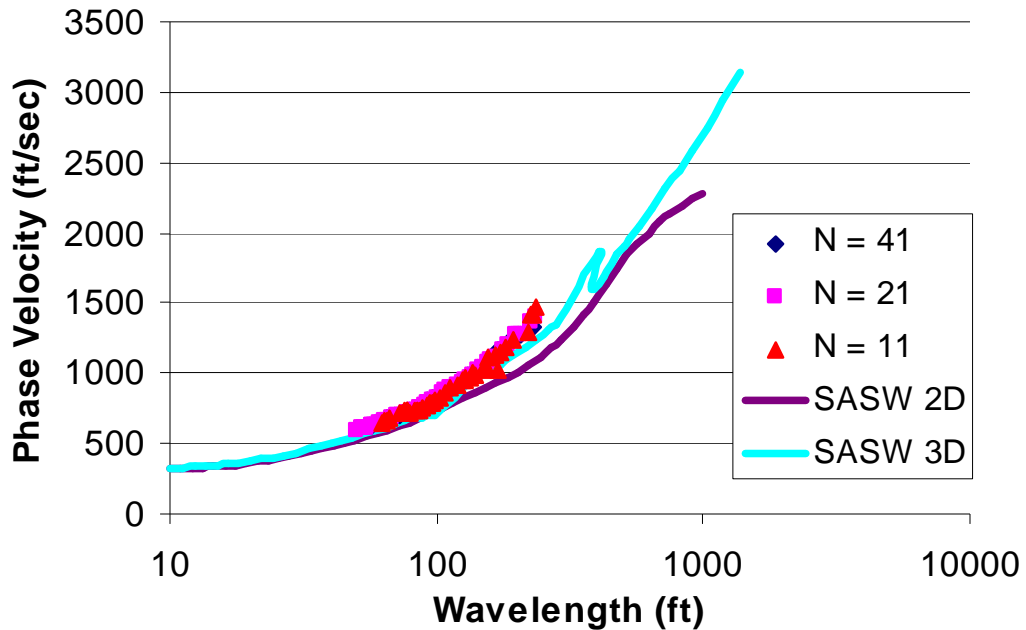

Figure 6.53   Comparison of SASW 2-D and 3-D Theoretical Dispersion Curves with MASW Fundamental Dispersion Curves with a 20Hz Ricker as source signal at -49.2 ft (-15 m), a 16.4-ft (5-m) Receiver Spacing and 41, 21 and 11 Geophones

6.3.3.4 Receiver Spacing Comparison

In this section, the effect of receiver spacing on shape of field experimental dispersion curves from MASW test is discussed based on field parametric study. A 3-8Hz chirp source signal was used. Seismic source was placed at -49.2 ft (-15 m) while the total test array is 656.2 ft (200 m) with varied receiver spacings. Three setups of spacing are used: 16.4, 32.8 and 65.6 ft (5, 10 and 20 m), which correspond to a total receiver

number of 41, 21 and 11. As mentioned earlier, MASW experimental dispersion curves are first compared with their equivalents from SASW. The SASW 2-D and 3-D theoretical dispersion curves are then used as references for MASW curves to compare.

Figure 6.54 shows the comparison between SASW and MASW experimental dispersion curves. It is generally known that larger receiver spacing induce severer spatial aliasing. As observed, all three setups produce similar fundamental mode curves at larger wavelength (up to 800 ft). The shortest usable data on fundamental mode is about 130 ft for all of them. The geophone spacing only affects the data on the second mode at short side of the wavelength range. As observed, the setup with $N = 41$ produces a clear second mode curve down to 40 ft as illustrated in Figure 6.54. A $N = 21$ setup yields a lower boundary of second mode to about 60 ft. The $N = 11$ setup gives second mode curves only from 150 ft. All three setups produce second mode curves up to 280 ft in wavelength.

Figure 6.55 shows the comparison between SASW theoretical and MASW fundamental dispersion curves from three setups with varying geophone number. A good overlap between SASW 3-D and MASW fundamental curves is generally observed except at the range between 170 to 330 ft in wavelength where all MASW curves are slight higher than the 3-D solution, which attributes to the lateral variability of the site. It is noted that all setups capture the trend of 3-D theoretical dispersion curve. This phenomenon is well explained because all test setups cover the total 656.2 ft (200 m) test array. All MASW fundamental curves start at about 110 ft in wavelength, indicating a finer receiver spacing is required to measure material at shallower depth.

To conclude, for the MASW tests with different receiver spacing, generally they produce similar results on the fundamental mode of experimental dispersion curves. A
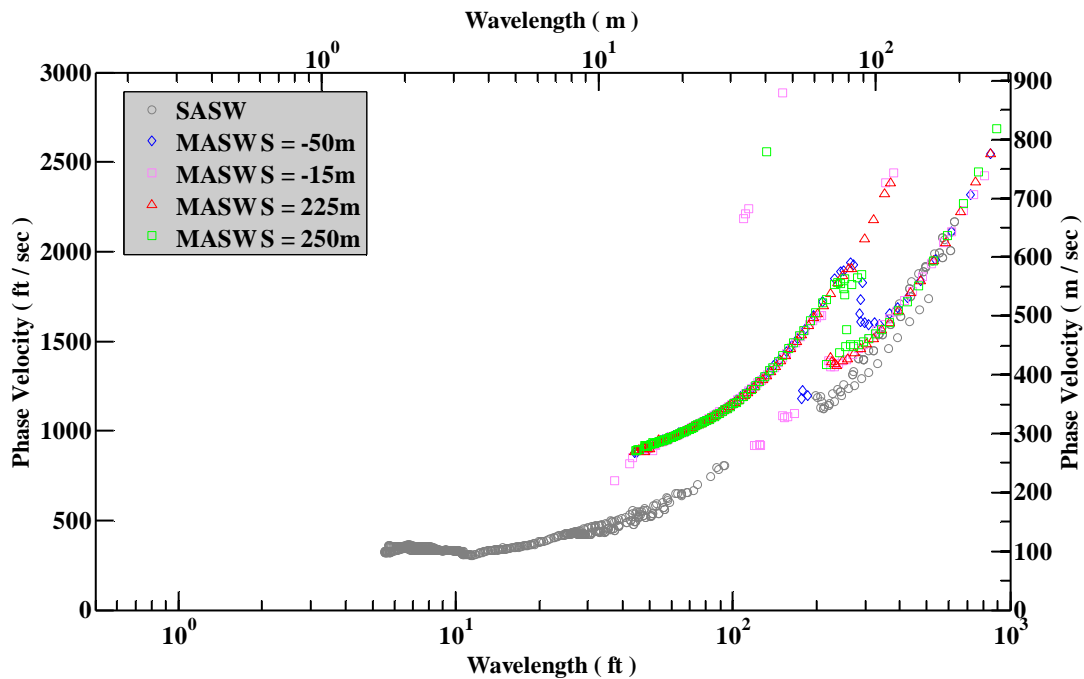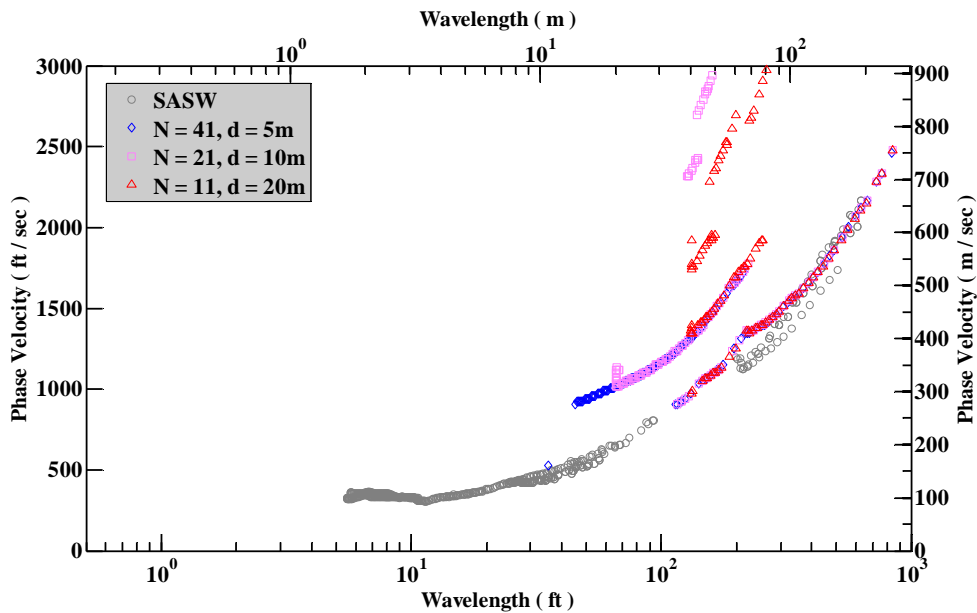
Figure 6.54   Comparison of Experimental Dispersion Curves between SASW Tests and MASW Tests Measured with a 3-8Hz Chirp as source signal at -49.2 ft (-15 m), 16.4, 32.8 and 65.6 ft (5, 10 and 20 m) as Receiver Spacing and a 656.2 ft (200 m) Test Array
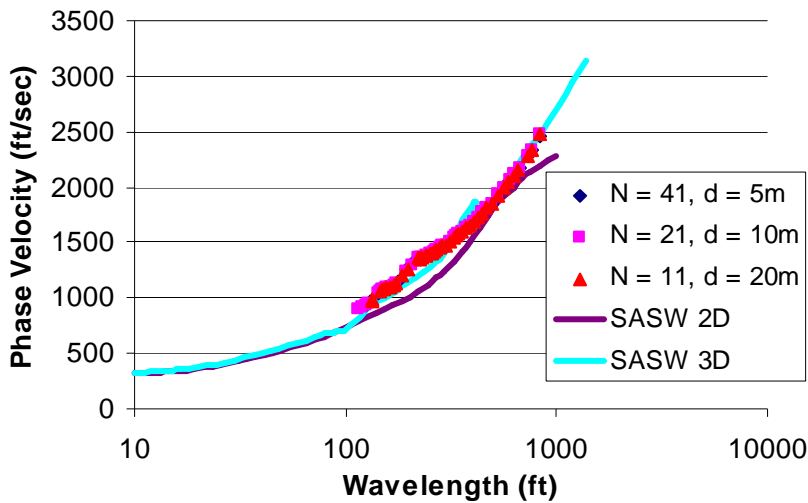
Figure 6.55   Comparison of SASW 2-D and 3-D Theoretical Dispersion Curves with MASW Results Measured with a 3-8Hz Chirp as source signal at -49.2 ft (-15 m), 16.4, 32.8 and 65.6 ft (5, 10 and 20 m) as Receiver Spacing and a 656.2 ft (200 m) Test Array

finer receiver spacing, in this test setup, will only improve the data range on the second mode.

6.4 FORWARD MODELLING

It is important to note that existing inversion algorithm may not be compatible with the dispersion curve obtained from beamforming technique since beamforming estimates a modal phase velocity rather than an apparent phase velocity (Zywicki and Rix, 2005). However, based on the results from numerical simulation and field test, beamforming produced similar results as SASW test. Based on Wood's finding (Wood, 2009), the 3-D model of WinSASW was able to predict the higher mode behaviour of some of the multi-channel dispersive data. The use of WinSASW 3-D solution is probably an better approximation of the matching progress for the fundamental dispersion curve. In this context, both the WinSASW 3-D and 2-D solution are used to match the fundamental dispersion curve from MASW testing for comparison.

Like SASW testing procedure, the dispersion curves of MASW tests from different sources and receiver spacings can be combined to construct a composite experimental dispersion curve, as illustrated in Figure 6.56. The curves are from three different test setups, a sledge hammer with a 3-ft receiver spacing for short wavelengths, a 3-8 Hz chirp signal and a 10-ft receiver spacing for intermediate wavelengths, and a 1-8Hz chirp signal and a 10-ft receiver spacing for large wavelengths. The 3-D solution is used to fit the MASW composite experimental dispersion curve as shown in Figure 6.57. A maximum wavelength of 1335 ft is reached by the 1-8Hz stepsine signal. The V_s profile from the matched 3-D solution to the composite dispersion curves is shown in Figure 6.58. The parameters used to generate the V_s profile is shown in Table 6.3.

The MASW composite dispersion curve is compared to the SASW experimental
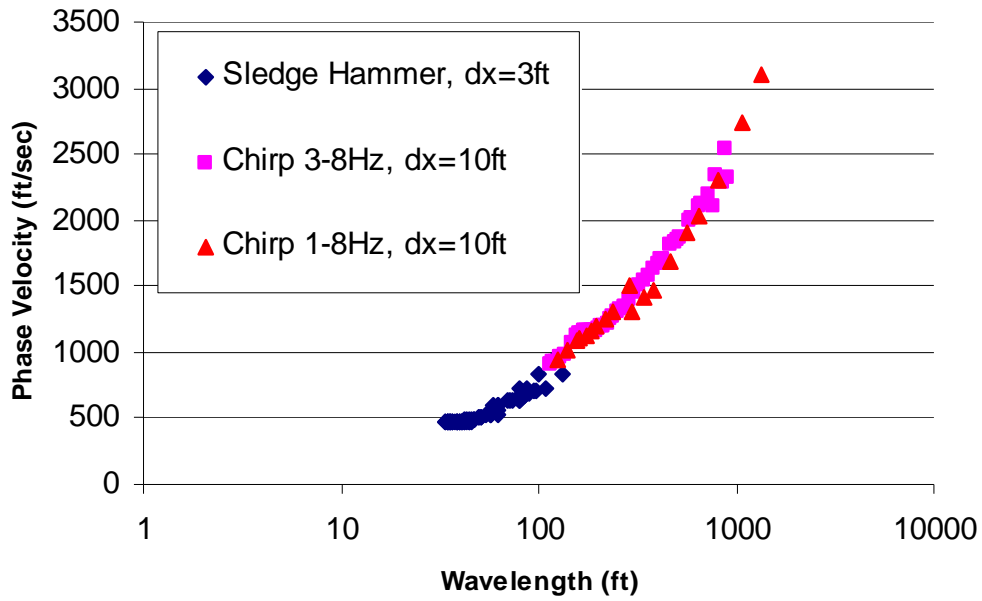
Figure 6.56 The MASW Composite Dispersion Curves from Three Setups
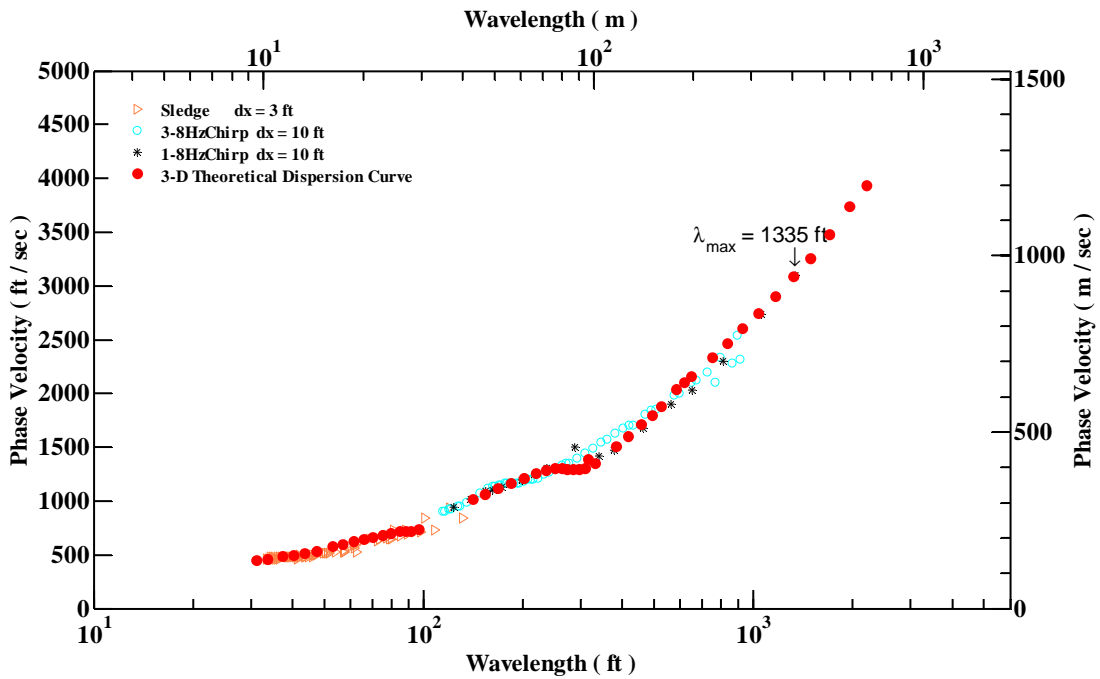
Figure 6.57 The Matching between the 3-D Theoretical Dispersion Curves to the Composite Experimental Dispersion Curves from Three MASW Testing Setups

151
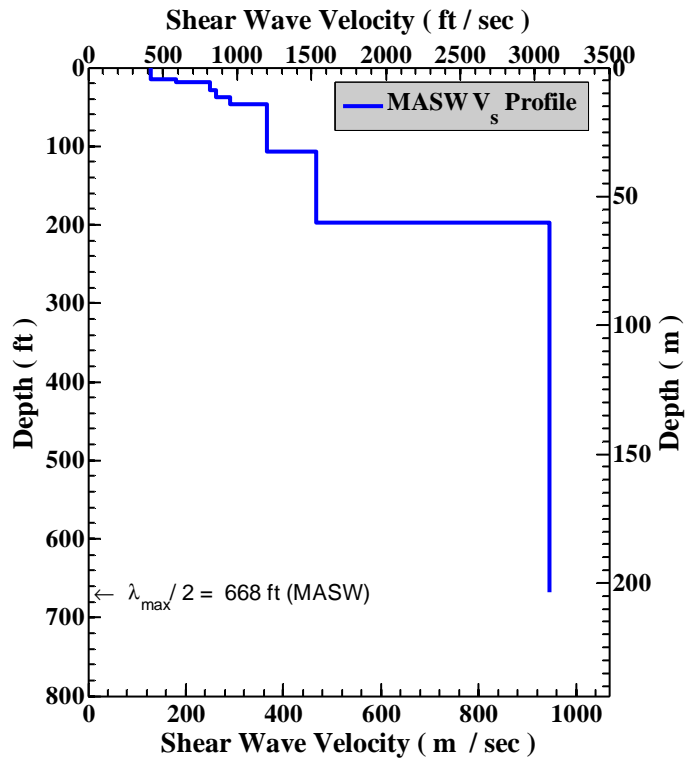
Figure 6.58   Shear Wave Velocity Profile from Matching the 3-D Solution to the MASW
Composite Dispersion Curve

Table 6.3   Profile Parameters Used to Develop the 3-D Theoretical Dispersion Curve
for the MASW Composite Dispersion Curves

Layer No.	Thickness, ft	Depth to Top of Layer, ft	P-Wave Velocity, ft/s	S-Wave Velocity, ft/s	Assumed Poisson's Ratio	Assumed Total Unit Weight, pcf
1	15	0	834 [o]	420	0.33	100
2	4	15	1171 [o]	590	0.33	100
3	10	19	1628 [o]	820	0.33	100
4	8	29	1707 [o]	860	0.33	100
5	9	37	1886 [o]	950	0.33	100
6	60	46 [◊]	5000	1200	0.47 [+]	120
7	90	106	5000	1530	0.45 [+]	120
8	Half Space	196	5369	3100	0.25	120

[o] P-wave velocity calculated from V_s and assumed value of Poisson's ratio.
[◊] Water table assumed at a depth of 46 ft
[+] Not assumed but back-calculated from $V_p = 5000$ fps and V_s

152
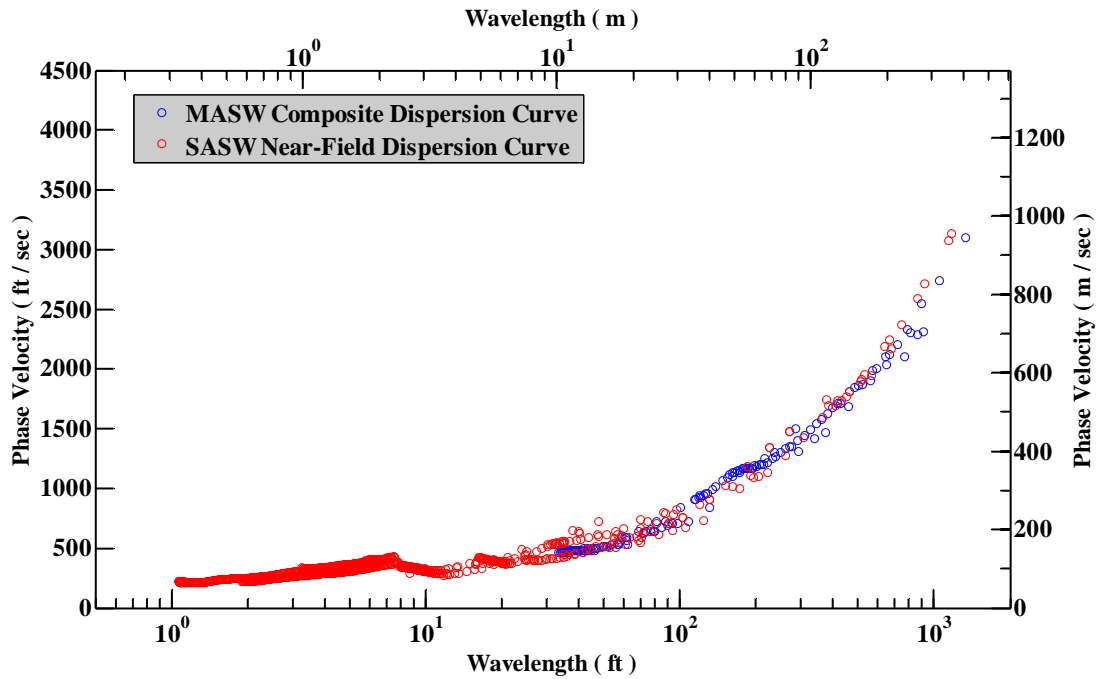
Figure 6.59 Comparison between the SASW Experimental Dispersion Curves with
Near-Field Data and the Composite Experimental Dispersion Curves from
Three MASW Testing Setups

dispersion curves with near-field data from the second trip in Figure 6.59. The corresponding V_s profile to this composite dispersion curve is compared to the V_s profile from SASW testing with near-field data during the second trip, as shown in Figure 6.60. At larger wavelength (about 1000 ft) in Figure 6.59, the near-field data from SASW analysis predicts a higher phase velocity than the MASW analysis does.It is seen in Figure 6.60 that two testing techniques yield similar value down to about 100 ft. The shear wave velocity profile from the SASW tests with near-field data predicts a slightly shallow depth to the "bedrock- like" material about 160 ft with a V_s value of 3500 fps. The composite MASW data predicts the depth to the "bedrock-like" material as 200 ft with a value of 3100 fps. It is also noted that the top 15-ft material of the MASW V_s

profile is assumed to have a constant value since no resolution of experimental dispersion curve existed from the MASW analysis.

The 2-D WINSASW theoretical solution is also used to match the MASW composite dispersion curve as shown in Figure 6.61. The resulting V_s profile based on the matching with 2-D theoretical dispersion curve is shown in Figure 6.62. The parameters used to generate the V_s profile is shown in Table 6.4. It is seen that both the depth and V_s value of the "bedrock-like" material from the 2-D fitting are different from the 3-D fitting. The main difference occurs at the deep depths.
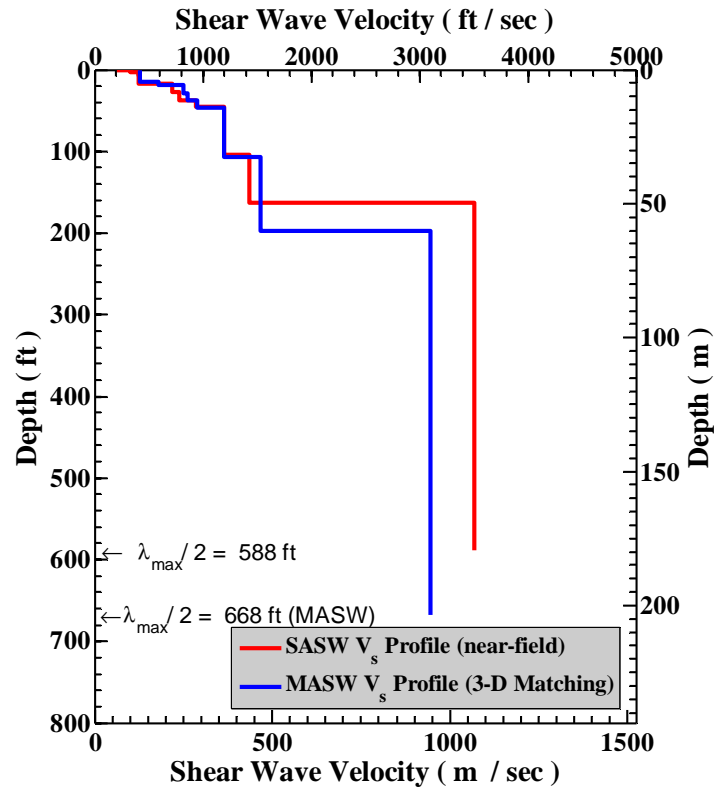
Figure 6.60 Comparison between Shear Wave Velocity Profiles from SASW Testing with Near-Field Data and MASW Testing with Composite Data

154
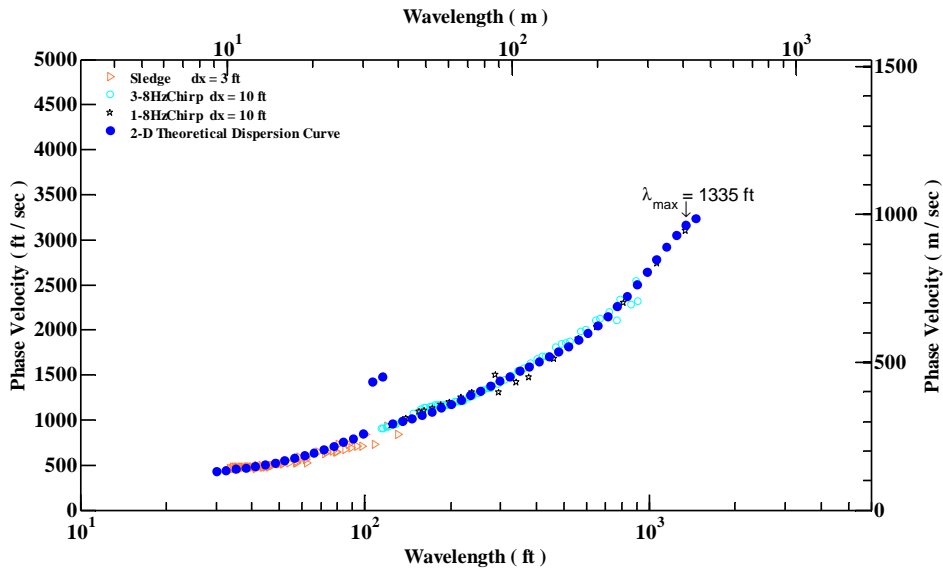
Figure 6.61   The Matching between the 2-D Theoretical Dispersion Curves to the
Composite Experimental Dispersion Curves from Three MASW Testing
Setups
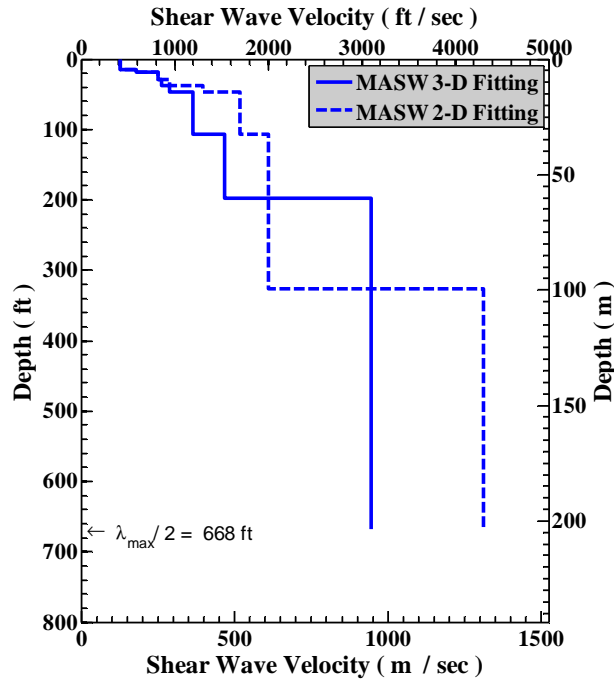
Figure 6.62   Comparison of Shear Wave Velocity Profiles from Matching the 3-D and 2-
D Solutions to the MASW Composite Dispersion Curve

155

Table 6.4   Profile Parameters Used to Develop the 2-D Theoretical Dispersion Curve
for the MASW Composite Dispersion Curves

Layer No.	Thickness, ft	Depth to Top of Layer, ft	P-Wave Velocity, ft/s	S-Wave Velocity, ft/s	Assumed Poisson's Ratio	Assumed Total Unit Weight, pcf
1	15	0	834 [o]	420	0.33	100
2	4	15	1171 [o]	590	0.33	100
3	10	19	1628 [o]	820	0.33	100
4	8	29	1886 [o]	950	0.33	100
5	9	37	2581 [o]	1300	0.33	100
6	60	46 [◊]	5000	1700	0.43[+]	120
7	220	106	5000	2000	0.40[+]	120
8	Half Space	326	7448	4300	0.25	130

[o] P-wave velocity calculated from V_s and assumed value of Poisson's ratio.
[◊] Water table assumed at a depth of 46 ft
[+] Not assumed but back-calculated from $V_p = 5000$ fps and V_s

6.5 DATA INTERPOLATION

6.5.1 Frequency Domain Interpolation

Performing interpolation on a sequence of raw signals is sometimes used in post-processing of field data. From SASW testing, the resolution of a phase plot in frequency domain is controlled by the time interval and number of recorded data points, which is well explained by the Nyquist sampling theorem. If the time domain signal is ill-sampled by insufficient number of points or time interval, there are less usable data point on the wavelength–velocity plot. One way to improve the resolution in frequency domain (interpolation) is "zero padding". The extension of data in one domain results in an increased resolution in the other domain. The most common form of zero padding is to append a string of zero-valued samples to the end of a zero-offseted time-domain sequence. An example of the zero-padded phase plot comparing to the original phase plot is shown in Figure 6.63 (Rosenblad, 2000).

156
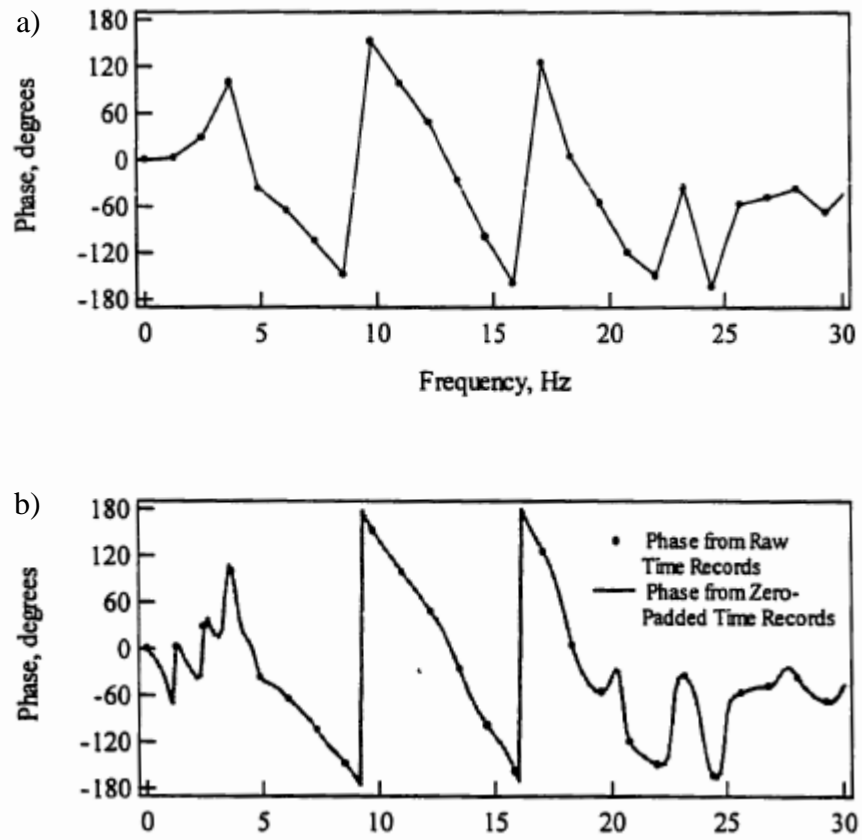
Figure 6.63 Comparison of Phase Plots from (a) Original Time Records and (b) Zero-
Padded Time Records (after Rosenblad, 2000)

6.5.2 Spatial Domain Interpolation

Spatial domain is the procedure of estimating the value of properties at unsampled sites within the area covered by existing measurements, in almost all cases that the interpolated locations must be interval or ratio scaled of the measured locations. The reasoning behind the spatial interpolation is Tobler's first law of geography: "Everything is related to everything else, but near thing are more related than distant things"(Tobler, 1970).

In terms of geophysics, seismic traces are sometimes interpolated at locations without receivers. One of many influential interpolation technique, First-Order-Frequency-Space-Domain interpolation, was proposed by Spitz (1991) to address the data set with spatial aliasing problems. The method is based on the assumption that linear events present in a sequence of signals recorded by equally spaced receivers. The predictability of linear events in the f-x domain allows the missing traces to be expressed as the output of a linear system.

As shown in section 6.3.3.4, the larger the receiver spacing is, the severe the spatial aliasing the test results are (mainly for the second mode). In this section, the 47-channel time domain record for a sledge hammer as the seismic source with a 3-ft spacing is used to study the possibility of recover extra dispersion curve data from the spatial-aliased zone. The original record with 47 channels is shown in Figure 6.64. A receiver spacing of 12 ft is assigned when only channel 1, 5, 9 through 45 (12 channels in total) are used in the MASW analysis, as illustrated in Figure 6.65a. Then, the wavefield is interpolated into 23 channels. The interpolated 23 channels, along with the original 23 channels (Channel 1, 3, 5 through 45), as shown in Figure 6.65b and c, are analyzed to

158
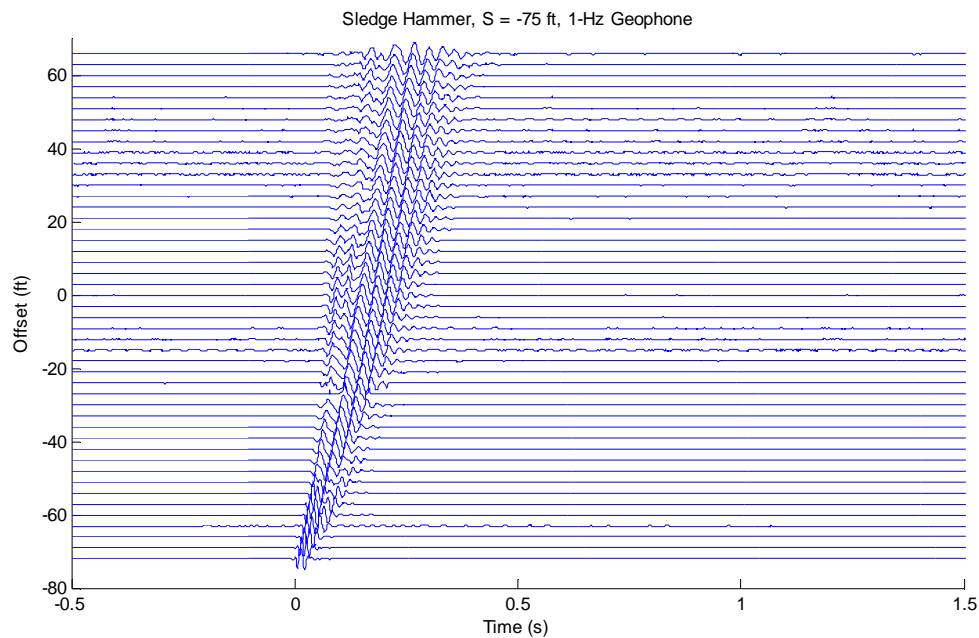
Figure 6.64 Wavefield Collected with a Sledge Hammer, 47 1-Hz Geophones Placed with a 3-ft Spacing

study the effectiveness of interpolation on discovering data hidden by spatial-aliased zone. The corresponding experimental dispersion curves are shown in Figure 6.66. It is seen that the original 23-channel wavefield with a 6-ft receiver spacing produced a wavelength down to about 12 ft, whereas from the wavefield with 12-channel and a 12-ft spacing, the shallowest wavelength on the experimental dispersion curve is about 24 ft. The interpolated 23-channel wavefield with a 6-ft receiver spacing produced similar results to the original 23-channel wavefield with the same spacing, mainly recovered the information of second mode from 12 to 24 ft in wavelength. It is observed that at this site, the spatial interpolation technique can recover some information on higher mode of experimental dispersion curve hidden by test setup with larger receiver spacing, namely spatial aliasing effect.

159
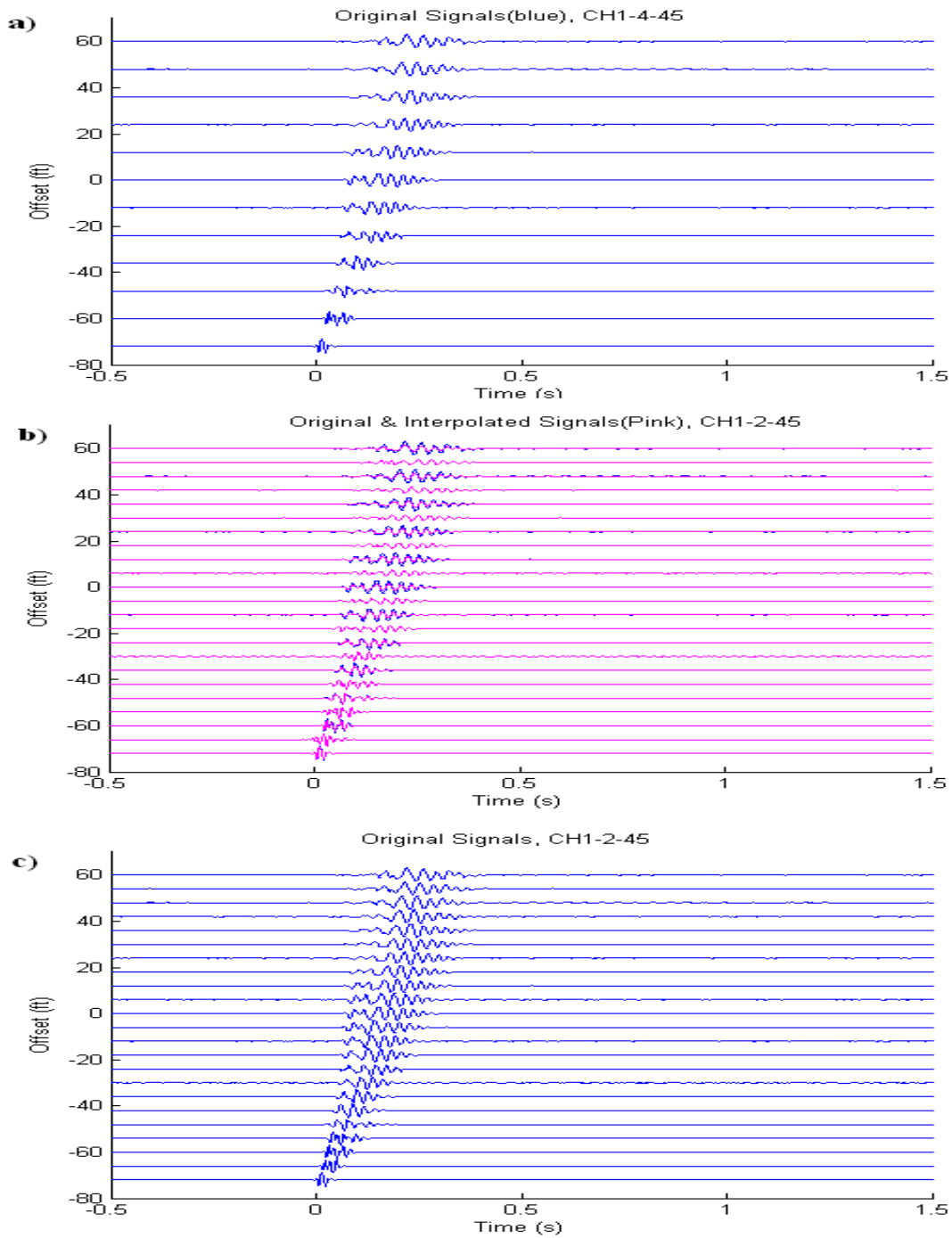
Figure 6.65   Wavefields Used in MASW Analysis with a) Original 12-Channel Signals with a 12-ft Spacing, b) Interpolated 23-Channel Signals with a 6-ft Spacing and 3) Original 23-Channel Signals with a 6-ft Spacing, All Collected with a Sledge Hammer
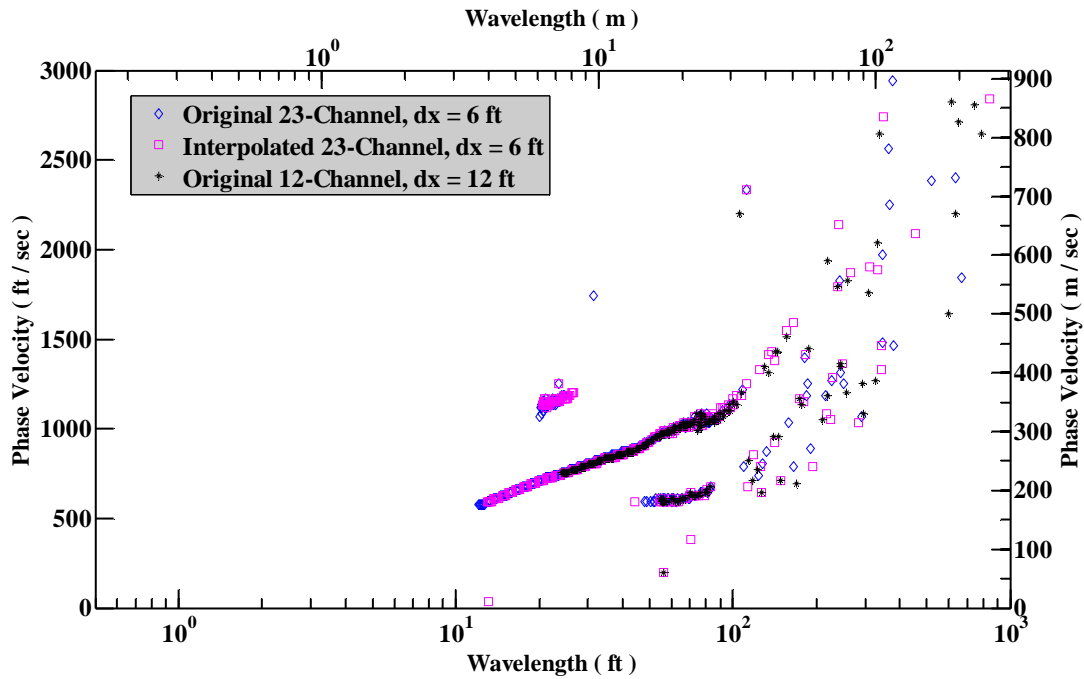
Figure 6.66   Comparison of Experimental Dispersion Curves from a) Original 23-
Channel Wavefield with a 6-ft Spacing, b) Interpolated 23-Channel
Wavefield with a 6-ft Spacing and c) Original 12-Channel Wavefield with a
12-ft Spacing

6.6 EXISTING INFORMATION

In this section, the V_s profile from SASW tests during the second trip is compared
to other relevant geotechnical and geological information at the Hornsby Bend site.

6.6.1 Cone Penetration Tests

The CPT test results at the center of the test array, including sleeve friction (tsf), friction
ratio and cone resistance (tsf), are plotted in Figure 6.67. Based on the CPT results, it is
see that five different types of material at different depth range are revealed by the CPT
method: (1) a soft shallow layer from ground surface to 6 ft deep, (2) a sand-like layer
from 6 to 15 ft, (3) a clay-like layer from 15 to 25 ft, (4) a sand-like layer from 25 to 45 ft
and (5) a stiffer material, which stopped the cone from penetrating, is encountered at 45
ft.
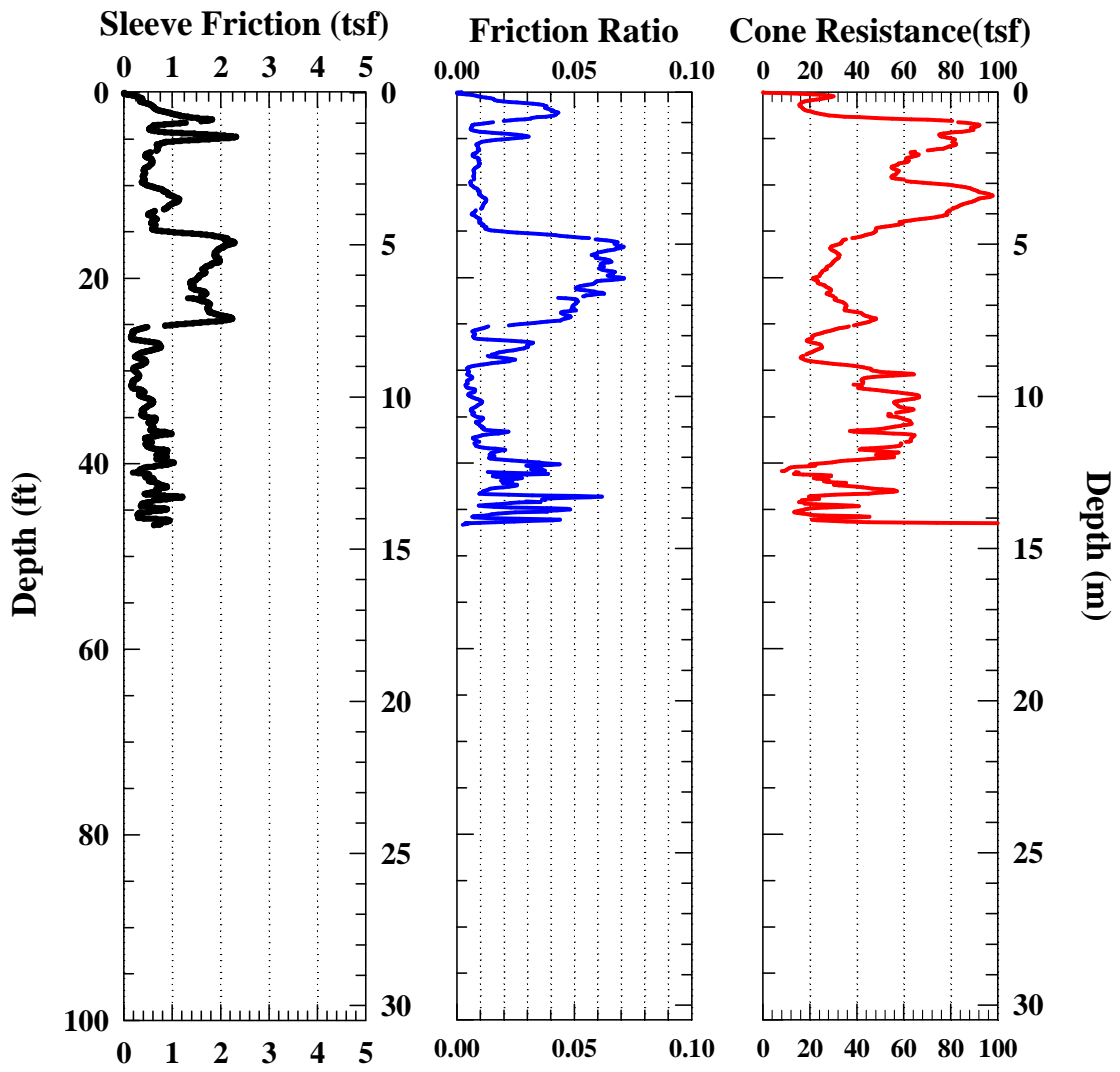
Figure 6.67   Cone Penetration Test Results at the Center of the Test Array
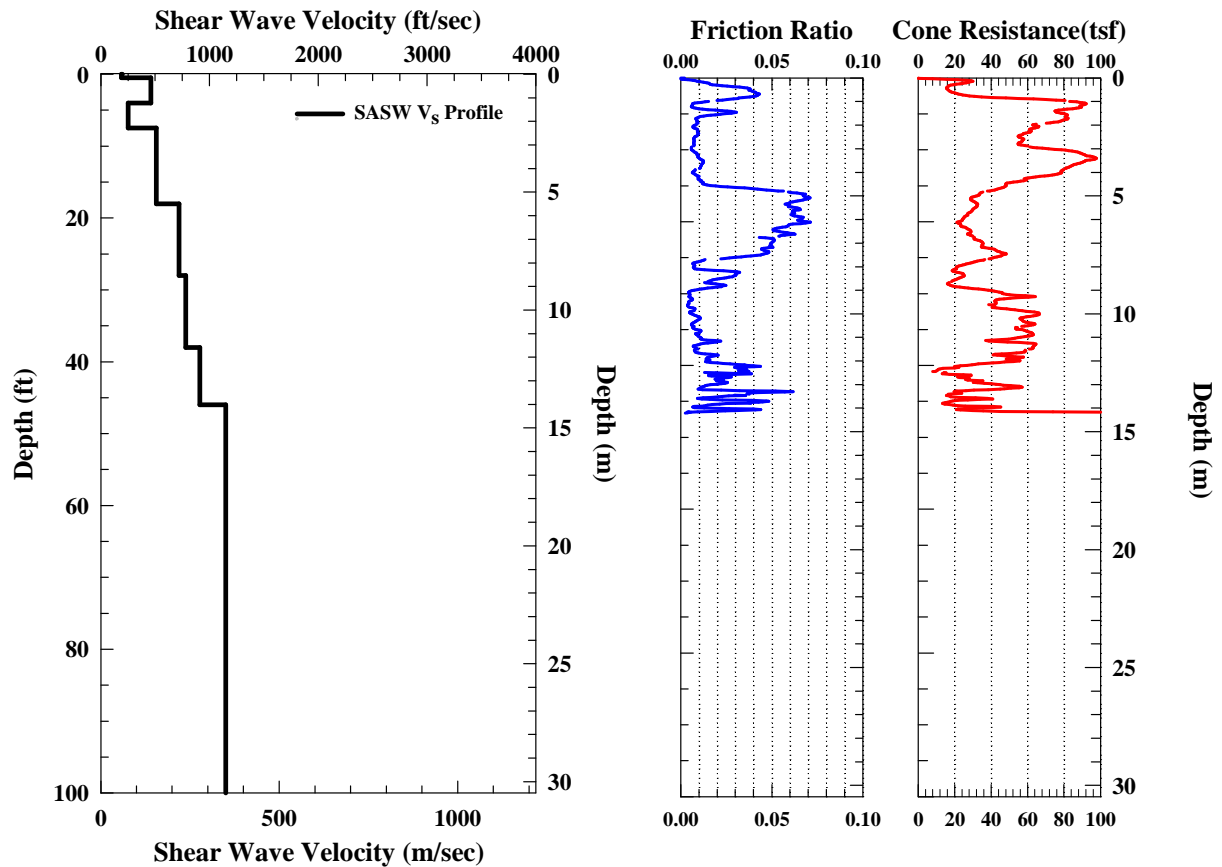
Figure 6.68　Comparison of Cone Penetration Test Results and the SASW V_s Profile at the Center of the Test Array

　　　　The comparison between SASW V_s profile from the second trip and the CPT results is shown in Figure 6.68. It is seen that not like CPT results, the V_s profile presents a graduate increase in shear wave velocity along depth except a small inversion at about 4 to 7.5 ft. One possible explanation of the difference between two tests is that the overburden stress for soft material at depth range of 15 to 25 ft worked as a compensation in shear wave velocity thus no inversion in V_s profile at that depth range is observed.

6.6.2 Borehole Records

Southwestern Laboratories performed a series of boreholes to investigate the site condition at Hornsby Bend for a waste-to-energy plant in 1985 (Rix, 1988). These borings were drilled with a hollow-stem auger and continuous sampling system. A log of a borehole is shown in Figure 6.69. There are four layer which was distinguished by Rix(1988) from the boring: (1) a hard silty clay layer from the surface to 13.5 ft, (2) a hard silty clay layer interbedded with silty fine sand seams from 13.5 to 33.5 ft, (3) a loose to medium dense silty fine sand layer from 33.5 to 45 ft and (4) a hard gray clay layer extending from 45 ft to maximum depth of the boring, 50 ft. The clay layers are part of the Taylor Marl formation. It is seen that the boring records generally agree with the CPT test results.

6.6.3 Borehole Records

Seismic CPT tests were also performed at the center of the test array by Mr. Changyoung Kim. The analyzed V_s profile from SCPT tests is plotted again the shear wave velocity profile from SASW tests in Figure 6.70. It is seen that, in general, the SCPT V_s value is larger than shear wave velocity measured by SASW tests. The difference between two test results can mainly be attributed to the fact that SASW results are globalized measurements of the whole test array while SCPT results only represent localized measurements near the tested hole.

6.7 SUMMARY

In this chapter, the test resulted from both SASW and MASW tests during the first and second trips are discussed. The experimental dispersion curves and V_s profiles from SASW tests are used as reference for MASW test results to compare.
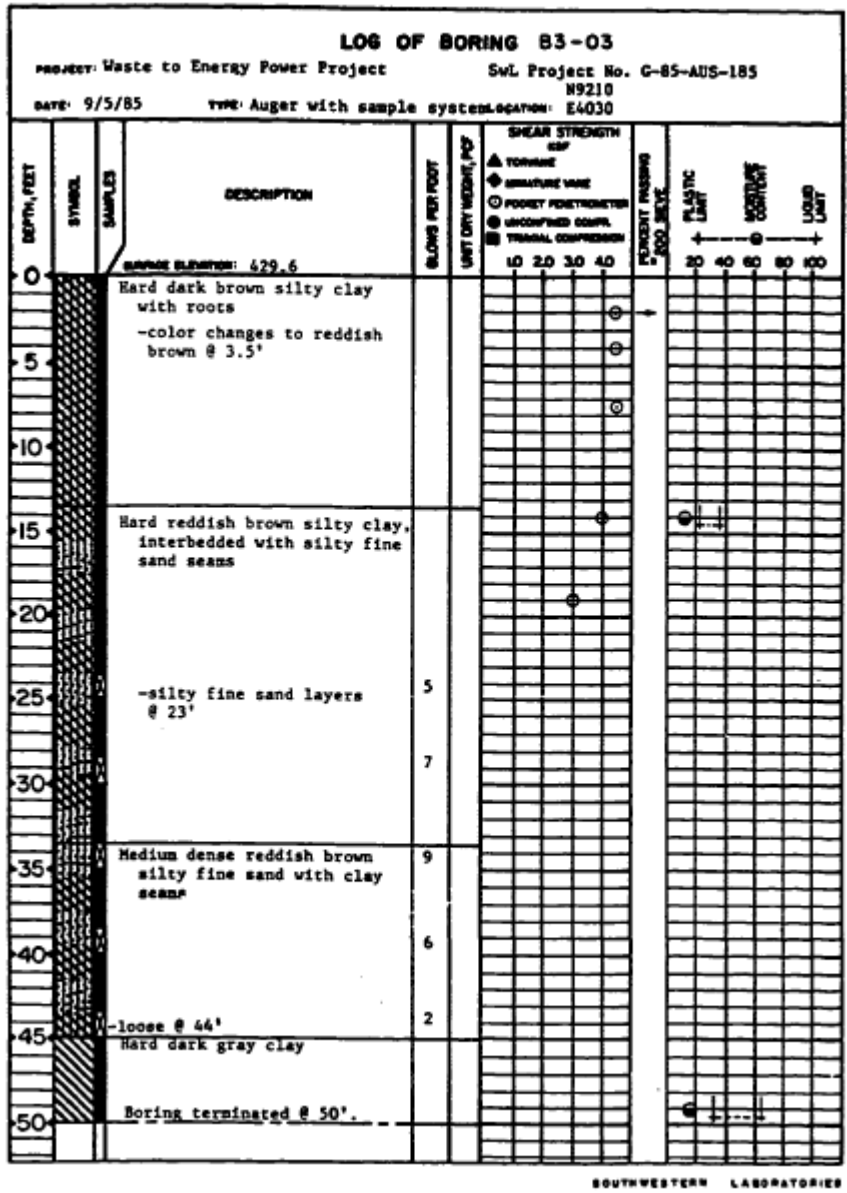
Figure 6.69 Log of a Borehole at the Hornsby Bend Area (from Rix, 1988)
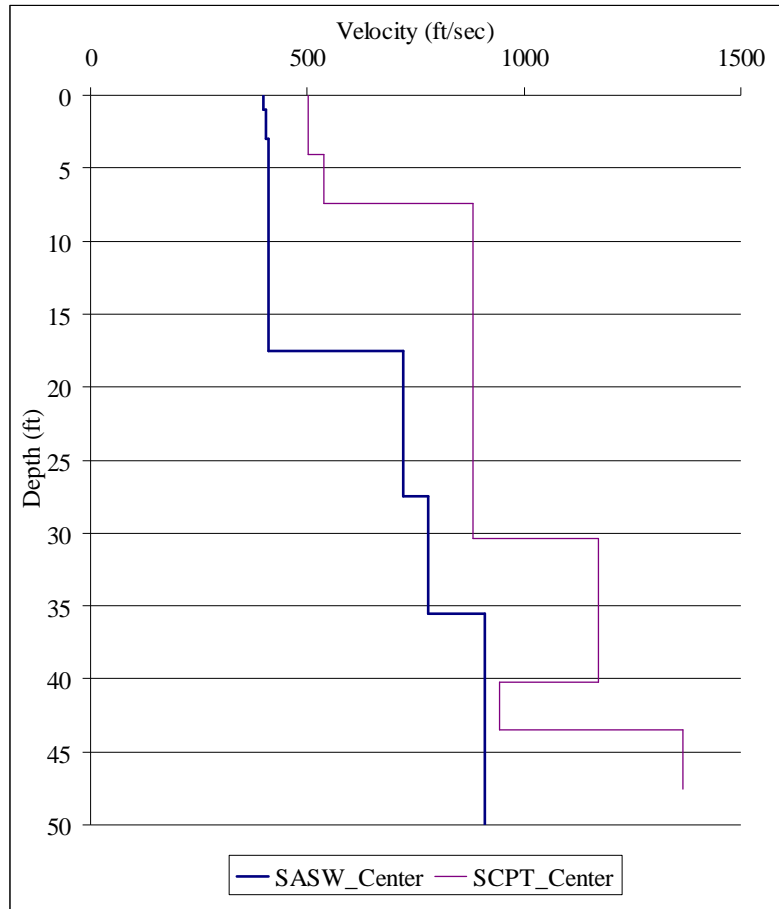
Figure 6.70 Comparison of V_s Profile from SASW and SCPT tests at the Center of the Test Array (Courtesy of Kim)

A standard MASW test setup, composed of a 12-lb sledge hammer, 24 geophones with a receiver spacing of 3 ft, was used to study the performance of this setup in charactering material properties at the Hornsby Bend site. It is found that the setup was able to provide a robust estimate of experimental dispersion curve from about 30 to 100 ft in wavelength by comparing it to the experimental dispersion curve from SASW tests. Thus, the materials at the depths between 15 to 50 ft can be characterized based on the assumption that depth equals to one half of wavelength. At this site, it is difficult for the

traditional MASW test setup to explore material shallower or deeper than the range mentioned above.

The source offset was altered to study the impact of source-receiver distance on the experimental dispersion curves of MASW tests. It is observed that as the source moved away from the first geophone, the number of usable data point on the fundamental dispersion curves decreased. Also, there is less information presented at short wavelength when larger source offset was used. This phenomenon is observed in both the test setups with 3-ft and 10-ft receiver spacings and a sledge hammer, and the test setup with a 16.4 –ft (5-m) receiver spacing and T-Rex as the seismic source. It is concluded that source offset does impact the shape of resulting dispersion curve by: reducing the number of usable data on the fundamental mode of experimental dispersion curve when the offset increases, and vice versa.

The source type were also studied by switching different input source signal with various frequency contents while maintaining the rest parameters of the MASW testing setup (source offset, geophone spacing, geophone type and number of receiver). Beside the hammer impact, signals generated by either Liquidator (for 3-ft and 10-ft spacings) or T-Rex (for 16.4-ft spacing) were studied. They were four different chirp signals (3-8 Hz, 8-20 Hz, 20-25 Hz and 25-35 Hz), one 20-Hz Ricker wavelet and two stepsine signals (100-10Hz and 20-3Hz). In addition, a 80-1 Hz stepsine was used with a 10-ft spacing to investigate deeper materials. It is observed that source type plays a dominant role in defining the shape of experimental dispersion curve. The 12-lb sledge hammer produced the limited data of the fundamental-mode curve at short wavelength (30 – 100 ft); the 20-Hz Ricker and 8-20 Hz chirp generated reliable dispersion curves at intermediate range in terms of wavelength (40 – 200 ft); the 3-8 Hz chirp and 20-3 Hz stepsine produced

similar results at larger wavelength (100 to 700 ft); and the maximum reliable wavelength, about 1400 ft, was acquired by a source signal of 80-1 Hz stepsine.

The number of receiver was changed with the same receiver spacing to study its impact on MASW test results. For the second trip, four sets of receivers (12, 24, 36 and 47 geophones) were compared with both 3-ft and 10-ft spacings. It is seen that with the 3-ft spacing, the dispersion curves are different from each other when different numbers of receivers were used, and none of them agree with the SASW results from about 200 to 800 ft in wavelength, which attributes to the lateral variability of the site. The different test setups with a 10-ft spacing produced similar results and agree well with the SASW measurements. For the first trip, three sets of receivers (11, 21 and 41) were used with a 16.4-ft spacing. In these test setups, the resulting dispersion curves agree well with the SASW measurements. Also, it is observed that the setup with larger number of receiver measured deeper material, while the setup smaller number of receiver produced more information about the shallow materials. To conclude, the MASW test setups with different number of receiver produced similar results as SASW tests, when large geophone spacings were used (10-ft and 16.4-ft). The reason that different test setups with a 3-ft receiver spacing does not agree well with SASW measurements may attribute to lateral variability of the site, or the incapability of the test setup to characterize deep material with a short test array.

The influences of receiver spacing on the dispersion curves can be studied by comparing the results with the same total test array but varying receiver spacing. For the second trip, two experiments were studied based on the measurement with 47 geophones as well as 3-ft and 10-ft spacings. A test array with a total length of 132 ft was constructed with the following three setups: 45 receivers and a 3-ft spacing, 23 receivers and a 6-ft spacing, 12 receivers and a 12-ft spacing. The second test array with a total

length of 440 ft was constructed by: 45 receivers and a 10-ft spacing, 23 receivers and a 20-ft spacing, 12 receivers and a 40-ft spacing. For the first trip, a test array with a total of 656.2-ft (200-m) was used with three setups: 41 receivers and a 16.4-ft spacing, 21 receivers and a 32.8-ft spacing, 11 receivers and a 65.6-ft spacing. All tests show that larger receiver spacing results in severer spatial aliasing in the f-k plots. However, the fundamental mode of dispersion curves were less influenced by the spatial aliasing induced by an increased receiver spacing than the higher mode of dispersion curves.

Two types of receiver, 1-Hz geophone and 4.5-Hz geophone, were used to study the influence of geophone type on test results. Both of the receivers produced similar results given the fact that same receiver spacing and number of receiver were used. The only exception is at the larger wavelength (about 1000 ft) where 1-Hz geophones continue producing a clear trend of dispersion curve, in contrast, 4.5-Hz geophones yielded a scattered trend, thus less reliable data due to the restriction from its mechanical design at low frequencies.

It is generally observed that fundamental dispersion curves from MASW testing agree with the experimental dispersion curve from SASW testing. In this context, both WinSASW 2-D and 3-D theoretical solutions are used to match the fundamental mode of the MASW results. This approximation could lead to biased result for the MASW analysis. Thus, a new forward modeling algorithm and inversion program should be developed to match not only the fundamental mode, but also the higher modes of the MASW experimental dispersion curves on a theoretically correct basis.

Reference geological information at the Hornsby Bend site is presented with CPT results and a boring log. Even it is found based on the geological information that a clay-like interbed existed at depths from 15 to 30 ft, both surface wave methods did not find a corresponding inversion zone in the form of shear wave velocity. This may be attributed

to the fact that clayey material possesses higher shear wave velocity than sandy material given it exists at deeper depth, thus has more overburden stresses. Both methods predicted a velocity contrast of stiff material about 46 ft, which generally agree with CPT and borehole results. SCPT test results were also compared to the SASW V_s profile. The difference between two V_s profile is mainly due to the lateral variability of the site.

Chapter 7   SASW Testing on the Big Island, Hawaii

7.1 INTRODUCTION

To develop the empirical ground motion prediction models for the purposes of earthquake hazard mitigation and seismic design in Hawaii, knowledge of the subsurface site conditions beneath strong-motion stations is very important and always desired. USGS strong-motion sites on the Big Island were installed to record each damaging earthquake on the ground or in man-made structures. The strong-motion stations that recorded PGA from the 2006 M 6.7 Kiholo Bay mainshock are shown in Figure 7.1.

To understand better the ground motions that were recorded during the 2006 Kiholo Bay earthquake, Spectral-Analysis-of-Surface-Waves (SASW) testing was performed near 22 free-field, USGS strong-motion sites to obtain shear-wave velocity (V_s) data. V_s profiling was performed to reach depths of more than 30 m (100 ft) at each station. Of the 22 strong-motion stations, 19 stations are situated on sites underlain by basalt, based on surficial geologic maps. However, these sites have varying degrees of weathering and soil development. The remaining three strong-motion stations are located on alluvium or volcanic ash. The V_s profiles from SASW testing were used to calculate the V_{s30} (average V_s in the top 30 m) value at each station. Based on these V_{s30} values, the basalt ranged from 906 to 1,908 ft/s (NEHRP site classes C and D), because most sites were covered with soil of variable thickness (Wong et al., 2011). These low V_s values turned to be rather surprising and the material profiles are further characterized and discussed in this chapter.

To study the "basalt" profiles at the 19 strong-motion stations, materials in the profiles were characterized and grouped based on their V_s values in comparison with reference profiles for sand and gravel. The reference profiles were based on Menq, 2003.
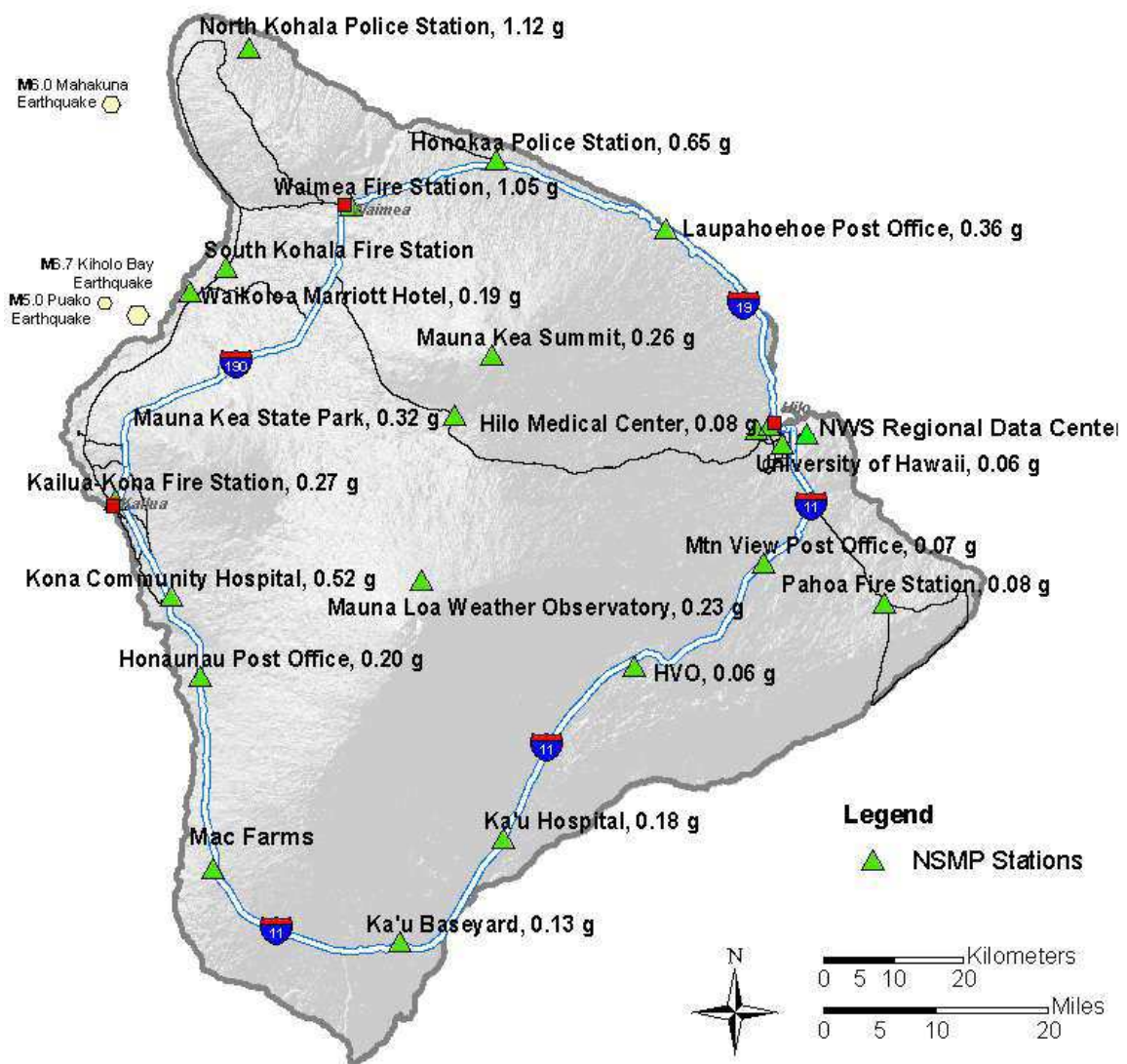
Figure 7.1   USGS strong motion stations and recorded PGA's from the 2006 **M** 6.7
Kiholo Bay Mainshock (from Wong et al, 2011)

Based on these comparisons, a National Earthquake Hazards Reduction Program (NEHRP) site class map was developed for the Big Island (Wong et al, 2011). The new V_s data were significant input into an update of the USGS statewide hazard maps and to the operation of ShakeMap on the Island of Hawaii.

7.2 SASW V_S RESULTs

Before the present study, only a few shallow CPT (cone penetrometer test) measurements to infer V_s in soft soils have been performed on the Big Island. The SASW surveys took place from 7 to 17 January 2008 and were performed by Mr. Ivan Wong, Professor Brady Cox, Professor Kenneth Stokoe and Mr. Cecil Hoffpauir. The 22 free-field strong-motion sites surveyed are shown on Figure 7.1. Most of the sites are fire stations, police stations, hospitals, or post offices. Surveys were generally performed within 100 ft of the location of the USGS strong-motion instrument. For a few sites, this was not possible due to lack of space to perform the surveys and so the distance was as much as 200 ft.

Active seismic sources are required for the SASW surveys. A sledge hammer was used for the shorter wavelengths, λ, less than about 50 ft. The larger source used to create wavelengths up to about 600 ft long in this study was the National Science Foundation's Network for Earthquake Engineering Simulation (NEES) mobile vibrator called ―Thumper (Figure 7.2). Thumper, housed and operated by UT, is a moderate- to high-frequency vibrator. Some important characteristics of Thumper are: mounted on a Ford F650 truck, total weight of about 10,000 kg, and two vibrational orientations (field transformable in a few hours), vertical or horizontal. The maximum force output is about 27 kN over the frequency range of 17 to 225 Hz with the output decreasing outside this frequency band.

Figure 7.2   Thumper Operating in the parking lot at Hawaiian Volcano Observatory

In the Hawaii surveys, the full output of Thumper was used in the SASW surveys. A stepped sine excitation was used to collect the surface wave data at all sites. During this excitation, frequencies from about 200 to 2 Hz were stepped through over a time span of several minutes. The dwell time at low frequencies was greater than at high frequencies in an attempt to increase the signal-to-noise ratio at low frequencies.

An example composite field dispersion curve collected on the Big Island is presented on Figure 7.3a. These data were collected at the Pahoa Fire Station using a sledge-hammer source with receiver-to-receiver spacings of 6, 12, 15, and 30 ft and Thumper as the source with receiver-to-receiver spacings of 25, 50, 75, 100, 150, and 200 ft. The theoretical dispersion curve and its fit to the compacted curve developed in the forward modeling process are shown on Figure 7.3b. The composite field dispersion

curve is composed of 3,196 data points that cover a frequency range from about 10 to 200 Hz. This frequency range corresponds to a wavelength range of 2.4 to 240 ft. The goodness-of-fit between the theoretical and compacted dispersion curves is represented by the root mean square (RMS) error on Figure 7.3b and by the mean (μ) and standard deviation (σ) of $\triangle V_R/V_R$ in Figure 7.3c, where V_R is from the compacted dispersion curve and V_R is the phase velocity difference between the compacted dispersion curve and theoretical dispersion curve at the same frequency. In this case, the RMS error is 59.4 ft/s, and the mean and standard deviation are -0.5% and 5.6%, respectively. Dr. Lin (2011) evaluated these data and found that, as presented in Wong et al (2011), typical values found for the 22 sites have RMS errors (for V_R) ranging from about 30 to 180 ft/s, ranging from -0.4 to 0.5 %, and ranging from 3.3 to 6.5 %.

In terms of the resolution in the V_s profiles, the resolution decreases with depth for all nonintrusive, surface-wave-based methods. For SASW testing on the Big Island, consider the V_s profile of the Pahoa Fire Station. This profile consists of 9 layers, with the thickness increasing with depth from 1 ft for the top layer to 50 ft for the 8th layer (Figure 7.4). The 9th layer includes the half-space but only 20 ft of the half-space is presented because the V_s profile is shown only to a depth equal to 0.5 times the maximum wavelength in the composite field dispersion curve. This criterion is used so that the resolution of V_s in the lower portion of the profile is within ±10% to ±15%.

To demonstrate this resolution, consider Figures 7.4a and 6.4b, where the value of V_s in layer 5 has been varied by ±10% from the original best-fit profile (Wong et al., 2011). As seen in Figure 7.4b, these ±10% changes to layer 5 result in theoretical dispersion curves that no longer fit the compacted field dispersion curve. As such, the "true" V_s for layer 5 is well within 10% in the forward modeling process and the

175
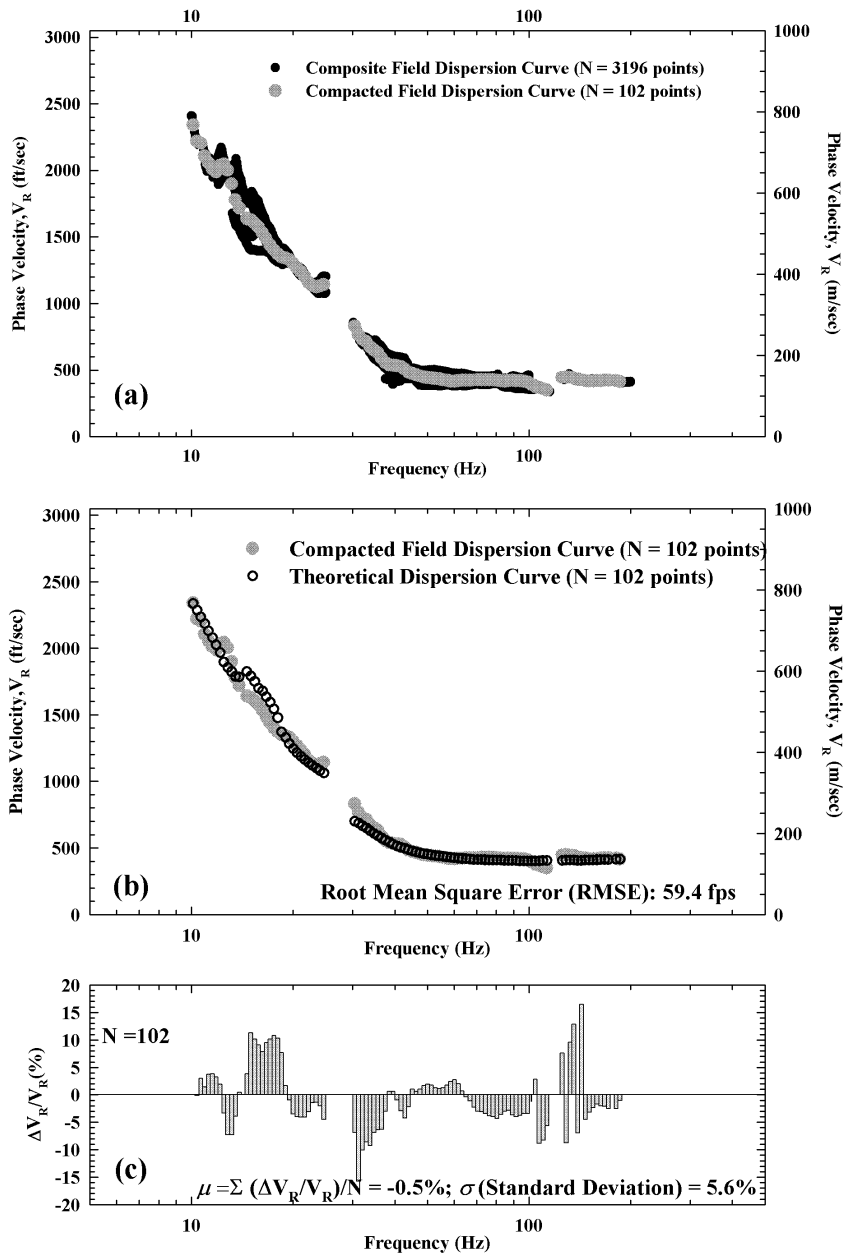
Figure 7.3   SASW Forward Modeling Process and Goodness-of-Fit Evaluation for the
Survey at the Pahoa Fire Station: (a) Developing the Compacted Field
Dispersion Curve, (b) Fitting the Compacted Dispersion Curve with a
Theoretical Dispersion Curve, and (c) Determining the Mean and Standard
Deviation of the Best Fit. RMSE is the RMS error (Courtesy of Lin, 2011).

resolution is expected to be even better for the shallower layers. Similarly, in Figures 7.4c and 7.4d, the V_s of layer 8 has been varied by $\pm 10\%$ from the original best-fit profile. In this case, the fit of the original theoretical dispersion curve is still better than the varied profile, indicating that the original V_s profile can be considered, in general terms, to be within 10% of the "true" V_s value in that depth range over that lateral distance tested. These results are typical of the 22 sites tested on the Big Island.

The V_s profiles for the 22 surveys at the strong motion sites are shown on Figures 7.5 through 7.10. These profiles are taken from Wong et al., 2011. The profiling depths ranged from 100 to 318 ft (Table 7.1). For about 1/3 of the sites, the profiling depth was 124 ft or less. In these cases, the shallower profiling depths resulted from one or more of the following: (1) the available space at the site was insufficient for the longer arrays (source to furthest receiver of 400 to 600 ft) required to profile deeper, (2) there was a significant velocity jump (increase of 40% or more) in the top 100 ft, and (3) there was a substantial thickness (40 ft or more) of soft soil ($V_s < 500$ ft/s) in the upper portion of the site.
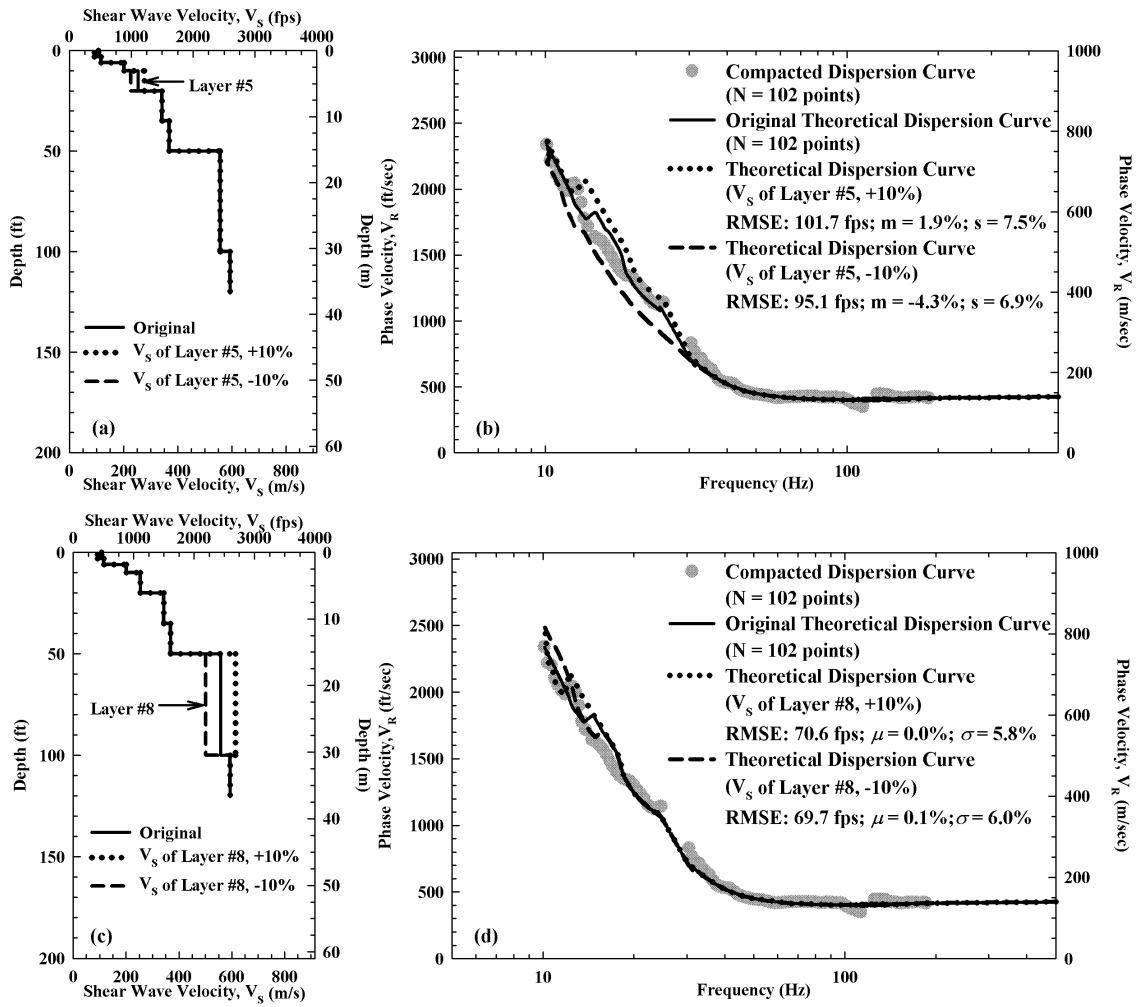
Figure 7.4   SASW Parametric study of resolution in the V_s profile at the Pahoa Fire Station: (a) Varying V_s of Layer #5 and (b) Effect on the Theoretical Dispersion Curves, (c) Varying V_s of Layer #8 and (d) Effect on the Theoretical Dispersion Curves (Courtesy of Lin, 2011).

178
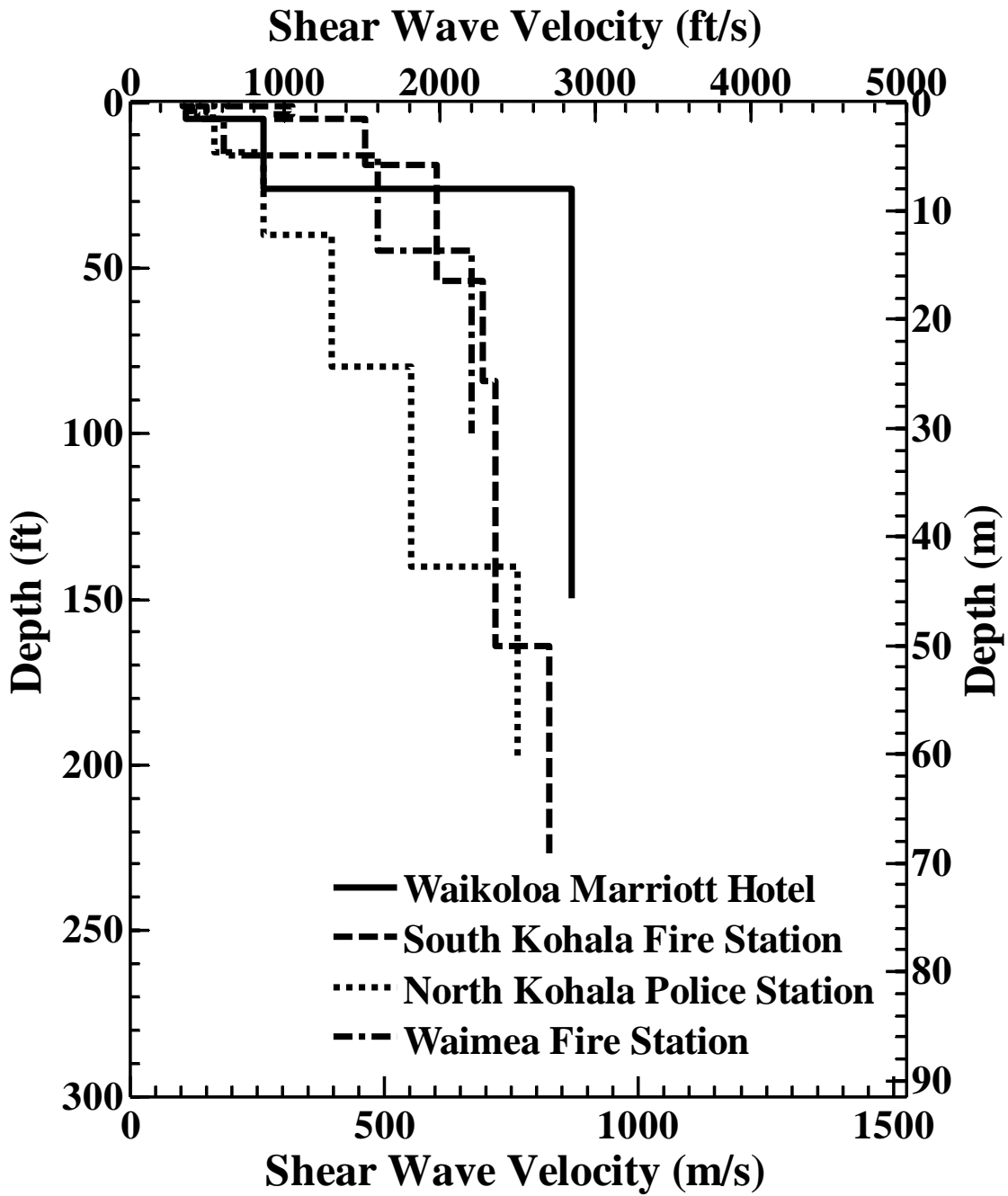
Figure 7.5 V_s profiles at Waikoloa Marriott Hotel, South Kohala Fire Station, North Kohala Police Station, and Waimea Fire Station (from Wong et al., 2011)
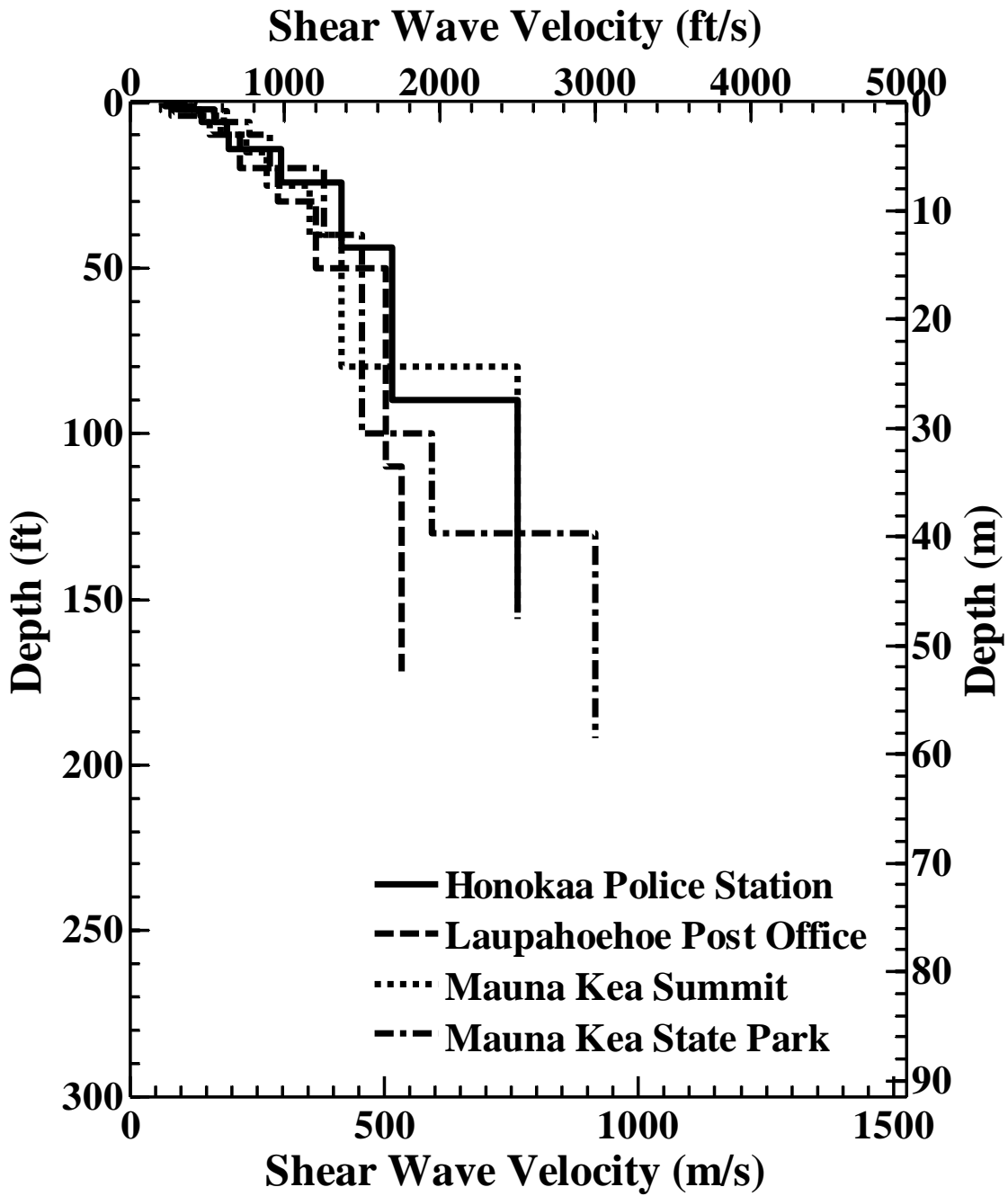
Figure 7.6 V_s profiles at Honokaa Police Station, Laupahoehoe Post Office, Mauna Kea
Summit, and Mauna Kea State Park(from Wong et al., 2011)
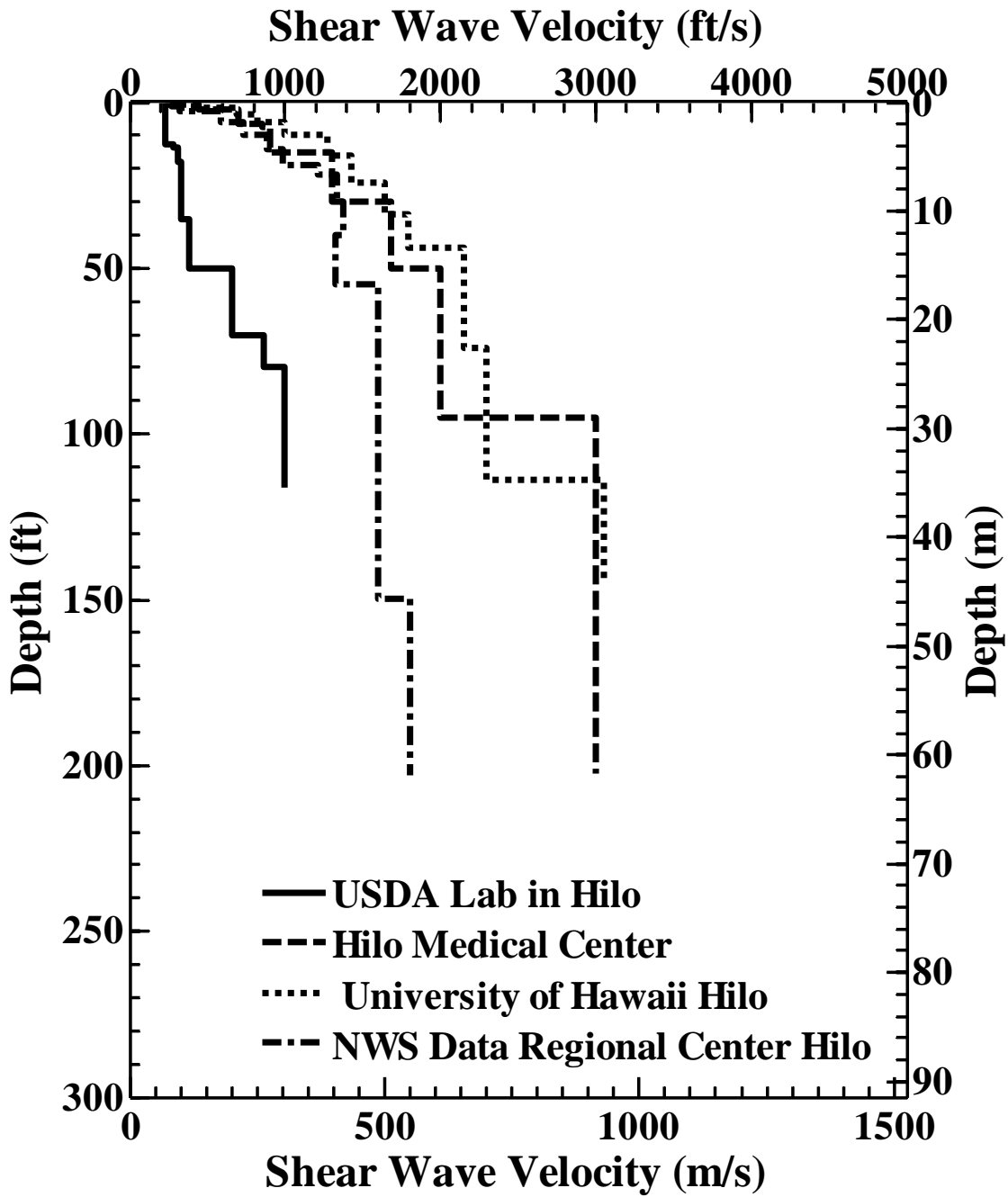
Figure 7.7 V_s profiles at USDA Lab in Hilo, Hilo Medical Center, University of Hawaii, Hilo, and NWS Data Regional Center, Hilo (from Wong et al., 2011)

181
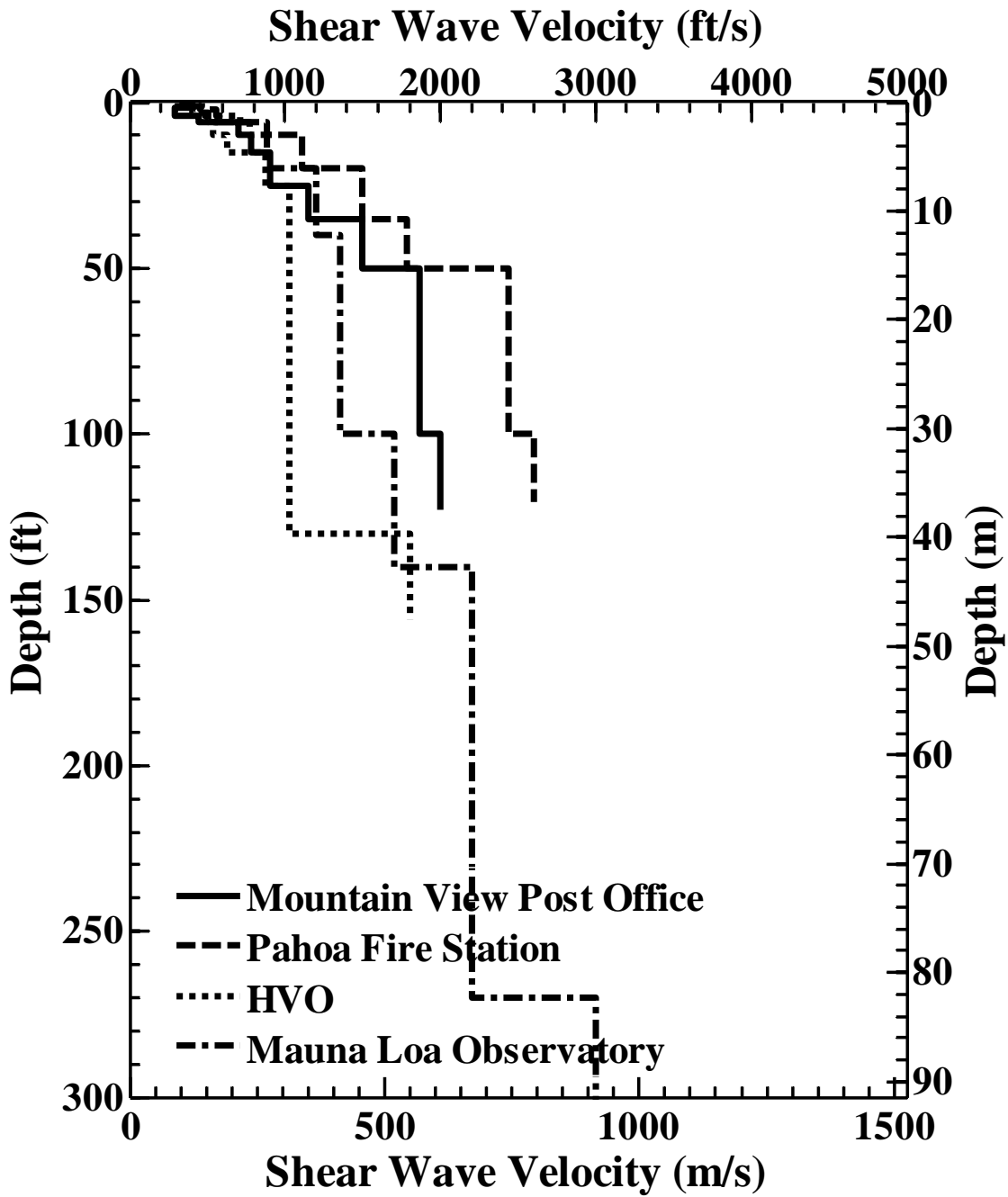
Figure 7.8 V_s profiles at Mountain View Post Office, Pahoa Fire Station, HVO, and
Mauna Loa Observatory (from Wong et al., 2011)
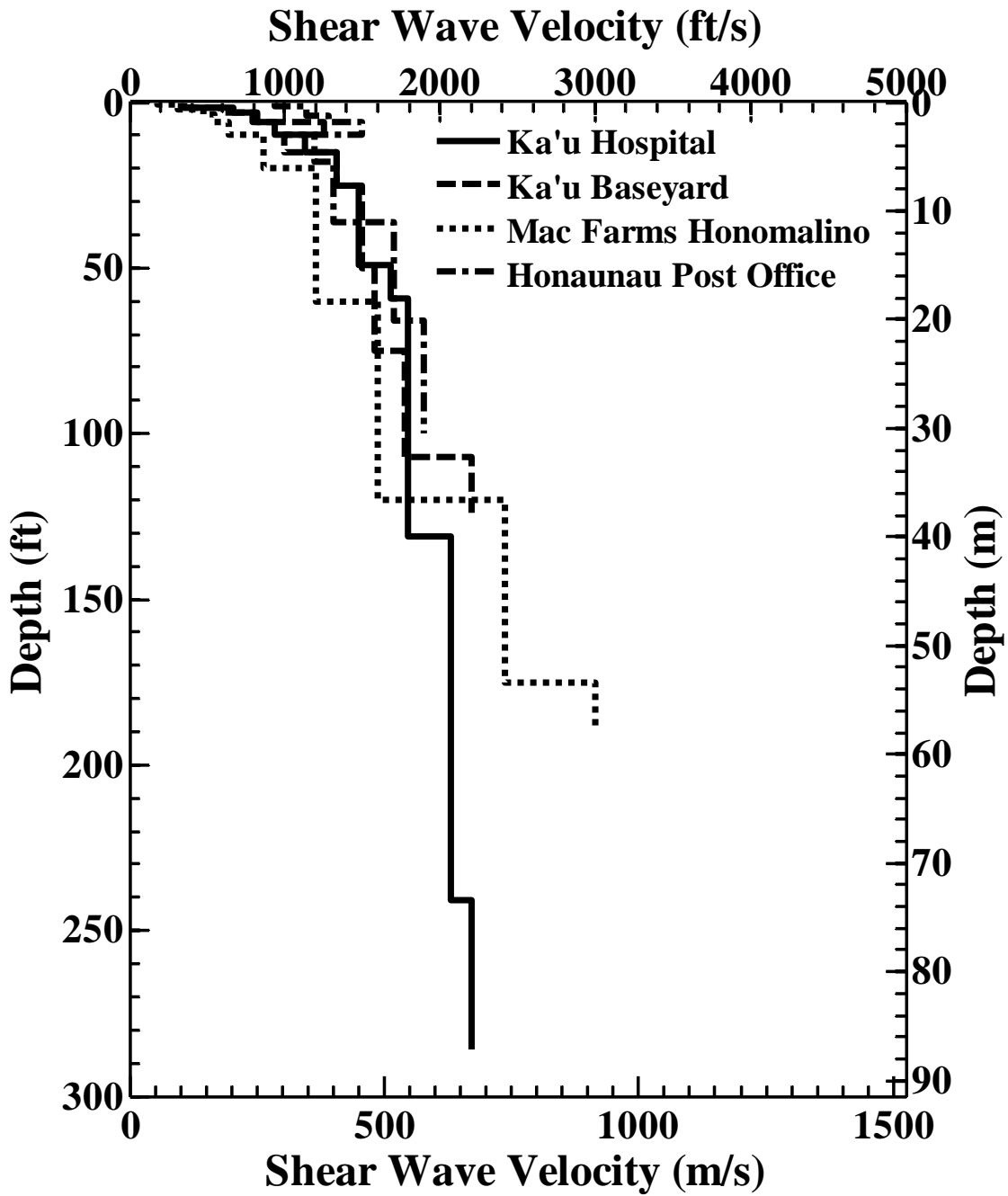
Figure 7.9 V_s profiles at Ka'u Hospital, Ka'u Baseyard, Mac Farms, Honomalino, and Honaunau Post Office (from Wong et al., 2011)

183
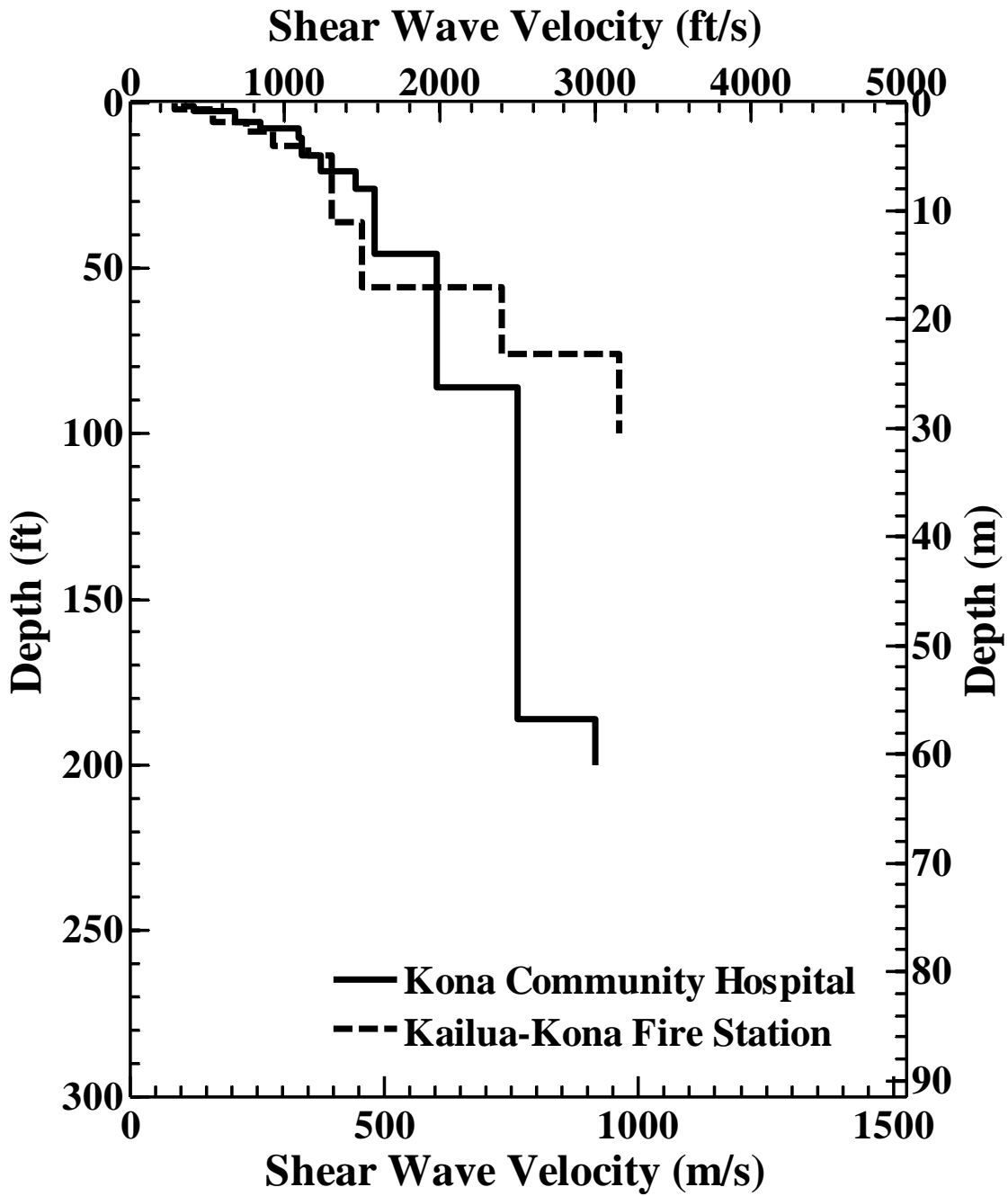
Figure 7.10 V_s profiles at Kona Community Hospital and Kailua-Kona Fire Station (from Wong et al., 2011)

Station No.	Station Location	Longitude (degrees)	Latitude (degrees)	Maximum Profile Depth (ft)	V_{S30}* (ft/s)	NEHRP Site Class[†]	Geotechnical Layering Profiles Based on V_S[‡]
2810	Kailua-Kona Fire Station	-155.9923	19.6477	100	1418	C	13 ft soil/43 ft weathered basalt/basalt
2812	Ka'u Hospital, Pāhala	-155.4723	19.1999	286	1389	C	1.5 ft soil/284 ft weathered basalt
2816	Pahoa Fire Station	-154.9466	19.4934	120	1497	C	10 ft soil/40 ft weathered basalt/basalt
2817	University of Hawaii, Hilo	-155.0805	19.7034	144	1615	C	1.5 ft soil/42.5 ft weathered basalt/basalt
2818	USDA Laboratory, Hilo	-155.0974	19.7277	116	437	E	70+ ft very soft soil/46+ ft soft soil
2822	Ka'u Baseyard, Waiohinu	-155.6150	19.0700	124	1365	C	1.5 ft soil/120 ft weathered basalt
2824	Mauna Loa Weather Observatory	-155.5770	19.5363	318	1120	D	140 ft soil/130 ft weathered basalt/basalt
2825	Waimea Fire Station	-155.6614	20.0230	100	1375	C	16 ft soil/29 ft weathered basalt/basalt
2826	North Kohala Police Station	-155.8010	20.2300	198	1006	D	80 ft soil/60 ft weathered basalt/basalt
2829	Mauna Kea State Park	-155.5300	19.7520	192	1150	D	100 ft soil/30 ft weathered basalt/basalt
2830	Mauna Kea Summit	-155.4730	19.8260	156	1149	D	80 ft soil/basalt
2832	Honokaa Police Station	-155.4625	20.0775	154	1205	C	24 ft soil/66 ft weathered basalt/basalt
2833	Laupahoehoe Post Office	-155.2326	19.9835	172	1005	D	50 ft soil/122 ft weathered basalt
2834	Mac Farms, Honomalino	-155.8680	19.1690	189	1086	D	120 ft soil/basalt
2836	Hawaiian Volcano Observatory	-155.2880	19.4200	156	890	D	130 ft soft soil/26+ ft soil
2839	Hilo Medical Center	-155.1150	19.7220	202	1430	C	15 ft soil/80 ft weathered basalt/basalt
2845	Honaunau Post Office	-155.8805	19.4174	100	1559	C	100 ft weathered basalt
2846	Mountain View Post Office	-155.1083	19.5504	123	1159	D	35 ft soil/88+ ft weathered basalt
2847	Waikoloa Marriott Hotel, Anaehoomalu	-155.8870	19.9190	150	1550	C	26 ft soil/basalt
2849	Kona Community Hospital, Kea Lakekua	-155.9181	19.5215	200	1476	C	8 ft soil/78 ft weathered basalt/basalt
2852	South Kohala Fire Station, Kamuela	-155.8343	19.9464	266	1902	C	3.5 ft soil/50.5 ft weathered basalt/basalt
2853	NWS Data Regional Center, Hilo	-155.0460	19.7154	203	1176	D	203 ft soil

* V_{S30} is computed from the V_S profile. The number of significant digits does not reflect the uncertainty in these values.

‡ Soil refers to stiff soil category shown in Figure 14. Weathered basalt refers to material category shown in Figure 13. Basalt refers to material category shown in Figure 12. Minimum thickness.

† NEHRP Site Class V_{S30}

A	> 5,000 ft/s
B	2,500 to 5,000 ft/s
C	1,200 to 2,500 ft/s
D	600 to 1,200 ft/s
E	< 600 ft/s

Table 7.1 Site Characteristics and NEHRP Site Classes of the Strong Motion Stations on the Island of Hawaii (from Wong et al., 2011)

In the forward modeling of each field dispersion curve, the depth to the water table (10 to 140 ft) was estimated based on the surrounding topography and elevation relative to the ocean. Sensitivity analyses indicate that V_s profiles are not sensitive to the water table depth once reasonable estimates are included in the modeling process (Wong et al., 2011). Changing the depth to the water table by a factor of two at all 22 stations results in 0.0% difference in V_{s30} at 19 stations and at most 4.4% at HVO (from Lin, 2011).

7.3 GEOTECHNICAL SITE CHARACTERIZATION

As part of this dissertation research, estimates of the general categories of geotechnical materials within each profile were attempted. To perform this work, the V_s-depth profiles were subdivided and grouped according to relative trends expected for various geotechnical materials. A template of V_s-depth trends was developed that was then used to categorize the materials. This template is shown on Figure 7.11. The trend for basalt, referred to as unweathered basalt herein, is defined by any material with $V_s \geq$ 2,200 ft/s at depths $\leq$ 75 ft and $V_s \geq$ 2,500 ft/s at depths > 75 ft (essentially a NEHRP B material). The trends compared with other materials are based on V_s depth relationships of medium dense sand (SP) and dense gravel (GW) taken from the work of Menq, 2003. The sand and gravel were each assumed to have relative densities of about

Shear Wave Velocity (ft/sec)

0   1000   2000   3000   4000   5000

Depth (ft): 0, 50, 100, 150, 200

Depth (m): 0, 15, 30, 45, 60

water table at 35 ft

Shear Wave Velocity (m/sec)

0   500   1000   1500

Legend:

- - - **Medium Dense Sand**
  (V_{s30} : 848 ft/sec)

— — **Dense Gravel**
  (V_{s30} : 1103 ft/sec)

—— **Unweathered Basalt**
  Lower Boundary
  $V_s \geq 2200$ fps at depth ≤ 75 ft
  $V_s \geq 2500$ fps at depth > 75 ft

Notes (Menq 2003):

Medium Dense Sand (SP)

$V_s = 820 \cdot (\sigma_0' / P_a)^{0.27} ... ft/sec$
$C_u = 4 \quad D_{50} = 0.5mm$
$D_r = 75\% \quad e = 0.44$

Dense Gravel (GW)

$V_s = 1019 \cdot (\sigma_0' / P_a)^{0.33} ... ft/sec$
$C_u = 35 \quad D_{50} = 5mm$
$D_r = 95\% \quad e = 0.25$

where:

σ_0': effective isotropic confining pressure,
P_a : atmospheric pressure in same units as σ_0',
C_u : uniformity coefficient,
D_{50}: mean grain size,
D_r : relative density, and
e : void ratio.

Also, σ_0' calculated assuming:
$\gamma_{dry,sand}$: 115 pcf
$\gamma_{dry,gravel}$: 132 pcf, and
K_0' : earth pressure coef. = 0.5.

Figure 7.11   Template of V_s – Depth Relationship used to Categorize Geotechnical Materials of the 22 Sites

187

75% and 95%, respectively, and the water table depth was assumed at 35 ft. Equations for the V_s-depth relationships for the sand and gravel are given in the note on Figure 7.11. In terms of site classes, the V_{s30} values of the sand and gravel are 848 and 1,103 ft/s, respectively, which both correspond to NEHRP site class D (V_s = 600 to 1200 ft/sec) so that the medium dense sand is near the mid-range of site class D and the dense gravel is slightly below the site class D and E boundary.

The stiffest material measured at the sites is considered to represent unweathered basalt. This material was encountered within the top 200 ft at 14 sites (Figure 7.12). The V_s profiles of the unweathered basalt over the depths that they were measured along with the median, and 16 and 84th percentile profiles are shown in Figure 7.12. The V_s values range from 2,200 to 3,200 ft/s. The coefficient of variation (c.o.v. = standard deviation /mean) and number of profiles is also shown in Figure 7.12. The c.o.v. is quite low (< 0.15) over the depth range of about 50 to 200 ft, where at least three or more profiles were determined.

The second V_s-profile group is shown in Figure 7.13. This group was measured at 16 sites and is defined by: (1) a significant increase in V_s with depth in the top 50 ft, and (2) median V_s values somewhat higher than dense gravel below about 5 ft but considerably less than unweathered basalt in the top 140 ft. This group is considered to represent partially weathered basalt that contains some voids, fractures, etc. This material can be seen in some shallow cuts in near-surface basalt such as is present near the Waikoloa Marriott Hotel. The c.o.v. of this material decreases with depth in the top 35 ft, below which the c.o.v. is 0.12.

The third and last grouping is shown in Figure 7.14. This group was evaluated at 16 sites and is defined by median V_s values equal to or slightly above dense gravel at depths greater than 25 ft. It is interesting to observe how closely the V_s-depth trend
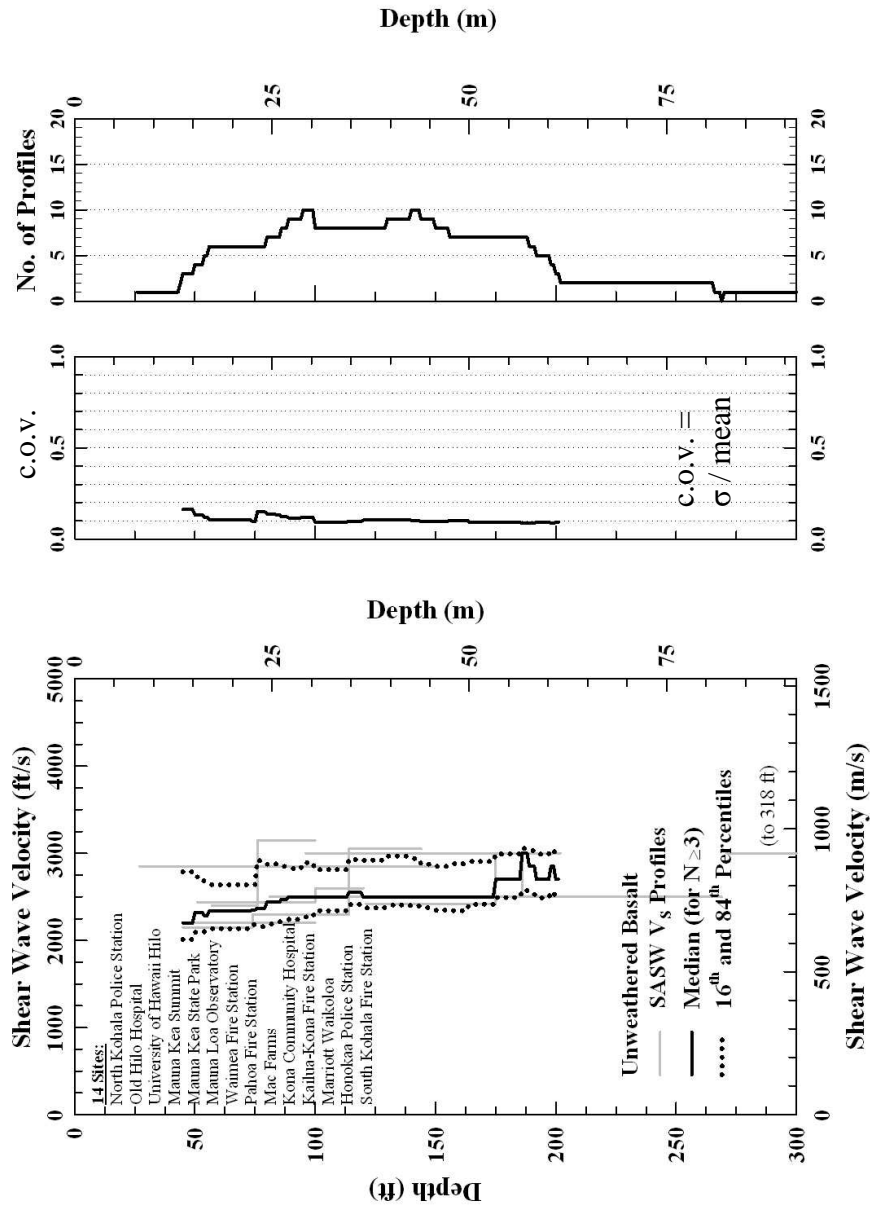
Figure 7.12   Statistical Analysis of the Unweathered Basalt V$_s$ profiles

189
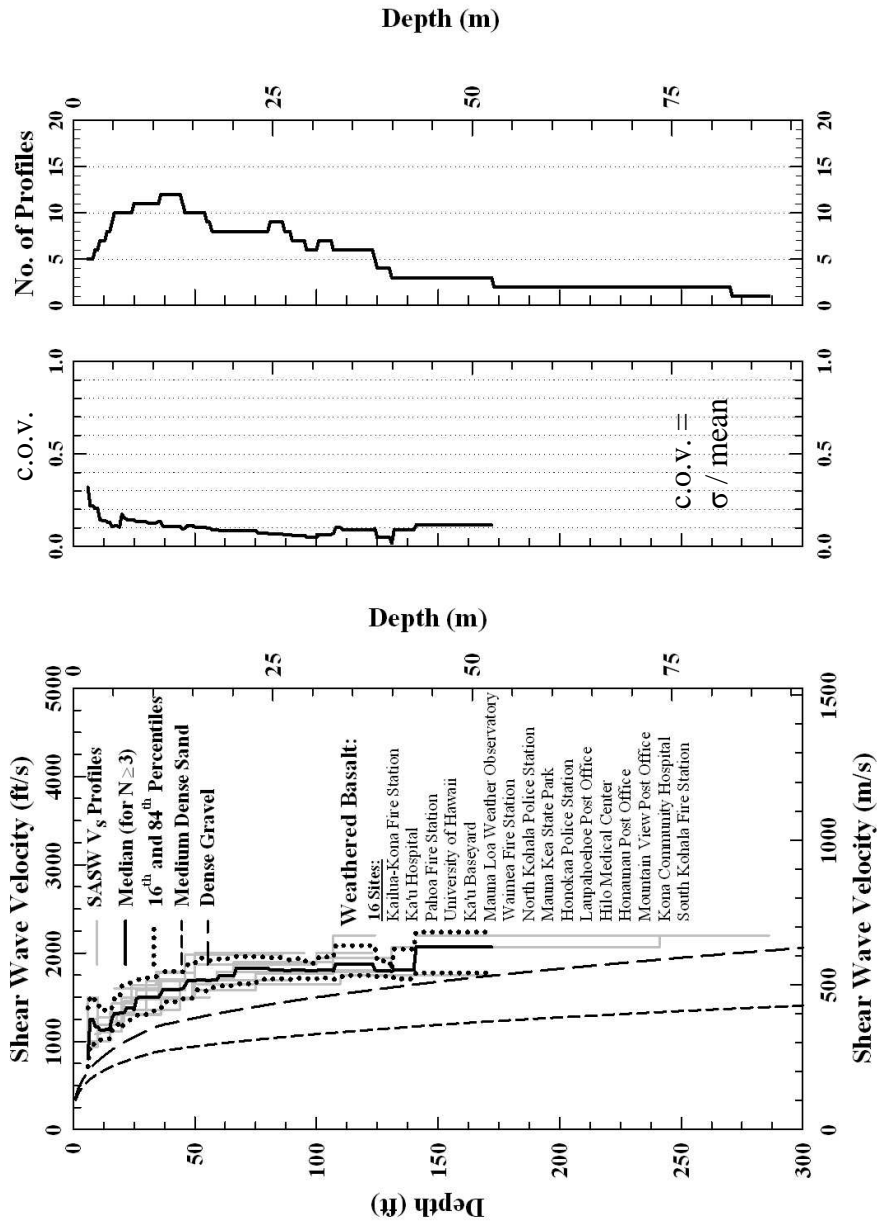
Figure 7.13   Statistical Analysis of the Partially Weathered Basalt V_s Profiles

190
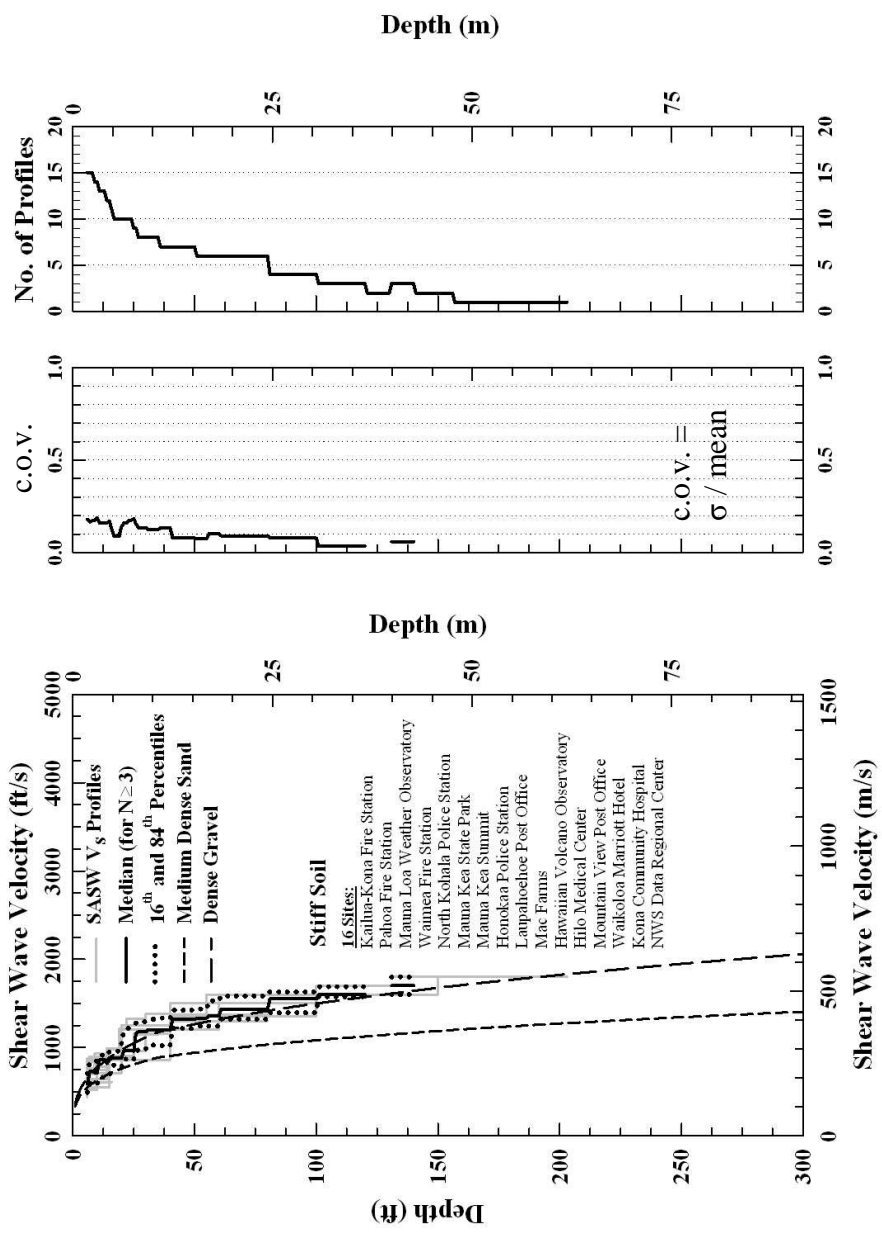
Figure 7.14   Statistical Analysis of the Stiff Soil V_s profiles

191

follows the dense gravel profile. Below about 30 ft, the COV of this material is also 0.12. This material is considered to represent stiff soil.

One or more of the three general categories of materials were encountered at 21 of the 22 sites. The thicknesses of these layers in each profile is given in Table 7.1. As noted above, the "soil" identified in the layering profiles in Table 7.1 is actually the "stiff soil" group presented in Figure 7.14. At two sites, the U.S. Department of Agriculture (USDA) Laboratory and Hawaiian Volcano Observatory (HVO), softer soil was also encountered in these V_s profiles which are shown in Figures 7.7 and 7.8. This softer material was not characterized any further as it was felt that the V_s values by themselves were insufficient for this purpose.

7.4 ESTIMATED GEOTECHNICAL PROFILES

As discussed above and as presented in Table 7.1, layered geotechnical profiles for the 22 strong-motion station sites were estimated. As examples of these profiles, four geotechnical profiles are presented in Figure 7.15. It should be noted that each one of these geotechnical profiles was considered to be on basalt and, before the V_s profiling, was assigned a NEHRP site class of B; hence, V_s between 2500 and 5000 fps. As seen in Figure 7.15, two of the sites are site class C and two are site class D. Clearly, the additional benefit of the V_s profiles in helping to identify the subsurface geology is shown in this effort.

7.5 CONCLUSION

SASW surveys were performed at the 22 free-field, strong-motion sites of the USGS Hawaii Strong Motion Network on the Big Island. V_s profiles reaching depths ranging from 100 to 318 ft were obtained. Most of the surveyed sites were located on basalt or weathered soil atop basalt and correspond to NEHRP site class C or D. Based on
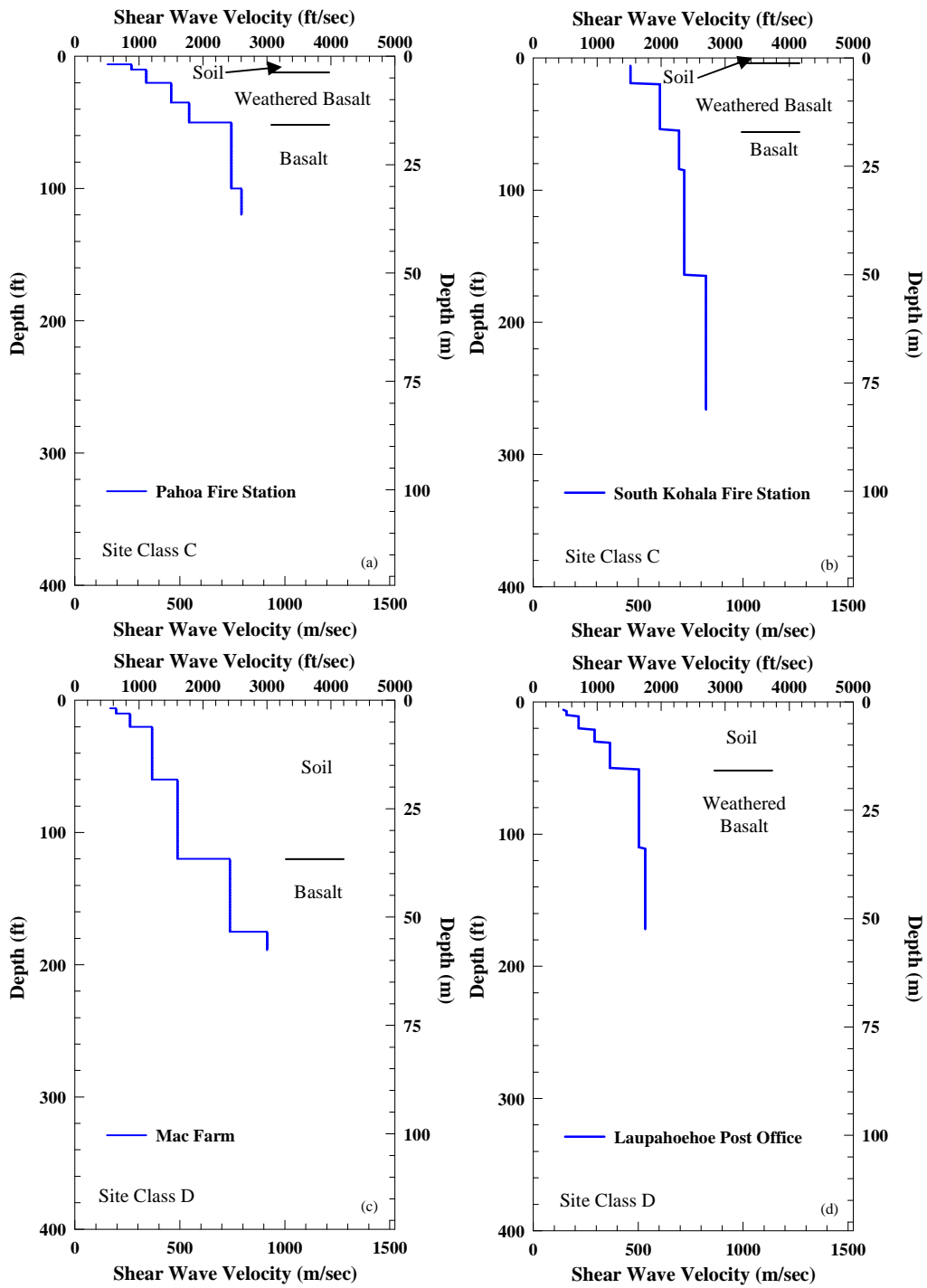
Figure 7.15 Examples of the Geotechnical Profiles at Strong-Motion Recording Stations
Estimated from the V_s profiles

this information, Wong (Wong et al, 2011) developed a new NEHRP site class map that provides a more realistic foundation for ground shaking hazard assessments than the previous map (URS, 2006) because it is based on SASW-based estimates of V_{s30}. However, the limited number of SASW tests, the variability in V_{s30} values for geologic map unit groups, and the absence of SASW data for several of the geologic map unit groups, additional SASW surveys and further analyses outlined in this chapter would reduce the uncertainty in the NEHRP site class map and ground shaking hazard assessments.

Chapter 8 V_s Profiling at a Site in Canada

8.1 INTRODUCTION

In this chapter, the findings from Spectral-Analysis-of-Surface-Waves (SASW) tests that were performed at 14 locations as part of a geotechnical engineering investigation of a project site in British Columbia, Canada are presented. Field testing was performed using a large D8K Caterpillar bulldozer as the high-energy source following the generalized SASW test procedure (Stokoe et al., 1994). Eleven of the 14 SASW test sites were spread around an area with plan dimensions of about 1200 by 2400 ft. Two other sites were located somewhat to the west of this area while a third site was located about 1000 ft northwest and situated on bedrock. SASW testing in the field was conducted by Professor Kenneth Stokoe and Mr. Changyoung Kim from the University of Texas at Austin (UT). Analysis of the SASW data to develop shear wave velocity profiles was performed by Mr. Jiabei Yuan.

The goal of the seismic investigation was to characterize the shear wave velocity (V_s) of the soil/rock profiles at the project site, thereby helping to characterize the site for use in evaluating potential problems during possible future earthquakes. The goals in terms of this dissertation were to: (1) compare the V_s profiles from the different test locations to investigate the stiffnesses of different geologic materials, the variability in the material stiffnesses, and the estimated depth to bedrock, and (2) to compare the V_s profiles to existing geological and geotechnical information such as nearby boreholes, cone penetration test results and so forth. To help identify the stiffness of the bedrock, one of the fourteen sites was located away from the main project site to an area where bedrock is close to the surface.

After the shear wave velocity profiles for all sites were evaluated, grouping of the profiles based on shear wave velocity values were created to interpret geotechnical material types and the distribution in the material types. A reference V_s profile for soft soil from Imperial Valley (Lin and Stokoe, 2008) and two empirical V_s profiles for dense sand and dense gravel (based on Menq, 2003) were used to assist in material characterization. Comparison between V_s groups and existing geological information were made to better understand the relationship between shear wave velocity profiles and other engineering parameters measured from CPT, SPT and other geotechnical tests.

8.2 SASW FIELD TESTING

The basic configuration of the source and receivers used in SASW field testing at each array location is illustrated in Figure 8.1. Three receivers were used at each source/receiver set-up. This arrangement enabled two sets of SASW test results (two individual dispersion curves) to be obtained at the same time. Typical source-receiver spacings are presented in Table 8.1.

8.3 SASW RESULTS

An example of matching the experimental dispersion curve with a theoretical dispersion curve is shown in Figure 8.2. The field data were gathered at site No. 6. The theoretical dispersion curve which is considered to match (best fit) this composite field dispersion curve is shown in Figure 8.2. The shear wave velocity profile for the site is presented in Figure 8.3. The parameters used to generate the theoretical dispersion curve in Figure 8.3 are listed in Table 8.2. For the maximum receiver spacing of 300 ft, the normal procedure of SASW analysis generally use a maximum wavelength of 600 ft. In this case, near-field data were used to investigate the deeper material as illustrated by a maximum wavelength

196
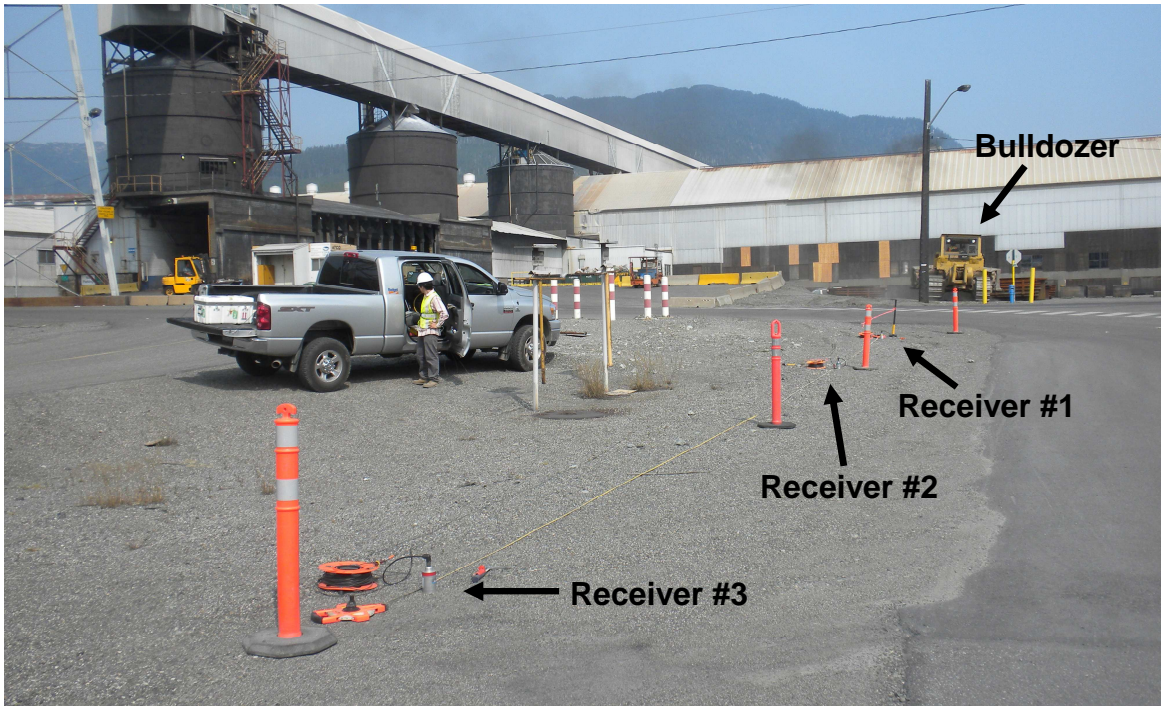
Figure 8.1   Photograph of Three, 1-Hz Geophones at one Receiver Set-up; SASW Site
          No. 3 at the Project Site.

Table 8.1   Typical Source-Receiver Spacings Used in SASW at the Project Site in
          Canada

Distance			Impact Direction		Source	Frequency (Hz) Range	No. of Pts.	Window
S-R1*	R1-R2#	R2-R3$^\Delta$	Forward	Reverse				
3	3	6	√	√	Hammer	0 – 400	400	Rect
9	9	18	√	√	Hammer	0 – 200	400	Rect
25	25	50	√	n/a	Bulldozer	0 – 100	400	Hanning
75	75	150	√	n/a	Bulldozer	0 – 40	400	Hanning
100	100	200	√	n/a	Bulldozer	0 – 20	200	Hanning
150	150	300	√	n/a	Bulldozer	0 – 16	200	Hanning

* S-R1: Distance from source to first receiver
# R1-R2: Distance from first receiver to second receiver
$^\Delta$ R2-R3: Distance from second receiver to third receiver

of 827 ft from the 300 ft spacing. As shown in Figure 8.3, the maximum profile depth is λ_{max} /2 which is 413 ft,

To generate the theoretical dispersion curves used to match the field dispersion curves, some assumptions have to be made. The depths of the water table for the fourteen sites were assumed to be 12 ft based on information supplied by geotechnical engineers using existing borings and wells. First, the unit weight and Poisson's ratio of the material must be assumed. Above the water table, Poisson's ratio was based on the V_s values determined in the forward modeling process.   If the V_s value was between 300 and 2000 fps, Poisson's ratio was taken to be 0.33. However, if the soil layer was below the water table, the value of Poisson's ratio was determined by assuming V_p to be 5000 fps and calculating Poisson's ratio based on the assumed V_s and V_p (5000 fps) values. This calculation of Poisson's ratio was performed in WinSASW once the layer was designated as being below the water table.

The unit weights assumed in this study were also based on the V_s values. Generally, if V_s was between 300 and 2000 fps, the unit weight was assumed to be 114 pcf. If V_s was greater than 2000 fps and below water table, the unit weight was assumed to be 130 pcf.

All shear wave velocity profiles are shown in Figure 8.4, with a statistical analysis of the V_s data. A large variation in V_s (hence in material distribution) exists from 50 to over 250 in depth. Upon looking at Figure 7.4, it is obvious that very soft soils exist at depth at some sites. For example, at a depth of 100 ft, shear wave velocities vary from 700 to 2500 fps (very soft soil to bedrock-like material). The high value of the coefficient of variation (c.o.v.) over the depth range, from 0.3 to 0.6, indicate that different materials are mixed in the statistical analysis. It is expected that a "uniform" material has a small c.o.v. of less than 0.15 (Lin et al., 2008). As a result, the V_s profiles are subdivided into
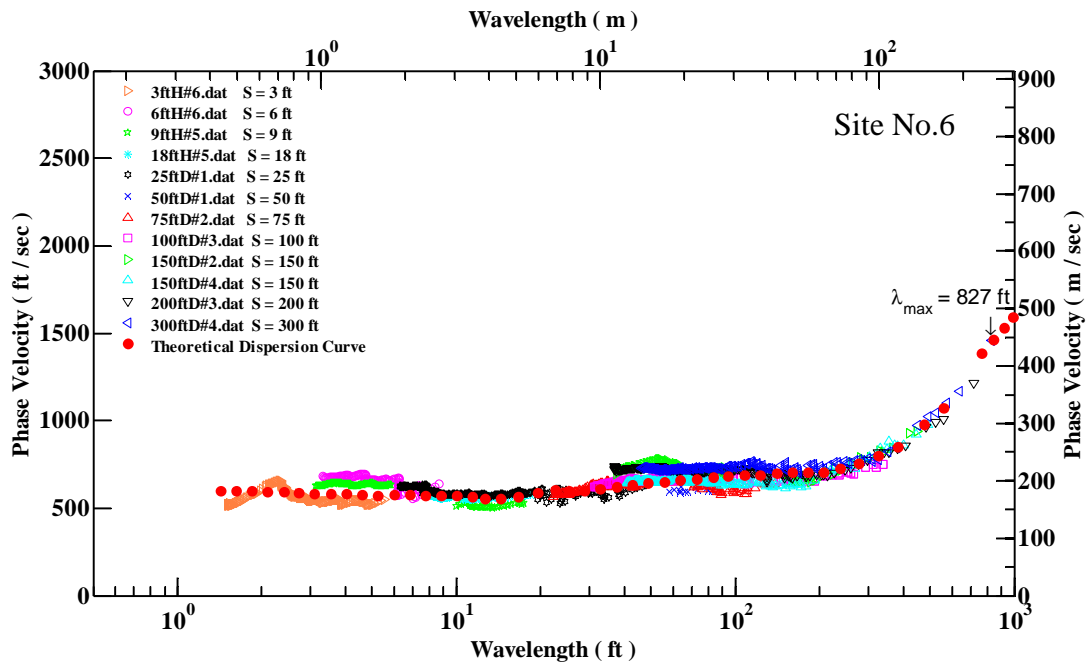
Figure 8.2   Comparison of the Fit of the Theoretical Dispersion Curve to the Composite
Experimental Dispersion Curve at one SASW Site No. 6

Table 8.2   Parameters Used to Obtain the V_S Profile at SASW Site No. 6 in British
Columbia, Canada

Layer No.	Thickness, ft	Depth to Top of Layer, ft	P-Wave Velocity, ft/s	S-Wave Velocity, ft/s	Assumed Poisson's Ratio	Assumed Total Unit Weight, pcf
1	1	0	1271°	640	0.33	114
2	4	1	1191°	600	0.33	114
3	7	5	1171°	590	0.33	114
4	13	$12^{\diamond}$	5000	680	0.49^{+}	114
5	75	25	5000	720	0.49^{+}	114
6	110	100	5000	730	0.49^{+}	114
7^{*}	99999	210	5000	2000	0.40^{+}	130

^{o} P-wave velocity calculated from V_s and assumed value of Poisson's ratio.

$*$ Layer extends below maximum depth of the V_s Profile.

$^{\diamond}$ Water table assumed at a depth of 12 ft

$^{+}$ Not assumed but back-calculated from $V_p = 5000$ fps and V_s

199
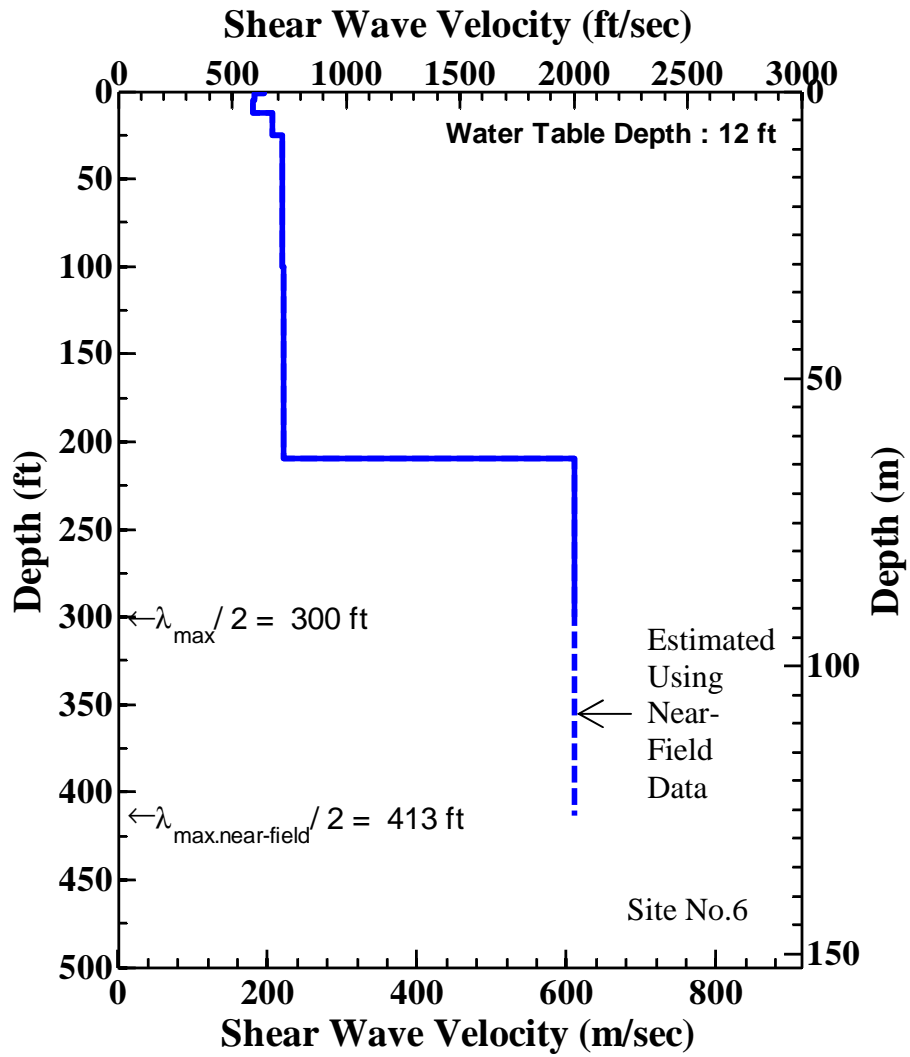
Figure 8.3   Final Shear Wave Velocity Profile Determined at SASW Site No. 6
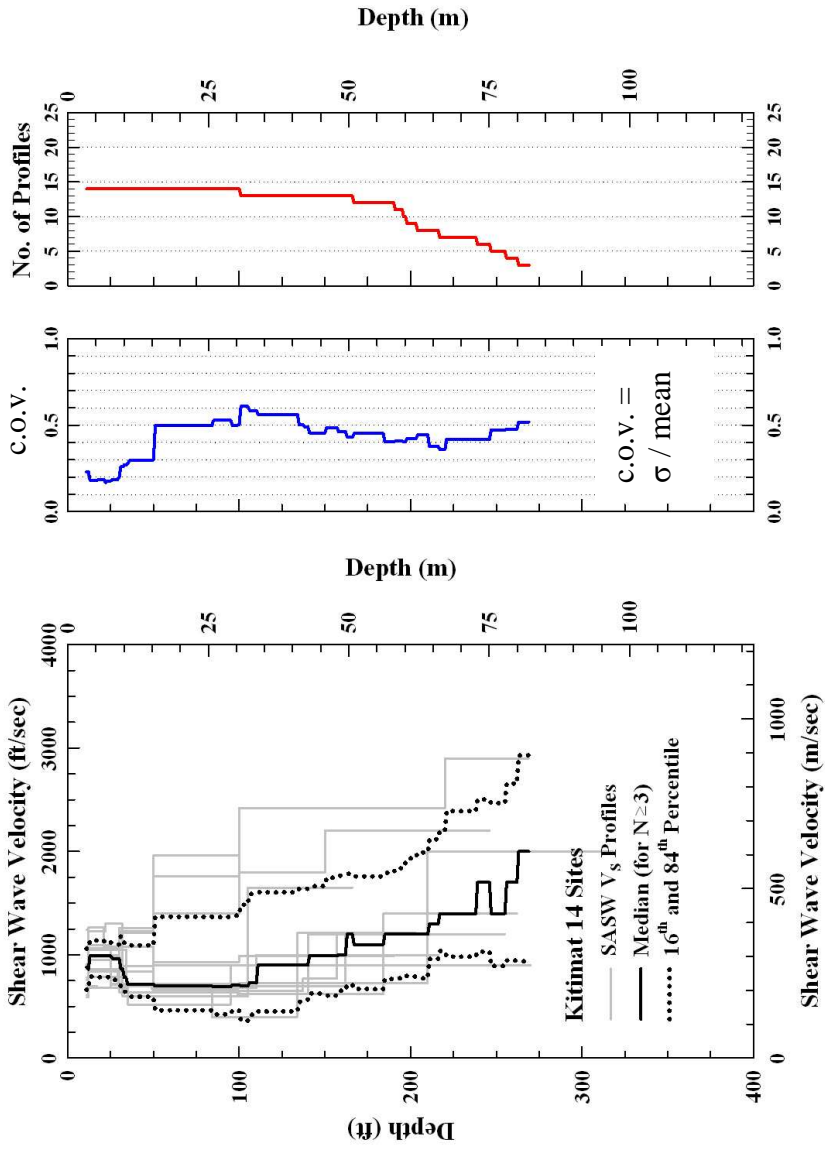
Figure 8.4   Statistical Analysis on 14 Shear Wave Velocity Profiles Determined at the Project Site in Canada

different material groups based on reference V_s curves as discussed in the next section.

8.4 V_S PROFILE GROUPINGS

8.4.1   Summary of V_s Profiles

The V_s profiling depths ranged from a minimum of 100 ft at Site No. 11 (the "bedrock" site) to a maximum of 413 ft at Site No. 6, as shown in Figure 8.3. The profiling depths were primarily controlled by: (1) the overall site stiffness, (2) the thickness and stiffness of the soil over the bedrock, (3) the velocity contrast between the soil and bedrock and (4) the extent of available space at the site over which to locate a linear SASW source-receiver array.

8.4.2   Comparison of Measured and Reference V_s Profiles

To obtain a sense of how soft or stiff the material at each site is, each V_s profile is compared with reference V_s profiles estimated for soft soil, dense sand and dense gravel (similar to the approach used in Chapter 7). These reference profiles, as well as the lower-boundary bedrock V_s profile, are shown in Figure 8.5. The reference V_s profile for soft soil comes from the median V_s profile evaluated from 23 profiles measured in Imperial Valley, CA. These soils are layers of loose sands, silts and clays (Lin and Stokoe, 2008). The reference V_s profiles for the dense sand and dense gravel are estimated from a laboratory study of the dynamic stiffness of sands and gravels by Menq, 2003. The reference rock profile is estimated based on the existing geological information at the project site.

As noted earlier, one site, SASW Site No. 11, was tested because bedrock was close to the surface. This "bedrock" V_s profile is shown in Figure 8.6. By comparing the "bedrock" profile with the reference sand and gravel profiles, the interpreted material profile is: (1) 0-15 ft is soil, (2) 15-50 ft is dense granular material with gravel and

cobbles, and (3) 50-100 ft is bedrock. The addition of larger gravel and cobbles is the reason for the V_s values slightly above the dense gravel curve in the 15 to 50 ft depth range. The "bedrock" site, combined with V_s values at depth at two other sites (Sites 10 and 12), show that V_s values greater than about 1800 fps at depths less than or equal to 150 ft and V_s values greater than about 2200 fps at depths to about 270 ft (the deepest profiling depth at a site where bedrock was thought to be encountered) likely represent bedrock as discussed in the next section.
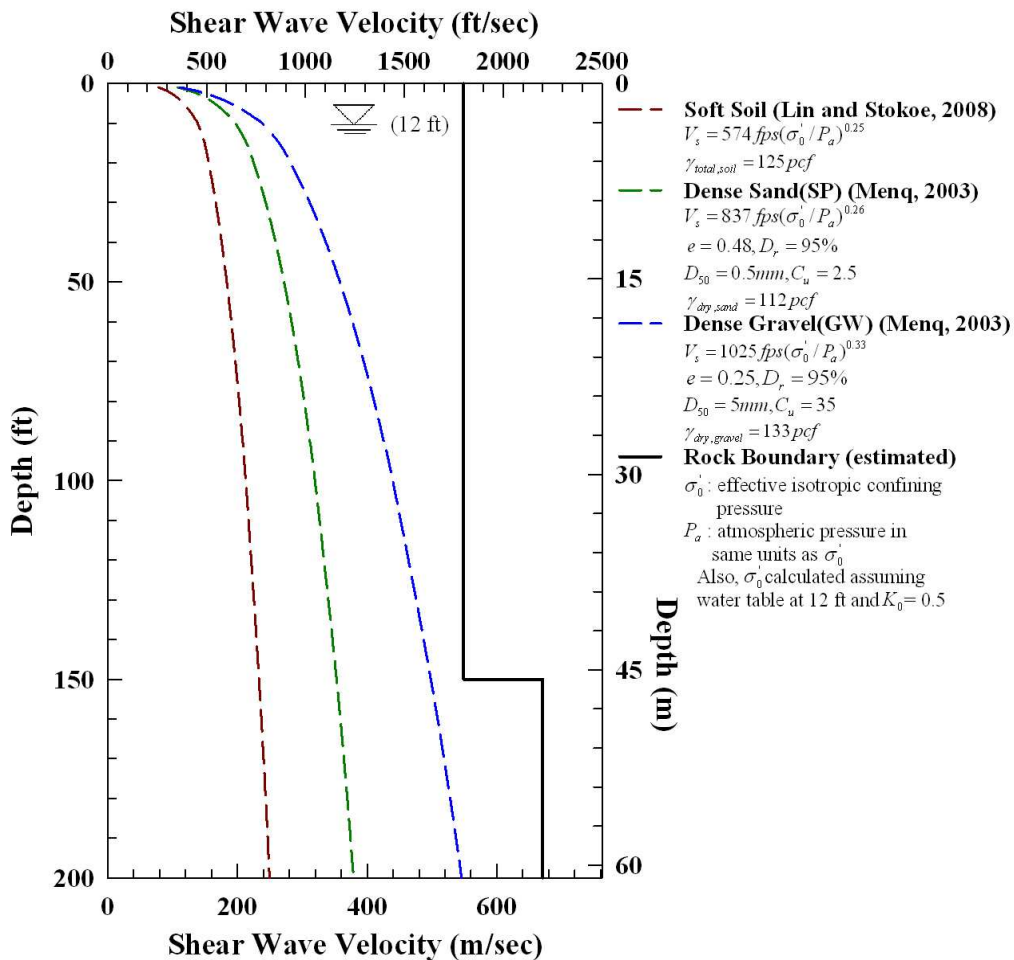
Figure 8.5   Reference V_s Profiles for Soft Soil, Dense Sand and Dense Gravel

203
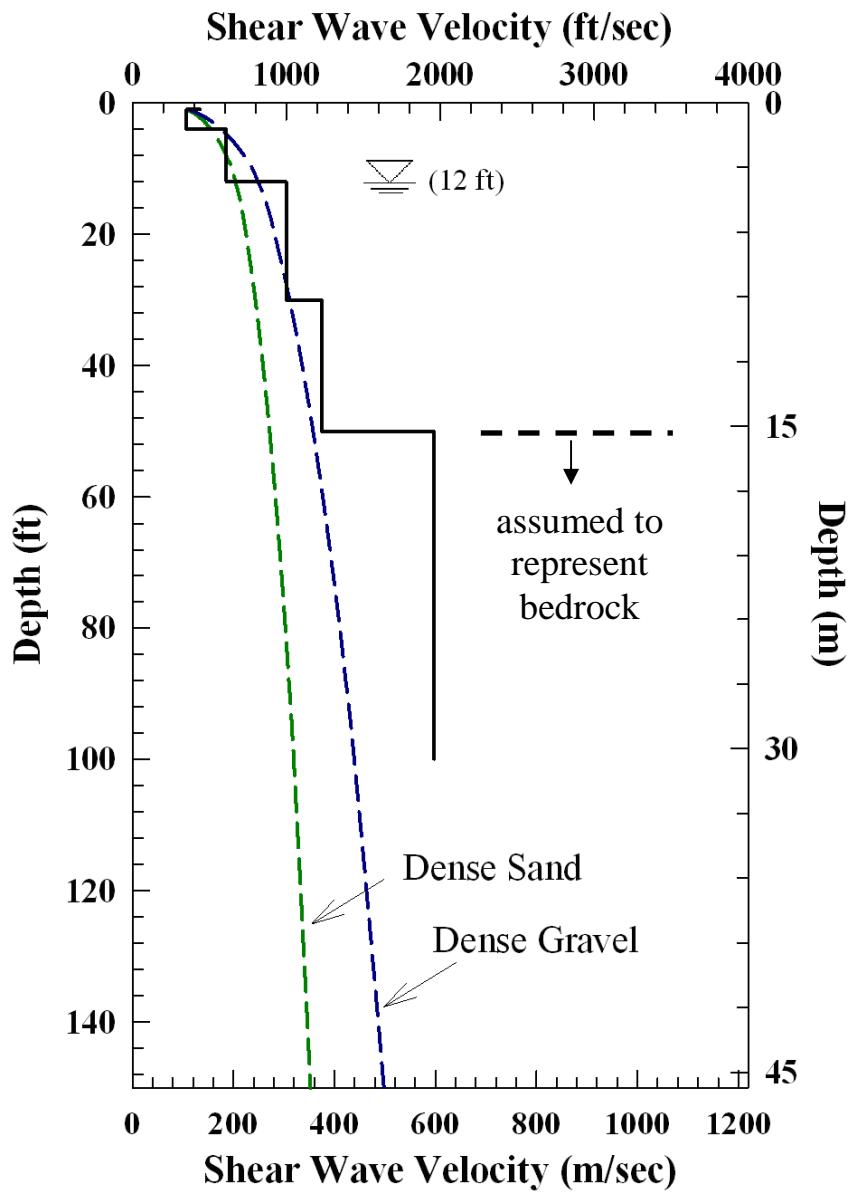
Figure 8.6   Comparison of the V_s Profile at the "Bedrock" Site (SASW Site No. 11) with the Reference V_s Profiles for Dense Sand and Dense Gravel

8.4.3 Sub-Dividing V_s Profiles by "Interpreted" Material Type

To investigate the V_s profiles further, each profile was sub-divided into V_s ranges. Of the 14 SASW sites, 12 sites have geotechnical data from one or more boreholes, Standard Penetration Test (SPT), Cone Penetration Test (CPT) or Seismic Cone Penetration Test (SCPT) investigations. The fourteen sites and associated near-by geotechnical field tests are listed in Table 8.3. Upon reviewing the 12 profiles, six V_s ranges were selected. With the six V_s ranges, each portion of all fourteen profiles that fell into a given range was then combined and statistical analyses were performed. These groups and associated V_s ranges are defined below and are presented in Figures 8.7 to 8.12.

Table 8.3   Reference Field Tests Used to Compare with the V_S Profiless from the SASW Tests at the Project Site, BC, Canada

Site Name	Elevation (ft)	SASW	Borehole	SPT	CPT	SCPT
Site 1	11.89	√				
Site 2	9.93	√	√	√	√	√
Site 3	10.57	√	√	√	√	√
Site 4	10.00	√			√	√
Site 5	9.95	√			√	√
Site 6	10.91	√	√	√		
Site 7	11.19	√	√	√		√
Site 8	13.43	√	√	√		
Site 9	13.11	√	√	√	√	√
Site 10	16.39	√	√	√		
Site 11	22.89	√				
Site 12	18.87	√	√	√		
Site 13	9.03	√	√	√		
Site 14	8.63	√	√	√		

1. Group 1: bedrock,

   • Presented in Figure 8.7.
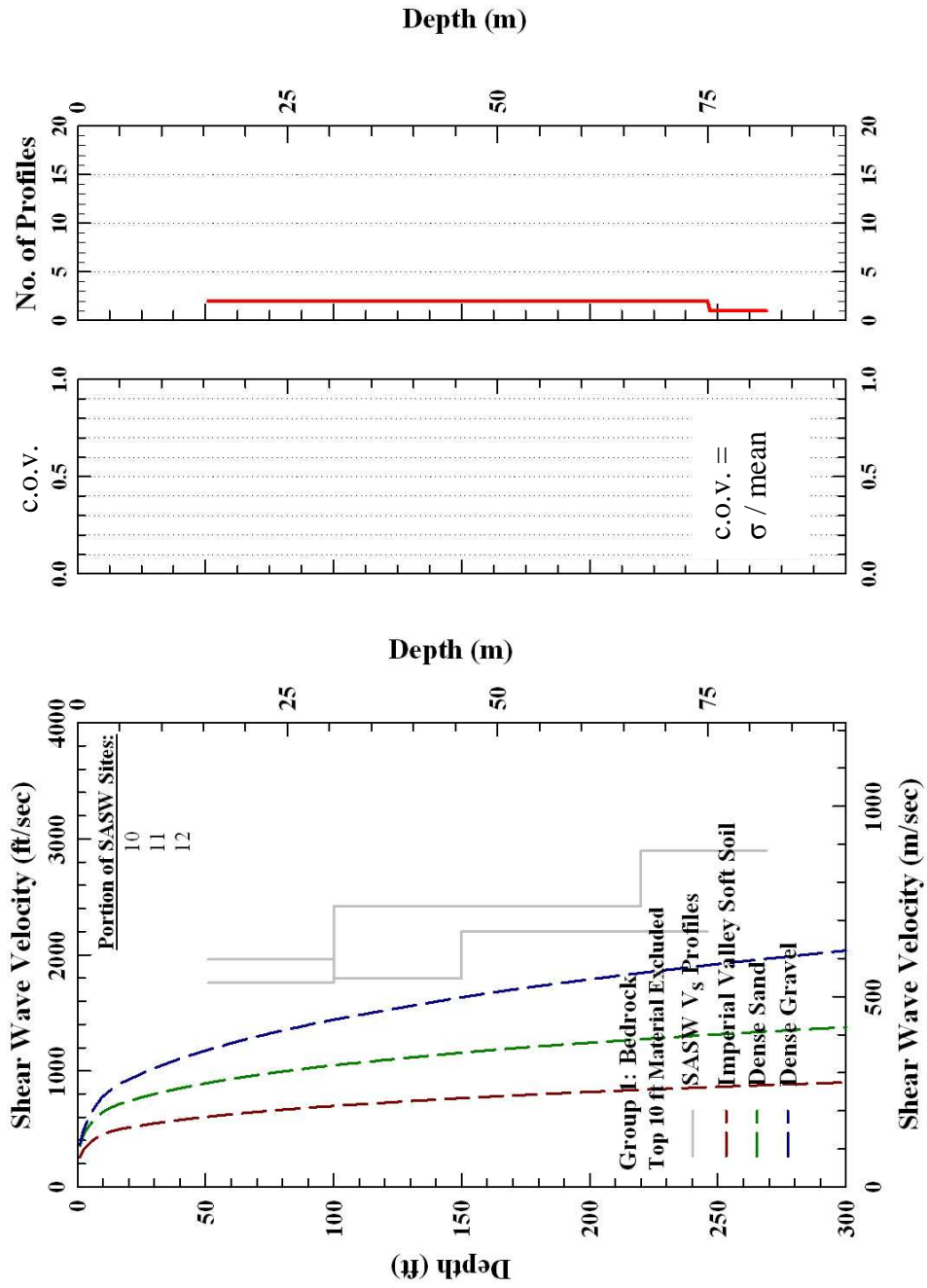
Figure 8.7 Comparison of the V_s Profile in Group 1 (Bedrock) with the Reference Soft Soil, Dense Sand and Dense Gravel Profiles

206
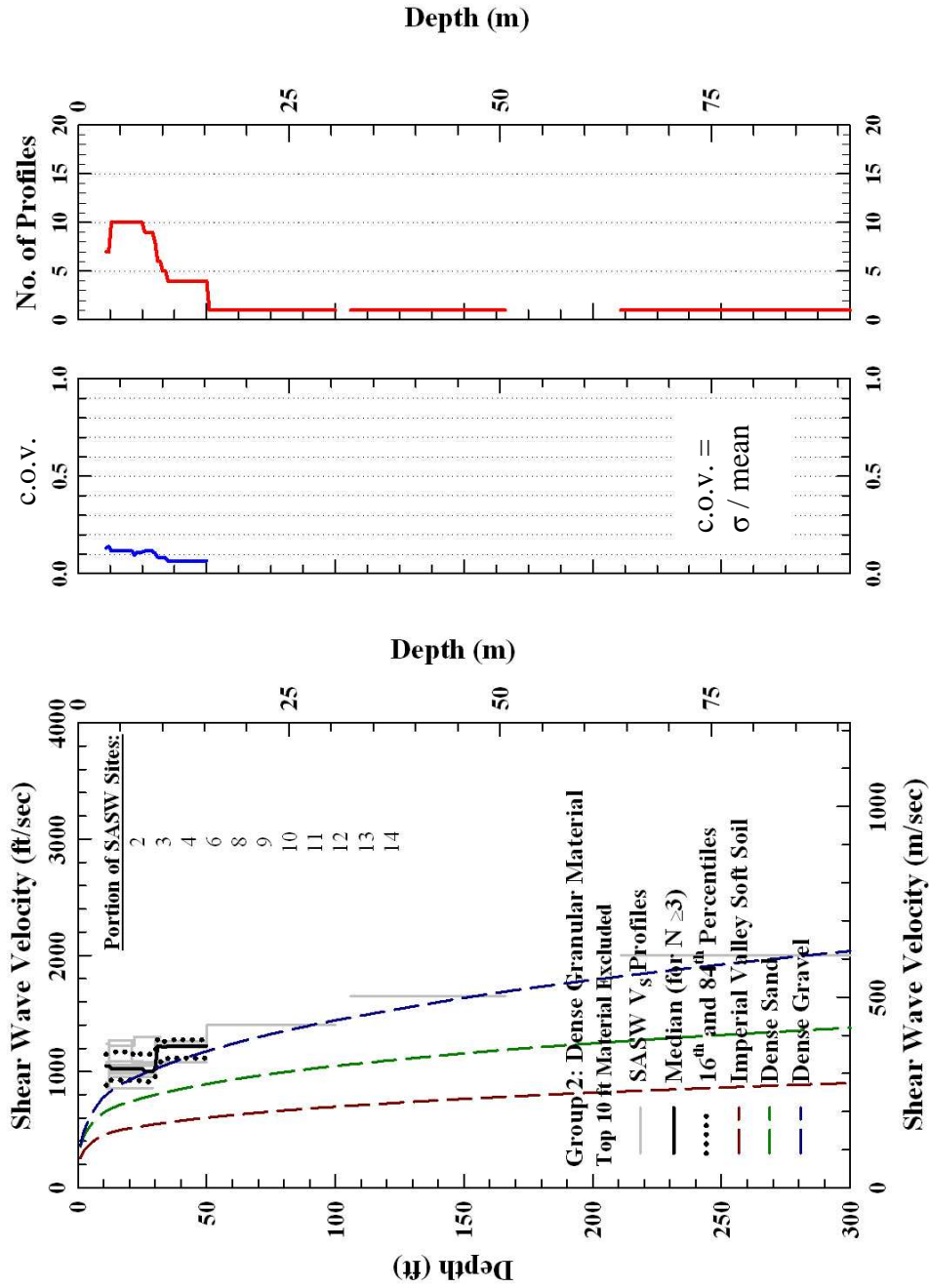
Figure 8.8   Statistical Analysis of the V_s Profile in Group 2 (Dense Granular Material) and Comparison with the Reference Soft Soil, Dense Sand and Dense Gravel Profiles
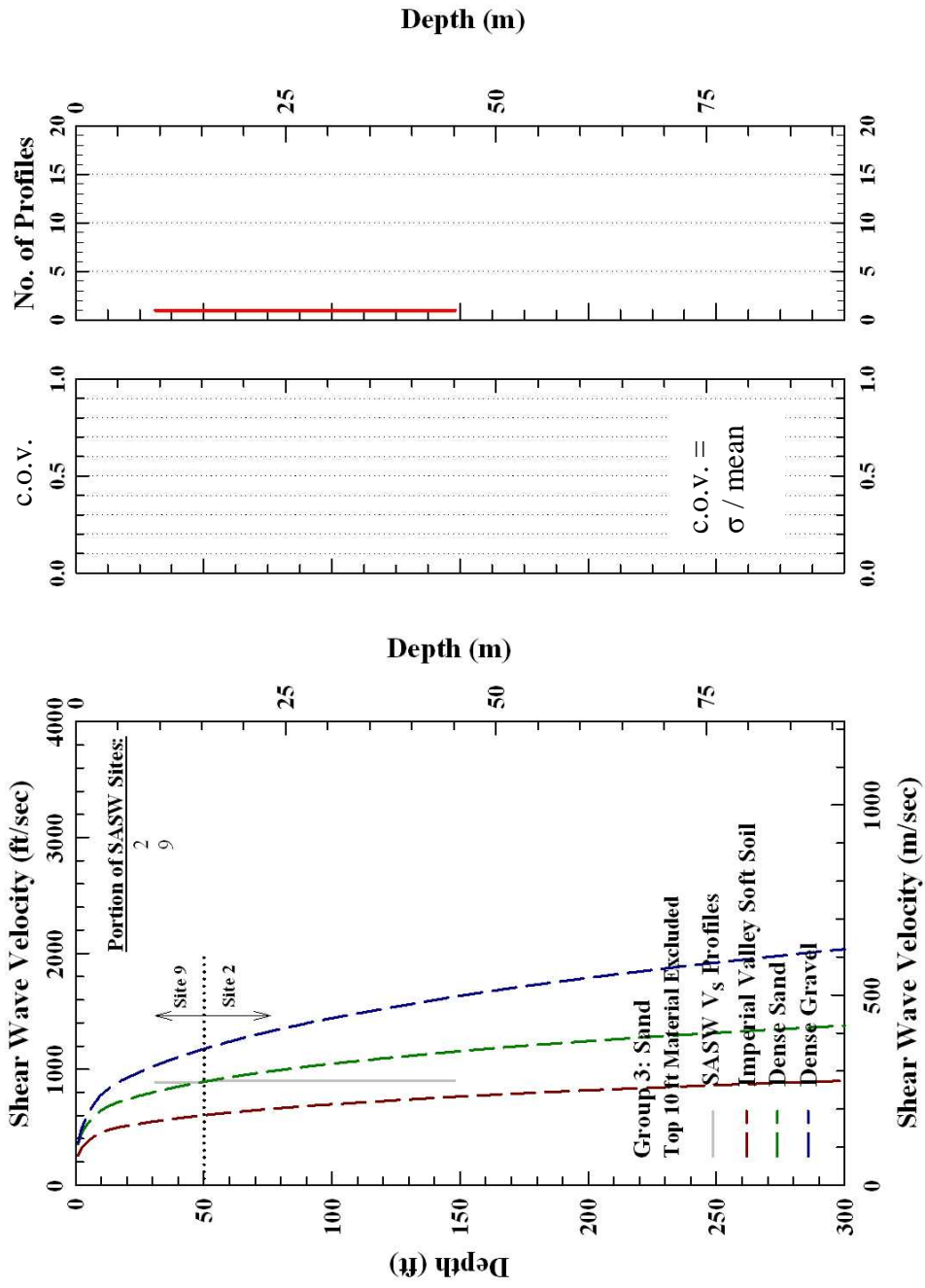
Figure 8.9   Comparison of the V_s Profile in Group 3 (Dense Sand Grading to a Less Dense Sand with Increasing Depth) with the Reference Soft Soil, Dense Sand and Dense Gravel Profiles

208
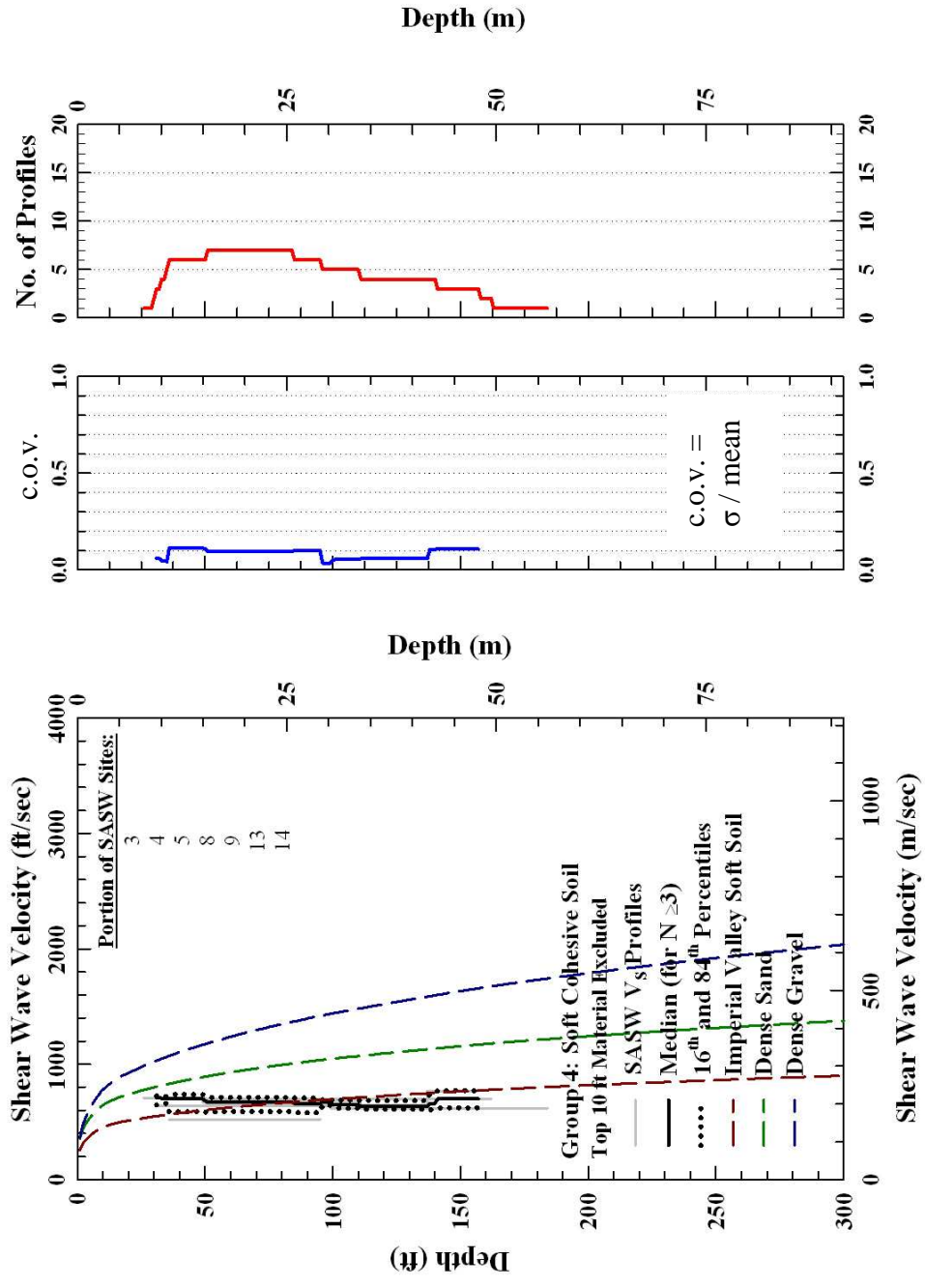
Figure 8.10 Statistical Analysis of the V$_s$ Profile in Group 4 (Soft Cohesive Soil) and Comparison with the Reference Soft Soil, Dense Sand and Dense Gravel Profiles

209
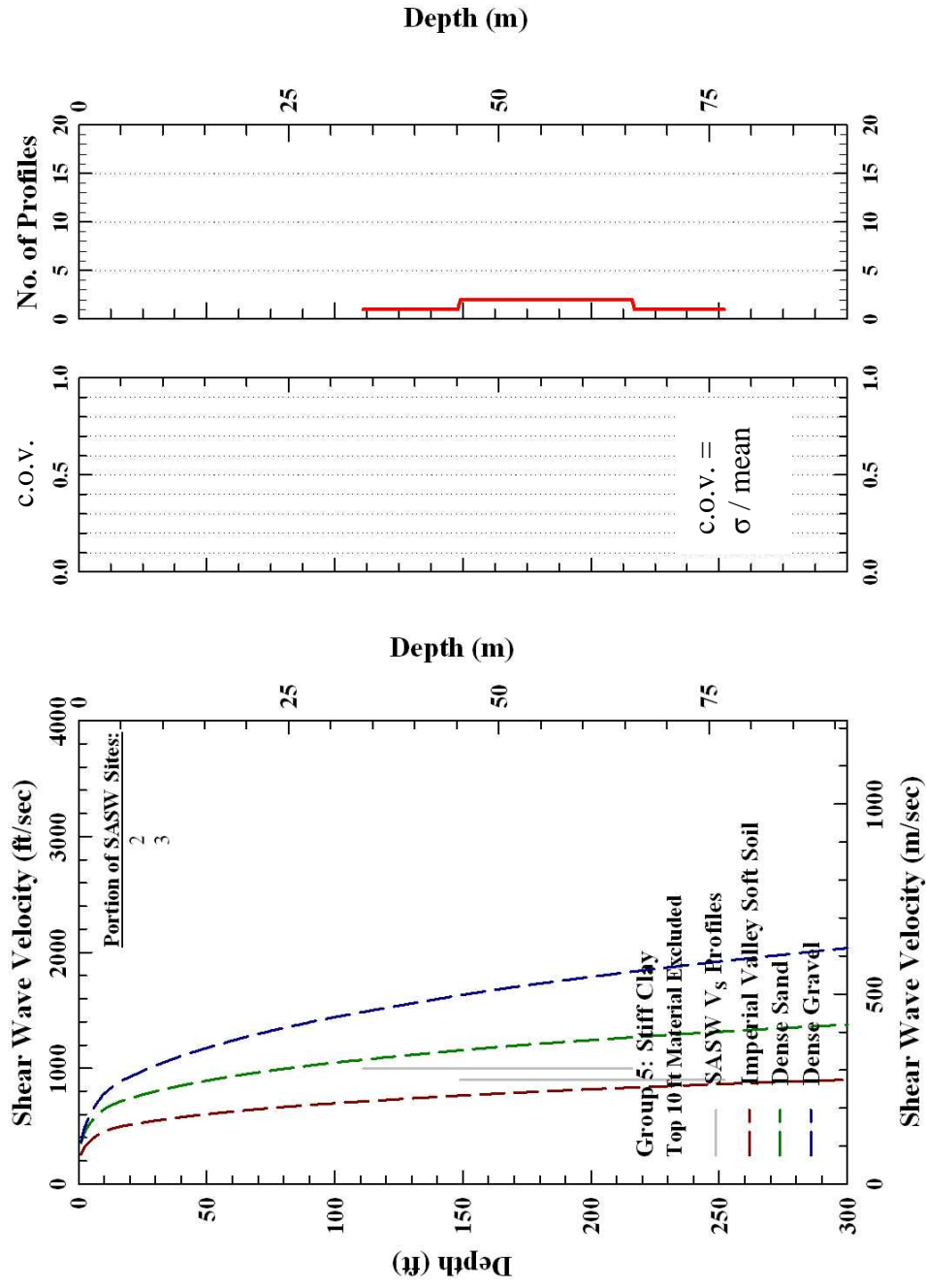
Figure 8.11   Comparison of the V_s Profile in Group 5 (Stiff Clay with Decreasing Stiffness with Increasing Depth) with the Reference Soft Soil, Dense Sand and Dense Gravel Profiles

210
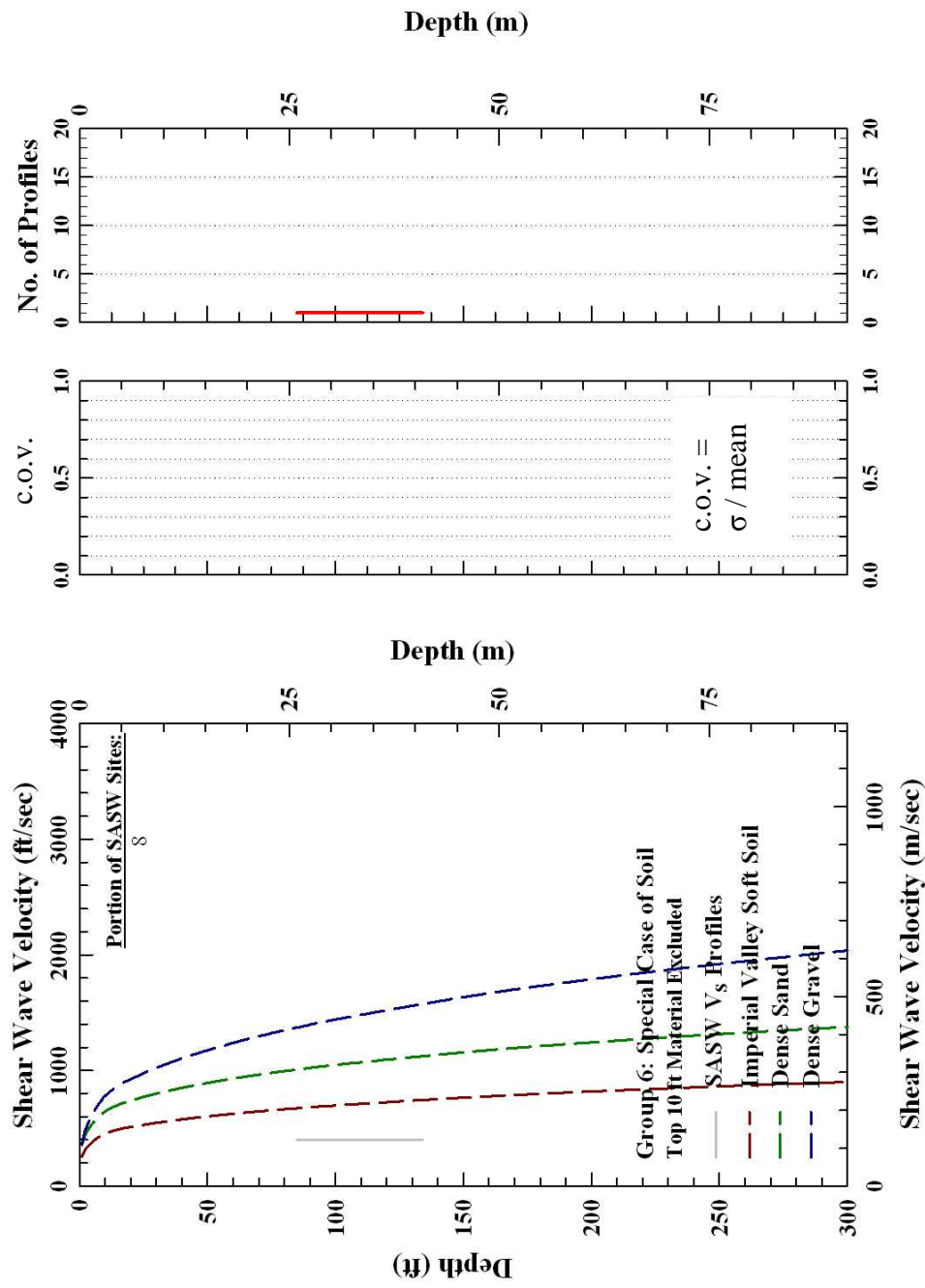
Figure 8.12   Comparison of the V_s Profile in Group 6 (Special Case of Soft Cohesive Soil) with the Reference Soft Soil, Dense Sand and Dense Gravel Profiles

211

- $V_s \geq 1800$ fps at depth ≤ 150 ft and $V_s \geq 2200$ fps at 150 ft $<$ depth $\leq$ 280 ft

- Numbers of sites involved: 10, 11 and 12.

2. Group 2: dense granular material with gravel and cobbles,

   - Presented in Figure 8.8.

   - V_s closely follows, but is slightly above, the gravel curve due to the addition of larger gravel particles and cobbles.

   - Numbers of sites involved: 2, 3, 4, 6, 8, 9, 10, 11, 12, 13 and 14.

3. Group 3: dense sand grading to a less dense sand with increasing depth,

   - Presented in Figure 8.9.

   - Numbers of sites involved: 2 and 9.

4. Group 4: soft cohesive soil (mixtures of silt, clay and minor amount of sand),

   - Presented in Figure 8.10.

   - Numbers of sites involved: 3, 4, 5, 8, 9, 13 and 14.

5. Group 5: stiff clay with decreasing stiffness with increasing depth,

   - Presented in Figure 8.11.

   - Numbers of sites involved: 2 and 3.

6. Group 6: special case of soil with very low shear wave velocity,

   - Presented in Figure 8.12.

   - Numbers of sites involved: 8.

The V_s groups with three or more profiles have been statistically analyzed to estimate the material distribution with depth at the site. The top 10 ft of material in all V_s

profiles was eliminated in the statistical analyses because of the additional variability due to weather and site construction activities.

The median V_s profiles for Groups 2 and 4 are presented in Figures 8.8 and 7.10. (Note – Groups 1, 3, 5 and 6 had only two profiles or less   so no median curve could be calculated.)   The V_s profiles in Figures 8.8 and 8.10 also include the 16th and 84th percentiles, the coefficient of variation (c.o.v. = σ / mean) and the number of profiles. As seen in these two figures, the c.o.v. ranges from 0.05 to 0.12. As noted earlier, values of c.o.v. less than about 0.15 are found in similar soils (Lin and Stokoe, 2008). This c.o.v. value (0.15) is used to justify separating the soils into Groups 2 through 6. In other words, the bedrock and soils in Groups 1, 3, 5 and 6 exhibit V_s profiles that can not be combined with or without Group 2 and 4 to give c.o.v. ≤ 0.15.

8.5 COMPARISON OF SASW V_s PROFILES AND OTHER TEST RESULTS

As noted earlier, borings, CPT, SPT and Seismic CPT tests were also performed at the project sites. Table 8.3 summarizes the reference boreholes close to each SASW array. Comparison between grouped SASW V_s profiles and boring records, SPT and SCPT results are presented below as a case study of how well the different measurements predict similar site conditions.

8.5.1   Comparison between Group-1 V_s Profiles and Existing Boring Records

"Bedrock" material as defined in Group 1 was found at Sites 10, 11 and 12 in the SASW V_s profiles. No boring was drilled at Site 11. At Site 10, the center of the SASW array had two nearby boreholes. A comparison between the V_s profile, material type and SPT results is shown in Figure 8.13. It is observed that at depths of 75 and 100 ft, dense material was met in boreholes and the borings were stopped. In terms of the V_s profile, an increase of shear wave velocity from 1400 fps to 1800 fps occurred in this depth range.
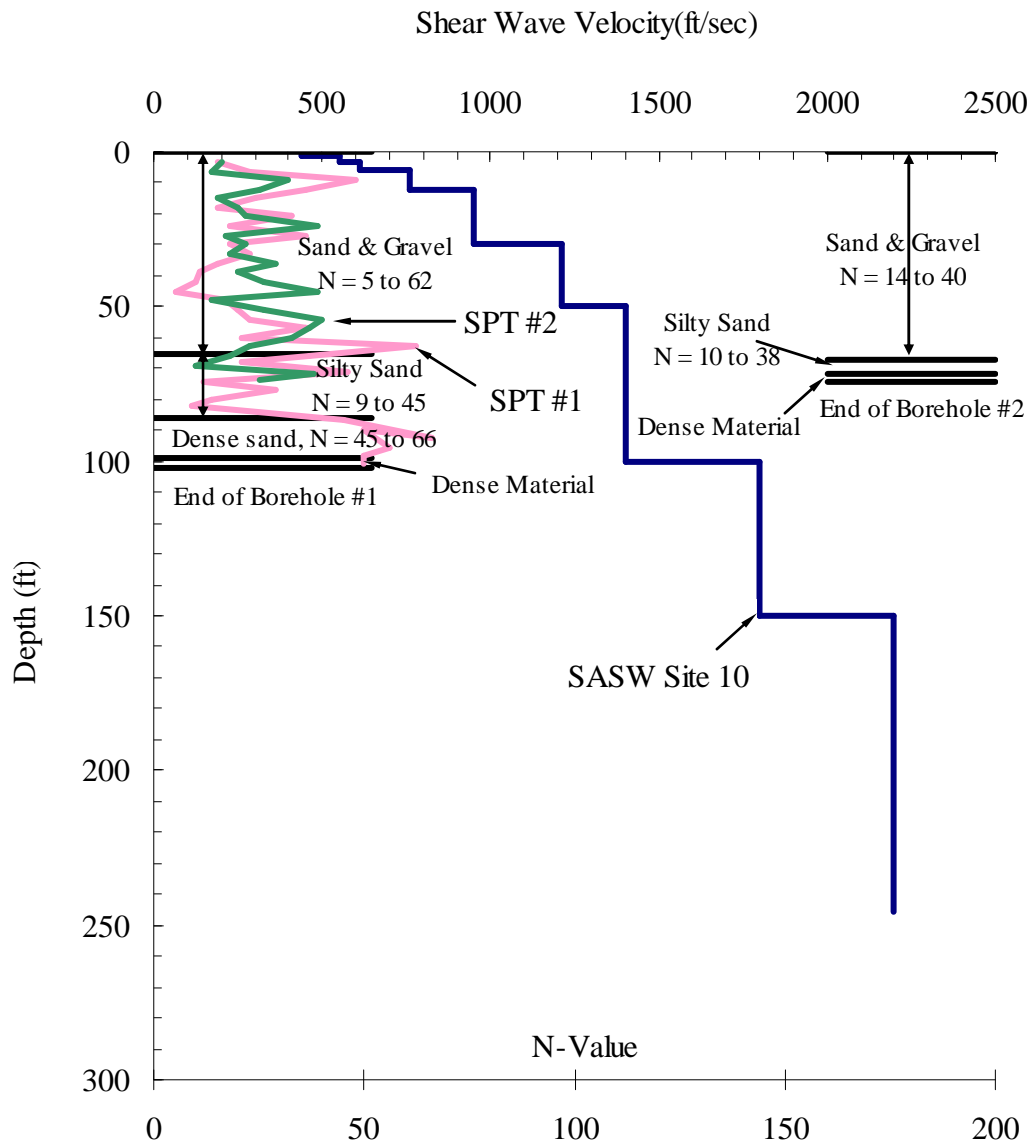
Figure 8.13   Comparison of the V_s Profile at SASW Site 10 with Material and SPT
Profiles from Boreholes #1 and #2

214

Although this V_s value is not much above that predicted for dense gravel, this agreement was taken to signify a shear wave velocity of fractured bedrock. The "bedrock" depths of 75 and 100 ft in the two boreholes was taken to indicate the lateral variability in the top of fractured and/or weathered bedrock.

For SASW Site 12, the comparison between the shear wave velocity profile and borehole results is presented in Figure 8.14. Both Boreholes #3 and #4 were drilled to a depth of about 50 ft and show sand and gravel with possible cobbles. It was reported that some cobbles were observed on the surface. The materials are generally medium dense to dense. When hard, rock-like material is encountered, the borehole generally ends at that depth. Thus, no CPT, SCPT or SPT data exists to compare with V_s profiles for bedrock. With this information, the borings likely stopped near the top of weathered rock. A corresponding velocity change in the V_s profile at a depth of 50 ft from 1250 fps to 1760 fps supports this assumption. The V_s profile between 50 to 100 ft is slightly less than 1800 fps (1760 fps), thus this part was originally not considered as bedrock However, based on records from Boreholes #3 and #4, the depth range from 50 to 100 ft in the V_s profile is likely to be in weathered bedrock material. Therefore, these data were included in the statistical analysis of "Bedrock" material.

To conclude, based on the comparison of V_s profiles and limited borehole records, the SASW method generally seemed to provide a reasonable estimate of depth to the top of weathered bedrock. The variation of depths to bedrock from borehole records shows lateral variability at the site. However, the SASW method provides an averaged measurement of bedrock depth over some lateral extent, with the lateral extent increasing

215
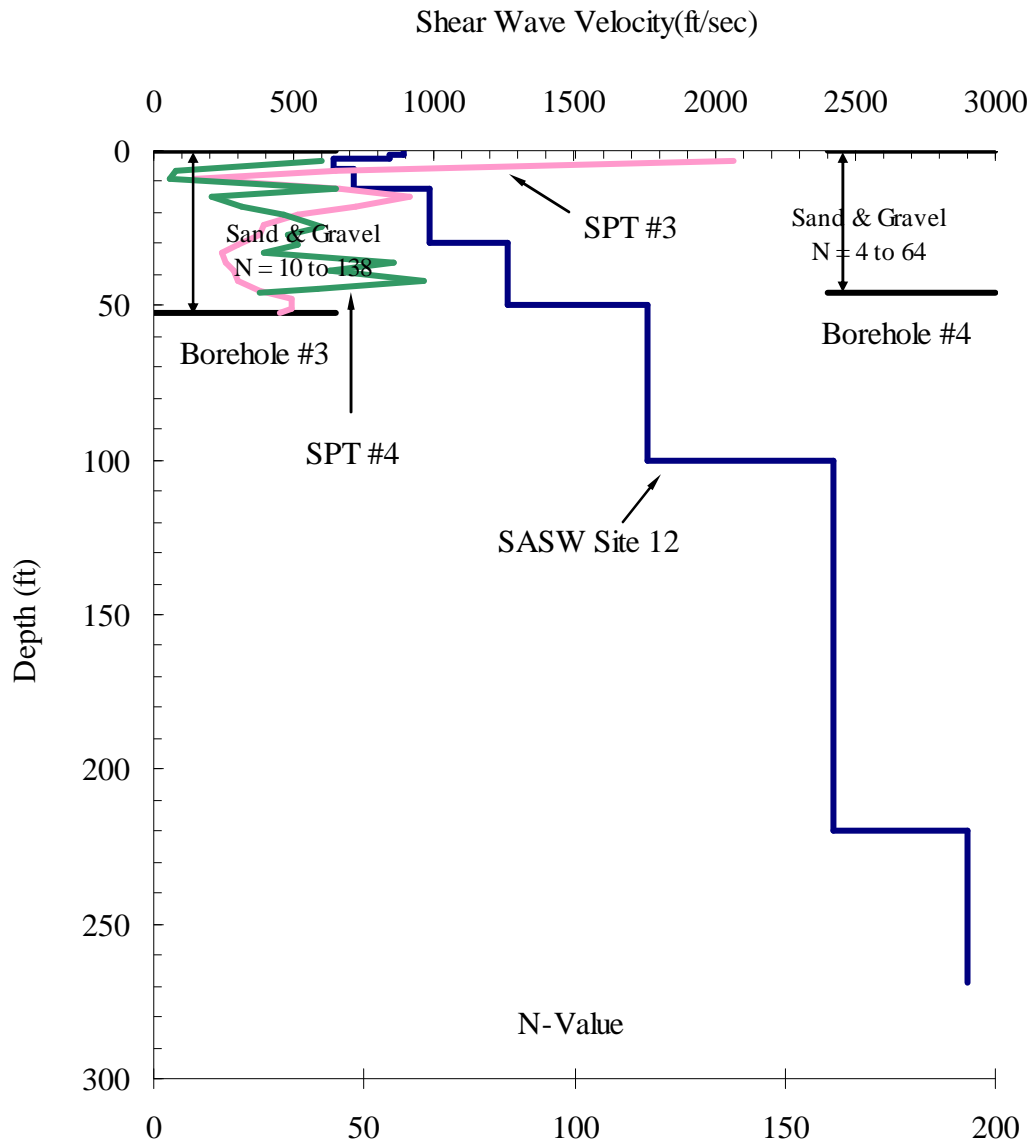
Figure 8.14 Comparison of the V_s Profile at SASW Site 12 with Material and SPT Profiles from Boreholes #3 and #4

as depth increases.

8.5.2 Comparison between Group-2 V_s Profiles and Existing Boring Records

Group 2 materials have V_s values slightly above the dense gravel curve as shown in Figure 8.8. It can be seen from boring records that, this group corresponds to dense granular materials which mainly exist at shallow depths ($\leq$ 50ft). For example, at SASW Site 2, the top 54 ft of materials is a mixture of dense and very dense sand and gravel from 0 to 35 ft underlain by loose gravelly sand from 35 to 54 ft as shown in Figure 8.15. The N-value profile shows a similar trend as V_s profile in the dense granular material but not in the loose granular material. The boundary in the SPT profile between dense sand/gravel and loose gravelly sand is not shown in the V_s profile.

Another example of comparing the V_s profile and near-by borings in gravel is shown in Figure 8.13. Two SPT profiles are shown in the figure. In the first 65 ft, the general trend in the SPT values is increasing, with the exception of SPT #1 around a depth of 45 ft. This apparently loose material is not identified in the SASW profile. The likely reason is that the layer is not continuous laterally as seen by comparing the two nearby SPT profiles. Also, the silty sand layer at depths from 65 to 85 ft has a low blowcount. In shear wave velocity profile the value of V_s does not drop accordingly. Again, the likely reason is the lateral variability, hence the lack of continuous material stiffness and thickness, that is seen by comparing Borings #1 and #2 and SPT profiles #1 and #2.

8.5.3   Comparison between Group-3 V_s Profiles and Existing Boring Records

Group 3 materials are categorized as sand with stiffness generally decreasing with increasing depth. These materials have shear wave velocities in the range of dense sand materials from about 30 to 80 ft. From 80 to 150 ft, the sand is becoming less dense or the material is changing because the fine content seems to b increasing. These materials are found only at SASW Sites 2 and 9. As illustrated in Figure 8.16, the Group 3 materials in the depth range from 54 to 147 ft were identified by CPT #1 as a sand mixture with clay, with this material having a constant V_s value of 900 fps over the 54 to 147 ft depth range at Site 2. At Site 9 in Figure 8.17, the Group 3 materials fall into a zone of compact sand and gravel from 20 to 72 ft with lower blowcount.
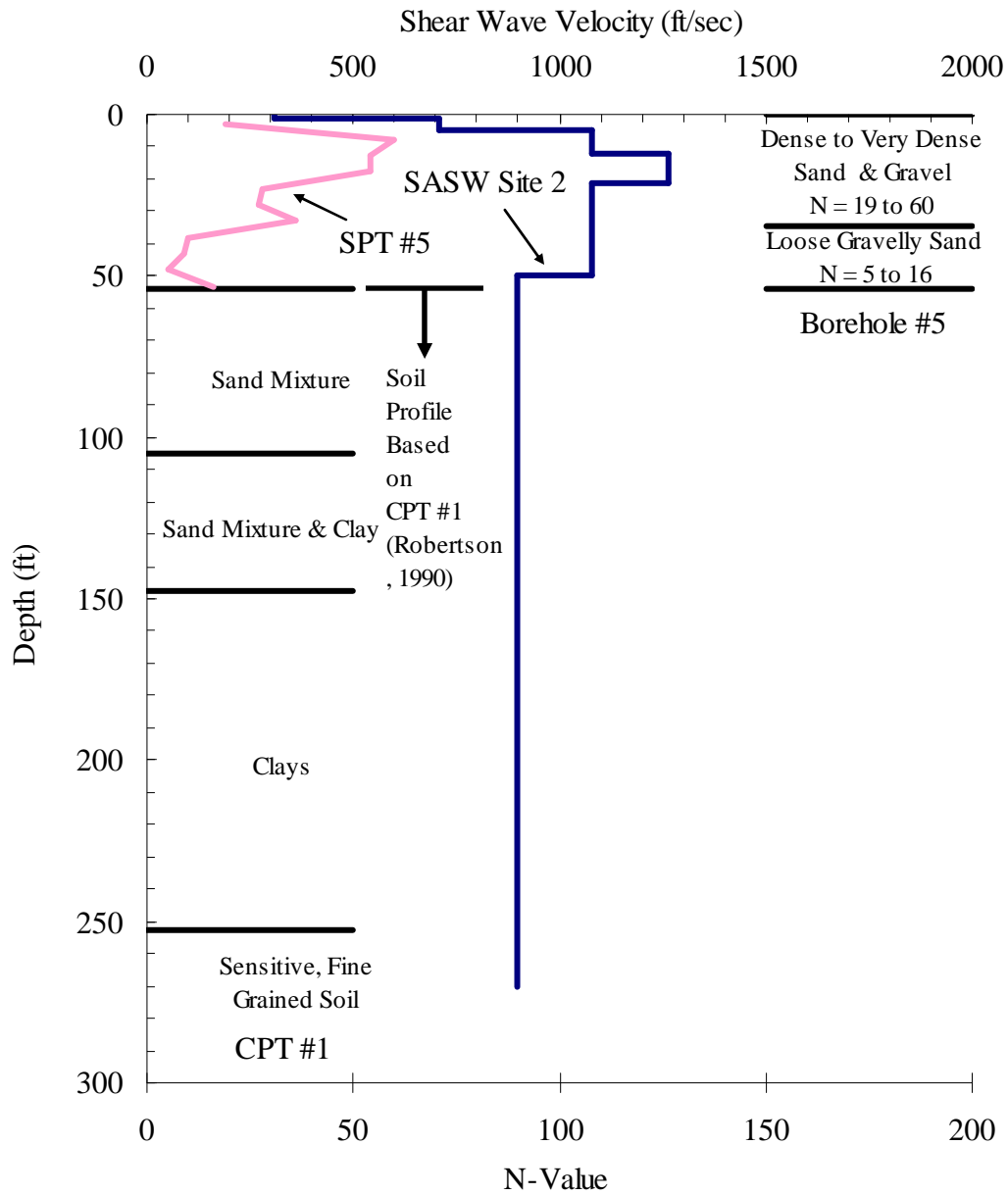
Figure 8.15 Comparison of the V_s Profile at SASW Site 2 with Material and SPT Profiles from Borehole #5

Figure 8.16 Comparison of the V_s Profile at SASW Site 2 with Material and CPT
Profiles from Borehole #5 and CPT #1
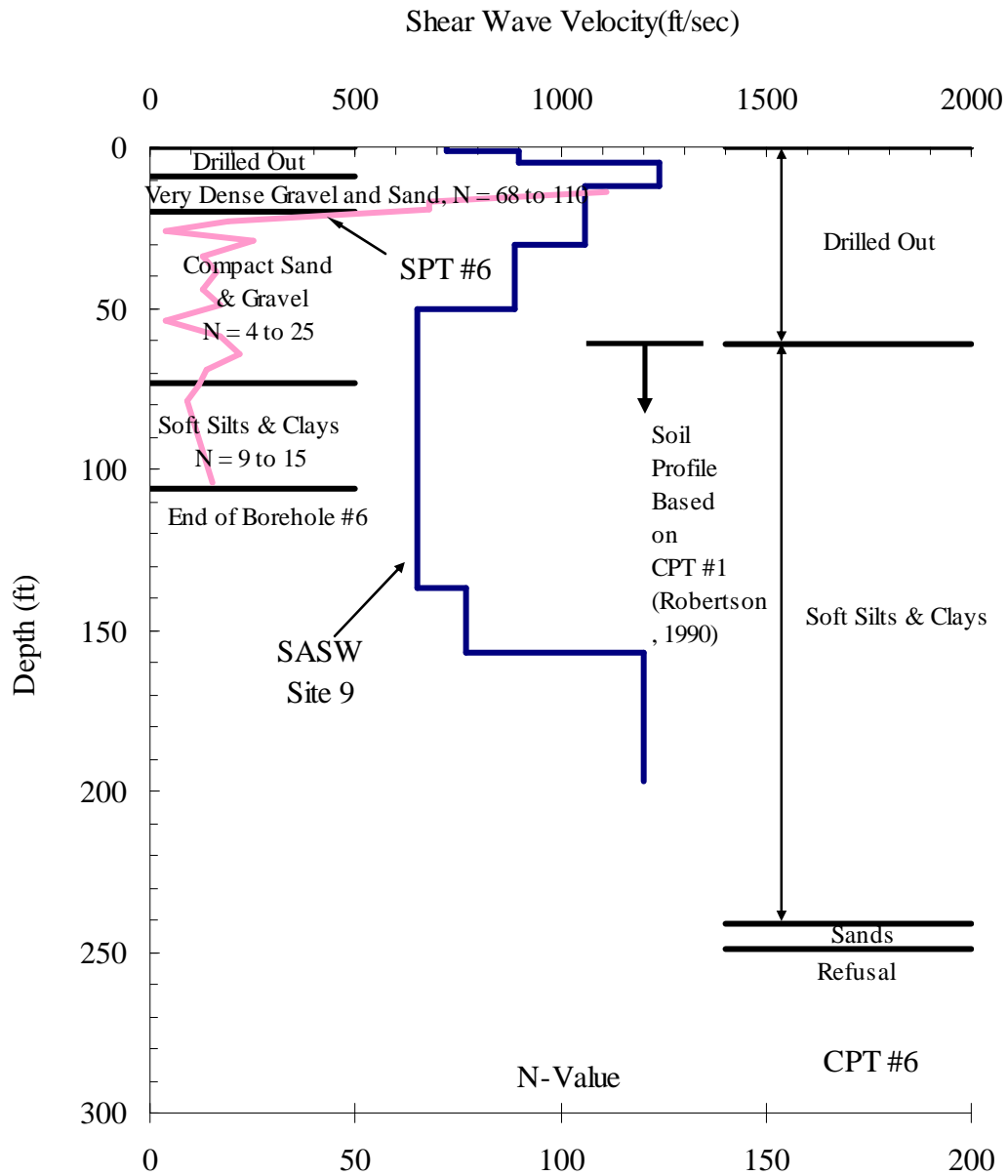
Figure 8.17   Comparison of the V_s Profile at SASW Site 9 with Borehole and SPT
Profiles from Borehole #6 and CPT #6

8.5.4 Comparison between Group-4 V_s Profiles and Existing Boring Records

Group 4 materials are termed soft cohesive soil which have a shear wave velocity profile close to soft soil in Imperial Valley, CA. For example, the V_s profile at SASW Site 14 with borehole information and SPT results are shown in Figure 8.18. The material depth from about 35 to 95 ft is categorized as soft silt and sand with organic material from Borehole #7. This soft soil is also shown by the low V_s values in this depth range and the velocities compare well with the soft soils in Imperial Valley. These materials below 35 ft also exhibit relatively low blowcount values as expected. Borehole #7 ended at about 95 ft so no geological information below that depth is available. Interestingly, the V_s results identify the material boundary at about 35 ft between the upper gravel and the soft soil. Similarly, at SASW Site 13 in Figure 8.19, the V_s profile in the depth range of 30 to 187 ft is grouped as soft soil, and nearby Borehole, #8, reveals the existence of soft silt from 32 to 192 ft with blowcount varying from 0 to 33. The SPT results confirm the soft material in this depth range. It is noted that a soft zone (a silt layer) below the dense sand layer at a depth of about 220 ft was found in Borehole #8. This soft zone is not shown in the SASW V_s profile. The reasons for this "miss" are likely the lake of resolution at deeper depths in detecting thinner layers with velocity inversions and the possible lake in lateral continuity of this soft layer. It is concluded that at both sites, the Group 4 materials, soft cohesive soil, were defined in terms of both general depth range and low velocity values by the SASW method.

Figure 8.18 Comparison of the V_s Profile at SASW Site 14 with Borehole and SPT Profiles from Borehole #7
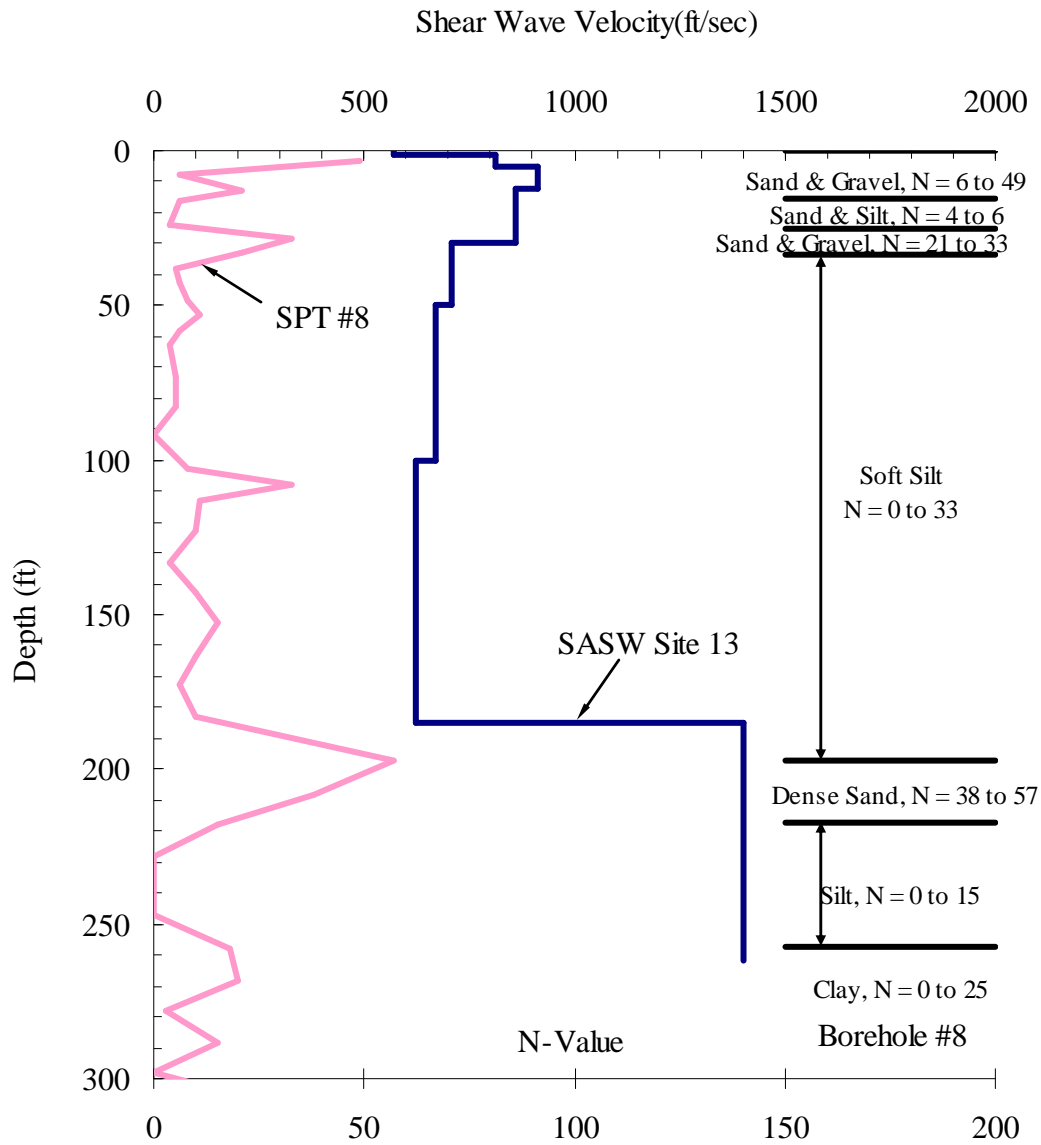
Figure 8.19 Comparison of the V_s Profile at SASW Site 13 with Borehole and SPT
Profiles from Borehole #8

8.5.5 Comparison between Group-5 V_s Profiles and Existing Boring Records

Group 5 materials are considered to be stiff clay. These materials are included in parts of profiles from SASW Site 2 and 3, Figures 8.16 and 8.20, respectively. These materials exhibit shear wave velocities around 1000 fps at relatively deep depths (from 100 to 250 ft). By comparing to reference curves, the material is stiffer than soft soil but softer than the reference curve of dense sand. Two boring logs were used to investigate the material in group 5. An example of this stiff clay is shown in Figure 8.20 from 110 to 220 ft at Site 3. Based on CPT #9, the corresponding materials are clay and silt mixtures.

8.5.6 Comparison between Group-6 V_s Profiles and Existing Boring Records

Group 6 materials are termed "special case of soil" with low shear wave velocity. This soil was present in the SASW V_s profile at Site 8 in the relatively deep depth range of 85 to 135 ft (see Figure 8.21). SASW Site 8 is the only site where this material was found. Nearby Boreholes #11 and #12 show that the material is likely soft silt or clay with very low blowcount values. However, the velocity contrast shown in the V_s profile in the 85 to 135 ft depth range is not clearly shown in the borehole or SPT results as seen by reviewing Figure 8.21. However, the SASW dispersion curve clearly shows this inversion.

Shear Wave Velocity(ft/sec)

Figure 8.20 Comparison of the V_s Profile at SASW Site 3 with Borehole and SPT
Profiles from Borehole #9, 10 and CPT #9

Shear Wave Velocity(ft/sec)

0   500   1000   1500   2000

Depth (ft)

0

Drilled Out
Dense Gravel, N = 19 to 39
Loose Sand, N = 4 to 12
Soft Silt
and Clay
N = 2 to 6

SPT #9

Drilled Out
Dense Sand, N = 60 to 75

Dense Sand & Gravel
N = 19 to 68

End of Boring #9

Sand
N = 7 to 12

50

Bottom of
Borehole #10

SPT #10

Soil
Profile
Based
on
CPT #9
(Robertson
, 1990)

Clay and Silt
Mixtures

100

150

200

Refusal

SASW Site 3

250

N-Value

300

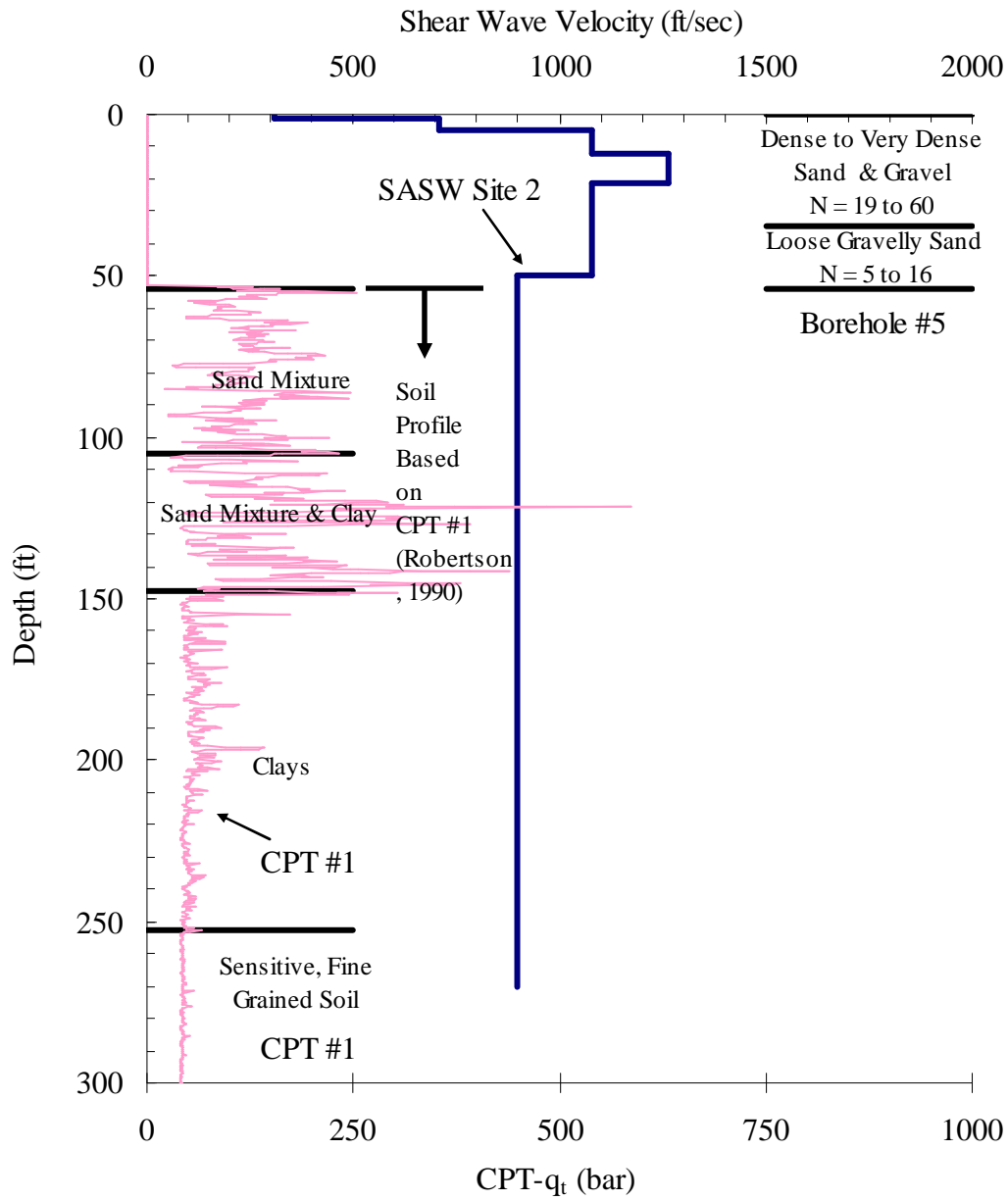0   50   100   150   200

Figure 8.20 Comparison of the V_s Profile at SASW Site 3 with Borehole and SPT
Profiles from Borehole #9, 10 and CPT #9

Figure 8.21 Comparison of the V_s Profile at SASW Site 8 with Borehole and SPT
Profiles from Boreholes #11 and 12

8.6 LATERAL VARIABILITY STUDY

Lateral variability at the project site was studied using the existing boring logs. Three SASW sites, each with two logs as references, were used to show lateral variability in the material.

The first comparison is presented in Figure 8.22 in which the shear wave velocity profile at SASW Site 10 is compared to two nearby boring logs. It is seen that both logs demonstrate a sand/gravel layer from the ground surface to a depth of about 65 ft. The Borehole #1 shows a 20-ft silty sand layer which is in contrast to Borehole #2 in which a thinner, 7-ft thick layer of silty sand was found. Both records ended at depth where stiff, 'bedrock-like' material was encountered. It is observed that the depth to the stiff material varied in the two boring logs (100 ft in #1 vs 75 ft in #2). Since Borehole #1 is closer to the center of test array, the depth to stiff material agrees well with the Group-1 material from the SASW V_s profile at Site 10.

The geological settings from two nearby boreholes at SASW Site 3 are shown in Figure 8.23. Both boreholes have a similar drilled-out depth of 10 ft due to the existence of granular material with cobbles at ground surface. It is again observed that lateral variability exists according to SPT blowcounts and the depth to the soft silt and clay layer from the boring and CPT records. The V_s profile produced a good estimate of the thickness of sand/gravel materials at shallow depth (25 ft or less). However, in the depth range of 25 to about 50 ft, the dense sand and gravel in Borehole #9 was not detected. Rather, the soft silt and clay in Borehole #10 was detected. This difference is attributed to lateral variability at the site. The V_s profile did not predict the depth to stiff material at a

228
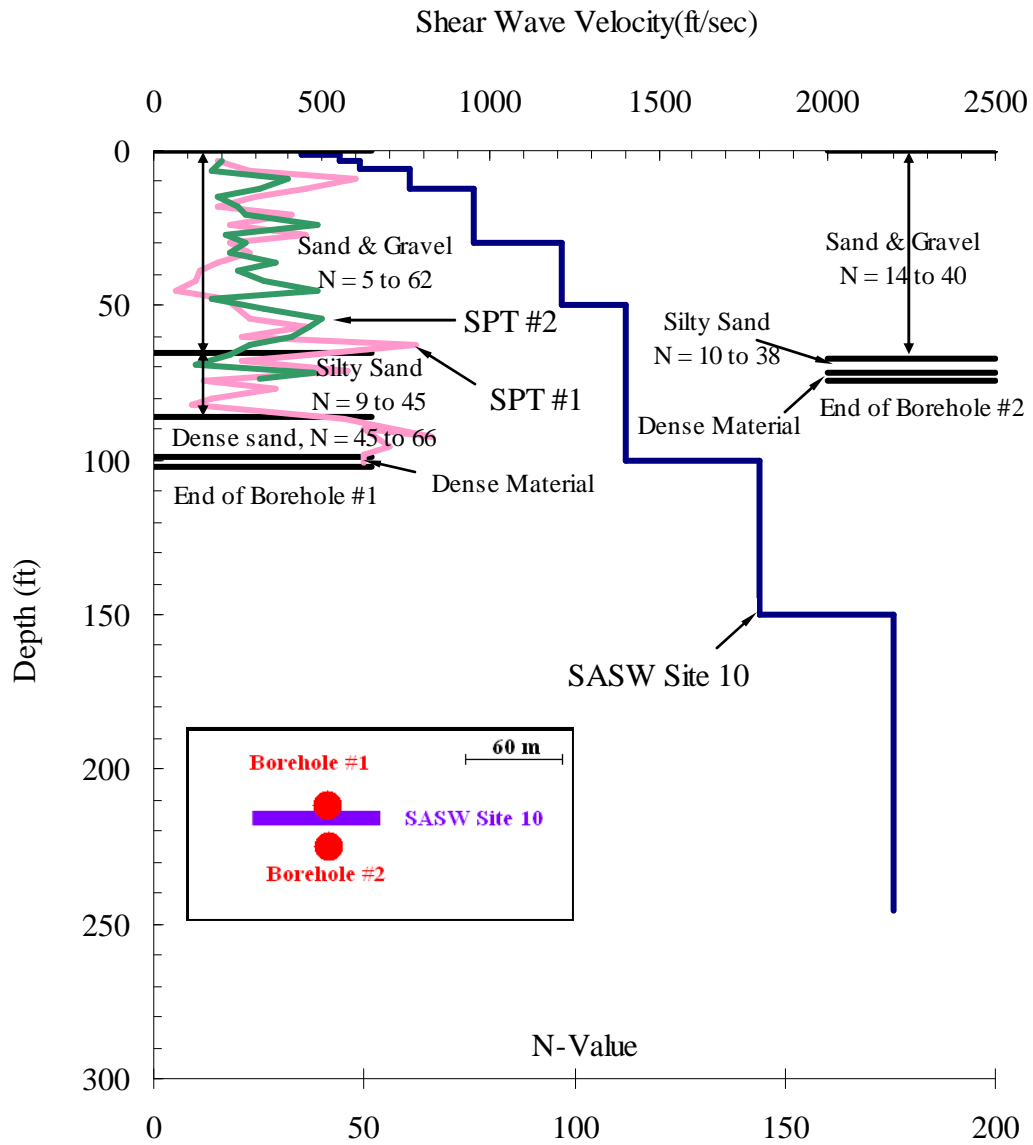
Figure 8.22 Comparison of the V_s Profile at SASW Site 10 with Borehole and SPT Profiles from Boreholes #1 and #2
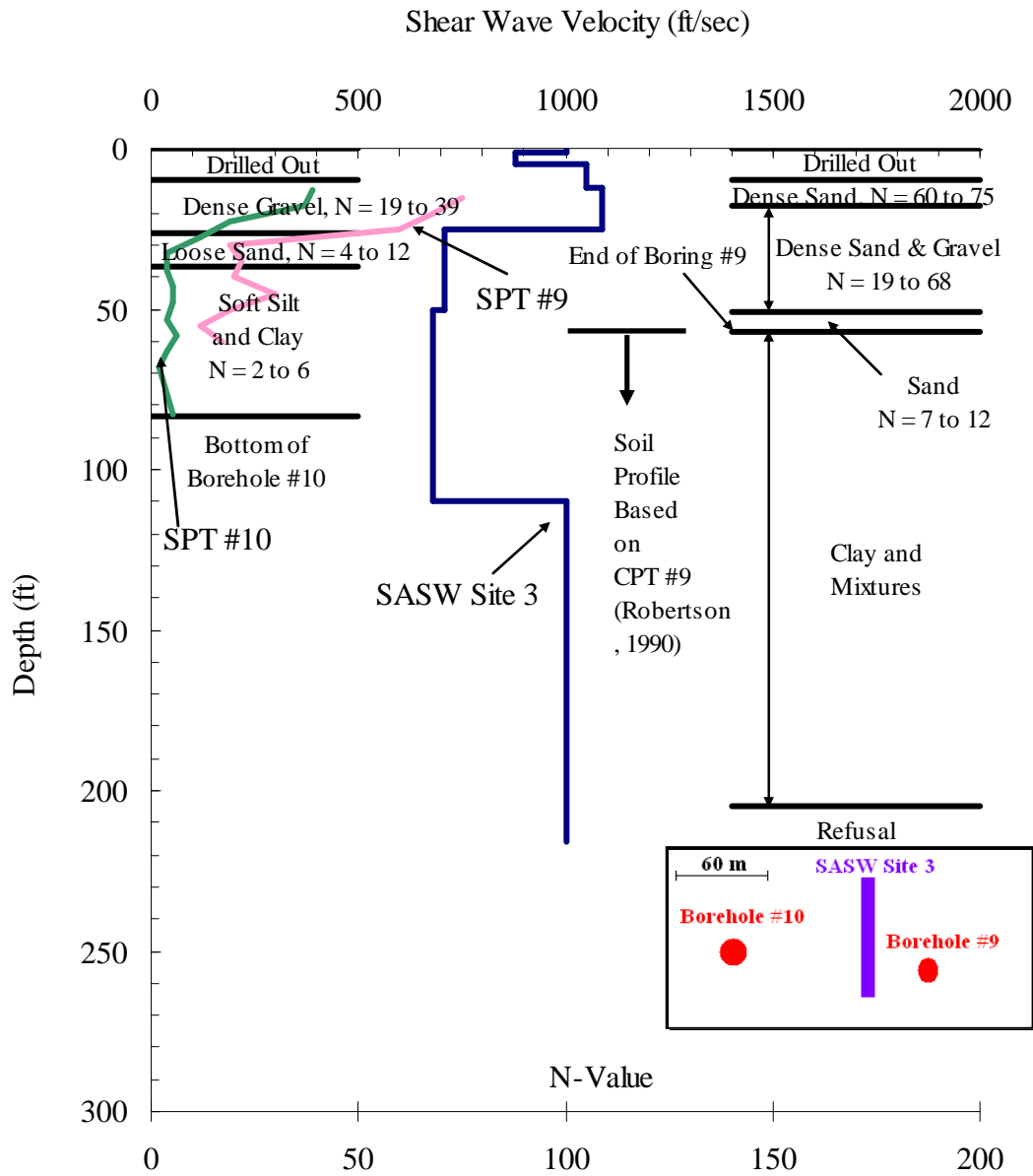
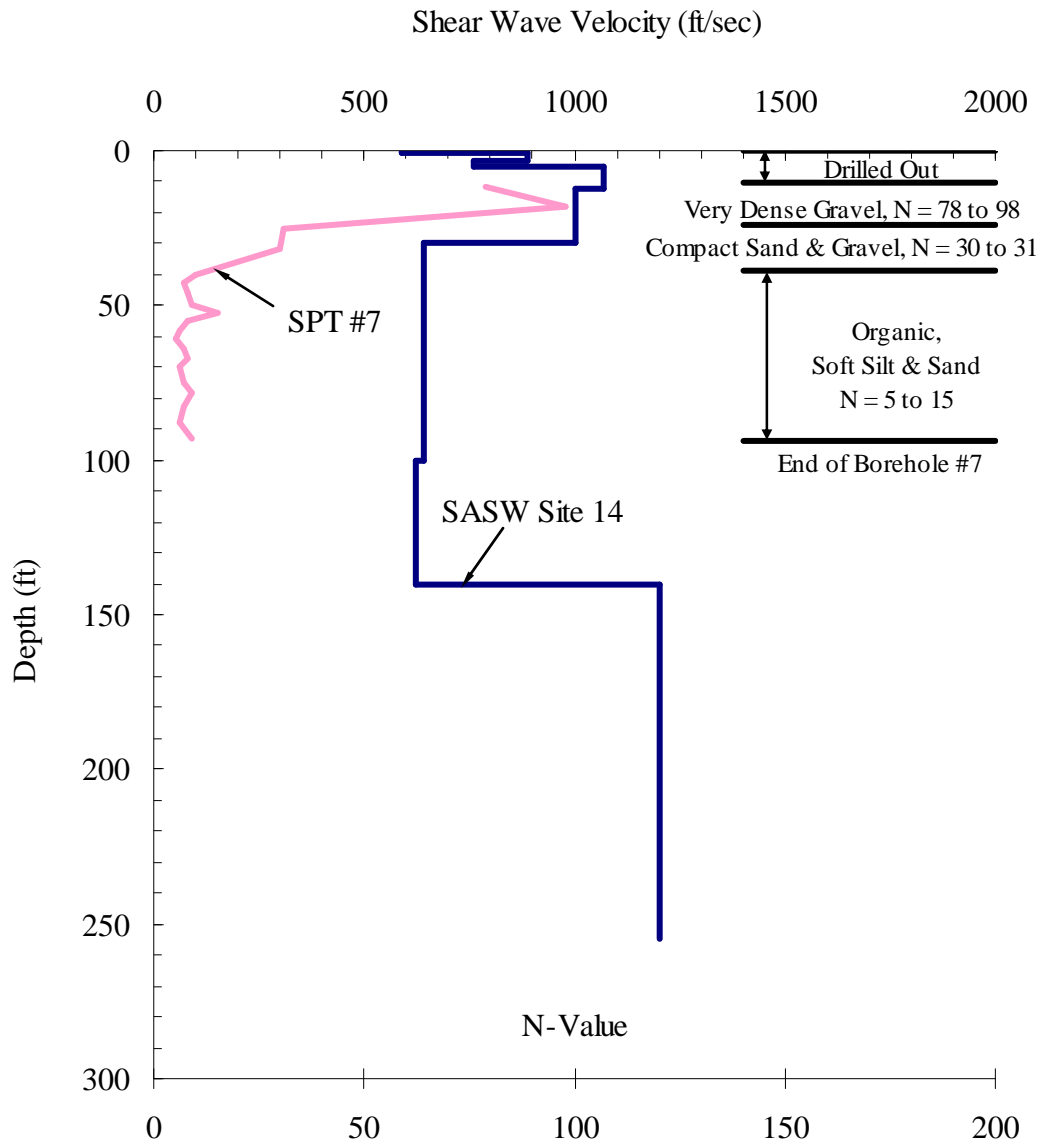Figure 8.23 Comparison of the V_s Profile at SASW Site 3 with Borehole and SPT Profiles from Boreholes #9 and #10 and CPT #9

230

depth of about 200 ft, mainly due to the limitation of energy produced by the bulldozer at the largest receiver spacing required to sample below a depth of 200 ft.

In Figure 8.24, the V_s profile is compared to the geological information from two boring logs near SASW Site 8. The top sand/gravel layers from both logs are similar in terms of layer thickness, which also agrees with the SASW V_s profile. The two logs show different estimates of the silt layer, one from 45 to 93 ft in Borehole #11 and another from 27 to 105 ft in Borehole #12. Both logs show a layer of silty clay down to about 250 ft where stiff materials are encountered. Disagreement is observed from the V_s profile at a depth of 137 ft, where SASW tests shown a velocity increase from 400 to 1200 fps. No evidence of material change at this depth is shown by both borehole records. It is possible that stiff materials at this depth were sampled locally by surface waves since the measurement at the larger receiver spacing (200 ft) was only performed at one end of the SASW test array which was near to the mountain and away from the water.

To conclude, lateral variability in material distribution clearly exists at the project site. The clossness of the matching between global measurements from SASW testing and localized measurements from borings and CPT is highly dependent on the lateral variability of the site.

8.7 COMPARISON OF RESULTS FROM SASW AND SCPT TESTS

8.7.1   Comparisons of V_s Profiles

The comparison between SCPT V_s profiles and SASW V_s profiles are shown in Figures 8.25 through 8.28. As seen in these figures, there are differences between the two types of V_s profiles. The main differences between the two techniques are attributed to
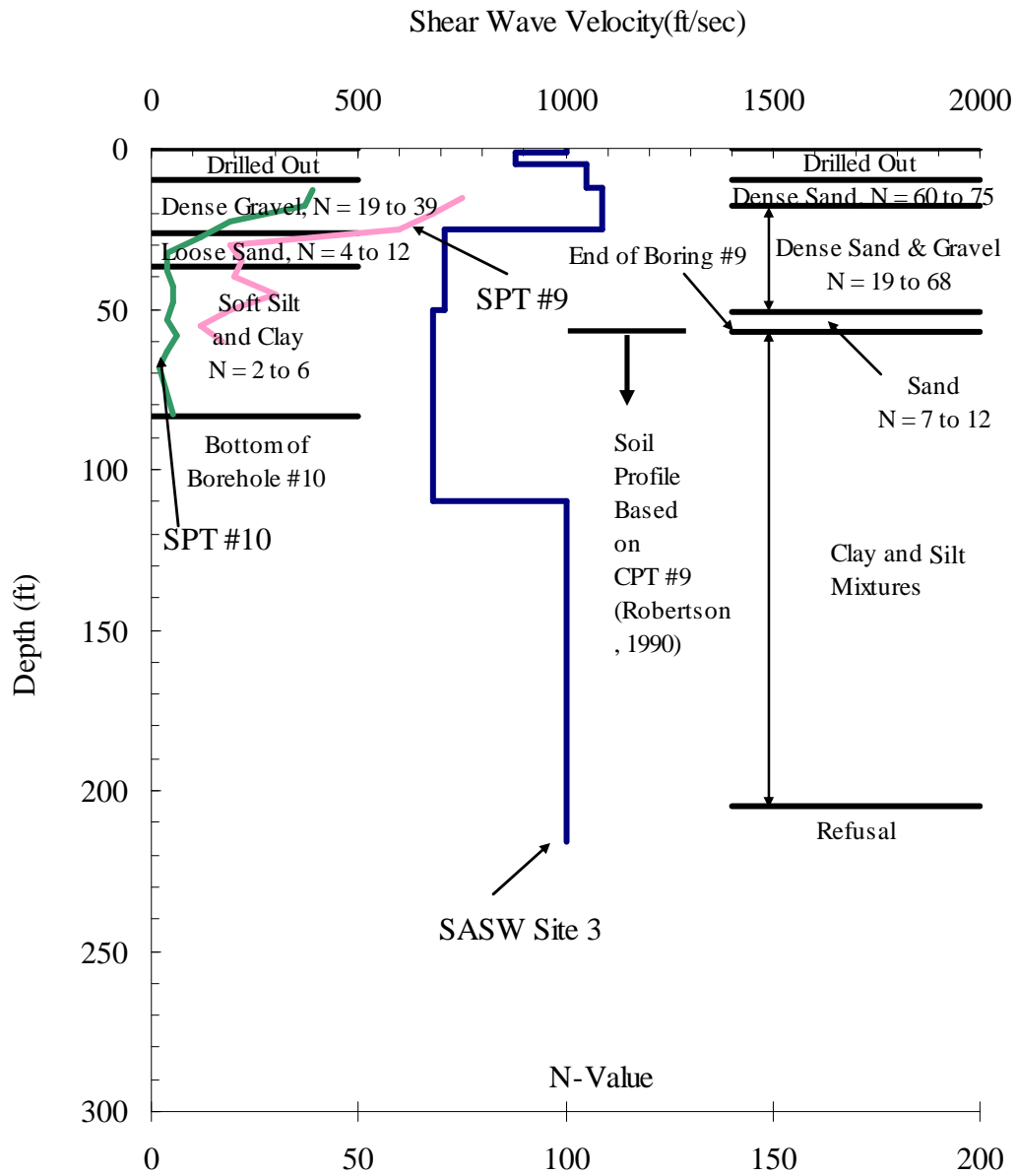
Shear Wave Velocity (ft/sec)
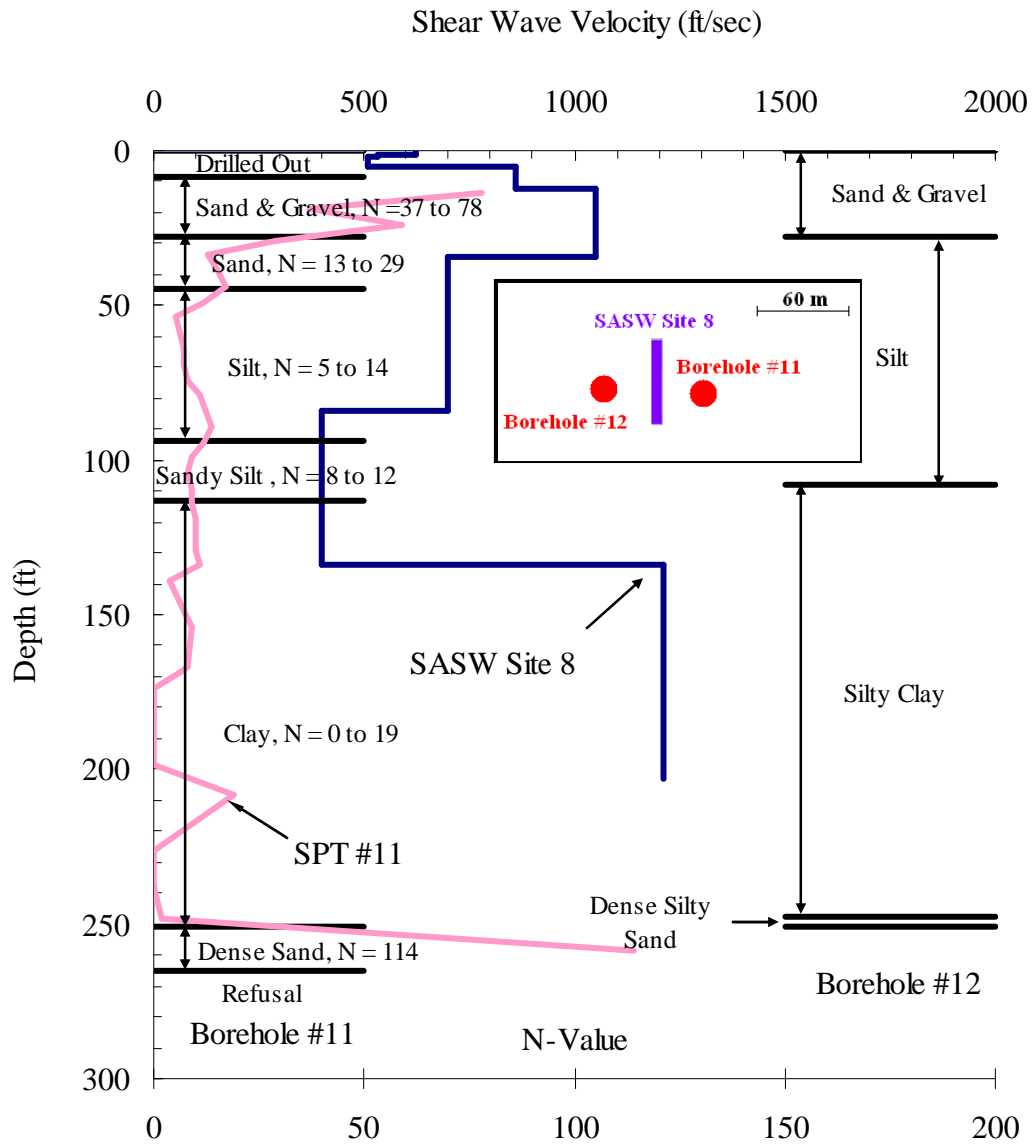
Figure 8.24 Comparison of the V_s Profile at SASW Site 8 with Borehole and SPT
Profiles from Boreholes #11 and #12
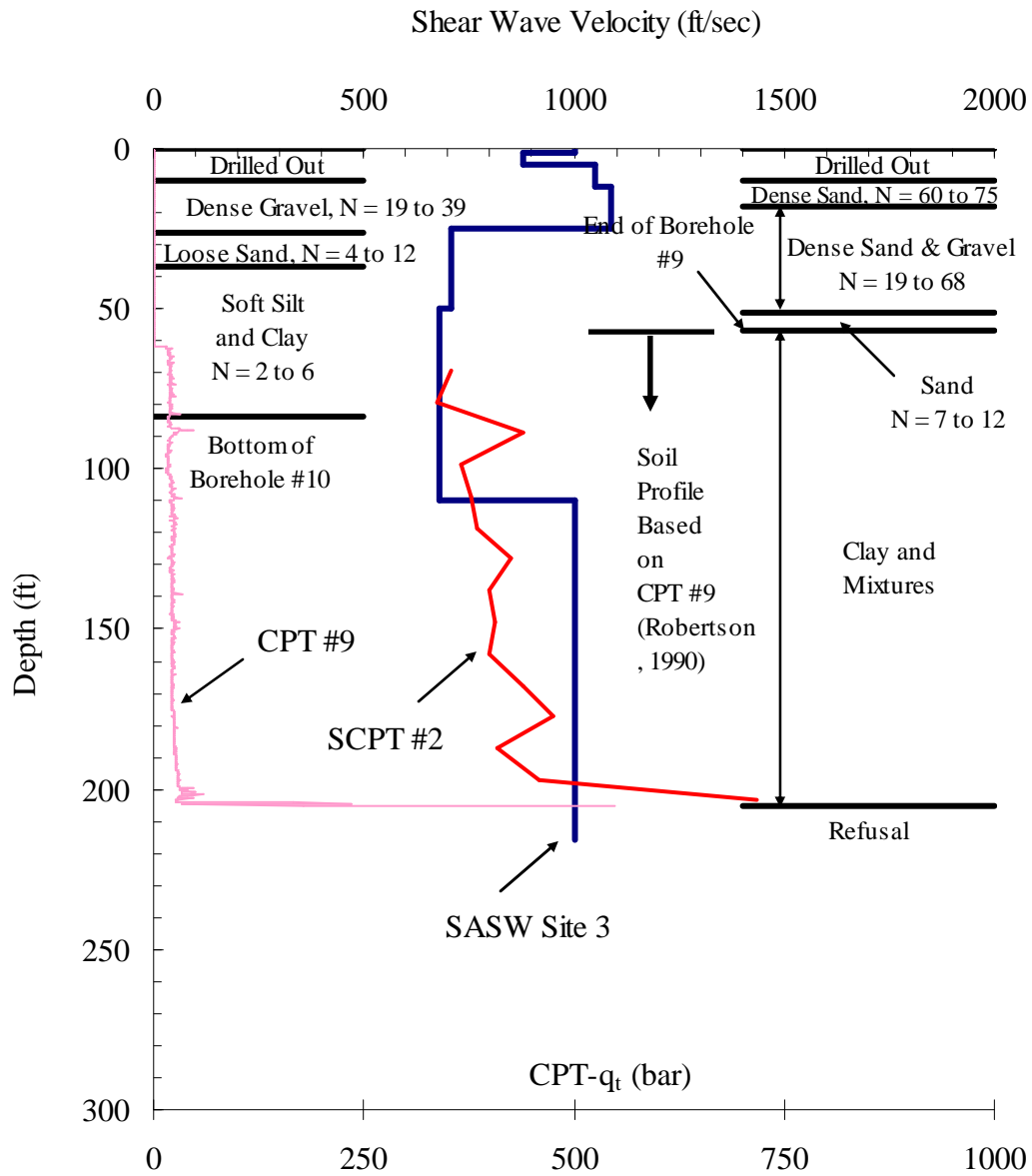
Figure 8.25 Comparison of the V_s Profile at SASW Site 3 with the V_s Profile from SCPT #2 and Borehole and CPT Profiles from Boreholes #9 and #10
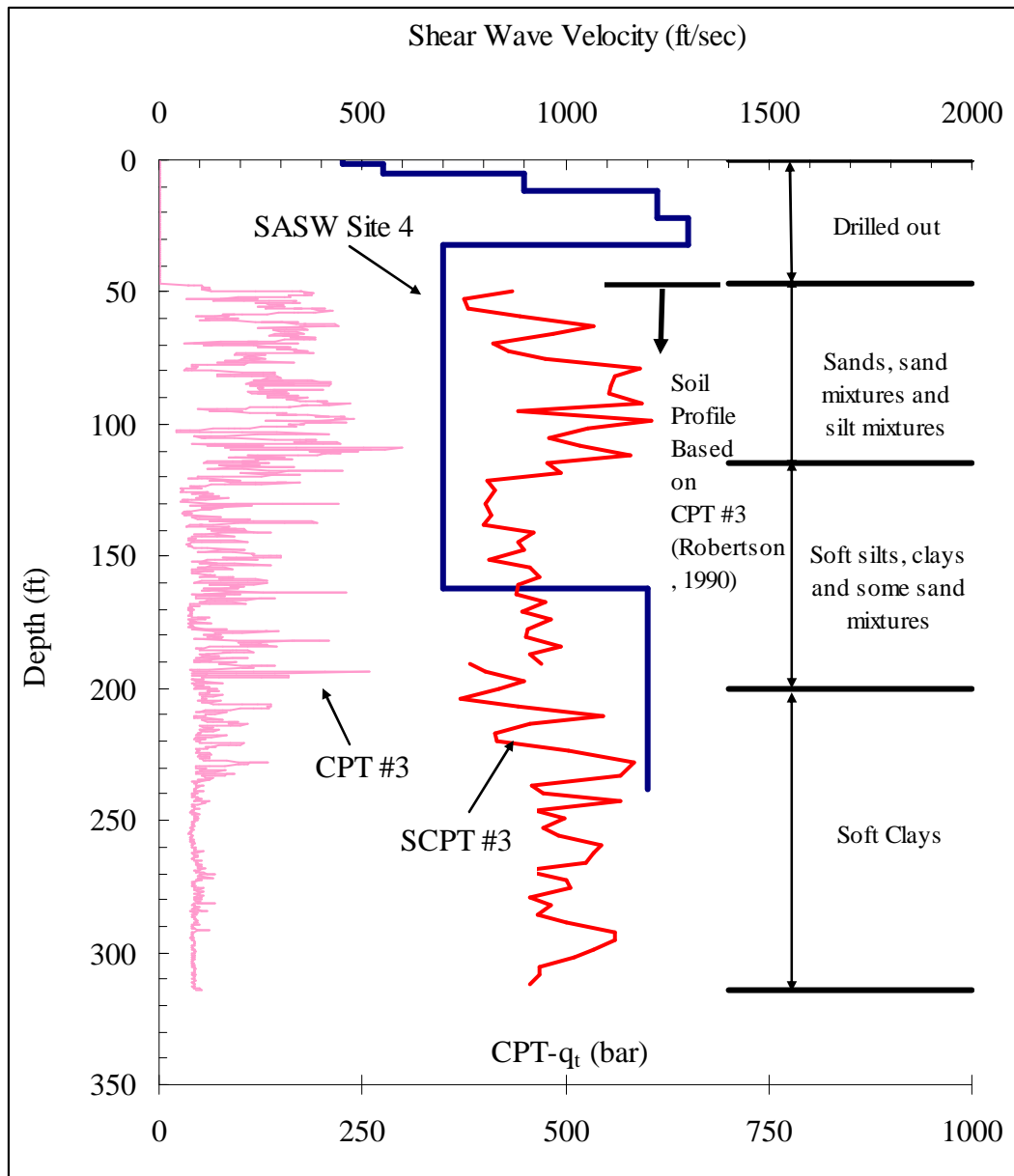
Figure 8.26 Comparison of the V_s Profile at SASW Site 4 with the V_s Profile from SCPT #3 and the CPT Profile from CPT #3
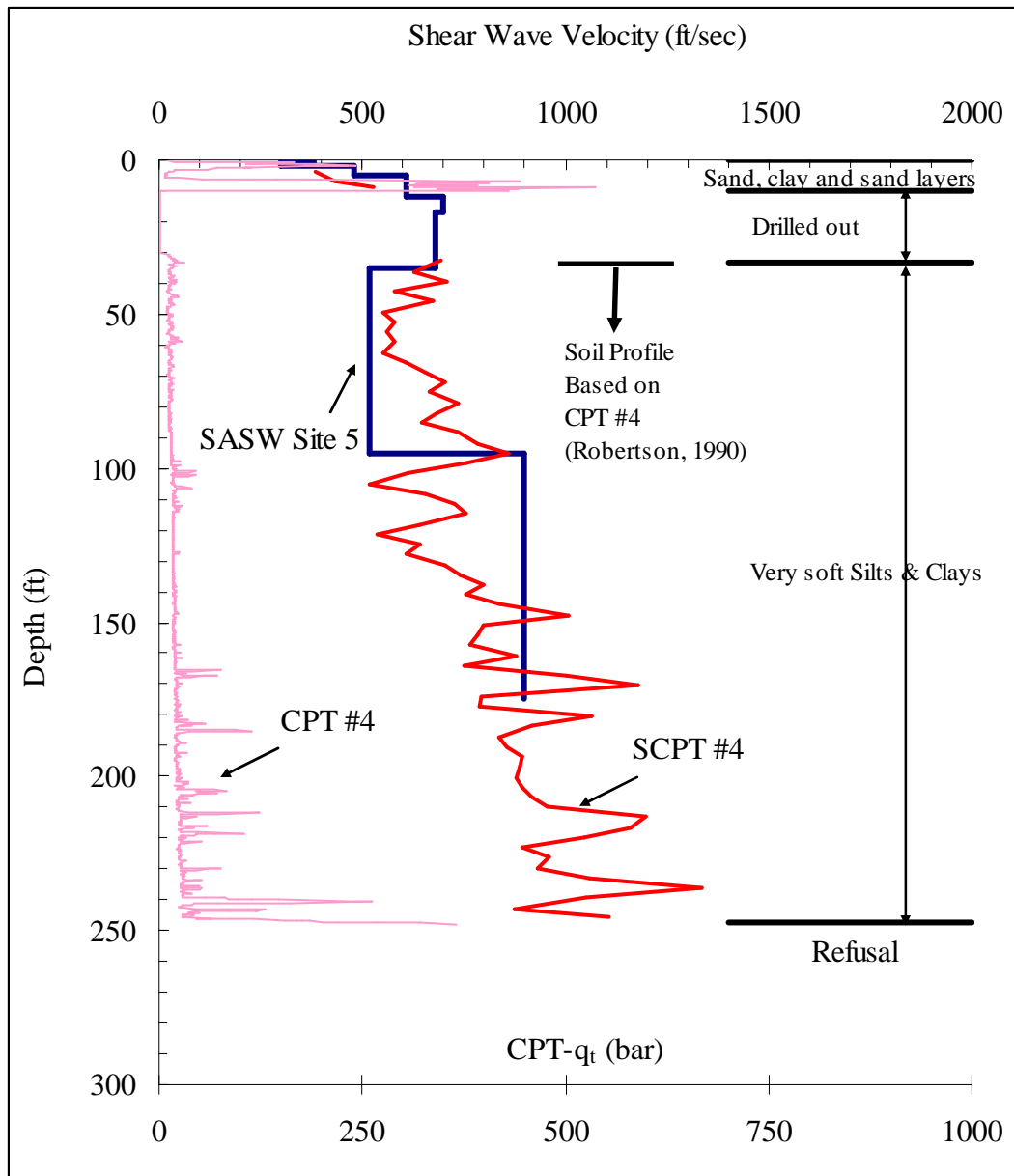
Figure 8.27 Comparison of the V_s Profile at SASW Site 5 with the V_s Profile from SCPT #4 and the CPT Profile from CPT #4
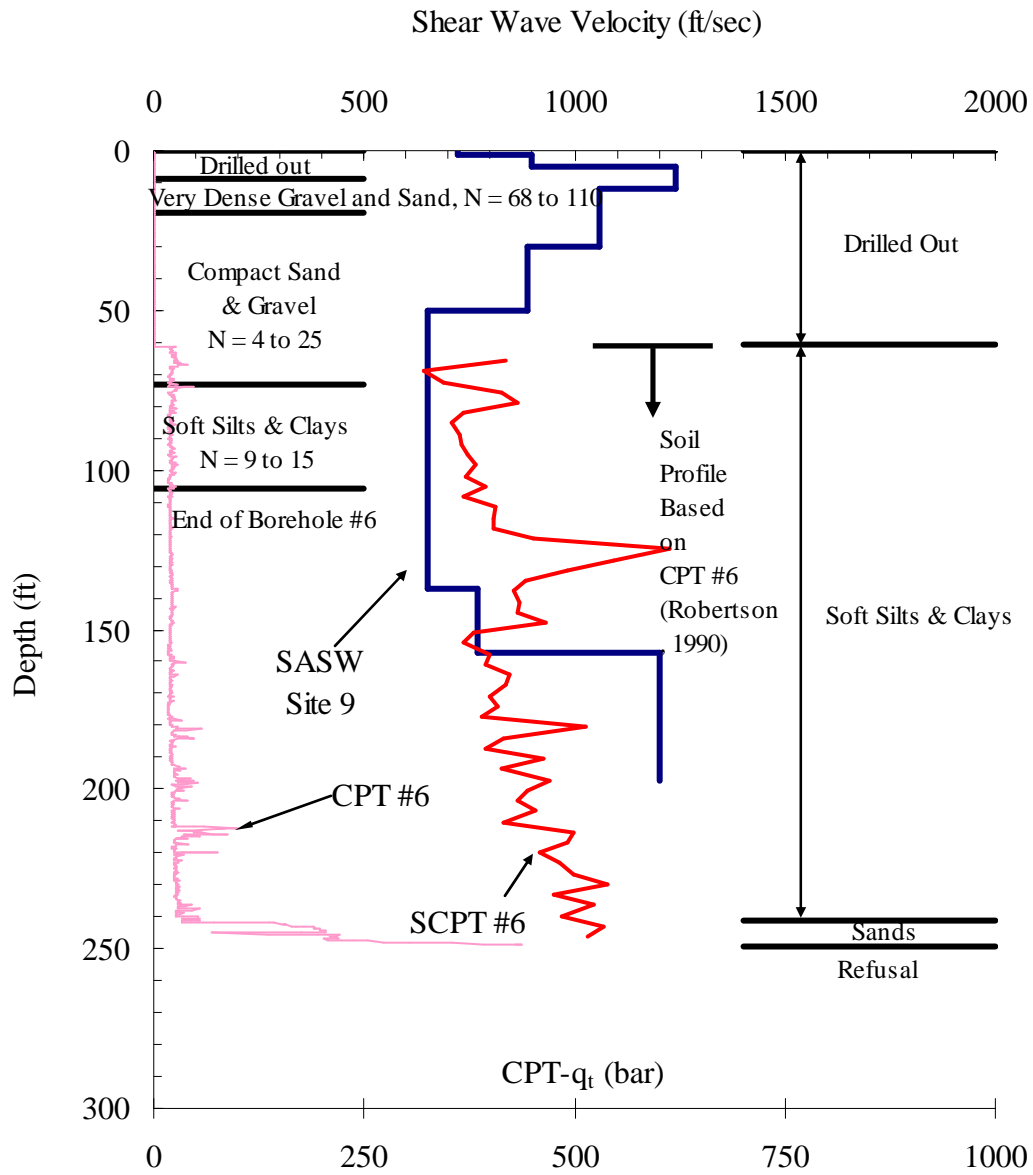
Figure 8.28 Comparison of the V_s Profile at SASW Site 9 with the V_s Profile from SCPT #6 and the CPT Profile from CPT #6

the facts that: (1) the V_s profile from the SASW test is a global measurement which represent averaged properties over the length of the test array, whereas the V_s profile from the SCPT test is a localized measurement of the material close the hole area over a depth interval of 1 m at each measurement depth, (2) the SASW test evaluates V_s generally in the frequency range of 5 to 50 Hz for depths greater than about 25 ft while the SCPT evaluates in the frequency range of 100's Hz, and (3) the resolution of SASW V_s profile depends on the geophone spacings and recording time interval, with the V_s profile at deep depths averaging over larger distances. The resolution of the SCPT results does not vary with depth so that it can detect localized anomalies at depth. Often the SCPT method produces 5 to 10% higher shear wave velocity profile than SASW test does at the same location, likely due to excitation frequencies. Based on boring logs, a cross-section of the geological conditions crossing SASW Site 9 is shown in Figure 8.29 (Lewis, 2011). Clearly lateral variability is shown.

Figure 8.29   A Cross-section of the Geological Condition at the Project Site and in the
         Area of SASW Site 9 (from Lewis, 2011)

8.7.2   Comparisons of SASW and Equivalent SCPT Dispersion Curves

To investigate differences in the V_s profiles determined by the SASW and SCPT measurements, V_s profiles from the SCPT were converted to "equivalent" SASW dispersion curves. However, upon reviewing the V_s profiles from the SASW and SCPT tests, it can be seen that the SCPT V_s profiles only include data for a portion of the depth at each site generally due to the fact that no SCPT test could be performed in the shallow gravel/cobble materials. Therefore, for shallow depths without SCPT data, V_s values from the SASW profiles were used to construct the SCPT V_s profiles from the ground surface to the top of the actual SCPT measurements. Theoretical dispersion curves were then generated for the composite SCPT V_s profiles at SASW Sites 3, 4, 5 and 9 as shown in Figures 8.30 through 8.33. The V_s profiles and theoretical dispersion curves for these four sites are shown in Figures 8.34 through 8.37. Based on the comparison of the equivalent SCPT and the SASW dispersion curves, the following conclusions can be drawn.

1. Clearly, significant lateral variability at the project site contributes to the difference between the localized SCPT values and the global SASW values. This lateral variability is well shown by the two different geologic profiles (boring records) near SASW Site 8.

2. At Site 5, the SCPT and SASW theoretical dispersion curves agree quite well, with only small differences as seen in Figure 8.36.

3. At Site 4, the SCPT V_s profile at wavelengths ≥ 70 ft does not agree with the field dispersion curves, most likely indicating lateral variability in the materials.
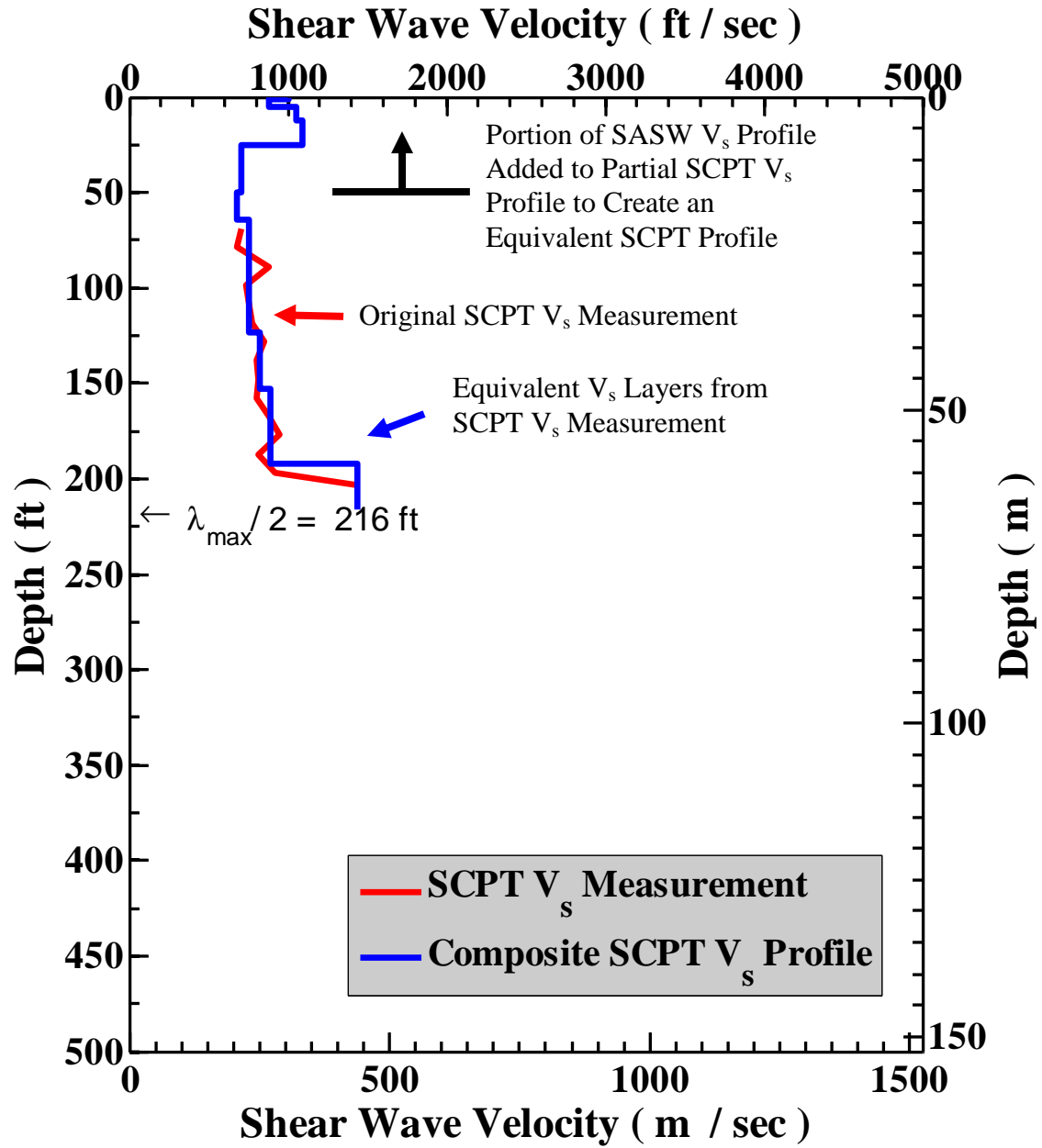
Figure 8.30 Composite SCPT V$_s$ Profiles at SASW Site 3 Used to Generate an
Equivalent SCPT Dispersion Curve
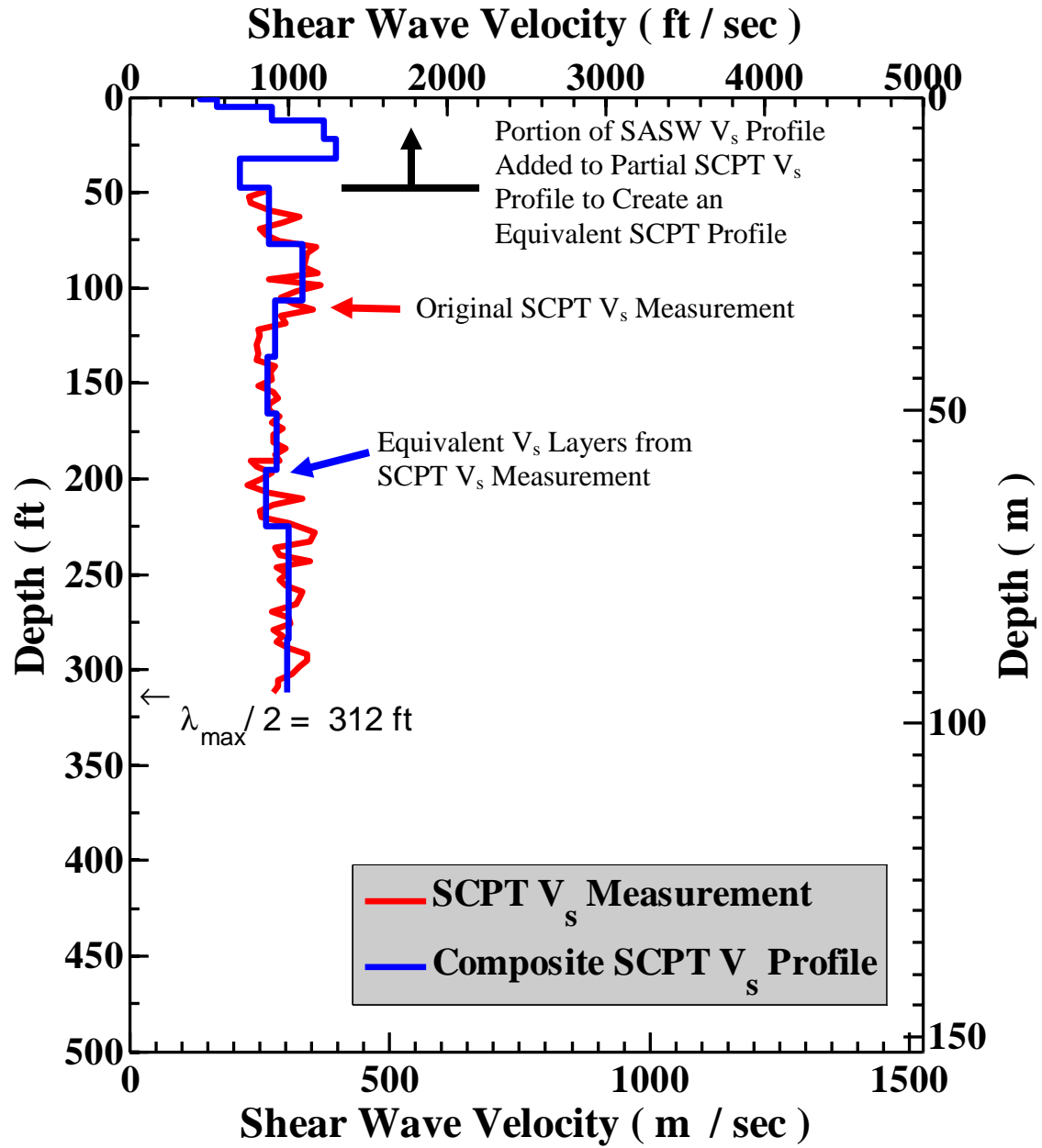
Figure 8.31   Composite SCPT V_s Profiles at SASW Site 4 Used to Generate an
Equivalent SCPT Dispersion Curve
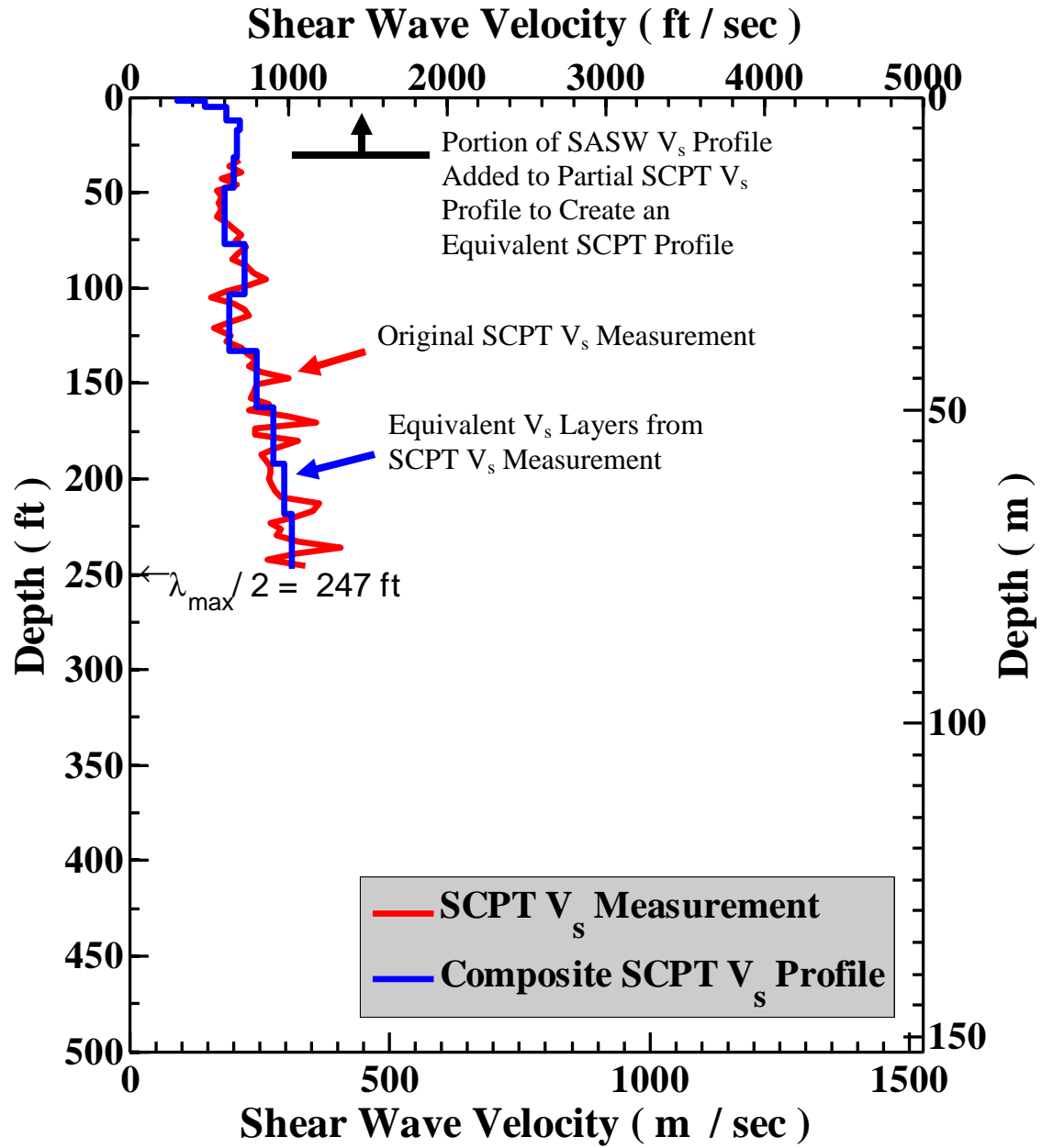
Figure 8.32 Composite SCPT V_s Profiles at SASW Site 5 Used to Generate an
Equivalent SCPT Dispersion Curve

Figure 8.33 Composite SCPT V_s Profiles at SASW Site 9 Used to Generate an
Equivalent SCPT Dispersion Curve
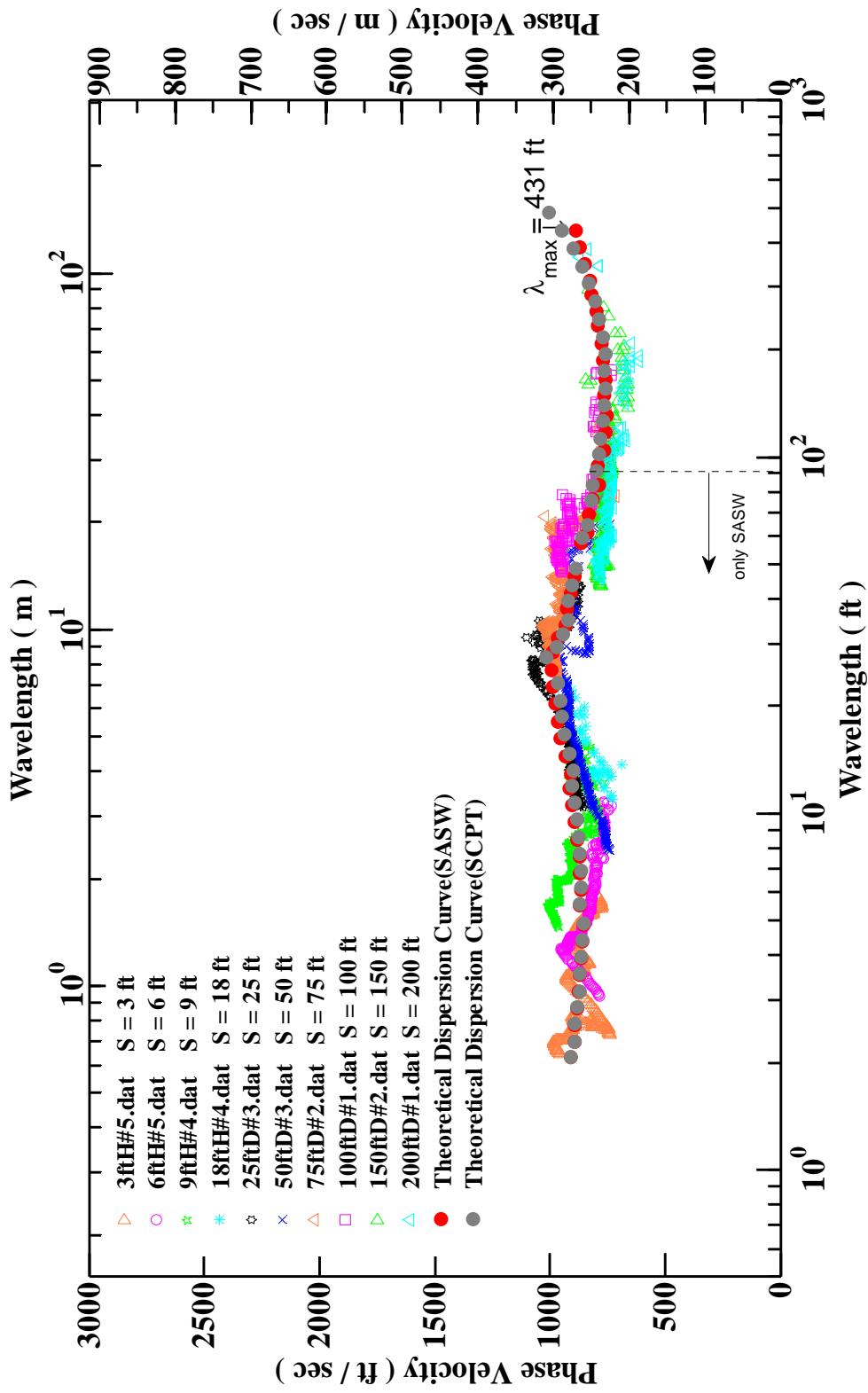
Figure 8.34   Comparison of Theoretical Dispersion Curve Calculated from Composite SCPT and Field and Theoretical Dispersion Curves from SASW Measurements at Site 3
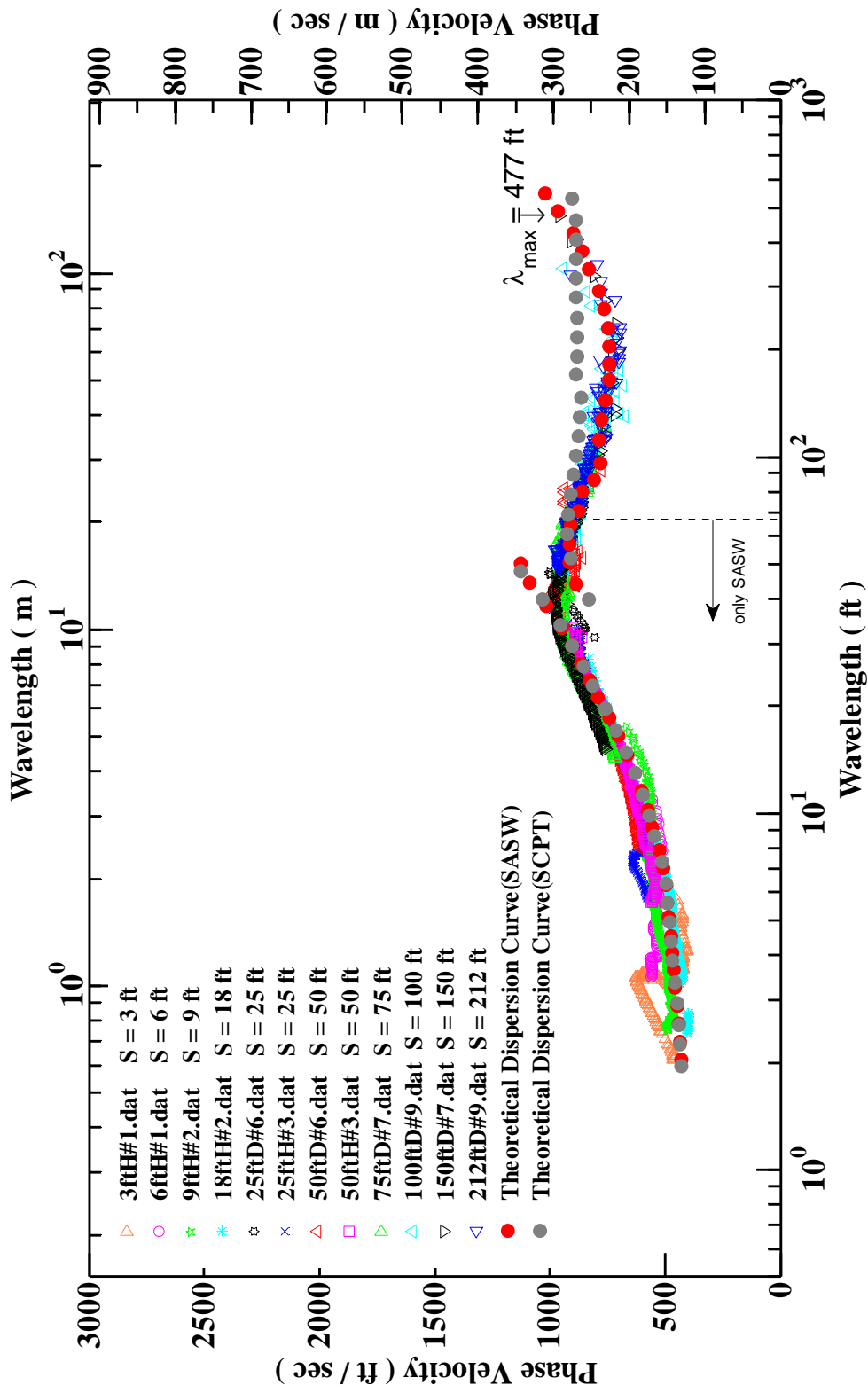
Figure 8.35   Comparison of Theoretical Dispersion Curve Calculated from Composite SCPT and Field and Theoretical Dispersion Curves from SASW Measurements at Site 4

244
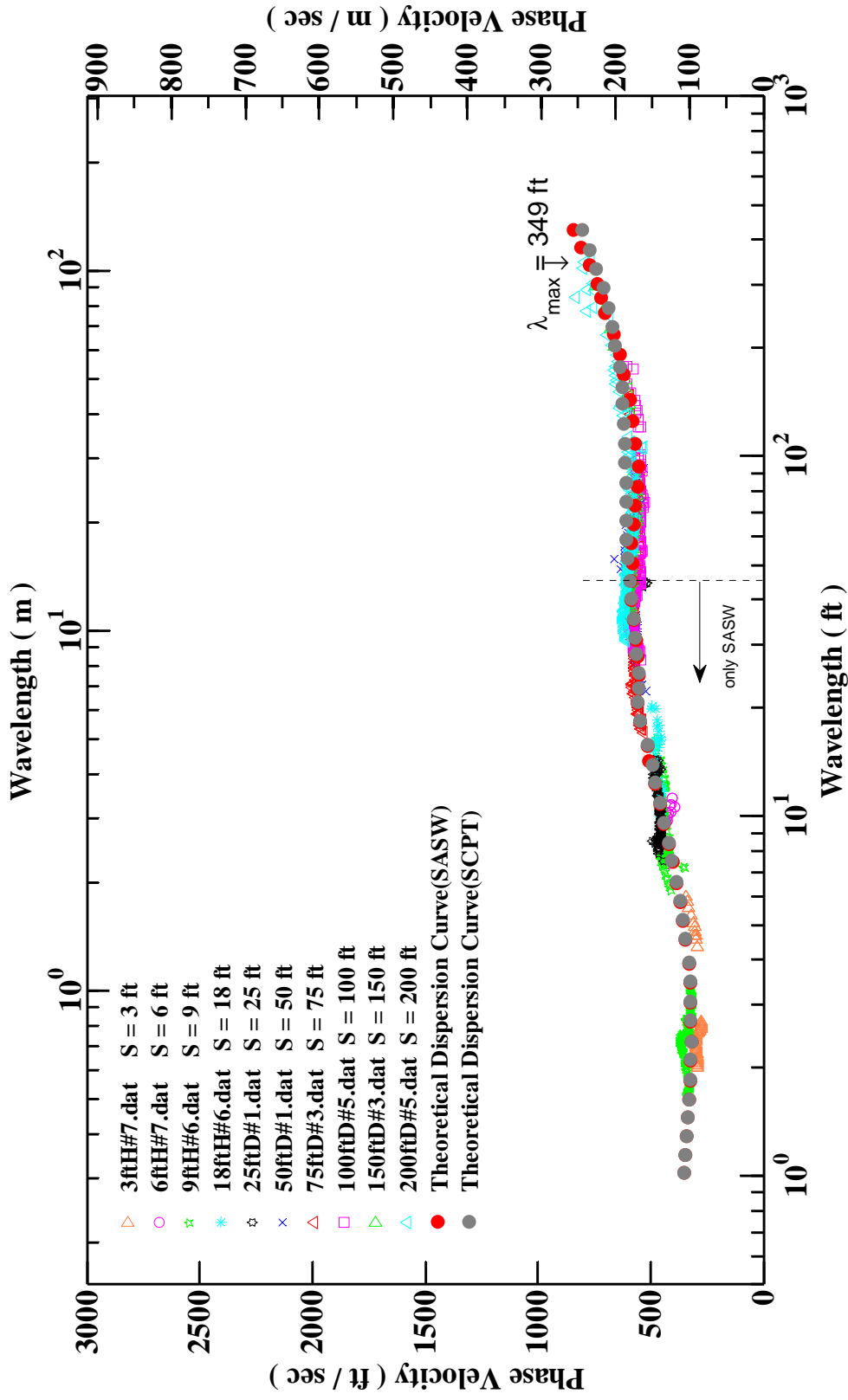
Figure 8.36   Comparison of Theoretical Dispersion Curve Calculated from Composite SCPT and Field and Theoretical Dispersion Curves from SASW Measurements at Site 5
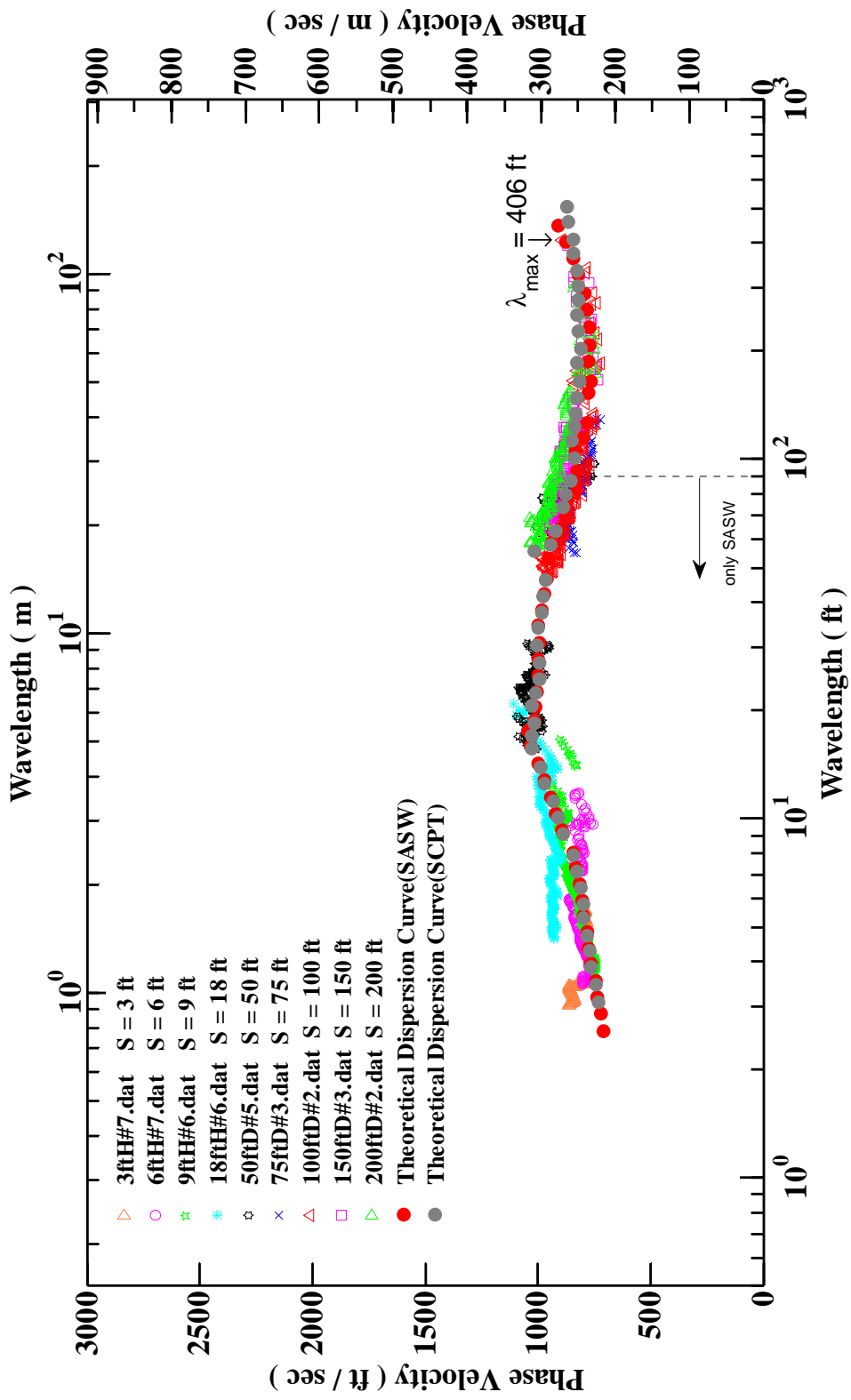
Figure 8.37 Comparison of Theoretical Dispersion Curve Calculated from Composite SCPT and Field and Theoretical Dispersion Curves from SASW Measurements at Site 9

246

4. At Site 9, the SCPT did not sample the stiffer material at depths of 160 to 200 ft as shown by the lack of fit to the SASW theoretical dispersion curve at wavelength greater than 100 ft. Again, this difference is most likely attributed to lateral variability.

These comparisons are made not to imply any errors in measurements but to show typical differences that should be expected at sites with high lateral variability between global and localized (at depth) V_s measurements.

8.8 CONCLUSIONS

The Spectral-Analysis-of-Surface-Waves (SASW) method is an in-situ, non-destructive method for determining shear-wave velocity and thus, stiffness of subsurface materials. As part of a geotechnical engineering investigation, SASW tests were performed at fourteen locations at an industrial site in British Columbia, Canada. Comparisons of velocity and stratigraphy between SASW, standard penetration test (SPT) boreholes, and seismic piezocone penetration test soundings (SCPT) were made. The results showed that: (1) the borings revealed significant lateral variability in material at a few test sites; (2) SASW testing with a large bulldozer as the seismic source, within the active industrial complex, allowed V_s profiling to depths of around 200 to 400 ft; and (3) good agreement was generally observed between SASW and SCPT results, once the difference between global and localized sampling was considered.

In this chapter, it is demonstrated that V_s profiles can be sub-divided based on the empirical relationships between depths and shear wave velocities for different materials. Good agreement between SASW V_s profiles and boring record is expected when lateral variability in material at a site is low. Lateral variability contributed to much of the difference between V_s profiles from SASW and SCPT tests. It is interesting to see how

V_s profiling with a global sampling method (SASW) method and a localized sampling method (SCPT) can contribute to improved subsurface information and better interpretation of the geotechnical setting at the site.

Chapter 9   Summary, Conclusions and Recommendations

9.1 SUMMARY

Shear wave velocity of geotechnical materials can be used in dynamic structural design and site amplification analysis. A widely used in-site method to assess the properties of geotechnical materials at small strain levels is surface wave testing. In this dissertation, three surface wave testing methods: Spectral-Analysis-of-Surface-Waves (SASW), Multichannel-Analysis-of-Surface-Waves (MASW, based on F-K transform) and Multichannel Surface wave method (based on Beamforming (BF)) were studied. The dissertation can be divided into the following three parts: (1) introduction of wave propagation theory and general procedures of surface wave testing, (2) numerical and field parametric studies with Spectral-Analysis-of-Surface-Waves, Beamforming and Multi-Channel-Analysis-of-Surface-Waves testing methods and (3) characterization of material by shear wave velocity profiles from SASW tests at two project sites.

The fundamentals of wave propagation in a uniform half-space and a uniform, horizontally-layered half-space are discussed herein. The dispersive nature of Rayleigh waves propagating in a vertically heterogeneous medium forms the basis of surface wave testing. The transfer matrix method, a technique used to calculate the theoretical solutions of dispersion curves, is presented in Chapter 2. The introduction is followed by a series of discussions on the performance and characteristics of existing forward modeling algorithms. It is concluded that the dynamic stiffness matrix method, proposed by Kausel and Rosset (1981), is able to generate dispersion curves for both plane Rayleigh wave, as presented by a 2-D solution, and combination of body and cylindrically Rayleigh waves, as presented by a 3-D solution.   Sensitivity studies were performed based on a layered model (as representing a generalized geotechnical soil system) to investigate the impact

of model parameters (layer thickness, density, V_s and V_p) on the shape of dispersion curves.

The general procedures for surface wave testing, SASW, BF and MASW are discussed. The original steady-state, Rayleigh-wave method is the method that began R-wave testing to characterize material properties but was cumbersome and empirically based. The SASW method significantly reduced field testing time and developed a sound, theoretical solution to analyze the field data. The MASW method uses multi-channel of receivers to collect data simultaneously and converts the wavefields into a frequency-wavenumber domain by F-K transform to find the ridges with maximum energy, which are then transformed into experimental dispersion curves. Beamforming technique also analyzes multichannel data and generates dispersion curves like the MASW method.

The results and discussions based on the analysis of synthetic seismograms from three models are presented in Chapter 4. The three models are used to represent geotechnical sites under three circumstances: (1) a bedrock site, (2) a normally dispersive site and (3) an inversion site. All data are processed with the SASW 3-D method, F-K and beamforming techniques to produce experimental dispersion curves, which are then compared to theoretical solutions in both modal and apparent phase velocities. It is found that SASW method produced results in apparent phase velocities, which agree well with the results from F-K and beamforming transform when dispersion data corresponding to the maximum energy among all modes along the frequency axis are used. However, the typical MASW method generally only uses the theoretical fundamental mode solution to fit the field data.

A comprehensive parametric study on source type, receiver type and test setup of surface wave testing at Hornsby Bend site is presented in Chapters 5 and 6. Two trips were made with different seismic sources (T-Rex and Liquidator) and receiver spacings.

The results from the SASW test performed at the center of the test array, were used as references to compare with the results from MASW testing. Different source signals (chirp, stepsine and Ricker wavelet, along with the impact from a 12-lb sledge hammer) with different frequency components were used both in the SASW, BF and MASW tests. Two types of geophones (vertical velocity transducers), one with a resonant frequency of 1-Hz, another of 4.5-Hz, were used as receivers with different spacings in both tests. For the MASW test, source-to-receiver spacings, number of geophones and geophone spacing were varied to study their impacts on the shape of experimental dispersion curves. Results from the SASW, BF and MASW tests are compared and discussed in terms of both dispersion curves and shear wave velocity profiles. Two signal processing techniques, one in the frequency domain aimed to interpolate ill-sampled phase plots, and another in the spatial domain for possible improvement of spatial resolution, were presented. CPT and SCPT results, along with a boring log at the Hornsby Bend area, were compared with V_s profiles from the SASW tests.

It is shown in Chapters 7 and 8 that the shear wave velocity profiles from SASW testing can be further interpreted and grouped into different material types based on comparison with empirical reference V_s profiles for various materials. Spectral-Analysis-of-Surface-Waves surveys were performed on the Big Island of Hawaii to obtain V_s information beneath the 22 USGS strong-motion stations. The shear wave velocity profiles were divided into portions that contained unweathered basalt, weathered basalt and stiff soil. The new V_s data were used to develop a NEHRP site class map for the Big Island. The SASW test results from a project site in British Columbia, Canada is shown in Chapter 8. The empirical relations between shear wave velocity and depth for soft soil, dense sand and dense gravel were used to differentiate portions of the V_s profile into different material types. Six groups of material were created based on the reference

profiles. The groups of interpreted material based on shear wave velocity from the SASW test are compared to the existing geological information, such as SCPT, CPT and SPT test results as well as boring logs.

9.2 CONCLUSIONS

By comparing the performance of SASW and MASW tests, it is concluded that: (1) In the SASW method, data are processed based on apparent phase velocity and analyzed with a theoretical 3-D solution to include the influence of various types of waves (body, fundamental and higher modes of Rayleigh waves). Thus, this method produces a correct representation of V_s profiles within the assumption made in the analysis (lateral uniformity, horizontal layering, etc) and (2) In the MASW method, data are processed based on modal phase velocity but analyzed with only the fundamental mode solution. It is observed that when higher modes dominate, the resulting V_s profile from the matching process with only the fundamental mode may lead to a biased result (overestimating material stiffness at the Hornsby Bend site). A better inversion program is needed to fit the MASW and BF field dispersion curves.

Based on the results from the parametric studies at the Hornsby Bend Sites, a few conclusions are made regarding the MASW testing technique:

1) Source energy plays a critical role in defining the experimental dispersion curve for the MASW testing (This point is also true for other surface wave methods). Stronger sources are always preferred for deeper material investigations. For example, a 12-lb sledge hammer can produce a maximum usable wavelength up to about 100 ft, whereas a 1-8 Hz chirp produced by

Liquidator can reach a maximum wavelength of about 1400 ft at the Hornsby Bend site.

2) Source offsets affects the shape of the experimental dispersion curve. As the source moves away from the receiver array, less information is obtained on the shallower material. Also, higher modes gradually dominate the apparent phase velocity as the source moves away from the receivers.

3) It is observed that by keeping the same length of the test array, receiver spacing has a noticeable influence on the usable range of the experimental dispersion curves from MASW testing. The larger the receiver spacing is, the more severe the spatial aliasing is in the test result. At this site, by comparing the performance of 3-ft, 10-ft and 16.4- ft (5-m) receiver spacings, it is observed that the problem of spatial aliasing mainly occurs at higher modes. By implementing a spatial interpolation technique, the dispersion curve in the aliased zone could be recovered for the data at the Hornsby Bend site.

4) By changing the number of receivers while maintaining equal receiver spacing, the total length of test array is altered and dispersion results are changed. These changes can be attributed to: (1) site lateral variability and (2) higher modes at larger receiver distances. At the Hornsby Bend site, it was found that higher modes play a more important role in defining the experimental dispersion curve. It was also discovered that an adequate length of the test array should be used to correctly capture material properties at deeper depths. This length is about 200 ft for the Hornsby Bend site.

5) Two types of receivers, 1-Hz geophones and 4.5-Hz geophones, were used in collecting vertical ground motions induced by seismic sources. They generally produced similar results given the same receiver spacing and number of

253

receivers used. However, 1-Hz geophones out-performed 4.5-Hz geophones since they have a better mechanical design at low frequencies.

Material characterization based on shear wave velocity profiles can be done by comparing measured V_s profiles to reference profiles for different materials once a general idea of material types is known. By comparing the interpreted V_s material groups to the existing geological information, good agreement was observed when lateral variability was low at the site. However, poor agreement can occur when lateral variability is high, since surface wave testing provides global measurements while CPT, boring and other traditional testing techniques generate localized measurements.

9.3 RECOMMENDATIONS

The research presented in this dissertation was conducted only at the Hornsby Bend site. Additional experimental studies should be carried out at other sites, e.g. strong velocity contrast at shallow depths, existence of thick inversion zones or dipping material boundaries, to study the characteristics of the surface wave methods.

A more robust forward modeling algorithm and inversion program should be developed for the experimental dispersion curves from the multi-channel surface wave testing. The approximation of using the 3-D or 2-D WinSASW solutions to match the "fundamental mode" of the MASW dispersion curve results in differences of V_s profiles estimated from different surface wave methods, which may leads to a biased estimate of V_s value for the MASW method.

Spectral-Analysis-of-Love-Waves(SALW) or Multichannel-Analysis-of-Love-Waves(MALW) should be carried out if multiple horizontal geophones are available to be used in the field testing. The potential of developing this technique is that it can be

combined with SASW (or MASW) to develop a more robust V_s profile. Again, a robust forward modeling algorithm should be developed to generate multi-mode theoretical dispersion curves for Love waves.

References

Abo-Zena (1979) "A Dispersion Function Computation for Unlimited Frequency Values". Geophysical Journal of the Royal Astronomical Society, Volume 58, Issue 1, pp. 91–105

A.E.H. Love (1911) "Some Problems of Geodynamics", Cambridge University Press

Al-Hundaidi, M.O. (1994) "Analysis of Dispersed Multi-mode Signals of the SASW Method using Multiple Filter/Crosscorrelation Technique." Soil Dynamics and Earthquake Engineering, Volume 13, Issue 1, pp. 13-24

Aki, K. and P.G. Richards (1980) "Quantitative Seismology, Theory and Methods", Vol. I and II, W.H. Freeman and Company, San Francisco.

ASTM, 2004, "Standard Method of Deep Quasi-Static Cone and Friction-Cone Penetration Tests of Soil"; ASTM Standard D 3441, ASTM International, West Conshohocken, PA, 7 pp.

ASTM, 2007, "The Method for Performing Electronic Friction Cone and Piezo-Cone Penetration Testing of Soils, Annual Book of Standards", ASTM D-5778-07 Volume 04,08, American Society for Testing and Materials, West Conshohocken, PA., 2007.

Dunkin J.W. (1965) "Computation of Model Solutions in Layered Elastic Media at High Frequencies" Bulletin of the Seismological Society of America, Volume 55, No. 2, pp. 335-358

Foinquinos M.R. (1991) "Analytical Study and Inversion for the Spectral Analysis of Surface Waves Method". Thesis, The University of Texas at Austin. 119pp

Foti, S. (2000) "Multistation Methods for Geotechnical Characterization Using Surface Waves", Ph.D. Dissertation, Politecnico di Torino, 222 pgs.

Fuchs, K. (1968) "The Reflection of Spherical Waves from Transition Zones with Arbitrary Depth- Dependent Elastic Moduli and Density". J. Phys. Earth Volumn 16, pp. 27-41

Fuchs, K. Muller, G. (1971) "Computation of synthetic seismograms with the reflectivity method and comparison with observations". Geophysical Journal of the Royal Astronomical Society, Volume 23, Issue 1, pp. 417–433

Fuhriman, M.D. and Stokoe, K.H., II (1993) "Crosshole Seismic Test at the Gilroy No. 2 and Treasure Island Sites Affected by the 1989 Loma Prieta Earthquake," Geotechnical Engineering Report GR93-1, Civil Engineering Department, University of Texas at Austin, Austin, TX, January, 259 pgs.

Gucunski, N., and Woods, R. D., (1992) "Numerical Simulation of the SASW Test," Soil Dynamics and Earthquake Engineering, Vol. 11, pp. 213-227

Gazetas G. (1982) "Vibration Characteristics of Soil Deposits with Variable Wave Velocity", International Journal for Numerical and Analytical Methods in Geomechanics, Volume 6, Issue 1, pp. 1–20

Gilbert F. and Backus G. E. (1966) "Propagator Matrices in Elastic Wave and Vibration Problems" Geophysics, Volume 31, pp. 326-332

Gucunski, N. and R.D. Woods (1991) "Inversion of Rayleigh Wave Dispersion Curve for SASW Test." Proceedings of the 5th International Conference on Soil Dynamics and Earthquake Engineering 127-138

Haskell, N. A., (1953) "The Dispersion of Surface Waves on Multilayered Media," Bulletin of the Seismological Society of America, Volume. 43, pp. 17-34.

257

Hardin, B.O., (1978) "The Nature of Stress-Strain Behavior for Soils," Proceedings, Earthquake Engineering and Soil Dynamics, ASCE Specialty Conference, Pasadena, California, pp. 3-90.

Idriss, I.J., Dobry, R., Doyle, E.H., and Singh, R.D. (1976) "Behaviour of Soft Clays under Earthquake Loading Conditions," Proc. Eight Annual Offshore Tech. Conf., 605- 616.

Jathal, J.K. (2003) "Investigation of V_s Profiles Measured by Borehole and Surface-Wave Seismic Techniques," Thesis, The University of Texas at Austin, 348 pgs.

Joh, S.-H. (1996) "Advances in the Data Interpretation Technique for Spectral- Analysis-of-Surface-Waves (SASW) Measurements," Ph.D. Dissertation, The University of Texas at Austin, 240 pgs.

Kausel, E., Roesset, J.M., (1981) "Stiffness Matrices for Layered Soils", Bulletin of the Seismological Society of America, Volume 71, No.6, pp 1743-1761

Kennett, B. L. N. (1983) "Seismic Wave Propagation in Stratified Media". Cambridge University Press.

Kennett, B. L. N. and Kerry, N. J. (1979) "Seismic Waves in a Stratified Half-space". Geophysical Journal of the Royal Astronomical Society, Volume 57, Issue 1, pp. 557–583.

Knopoff, L (1964) "A Matrix Method for Elastic Wave Problems", Bulletin of the Seismological Society of America, Volume 54; No. 1, pp. 431-438

Knopoff, L. (1958) "Surface Motion of a Thick Plate". Journal of Applied Physics, Volume 29, pp. 661-670

Krautkrämer, J. and Krautkrämer, H. (1990) "Ultrasonic Testing of Materials". Springer-Verlag, Berlin, Heidelberg, and New York.

Li, S. (2008) "Deep Downhole Testing: Procedures and Analysis forHigh-Resolution Vertical Seismic Profiling", Ph.D. Dissertation, The University of Texas at Austin, 288 pgs.

Lin, Y. (2007) "Characterizing V_S Profiles by the SASW Method and Comparison withOther Seismic Methods", Ph.D. Dissertation, The University of Texas at Austin, 277 pgs.

Lee, B., (1996) "Analytical Studies of Surface Wave Propagation Along the Seafloor for Application to Spectral-Analysis-of-Surface-Waves (SASW) Testing" PhD Dissertation, UT-Austin, 332pp

Lee G.S. and Ma C.C., (2000) "Transient Elastic Waves Propagating in a Multi-Layered Medium Subjected to in-Plane Dynamic Loadings. I. Theory Proceedings: Mathematical, Physical and Engineering Sciences" Volume. 456

Menq, F.Y. (2003) "Dynamic Properties of Sandy and Gravelly Soils," Ph.D. Dissertation, The University of Texas at Austin, 390 pgs.

Miller, R., Xia, J., (1999) "Using MASW to Map Bedrock in Olathe, Kansas" Report, Kansas Geological Survey, Lawrence, Kansas, 9 pp.

Mok, Y. J., (1987) "Analytical and Experimental Studies of Borehole Seismic Methods," Ph.D. Dissertation, The Department of Civil Engineering, The University of Texas at Austin, Austin, TX.

Orozco, M. C. (2004) "Inversion Method for Spectral Analysis of Surface Waves (SASW)", Georgia Institute of Technology, PhD Dissertation, 287pp

Owino, J.O., and Jacobs, L.J. (1999) "Attenuation Measurements Incement-Based Materials Using Laser Ultrasonics". Journal of Engineering Mechanics, Volume 125, No. 6, pp. 637-647

Park, C.B., Miller, R.D., and Xia, J., (1999) "Multichannel Analysis of Surface Waves (MASW)" Geophysics, Volume 64, pp. 800-808

Park, C.B., Miller, R.D., Ryden, N., Xia, J., and Ivanov, J., (2005) "Combined Use of Active and Passive Surface Waves" Journal of Engineering and Environmental Geophysics (JEEG), Volume 10, pp. 323-334.

Park, C.B., and Miller, R.D., (2006) "Roadside Passive MASW" Proceedings of SAGEEP, April 2-6, 2006, Seattle, Washington

Park, C.B., Miller, R.D., and Xia, J., (1998)a "Imaging Dispersion Curves of Surface Waves on Multi-Channel Record" Society Of Exploration Geophysicists, Annual Meeting Abstracts, pp. 1377-1380.

Park, C.B., Miller, R.D., and Xia, J., (1998)b "Ground Roll as a Tool to Image Near-Surface Anomaly" Society Of Exploration Geophysicists, Annual Meeting Abstracts, pp. 874-877

Rayleigh J.W.S. (1885) "On Waves Propagated along the Plane Surface of an Elastic Solid", Proc. London Math. Soc. Volume. 17, pp. 4-11

Richart, F. E., Jr., Woods, R. D., and Hall, J. R. Jr. (1970) "Vibrations of Soils and Foundations," Prentice Hall, Englewood Cliffs, New Jersey, 414 pp.

Rix, G. J. (1988) "Experimental Study of Factors Affecting the Spectral-Analysis-of-Surface-Waves Method", Ph.D. Dissertation, The University of Texas at Austin, 315 pgs.

Robertson. P.K., Campanella, R.G., Gillespie, D., and Rice, A. (1986) "Seismic CPT to measure in situ shear wave velocity", Journal of Geotechnical Engineering, 112(8): 791-803.

Roesset, J.M., Chang D.-W., and Stokoe, K.H., II (1991) "Comparison of 2D and 3D Models for Analysis of Surface Wave Tests," Proceedings of the 5th International Conference on Soil Dynamics and Earthquake Engineering, pp. 111-126.

Rosenblad, B.L. (2000) "Implementing the Spectral-Analysis-of-Surface Waves (SASW) Method Offshore," Ph.D. Dissertation, The University of Texas at Austin, 298 pgs.

Ryden, N. (2004) "Surface Wave Testing of Pavements", Doctoral Thesis, Lund University, 139 pgs.

Sanchez-Salinero, I. (1987) "Analytical Investigation of Seismic Methods used for Engineering Applications," Ph.D. Dissertation, The University of Texas at Austin, 401 pgs.

Schwab F, Knopoff L. (1972) "Fast Surface Wave and Free Mode Computations". ; in Methods in Computational Physics: Academic Press, New York, pp. 87-180

Spitz, S., (1991) "Seismic trace interpolation in the F-X domain" Geophysics, Volume 56, pp. 785–794.

Stokoe, II, K.H., Lin, Y.C., Cox, B., Kurtulus, A., Jung, M.J. (2005) "Shear Wave Profiling at the Waste Treatment Plant Site, Hanford, WA," Vols. I and II, Geotechnical Engineering Report GR05-1, University of Texas at Austin, July, 243 pgs.

Stokoe, K.H., II, S.H. Joh, and R.D. Woods (2004) "Some contributions of in situ geophysical measurements to solving geotechnical engineering problems", Proceedings of the International Site Characterization ISC'2 Porto, Portugal.

Stokoe, K.H., II, B.L. Rosenblad, J.A. Bay, B. Redpath, J.G. Diehl., R. Steller, I.G. Wong, P.A. Thomas, and M. Luebbers (2003) "Comparison of VS profiles from three seismic methods at Yucca Mountain", in Soil and Rock America 2003, P.J.

Culligan, H.H. Einstein, and A.J. Whittle (editors), Verlag Glückauf GMBH, 1, 299-306.

Stokoe, K.H., II, S.G. Wright, J.A. Bay, and J.M. Roesset (1994) "Characterization of geotechnical sites by SASW method", in Technical Report - Geophysical Characterization of Sites, R.D. Woods (editor), ISSMFE Technical Committee 10, Oxford Publishers, 13th International Conference on Soil Mechanics and Foundation Engineering, New Delhi, India.

Tian J.Y., (2000) "Comparison between Reverberation-Ray Matrix, Reverberation-Transfer Matrix, and Generalized Reverberation Matrix, Wave Propagation in Materials for Modern Applications" ISBN 978-953-7619-65-7 InTech 526pp

Thrower E. N. (1965) "The Computation of the Dispersion of Elastic Waves in Layered Media" Journal of Sound and Vibration, Volume 2, Issue 3, pp. 210-226

Thompson, W. T., (1950) "Transmission of Elastic Waves through a Stratified Solid Medium," Journal of Applied Physics, Vol. 21, pp. 89-93.

Tran, K. T. and Hiltunen D.R. (2008) "A Comparison of Shear Wave Velocity Profiles from SASW, MASW, and ReMi Techniques". Geotechnical Earthquake Engineering and Soil Dynamics IV, GSP 181, ASCE

Vahid G. (1997) "An Automated Inversion Procedure for Surface Wave Testing". Phd Dissertation. Rutgers University

Wolfe, E.W. and J. Morris (1996) "Geologic Map of the Island of Hawaii", U.S. Geological Survey Miscellaneous Investigations Series I-2524-A, scale 1:100,000.

Wood, C. M. (2009) "The impact of source type, source offset, and receiver spacing on experimental MASW data at soft-over-stiff sites", Thesis, University of Arkansas, 239 pgs.

Woods, R. D. (1968) "Screening of Surface Waves in Soils." J. Soil Mech. Found. Div., Am. Soc. Civ. Eng., 94(4), pp. 951–979.

Wong, I., K. Stokoe, B. Cox, F.-Y. Menq, C. Hoffpauir, and P. Okubo (2008) "Shear-Wave Velocity Profiling of the USGS Strong Motion Stations on the Island of Hawaii" (abs.), Seismol. Res. Lett., **79**, 339.

Wong, I.G., K.H. Stokoe, II, B.R. Cox, Y-C. Lin, and F-Y. Menq (2011) "Shear-Wave Velocity Profiling of Strong Motion Sites that Recorded the 2001 Nisqually, Washington, Earthquake", Earthquake Spectra, 27, 183-212.

Yang C. (1993) "Rayleigh Wave Exploration", in Chinese, China Geology Publishing House, 215 pp.

Youhua, F., Jiaqi, L., Bo, H., (2001), "Research on Theoretic Computation of Rayleigh Wave Dispersion Curve", Journal of Hunan University, Volumn.33(5)

Yoon, S. and Rix G.J. (2009), "Near-Field Effects on Array-Based Surface Wave Methodswith Active Sources", Journal of Geotechnical and Geoenvironmental Engineering, Volumn.135 No.3 pp.399-406

Zywicki, D.J. (1999). "Advanced Signal Processing Methods Applied to Engineering Analysis of Seismic Surface Waves," Ph.D. Thesis, Georgia Institute of Technology, 357 pp.

Zywicki, D. J. and Malladi, S. (2007). "Forward-Backward Cylindrical Beamformer and Geometric Spreading Weighting for Seismic Surface Wave Parameter Estimation." Proceedings of Geo-Denver 2007, Denver, CO.

Zywicki, D. J. and Glenn J. R. (2005), "Mitigation of Near-Field Effects for Seismic Surface Wave Velocity Estimation with Cylindrical Beamformers", American Society of Civil Engineers Journal of Geotechnical and Geoenvironmental Engineering, August, 2005, pp. 970-977

Vita

Jiabei Yuan was born in Hunan, China, on November 1, 1981, the son of Nansheng Yuan and Lina He. He graduated from Tongji University, Shanghai, China, and received Bachelor of Engineering degree in Civil Engineering in June 2003. He continued the study at China University of Geosciences in Beijing. He received his Master of Engineering degree in Geotechnical Engineering in June 2006. He enrolled at the University of Texas at Austin since August 2006.

Permanent address: Chigangchong, Changsha, Hunan, China, 410007

This dissertation was typed by the author